

Project THEMIS  
Technical Report No. 23  
STRATIFIED SHEAR FLOWS OVER  
A SIMULATED THREE-DIMENSIONAL  
URBAN HEAT ISLAND

by

S. SethuRaman  
and  
J.E. Cermak

Prepared under

Office of Naval Research  
Contract No. N00014-68-A-0493-0001  
Project No. NR 062-414/6-6-68 (Code 438)  
U.S. Department of Defense  
Washington, D.C.

"This document has been approved for public release  
and sale; its distribution is unlimited."

Fluid Dynamics and Diffusion Laboratory  
College of Engineering  
Colorado State University  
Fort Collins, Colorado



August 1973

CER73-74SS-JEC4

## ABSTRACT

### STRATIFIED SHEAR FLOWS OVER A SIMULATED THREE-DIMENSIONAL URBAN HEAT ISLAND

Three dimensional airflow over a rectangular heat island was studied for various conditions of approach flow in a wind tunnel. Three different thermal stratifications of the approach flow were selected for the study---neutral, ground based and elevated inversions. For each of these flows studies were conducted with and without roughness over the heat island for the conditions with and without heating of the island. Approach flow temperature profiles were modeled according to atmospheric data available in the literature.

For each of the twelve cases mentioned above, measurements of mean wind velocity, longitudinal velocity fluctuations, mean temperature and temperature fluctuations were made. In addition, mean concentration measurements of a radio-active gas released from a two-dimensional, ground-level line source upwind of the heat island were also made. Flow patterns were visualized for different cases with the help of a passive smoke source. Comparisons of data from the wind-tunnel measurements with the field data were made. Three-dimensional measurements of the mean wind velocity, temperature and turbulence have yielded valuable information concerning the flow of air around a typical urban heat island.

The mechanisms of the heat island observed in the wind-tunnel for different stratified flows were very similar to those observed in the field. The urban heat island plume that passes aloft downwind causes an appreciable reverse flow onto the heat-island. The helical vortices

at the edge of the heat island cause a reduction in the turbulence level resulting in high concentrations of the mass released from a continuous line source upwind of the heat island.

A theoretical model based on linearized equations of motions incorporating a boundary layer type velocity profile has been developed to predict the urban excess temperatures and velocities. Theoretical results compare fairly well with data obtained in the laboratory and in the field.

## ACKNOWLEDGMENTS

Financial support for this research study was provided by the Naval Office of Research by Contract Number N00014-68-A-0493-0001.

The author gratefully acknowledges this support.

## TABLE OF CONTENTS

<u>Chapter</u>		<u>Page</u>
	LIST OF TABLES . . . . .	ix
	LIST OF FIGURES . . . . .	x
	LIST OF SYMBOLS . . . . .	xix
I	INTRODUCTION . . . . .	1
II	THEORETICAL AND EXPERIMENTAL BACKGROUND . . . . .	4
	2.1 Physical basis of the urban heat island . . . . .	4
	2.2 Field studies . . . . .	6
	2.3 Theoretical studies . . . . .	13
	2.4 Wind tunnel studies of urban heat island . . . . .	16
	2.5 Concluding remarks . . . . .	17
III	THEORETICAL ANALYSIS . . . . .	19
	3.1 Development of the governing equations . . . . .	19
	3.2 Two dimensional model - General solutions . . . . .	20
	3.3 Three dimensional model - General solutions . . . . .	28
	3.4 Solutions for specific cases . . . . .	30
	3.4.1 Two dimensional model . . . . .	30
	3.4.2 Three dimensional model . . . . .	32
IV	EXPERIMENTAL EQUIPMENT AND DATA COLLECTION . . . . .	33
	4.1 Physical arrangement of the experiment . . . . .	33
	4.1.1 Electrical heater plates . . . . .	38
	4.1.2 Line source of tracer gas . . . . .	34
	4.2 Measurements . . . . .	35
	4.2.1 Mean velocity and turbulence . . . . .	35
	4.2.2 Surface temperature . . . . .	37
	4.2.3 Mean and fluctuating temperature . . . . .	38

TABLE OF CONTENTS (Continued)

<u>Chapter</u>	<u>Page</u>
4.2.4	Mean mass concentrations . . . . . 40
4.2.5	Flow visualization . . . . . 40
4.3	Similarity criteria . . . . . 41
4.4	Data collection . . . . . 45
V	DISCUSSION OF EXPERIMENTAL RESULTS . . . . . 46
5.1	Flow visualization . . . . . 46
5.2	Mean temperature distribution . . . . . 48
5.2.1	Surface temperature distributions and mean temperature profiles along the centerline . . . . . 48
5.2.2	Mean temperature distributions along the width of the heat island . . . 51
5.2.3	Mean temperature contours . . . . . 53
5.3	Development of different boundary layers over the model . . . . . 54
5.4	Mean velocity distributions . . . . . 55
5.4.1	Mean velocity profiles along the centerline . . . . . 55
5.4.2	Mean velocity profiles along the width of the heat island . . . . . 59
5.5	Turbulence profiles . . . . . 61
5.6	Temperature fluctuations . . . . . 63
5.7	Concentration distributions for the mass released from a two dimensional continuous line source located upwind of the heat island . . . . . 64
5.8	Shear velocity and roughness length . . . . . 66
5.9	Distribution of bulk Richardson numbers . . . . 68
5.10	Turbulent energy distribution . . . . . 69
5.11	Diffusion from continuous point sources . . . . 71

TABLE OF CONTENTS (Continued)

<u>Chapter</u>		<u>Page</u>
	5.12 Comparison of the airflow over smooth and rough heat island . . . . .	72
	5.13 Comparison of the experimental perturbed values with the theoretical results . . . . .	74
	5.14 Comparison of the wind-tunnel and field experimental results . . . . .	77
VI	CONCLUSIONS . . . . .	81
	REFERENCES . . . . .	83
	APPENDIX . . . . .	87
	FIGURES . . . . .	92

LIST OF TABLES

<u>Table</u>		<u>Page</u>
4.1	Performance Characteristics of the Meteorological Wind Tunnel . . . . .	88
4.2	Technical Data for the Temperature Compensated Probe (DISA55E30) . . . . .	89
4.3	Average Thickness of the Momentum Boundary Layers Over the Heat Island . . . . .	90
5.1	Footage Index for the Motion Picture . . . . .	91

## LIST OF FIGURES

<u>Figure</u>		<u>Page</u>
2.1	Day and nighttime energy balances in rural and urban regions . . . . .	92
3.1	Vertical profiles of the non-dimensionalized perturbed temperatures at the New York City center . . . . .	93
3.2	Predicted non-dimensional perturbed temperature profiles for different downwind distances for New York City (two-dimensional model with mountain function surface temperature distribution) . . . . .	94
3.3	Predicted non-dimensional perturbed vertical velocity profiles at different downwind distances for New York City (two-dimensional model with mountain function surface temperature distribution) . . . . .	95
3.4	Predicted non-dimensional perturbed longitudinal velocity profiles at different distances for New York City (two-dimensional model with mountain function surface temperature distribution) . . . . .	96
3.5	Comparison of the predicted non-dimensional perturbed temperature profiles for different surface temperature distributions for New York City . . . . .	97
3.6	Comparison of non-dimensional predicted perturbed temperature profiles obtained by the two-dimensional and the three-dimensional models for New York City for the mountain function surface temperature distribution . . . . .	98
4.1	Meteorological wind tunnel at Colorado State University . . . . .	99
4.2	A line sketch of the relative locations of the different components of the experimental arrangement (not to scale) . . . . .	100
4.3	Typical cross section of a heater . . . . .	101
4.4	Photograph of the variac assembly . . . . .	102
4.5	Sectional view of the line source . . . . .	103

LIST OF FIGURES (Continued)

<u>Figure</u>		<u>Page</u>
4.6	Details of the temperature compensated hot wire probe . . . . .	104
4.7	Calibration equipment for the hot wire . . . . .	105
4.8	Photograph of some of the instruments used for the experiments . . . . .	106
4.9	Photograph of the infra-red pyrometer . . . . .	107
4.10	Resistance-temperature relation for a tungsten wire . . . . .	108
4.11	A typical calibration curve for the Copper-Constantan thermocouple . . . . .	109
4.12	Sampling system for diffusion experiments . . . . .	110
4.13	Photograph of the diffusion sampling equipment . . . . .	111
4.14	Photographs of the experimental arrangement and a close-up view of the roughness elements . . . . .	112
5.1	Photograph - Neutral approach flow over neutral smooth heat island - elevated smoke source upwind . . . . .	113
5.2	Photograph - Stable approach flow over unstable smooth heat island - elevated smoke source upwind . . . . .	113
5.3	Photograph - Stable approach flow over neutral smooth heat island - ground smoke source at left side . . . . .	114
5.4	Photograph - Stable approach flow over unstable smooth heat island - two ground smoke sources at left side . . . . .	114
5.5	Photograph - Stable approach flow over unstable smooth heat island - ground smoke source at left side . . . . .	115
5.6	Photograph - Stable approach flow over unstable rough heat island - ground smoke source at left side . . . . .	115

LIST OF FIGURES (Continued)

<u>Figure</u>		<u>Page</u>
5.7	Photograph - Stable approach flow over neutral rough heat island - ground smoke source along the centerline over the heater . . . . .	116
5.8	Photograph - Stable approach flow over unstable rough heat island - ground smoke source along the center line over the heater . . . . .	116
5.9	Photograph - Stable approach flow over neutral smooth heat island - ground smoke source downwind . . . . .	117
5.10	Photograph - Stable approach flow over unstable smooth heat island - ground smoke source downwind . . . . .	117
5.11	Photograph - Stable approach flow over unstable rough heat island - ground smoke source downwind . . . . .	118
5.12	Photograph - Stable approach flow over unstable rough heat island - ground smoke source at upwind left corner . . . . .	118
5.13	Surface temperature distribution along the centerline for neutral flow over unstable rough heat island and Mean temperature profile at $x = 65.5$ feet and $y = 0$ for neutral flow over unstable rough heat island indicating details near the surface . . .	119
5.14	Mean temperature profiles along the centerline for neutral approach flow over an unstable rough heat island . . . . .	120
5.15	Surface temperature distribution along the centerline for stable flow over an unstable heat island - smooth and rough and Mean temperature profiles at $x = 65.5$ feet and $y = 0$ for stable flow over an unstable heat island - rough and smooth . . . . .	121
5.16	Comparison of mean temperature profiles along the centerline for stable flow over an unstable heat island for rough and smooth cases . . . . .	122

LIST OF FIGURES (Continued)

<u>Figure</u>		<u>Page</u>
5.17	Surface temperature distribution along the centerline for an approach flow with elevated inversion over an unstable rough heat island and Mean temperature profile at $x = 65.5$ feet and $y = 0$ for an approach flow with elevated inversion over an unstable rough heat island . . .	123
5.18	Mean temperature profiles along the centerline for a flow with elevated inversion over an unstable rough heat island . . . . .	124
5.19	Mean temperature profiles across the heat island for an unstable rough heat island with stable and elevated inversion approach flows . . . . .	125
5.20	Three dimensional development of the base of the elevated inversion for stable flow over an unstable rough heat island . . . . .	126
5.21	Mean temperature distribution along the width for neutral flow over unstable rough heat island at $x = 65.5$ feet for different heights . . . . .	127
5.22	Mean temperature distribution along the width for stable flow over unstable rough heat island at $x = 66$ feet for different heights . . . . .	128
5.23	Mean temperature distribution along the width for elevated inversion approach flow over unstable rough heat island at $x = 65.5$ feet for different heights . . . . .	129
5.24	Mean temperature distribution along the width of an unstable rough heat island for different approach flows at $x = 66$ feet and $z = 0.5$ inch . .	130
5.25	Mean temperature contours for stable flow over a neutral smooth heat island along the centerline (temperatures in degree F) . . . . .	131
5.26	Mean temperature contours for neutral flow over an unstable rough heat island along the centerline (temperatures in degree F) . . . . .	132
5.27	Mean temperature contours for stable flow over an unstable smooth heat island along the centerline (temperatures in degree F) . . . . .	133

LIST OF FIGURES (Continued)

<u>Figure</u>		<u>Page</u>
5.28	Mean temperature contours for stable flow over an unstable rough heat island along the centerline (temperatures in degree F) . . . . .	134
5.29	Mean temperature contours for elevated inversion approach flow over a neutral rough heat island along the centerline (temperatures in degree F) . .	135
5.30	Mean temperature contours for elevated inversion approach flow over an unstable rough heat island along the centerline (temperatures in degree F) . .	136
5.31	Mean temperature contours for neutral approach flow along the width of an unstable rough heat island at x = 66 feet (temperatures in degree F) .	137
5.32	Mean temperature contours for stable flow along the width of an unstable rough heat island at x = 66 feet (temperatures in degree F) . . . . .	138
5.33	Mean temperature contours for stable flow along the width of an unstable smooth heat island at x = 66 feet (temperatures in degree F) . . . . .	139
5.34	Mean temperature contours for elevated inversion flow along the width of an unstable rough heat island at x = 66 feet (temperatures in degree F) .	140
5.35	Development of thermal and internal boundary layers over the model . . . . .	141
5.36	Lateral mean velocity profiles across the wind tunnel with neutral approach flow . . . . .	142
5.37	Non-dimensional mean velocity profiles for neutral approach flow over a neutral, smooth heat island along the centerline . . . . .	143
5.38	Non-dimensional mean velocity profiles for neutral approach flow over a neutral, rough heat island along the centerline . . . . .	144
5.39	Comparison of non-dimensional centerline mean velocity profiles for neutral approach flow over smooth and rough heat islands . . . . .	145
5.40	Non-dimensional mean velocity profiles for neutral flow over an unstable, smooth heat island along the centerline . . . . .	146

LIST OF FIGURES (Continued)

<u>Figures</u>		<u>Page</u>
5.41	Non-dimensional mean velocity profiles for neutral approach flow over an unstable, rough heat island along the centerline . . . . .	147
5.42	Non-dimensional mean velocity profiles for stable approach flow over a neutral, rough heat island along the centerline . . . . .	148
5.43	Non-dimensional mean velocity profiles for stable approach flow over an unstable, rough heat island along the centerline . . . . .	149
5.44	Non-dimensional mean velocity profiles for stable approach flow over an unstable, rough heat island along the centerline . . . . .	150
5.45	Non-dimensional mean velocity profiles for the approach flow with elevated inversion over a neutral, smooth heat island along the centerline .	151
5.46	Non-dimensional mean velocity profiles for the approach flow with an elevated inversion over a neutral, rough heat island along the centerline . .	152
5.47	Non-dimensional mean velocity profiles for the approach flow with an elevated inversion over an unstable, smooth heat island along the centerline . . . . .	153
5.48	Non-dimensional mean velocity profiles for the approach flow with an elevated inversion over an unstable, rough heat island along the centerline .	154
5.49	Comparison of non-dimensional mean velocity profiles at $x = 66$ feet and $y = 0$ for different approach flows along the centerline . . . . .	155
5.50	Comparison of mean velocity profiles for stable approach flow over an unstable heat island with and without roughness along the width at $x = 66$ feet .	156
5.51	Mean velocity distributions along the width for different cases . . . . .	157
5.52	Mean velocity distributions along the width for different heights at $x = 65$ feet for stable approach flow over an unstable rough heat island .	158

LIST OF FIGURES (Continued)

<u>Figure</u>		<u>Page</u>
5.53	Mean velocity distributions along the width for different heights at $x = 65$ feet for the approach flow with elevated inversion over an unstable, rough heat island . . . . .	159
5.54	Non-dimensional vertical profiles of longitudinal velocity fluctuations at different distances along the centerline of an unstable, rough heat island for stable approach flow . . . .	160
5.55	Non-dimensional vertical profiles of longitudinal velocity fluctuations at different distances along the centerline of an unstable, rough heat island for an elevated inversion approach flow . . . . .	161
5.56	Non-dimensional vertical profiles of longitudinal velocity fluctuations at different distances along the centerline for different cases at $x = 69$ feet .	162
5.57	Non-dimensional profiles of longitudinal velocity fluctuations along the width of an unstable, rough heat island for neutral flow at $x = 66$ feet for different heights . . . . .	163
5.58	Non-dimensional profiles of longitudinal velocity fluctuations along the width of an unstable, rough heat island for stable approach flow at $x = 66$ feet for different heights . . . . .	164
5.59	Non-dimensional profiles of longitudinal velocity fluctuations along the width of an unstable rough heat island for elevated inversion approach flow at $x = 66$ feet for different heights . . . . .	165
5.60	Comparison of non-dimensional longitudinal velocity fluctuations along the width of an unstable, rough heat island for different approach flows at $x = 65$ feet and $z = 0.6$ inch . . . . .	166
5.61	Comparison of non-dimensional temperature fluctuations along the width of an unstable, smooth heat island for different approach flows at $x = 65.5$ feet and $z = 0.4$ inch . . . . .	167
5.62	Comparison of non-dimensional temperature fluctuation vertical profiles for neutral and unstable smooth heat islands for stable approach flows at $x = 68$ feet and $y = 0$ . . . . .	168

LIST OF FIGURES (Continued)

<u>Figure</u>		<u>Page</u>
5.63	Growth of the plume in the downwind direction based on the definition of boundary as 10 percent of the maximum concentration for different cases . . . . .	165
5.64	Iso-concentration lines for the tracer gas released from the two-dimensional continuous line source for a stably stratified approach flow over an unstable smooth heat island . . . . .	170
5.65	Vertical mean concentration profiles along the centerline of a neutral, smooth heat island for neutral approach flow . . . . .	171
5.66	Vertical concentration profiles along the centerline of unstable, smooth heat island for stable approach flow . . . . .	172
5.67	Concentration profiles along the width of an unstable, smooth heat island for stable approach flow at $x = 65.25$ feet for different heights . . .	173
5.68	Concentration profiles along the width of an unstable, smooth heat island for stable approach flow at $x = 66$ feet for different heights . . . . .	174
5.69	Shear velocity distribution along the centerline for various cases . . . . .	175
5.70	Distribution of bulk Richardson numbers along the centerline over an unstable, rough heat island for different approach flows . . . . .	176
5.71	Distribution of bulk Richardson number along the width for stable flow over an unstable, rough island at $x = 66$ feet . . . . .	177
5.72	Spectra of longitudinal component of turbulence for neutral flow over a neutral, rough heat island at $x = 68$ feet and $y = 0$ . . . . .	178
5.73	Spectra of longitudinal component of turbulence for stable flow over an unstable, rough heat island at $x = 68$ feet and $y = 0$ . . . . .	179
5.74	Vertical and lateral mean concentration profiles of Kr85 released from a ground level continuous point source at $x = 65.75$ feet and $y = 0$ for a stable approach flow over a rough heat island . . . . .	180

LIST OF FIGURES (Continued)

<u>Figure</u>		<u>Page</u>
5.75	Ground level mean concentrations of Kr85 released from a ground level continuous point source at x = 67.25 feet and y = 13 in. for a stable approach flow over a smooth heat island . . . . .	181
5.76	Mean temperature profiles across an unstable heat island for a stable approach flow for smooth and rough cases . . . . .	182
5.77	Comparison of mean velocity distributions across an unstable heat island for a stable approach flow for smooth and rough cases . . . . .	183
5.78	Non-dimensional vertical profiles of longitudinal velocity fluctuations at x = 69 feet and y = 0 inches for stable flow over smooth and rough heated islands . . . . .	184
5.79	Mean concentration profiles along the center-line for a stable flow over smooth and rough heat islands . . . . .	185
5.80	Comparison of non-dimensional perturbed temperatures computed by the two-dimensional and three-dimensional models with the laboratory data for an approach flow with inversion over a rough heat island . . . . .	186

LIST OF SYMBOLS

<u>Symbol</u>	<u>Definition</u>	<u>Dimension</u>
A,B	Non-dimensional constants	-
K	Wave number	L
S	A non-dimensional parameter characterizing the stratified flow	-
T	Mean temperature	T
g	Gravitational acceleration	$Lt^{-2}$
k	Eddy diffusivity	$L^2t^{-1}$
m	A dimensional constant	$L^{-1}$
n	Frequency of the eddies	$t^{-1}$
p	Wind pressure	$ML^{-1}t^{-2}$
r	Length measured along the radius of a circle	L
s	Constant stability factor	$L^{-1}$
u	Wind speed in the longitudinal direction	$Lt^{-1}$
v	Wind speed in the lateral direction	$Lt^{-1}$
w	Wind speed in the vertical direction	$Lt^{-1}$
x	Length measured in the longitudinal horizontal direction	L
y	Length measured in the lateral horizontal direction	L
z	Length measured in the vertical direction	L
L'	Monin-Obukhov's length	L
L <sub>1</sub>	A length representing half the width of the heat island	L
L <sub>2</sub>	Effective half width of a circular heat island	L

---

Symbols used to indicate dimension are:  
M - Mass, L - Length, t - Time, T - Temperature

LIST OF SYMBOLS (Continued)

<u>Symbol</u>	<u>Definition</u>	<u>Dimension</u>
$L_c$	A representative length for vertical conduction	L
$L_s$	Wave length of a gravity wave	L
$R_e$	Reynolds number	-
$R_f$	Flux Richardson number	-
$R_T$	Resistance at temperature T in ohms	-
$R_o$	Resistance at temperature $T_o$ in ohms	-
$R_{i_{le}}$	Bulk Richardson number	-
$T_{av}$	Average mean temperature	T
$T_h$	Mean temperature at height $Z_h$	T
$T_s$	Maximum surface temperature	T
$c_p$	Specific heat at constant pressure	$L^2 t^{-2} T^{-1}$
$c_v$	Specific heat at constant volume	$L^2 t^{-2} T^{-1}$
$k_o$	vonKarman constant	-
$t'$	Temperature fluctuation	T
$u_{rms}$	Root-mean-square value of the longitudinal turbulent velocity fluctuations	$LT^{-1}$
$u_l$	Non-dimensional wind speed	-
$u_\infty$	Free-stream wind speed	$LT^{-1}$
$Z_o$	Roughness length	L
$u_\delta$	Mean wind speed at a height equal to the thickness of the momentum boundary layer	$LT^{-1}$
$u_*$	Shear velocity	$Lt^{-1}$
$\theta$	Potential temperature	T
$\alpha$	Angle measured from the uniform flow direction	-
$\theta$	Non-dimensional perturbed temperature - $T'/T'_s$	-

LIST OF SYMBOLS (Continued)

<u>Symbols</u>	<u>Definition</u>	<u>Dimension</u>
$\phi$	Horizontal angle in the cylindrical coordinate system	-
$\delta$	Thickness of the momentum boundary layer	L
$\rho$	Air density	$ML^{-3}$
$\alpha_w$	Thermal coefficient of the wire material	$T^{-1}$
$( )_o$	Unperturbed quantity unless otherwise specified	-
$( )_c$	Denotes a quantity for the circular heat island	-
$(\bar{\quad})$	Denotes a mean quantity	-
$( )'$	Denotes a perturbed quantity in the theoretical model	-
$(\tilde{\quad})$	Denotes a non-dimensional quantity	-

## Chapter I

### INTRODUCTION

An urban complex acting as a heat source produces a positive temperature perturbation on the thermal field. This perturbation of increased temperature in the city relative to its rural environs is commonly referred to as the urban heat island and has significant effects on the dispersion of atmospheric pollutants over a city. The nature and type of urban terrain also influences the surface temperature distribution which in turn affects the vertical temperature patterns when coupled with the air flow over the city. In general, the maximum temperature in an urban heat island is found at the core of the city with the temperature decreasing rather uniformly away to a minimum temperature in the surrounding rural area. Of course, this is not always the case. For example, if a body of water exists at the periphery of a city, a discontinuity in the horizontal temperature distribution will occur. This can result in a strong stably-stratified flow over the city. On the other hand, if an urbanized area is situated immediately downwind of another, which is not of unusual occurrence the discontinuity may not be abrupt and the approach-flow temperature profiles will exhibit an elevated inversion and will have a profound influence on the air flow over the city.

Several field studies (Landsberg 1956, Bornstein 1968, Clarke 1970, Hilst and Bowne 1966) have been conducted in the past to understand the characteristics of the air flow over an urban heat island, but most of them are far from complete for two obvious reasons--lack of time and money. Moreover, the conditions in the field may change rapidly making it difficult to interpret the results effectively. Hence, field studies

of the past have been of limited nature to satisfy particular needs rather than to reach a comprehensive understanding of all aspects of the urban heat island, viz. wind velocities, air temperatures, and diffusion characteristics. Many attempts were also made to build numerical models and solve them with the help of computers primarily for two-dimensional models (Tag 1969, Myrup 1969, Yamada 1971). The atmospheric flow over an urban area with all its roughness and heating non-uniformities is far from being two-dimensional.

Laboratory studies of the past (Yamada 1971) were also two-dimensional and were restricted to study of temperature distributions. Therefore, a comprehensive study of the different physical and meteorological variables that contribute to the formation and maintenance of a three-dimensional urban heat island was undertaken under controlled conditions in a wind tunnel specifically designed to simulate atmospheric boundary layers.

Turbulent flow over aerodynamically rough surfaces is considered. To help understand more completely the transfer processes taking place in, above, and around the heat island, a study was made for twelve different cases. Variation of the meteorological or surface factors made each case different from the others. Three different approach flows, viz. neutral, ground-based stable stratification, and elevated inversion were investigated over both a smooth and a rough heat island. Each of the combinations of approach flow and surface roughness was studied with heating and without heating of the heat island. The main objectives of the study were:

1. To develop an understanding of the physical processes taking place in and around the heat island by means of flow visualization and analysis of corresponding quantitative experimental data;
2. to determine the characteristic features of diffusion through a study of the mean concentration fields created by a tracer gas released from a two-dimensional continuous line source located at ground level upwind of the heat island;
3. to evaluate the similarity between the flow over an urban heat island modeled in a meteorological wind tunnel and the full-scale flow and;
4. to develop simple linear two-dimensional and three-dimensional models that will predict the perturbed temperature and perturbed velocity distributions over a city and over the laboratory counterpart.

## Chapter II

## THEORETICAL AND EXPERIMENTAL BACKGROUND

A brief review of pertinent literature with particular reference to the urban heat island is given in this chapter.

### 2.1 Physical basis of the urban heat island

A city is a very complex meteorological region, creating its own meso-climates and micro-climates. This complexity is further enhanced if the cities are located along shorelines or in valleys creating local wind circulations. Energy balances in rural and urban areas which are chiefly responsible for the formation of the urban heat island are schematically represented in Fig. 2.1 (Munn 1966). Rural regions have a net daytime gain of energy through radiation at the ground surface and the process is reversed during the night. The above mentioned energy balance is modified in the urban area due to one or more of the following reasons:

- (1) Heating of the interior of the buildings (furnace heating);
- (2) asphaltic pavements and other structures characteristic of an urban area;
- (3) absence of surface moisture;
- (4) increased concentration of vehicular traffic and;
- (5) atmospheric pollution.

The reduced surface moisture lessens evaporation in the urban area and the energy that might have been used for the evaporation is absorbed by the urban structures. The thermal inertia of the urban building materials also prevents the rapid cooling after sunset leading to the storage of large amounts of solar energy and furnace heat.

The contribution by furnace heat is significant. The annual production of heat by combustion in New York City was estimated to be about  $2.8 \times 10^7$  cal of which 77 per cent was contributed by the residential and utility sources (Bornstein 1968). Bornstein also reports that the total energy released by combustion in Berlin is one-third of the energy received by direct solar radiation. The heat released by combustion for Fort Wayne, Indiana was estimated at 0.38 ly/min. (Davis, 1968).

In winter, large amounts of furnace heat are conducted to the interface between the earth and the atmosphere which in turn reduces the convection of energy from the atmosphere to urban surfaces during nocturnal hours. In summer, the large amounts of solar energy stored by the urban buildings and structures limit the convection of energy from the atmosphere. Thus the air above the city always remains warmer relative to the air above the surrounding rural areas. This phenomenon has become known as the "nocturnal urban heat island." The temperatures remain relatively high from street level to several hundred feet above the street. On the top of this warm layer, a nocturnal inversion is often formed. This elevated inversion restricts vertical dispersion of pollutants from the city and becomes intensified by radiational cooling of the upper surface of the pollution layer.

Diurnal variation of urban-rural temperature difference was observed in Vienna, Austria (Mitchell, 1961) for different seasons. Annual variation of average monthly maximum, mean, and minimum temperatures for Denver and Baltimore are also referred to by Mitchell. The variation in the climatic factors caused by the urban heat island can

very well be seen from a comprehensive set of data presented by Landsberg (1961).

## 2.2 Field studies

There have been several experimental field studies in the past to gather first-hand information about the urban heat island. Unfortunately, none of the studies have been complete presumably due to the enormous amount of time and money required. Moreover, the conditions in the field are so transient that deductive conclusions are difficult to obtain. Due to the above reasons, the data from the field studies pertain usually either to the velocities or to the temperature and very rarely to both the variables. A brief description of some of the field studies conducted in urban and rural areas and reported upon in the literature is given below. Many of these experiments have been conducted during nights when the urban heat-island phenomenon is more pronounced.

(a) Measurement of horizontal and vertical temperature gradients in San Francisco, San Jose and Palo Alto (Duckworth and Sandberg, 1954).

Duckworth and Sandberg selected three cities of different sizes to study the urban thermal structure under comparable synoptic conditions so as to identify the factors responsible for urban temperature differentials. Automobile-mounted thermistors were used to measure surface temperatures at the six-foot level. Vertical temperature profiles up to a height of 1000 feet were obtained with the help of wiresonde equipment. Some of the conclusions reached by them were:

- (1) temperatures increased from the rural to urban areas in direct proportion to the density of the building structures;
- (2) urban temperature excess increased with increasing city area (based on population) but at a relatively slow rate. Representative values of

this excess were 4-6°F for Palo Alto, 7-9°F for San Jose, and 10-12°F for San Francisco, the population of San Francisco being 24 times greater than that of Palo Alto;

(3) built-up areas generally introduced instability into the stable air up to about three times roof height;

(4) a "crossover" point sometimes existed over the urban area above which the urban air was cooler than the rural air at the same height.

Vertical temperature profiles observed over built-up and rural areas of San Francisco were also given by Duckworth and Sandberg.

(b) Measurement of vertical temperature profile in Louisville, Kentucky (DeMarrais, 1961). DeMarrais measured temperature difference at three levels on the WHAS-TV tower located in the downtown area of Louisville, Kentucky. He compared these with the data obtained over rural areas at other locations and arrived at the following conclusions:

(1) the lapse rate near the tower during the night showed marked difference from that observed during the daytime;

(2) a weak lapse rate was observed on top of a superadiabatic lapse rate within the city during nights.

(c) Study of Montreal urban heat island (Summers, 1964). Mean temperatures in the city and in the adjacent rural area around Montreal, Canada were measured. By comparing urban trends with suburban trends for sufficiently long periods of time, the effect of long-term climatic changes were eliminated and a residual temperature excess was obtained giving the temperature increase due to the growth of the city itself. For each month over a period of three years the excess of the mean monthly minima was computed.

The greatest city excess temperatures were found to occur in the summer and winter, while in the transition months they were somewhat less. Average excess in mean minimum temperature at city stations for different seasons and for a typical day in March 1962 were studied. A difference of 18°F was observed between McGill, a city station and St. Hubert, a rural station, separated by only seven miles. With the help of an automobile survey, the highest temperatures were found to be near the downwind end of the densely populated apartment-complex area.

(d) Measurement of air temperature patterns over Leicester, England (Chandler, 1967). Chandler studied the surface temperature patterns over Leicester, England which had a 1961 census population of 270,000 and an area of 27 square miles compared with a population of 8.25 millions covering an area of 750 square miles for London. He compared the heat-island of the two cities and concluded that the disparity between the size of the two cities had little effect on the intensities of the heat island. His other conclusions were:

- (1) high urban temperatures were caused by the shape of the buildings, the intervening spaces between them and the density of the built-up area;
- (2) nature of the wind profile and the trapping of air between the buildings contributed to the maintenance of the warmth of the city and;
- (3) in general, the heat island was generated mainly by the thermal effects of buildings.

Whereas Duckworth and Sandberg (1954) found the intensity of the urban heat island to increase with the city size, Chandler emphasized that the intensity was invariant with the size of the city. The conflicting conclusions of these two studies require further detailed

investigation in the field and in the laboratory before any generalizations can be made.

(e) Study of temperature fields in and around New York City (Bornstein, 1968). Bornstein studied the temperature fields up to a height of about 700 m over New York City. The main features of the temperature distribution were found to be:

- (1) an urban temperature excess which decreased rapidly with height;
- (2) one or more weak elevated inversions over the city;
- (3) strong ground-based inversions over the rural areas and;
- (4) the absence of surface inversions over the urban area. Bornstein also found high frequency of rural surface inversions and urban elevated inversions.

The largest temperature increase in a rural surface inversion of  $11.6^{\circ}\text{C}$  occurred over the greatest depth of 370m. Corresponding values for urban surface inversions were  $1.2^{\circ}\text{C}$  and 100 m respectively. In order to study the variation of urban temperature excess with height, the warmest urban sounding and a nearby sea level rural sounding were selected.

The urban-excess temperature profile observed by Bornstein (1968) is compared with the results of the theoretical model in Chapter III. Some of the conclusions that can be drawn from Bornstein's work are:

1. The intensity of the urban heat island exhibited by the magnitude of the urban temperature excess was maximum below 25 m and decreased to zero at 300 m . This indicated the rapidity with which the effect of the heat island decreased with height over a city.

2. temperature cross overs existed over the urban area indicating negative perturbations of mean temperature but, of lesser magnitude than the positive perturbations.

(f) Study of nocturnal urban boundary layer over Cincinnati, Ohio (Clarke, 1969). Clarke's measurements over Cincinnati included surface temperatures across the city by a sensor mounted on an automobile, coordinated upper level temperatures along the automobile route with the help of a helicopter and pilot balloon observations in both urban and rural areas. A pronounced modification of the vertical temperature structure of the rural air was seen as it flew over the urban area. The vertical extent of this modification, the "urban boundary layer" was observed to gradually increase with distance over the urban area along the direction of the wind.

Another significant observation of Clarke was the existence of the "urban heat plume," the outflow of urban air aloft downwind of the urban area. An urban boundary layer of height varying from 150 to 300 feet was observed in Cincinnati when strong inversion conditions existed upwind of the city. Clarke also noticed a superadiabatic lapse rate within the urban boundary layer in the downtown area and an isothermal lapse rate of weak inversion in the downwind rural areas.

(g) Measurement of air speed and temperature on a tall tower in the city of Philadelphia (Slade, 1969). Wind speed and mean temperatures were measured in the WFIL-WRCV-TV tower located in the northwestern section of the city of Philadelphia, about 12 km from the downtown area. Wind profiles were found to vary appreciably with the change in direction. Temperature profiles during the period  $1\frac{1}{2}$  -  $\frac{1}{2}$  hour prior to sunset were generally adiabatic. Average temperature profiles at different times of the day were observed by Slade. Average normalized

wind profiles for unstable, stable and neutral conditions were observed. Slade also measured the standard deviation of the horizontal wind-direction distribution and concluded that the wind-speed profiles and the turbulence profiles differed quite radically depending on the local upwind terrain.

(h) Measurement of mean temperatures in Durban, South Africa (Preston-Whyte, 1970). Preston-Whyte obtained mean temperatures from 28 midday traverses in the Durban area and developed a quantitative empirical model of their spatial distribution. They found in summer an elongated heat island with its center situated downwind of the central business district. This anomaly was accounted for as due to the displacement of the heat island by the sea breeze (east to west) away from the heat sources provided by the business district. The empirical model based on harmonic analysis of the measured data describes the spatial temperature wave across the center of the heat island.

(i) Urban wind velocity fields over Columbus, Ohio (Angell, Pack et al. 1971). Although many field studies have been made in the past to measure the urban and rural temperature profiles, attempts to investigate the air velocities over an urban area have been sparse due to the practical difficulties involved in obtaining reliable wind statistics within the built-up areas of a city. Angell et al. obtained some information about the wind pattern above Columbus, Ohio by flying constant-volume balloons across the city. The observations were made both in the lapse and inversion conditions.

They found wind over the urban area to have an anticyclonic turning at about 200 m which was found to be greater under inversion than under lapse conditions. Increase in the frictional force and the

formation of a mesoscale high-pressure system due to warmer temperatures were attributed to be the causes behind this anticyclonic turning of the wind. Observations of the vertical velocity above the city indicated an overall tendency for sinking motion upwind and rising motion downwind of the core of the city. The vertical velocity distribution under lapse and inversion conditions were measured and reported. The horizontal velocity difference distribution under lapse conditions in the urban and rural areas was also observed. The decrease in wind speed across the city on an average was found to be approximately 20 percent of the upwind speed under lapse conditions but very small under inversions.

(j) Diffusion experiments at Fort Wayne, Indiana (Csanady, Hilst, and Bowne, 1967). Fluorescent zinc sulfide tracer material was released from aircraft at an altitude of about 91 m at a distance of 1600 m of the first sampling line. A number of rotorod samplers were arranged along sampling lines approximately parallel to the release line to measure the time integral of concentration of the material as the cloud passes by. Their results indicated that (1) the vertical standard deviation of the dosage field grew approximately in direct proportion to the vertical turbulence level, (2) the rate of vertical growth was increased further by the heat island, and (3) an increase in the dosage over the rural areas. The roughness length  $z_0$  of 3 m obtained for the rural area appears large for the flat terrain around Fort Wayne. The dosage fluctuations measured were found to be consistent with a log-normal probability distribution of the fluctuations.

### 2.3 Theoretical studies of urban heat island

Analytical models of an urban heat island are rare because of the complexities involved. Most of the existing models are two-dimensional and involve numerical solutions. Attempts have been made to linearize the governing equations and solve the resulting single equation by different mathematical techniques. This section deals with some of the models that have been developed in the past to predict the nature of airflow over a heat source.

(a) Theoretical model of airflow over a localized heat source (Estoque and Bhumralker, 1969). The model is two-dimensional with the heat source infinitely long in the y-direction and narrow in x-direction. Local time derivative of density was neglected in the equation of continuity and the motion was assumed to be hydrostatic. Equations of continuity, motion and thermodynamic energy were considered. In addition, the equations of state and the Poisson equation were coupled. The effect of vertical mixing by penetrative convection was computed by appropriate formulas. Then the unknown variables - three components of mean velocity, temperature, pressure and density were determined as functions of  $x$ ,  $z$ , and  $t$  in the region of interest.

Distribution of perturbed temperature after three hours, when the initial prevailing flow was normal to the heat source was obtained by Estoque and Bhumralker. Conclusions of Estoque and Bhumralker based on the results of their numerical experiment were:

(1) When the prevailing flow is strong, and normal to the heat source, the induced perturbations on temperature and velocity are weak.

(2) Surface wind over the heat source is accelerated and the wind at the leeward edge is stronger causing downward motion of the air over the heat source.

(b) A numerical energy budget model of the urban heat island (Myrup, 1969). Myrup started with an energy-balance equation for the surface of the earth of the form,

net radiation flux = latent heat flux + sensible heat flux to the air + flux of heat into the soil.

Then he developed physical relationships for each of the terms in the right side of the above formulation so as to obtain a closed set of equations. The equations thus formed were then solved by numerical methods.

Myrup then computed the temperature excess for a hypothetical city over a rural site near Davis, California. The conclusion of Myrup based on the results of his model applied to the hypothetical city was that the most important parameters which determine the size of the heat island are the lessening of evaporation in the city, increased roughness of the city, thermal properties of the building materials and wind speed.

(c) Numerical studies of the heat-island circulations (Delage and Taylor, 1970). Delage and Taylor proposed a two-dimensional model to simulate the wind flow in a vertical cross section of the heat island. Initially stable thermal stratification was used as one of the boundary conditions. The formulation of the equations governing the flow were essentially the same as for Estoque and Bhumralker, but for the treatment of the boundary conditions and eddy coefficients.

Heat-island circulations were found to lead to the development of a symmetric double cell pattern. Delage and Taylor also observed a transitional multi-cell pattern in some cases before the final double cells. The influence of different parameters viz., heat-island size and intensity, eddy-transfer coefficients and the initial temperature stratification, on the steady-state circulation were investigated.

(d) Two-dimensional air flow over a heat-island (Yamada, 1971).

Yamada (1971) considered the  $x$  and  $z$  components of the equation of motion with the Boussinesq approximation, the relationship between vorticity and stream function, and the equation of energy as governing the airflow over a two-dimensional heat-island. Then he set forth to integrate these equations by finite difference techniques with boundary conditions that will essentially meet the requirements of a wind tunnel. His numerical results displayed the less frequent surface and the more frequent elevated inversion layers over the city.

(e) Linearized urban heat-island model (Olfe and Lee, 1971). Olfe and Lee (1971) considered planar inviscid flow over a heated island and carried out steady, linearized flow calculations to estimate perturbed temperature and velocities over the city. Basic linearized flow equations of conservation of mass, horizontal momentum, vertical momentum were solved for a sinusoidal perturbation in the surface temperature. Perturbed temperature profiles were calculated for New York City and compared with the field measurements (Bornstein, 1968).

Three-dimensional solutions for a circular heat island were calculated by superposing the planar solutions for the velocity and temperature perturbations in a manner similar to that of Scorer's mountain flow calculations (Scorer, 1949, 1956). One of the main deficiencies

of this model is that it uses a uniform mean velocity distribution which is far from reality. Moreover, the convection effects of the urban heat island to a great extent depends on the logarithmic velocity profiles commonly found in the atmosphere. Yet Olfe and Lee's model is a promising attempt to formulate a simple mathematical model for a three-dimensional urban heat island of circular form.

#### 2.4 Wind tunnel studies of urban heat island

Experimental studies on stratified flows over obstacles conducted in the past are very few. Experiments in a water channel were conducted by Long (1955). Similar experiments on stratified flow were conducted by Plate and Lin (1966). An attempt was made to model the flow over Fort Wayne, Indiana by Chaudhry and Cermak (1971) in one of the neutrally stratified large wind tunnels of Colorado State University. But the only basic wind tunnel measurements carried out on a heated boundary which may represent an ideal two-dimensional heat island is by Yamada (1971).

(a) Temperature measurements on a two-dimensional urban heat island (Yamada, 1971). Yamada (1971) measured mean temperature profiles of the air flowing over a two-dimensional heated area with a stably stratified approach flow. The windtunnel was 2 feet x 2 feet cross section and fifteen feet long. Mean velocity measurements were made by smoke wire and were few in numbers. Yamada compared the wind-tunnel data with the results of his numerical model and found good agreement.

(b) Modeling of flow and diffusion over an urban complex under neutrally stratified conditions (Chaudhry and Cermak, 1971). The city of Fort Wayne, Indiana was selected for the wind tunnel modeling due

to the existence of field observations for the diffusion of mass released from an elevated line source. A horizontal scale of 1:4000 and a vertical scale of 1:2000 was adopted. The vertical exaggeration was necessary in order to have an aerodynamically rough surface. Nichrome wires were used to heat the model to yield a mean surface temperature distribution similar to that of the prototype. Zinc sulfide particles were used as a tracer in the field and radio active Krypton-85 was used as the laboratory tracer. Diffusion characteristics were found to be similar between 10,000 feet and 40,000 feet. The dilution rate for ground level concentrations was in good agreement and the growth rate for plume height was equal. Average surface-dosage distributions for the model near the core of the city had good agreement with the field observations.

#### 2.5 Concluding remarks

From a survey of the past work on urban heat islands, it can readily be seen that although several field studies have been conducted, a comprehensive study involving velocity, turbulence and temperature profiles is yet to be done due to the complexities and the cost involved. Moreover, even if such a study is conducted in an urban-rural complex, it may not be sufficient to understand the mechanics of the heat island because of non-uniform roughness and heating involved. In addition, the results will be influenced by a particular nature of the city in question making it difficult to draw generalized conclusions.

On the other hand, exact theoretical solution of the equations governing the motion of air over a three-dimensional urban heat island in a closed form is very difficult because of more unknowns than the number of equations available to solve them. The alternate method of numerical solution with the help of a digital computer also becomes

complicated due to complex boundary conditions. This approach also becomes costly due to the requirement of enormous capacity for the computer to handle a three-dimensional problem.

With the difficulties facing the solution or even an understanding of the problem of the urban heat island, an attractive alternative appears to be the physical modeling in a wind-tunnel facility capable of simulating the atmospheric boundary layer. Here, the experiments can be conducted in controlled conditions. A physical understanding is also possible with flow-visualization techniques. But modeling parameters must be carefully selected and properly simulated in order to obtain satisfactory results.

## Chapter III

THEORETICAL ANALYSIS

A theoretical model based on linear analysis is developed which predicts the perturbations on temperature and velocities imposed by a heat island fairly closely for laboratory and field studies. Equations similar to that used by Olfe and Lee (1971) are adopted. The principle difference is in the introduction of a sheared velocity profile into the governing equations. Olfe and Lee assumed uniform flow with constant velocity. The introduction of a boundary layer velocity profile enhances the applicability of the model to the field and laboratory conditions. The equations governing the motion of the air over an urban heat island are developed in this chapter and their solutions by the linearization techniques are discussed. Comparison of the results with those obtained by Olfe and Lee for the heat island of New York City is also made. Experimental results are compared with theoretical predictions in Chapter V.

3.1 Development of the governing equations

From past studies on urban heat islands it can be inferred that the vertical region of influence is small compared to the atmospheric scale heights. For example, Bornstein (1968) observed the height to the base of an elevated inversion over New York City to be about 300 meters and Clarke (1969) found it to be about 220 meters over Cincinnati, Ohio. This permits the use of the Boussinesq approximation (Spiegel and Verneis, 1970) for the solution of the linearized equations. In addition to the Boussinesq approximation, the following modifications are made in the governing equations:

- (1) static vertical temperature gradient is replaced by its excess over the adiabatic gradient,
- (2) the buoyancy force is included in the momentum equation for the vertical direction, and
- (3) the specific heat at constant pressure  $c_p$  replaces the specific heat at constant volume  $c_v$ .

The above modifications make the equations governing convection in a perfect gas equivalent to those for an incompressible fluid. Eddy viscosity is neglected in this model and the effective eddy diffusivity is assumed constant. The equation of state corresponding to a perfect gas is used in the solution. A two-dimensional model is initially developed and made to be three-dimensional in a manner similar to that of Scorer (1956) and Olfe and Lee (1971) by superposing the two-dimensional solutions at various angles around a circular heat island.

The coordinate axes  $x$ ,  $y$ ,  $z$  are taken to be along the longitudinal horizontal direction (mean wind direction), lateral horizontal direction and vertical direction respectively. In the following analysis mean velocity is assumed to be a function of  $z$  only.

### 3.2 Two-dimensional model - General solutions

With the assumptions enunciated in Section 3.1, the two-dimensional equations governing the motion of air over an urban heat island are developed as below:

$$u = \bar{u}(z) + u'$$

$$v = 0 = v'$$

$$w = 0, w = w'$$

$$p = \bar{p} + p'$$

$$\begin{aligned}
T &= T_0 + T' \\
\rho &= \rho_0 + \rho'
\end{aligned}
\tag{3.1}$$

where  $v$  is the velocity in the  $y$  direction,

$u'$  is the perturbation velocity in the  $x$  direction,

$w'$  is the perturbation velocity in the  $z$  direction,

$\bar{p}$  is the mean pressure,

$p'$  is the perturbed pressure,

$T_0$  is the unperturbed temperature,

$T'$  is the perturbed temperature, and

$\rho_0$  and  $\rho'$  are the unperturbed and perturbed densities respectively.

Conservation of mass

$$\frac{\partial}{\partial x} (\bar{u} + u') + \frac{\partial}{\partial z} (w') = 0, \quad \text{reduces to}$$

$$\frac{\partial u'}{\partial x} + \frac{\partial w'}{\partial z} = 0 \tag{3.2}$$

Momentum equation in  $x$  direction

$$(\bar{u} + u') \frac{\partial}{\partial x} (\bar{u} + u') + w' \frac{\partial}{\partial z} (\bar{u} + u') = - \frac{1}{\rho_0} \frac{\partial p'}{\partial x}$$

reduces to

$$\bar{u} \frac{\partial u'}{\partial x} + w' \frac{\partial \bar{u}}{\partial z} + \frac{1}{\rho_0} \frac{\partial p'}{\partial x} = 0 \tag{3.3}$$

Momentum equation in  $z$  direction

$$(\bar{u} + u') \frac{\partial w'}{\partial x} + w' \frac{\partial w'}{\partial z} = - \frac{1}{\rho_0} \frac{\partial p'}{\partial z} - \frac{\rho' g}{\rho_0}$$

reduces to

$$\bar{u} \frac{\partial w'}{\partial x} + \frac{1}{\rho_0} \frac{\partial p'}{\partial z} + \frac{\rho' g}{\rho_0} = 0 \tag{3.4}$$

Thermodynamic energy equation

$$(\bar{u} + u') \frac{\partial T'}{\partial x} + w' \frac{\partial T'}{\partial z} + w' \frac{\partial T_0}{\partial z} - k \left\{ \frac{\partial^2}{\partial x^2} + \frac{\partial^2}{\partial z^2} \right\} T' = 0$$

Because

$$\frac{1}{T_0} \left\{ \frac{\partial T_0}{\partial z} \right\} = s + \frac{1}{T_0} \left\{ \frac{\partial T_0}{\partial z} \right\} \quad \text{adiabatic}$$

where  $s$  is a constant stability factor,

the energy equation reduces to,

$$\bar{u} \frac{\partial T'}{\partial x} + s T_0 w' - k \left\{ \frac{\partial^2}{\partial x^2} + \frac{\partial^2}{\partial z^2} \right\} T' = 0 \quad (3.5)$$

Differentiating Eq. 3.3 with respect to  $z$  and Eq. 3.4 with respect to  $x$  and combining the results to eliminate  $p'$  the following is obtained:

$$\bar{u} \left\{ \frac{\partial^2 u'}{\partial x \partial z} - \frac{\partial^2 w'}{\partial x^2} \right\} + w' \frac{\partial^2 \bar{u}}{\partial z^2} = \frac{g}{\rho_0} \frac{\partial \rho'}{\partial x} \quad (3.6)$$

From Eq. 3.2,

$$\frac{\partial w'}{\partial z} = - \frac{\partial u'}{\partial x} .$$

Substituting this relation into Eq. 3.6,

$$\bar{u} \left\{ - \frac{\partial^2 w'}{\partial z^2} - \frac{\partial^2 w'}{\partial x^2} \right\} + w' \frac{\partial^2 \bar{u}}{\partial z^2} = \frac{g}{\rho_0} \frac{\partial \rho'}{\partial x} \quad (3.7)$$

using perfect gas equation of state in the Boussinesq form,

$$\frac{\rho'}{\rho_0} = - \frac{T'}{T_0} \quad (3.8)$$

With the relation 3.8 substituted into Eq. 3.7,

$$\bar{u} \left\{ \frac{\partial^2}{\partial z^2} + \frac{\partial^2}{\partial x^2} \right\} w' - w' \frac{\partial^2 \bar{u}}{\partial z^2} = \frac{g}{T_0} \frac{\partial T'}{\partial x} \quad (3.9)$$

The horizontal dimensions of a typical heat island are several times larger than the vertical extent of influence. Hence the rate of variation of the pertinent quantities in the vertical direction will be far greater than that in the horizontal direction justifying the assumption that

$$\frac{\partial^2}{\partial x^2} ( ) \ll \frac{\partial^2}{\partial z^2} ( ) \quad (3.10)$$

where ( ) indicates any perturbation quantity.

With this approximation, Eq. 3.9 reduces to

$$\bar{u} \frac{\partial^2 w'}{\partial z^2} - w' \frac{\partial^2 \bar{u}}{\partial z^2} = \frac{g}{T_0} \frac{\partial T'}{\partial x} \quad (3.11)$$

Now by eliminating  $w'$  between Eq. 3.5 and Eq. 3.11 and using the approximation involved in Eq. 3.10,

$$\begin{aligned} \bar{u} \frac{\partial^2}{\partial z^2} \left\{ \frac{1}{sT_0} \left[ k \frac{\partial^2 T'}{\partial z^2} - \bar{u} \frac{\partial T'}{\partial x} \right] \right\} - \frac{1}{sT_0} \left\{ k \frac{\partial^2 T'}{\partial z^2} - \bar{u} \frac{\partial T'}{\partial x} \right\} \frac{\partial^2 \bar{u}}{\partial z^2} \\ = \frac{g}{T_0} \frac{\partial T'}{\partial x} \end{aligned} \quad (3.12)$$

Eq. 3.12 is non-dimensionalized in a way similar to that of Olfe and Lee.

Defining  $T'_s$  as the maximum surface-temperature perturbation,  $L_1$  as a length representing the half width of the heat island, and  $L_c = \left( \frac{kL_1}{u_\infty} \right)^{1/2}$ , a representative length for vertical conduction where  $u_\infty$  is the freestream velocity, dimensionless quantities are defined as,

$$\begin{aligned} \tilde{\theta} &= T'/T'_s, \\ \tilde{x} &= x/L_1, \\ \tilde{z} &= z/L_c, \text{ and} \\ \tilde{u}_1 &= \bar{u}/u_\infty \end{aligned} \quad (3.13)$$

With the dimensionless variables defined by Eq. 3.13 substituted in Eq. 3.12,

$$\tilde{u}_1 \frac{\partial^2}{\partial \tilde{z}^2} \left\{ \frac{\partial^2 \tilde{\theta}}{\partial \tilde{z}^2} - \tilde{u}_1 \frac{\partial \tilde{\theta}}{\partial \tilde{x}} \right\} - \left\{ \frac{\partial^2 \tilde{\theta}}{\partial \tilde{z}^2} - \tilde{u}_1 \frac{\partial \tilde{\theta}}{\partial \tilde{x}} \right\} \frac{\partial^2 \tilde{u}_1}{\partial \tilde{z}^2} = \frac{gskL_1}{u_\infty^3} \frac{\partial \tilde{\theta}}{\partial \tilde{x}} \dots \quad (3.14)$$

Eq. 3.14 involves two dimensionless parameters. One is the wind velocity ratio  $\tilde{u}_1 = \bar{u}/u_\infty$  and the other  $S = gskL_1/u_\infty^3$ . For a Prandtl number of order unity it can be shown that  $S = Ri/Re$  where  $Ri$  is the Richardson number and  $Re$  the Reynolds number. The parameter  $S$  can be interpreted as follows:

$$4S = \frac{4gskL_1}{u_\infty^3} = \left\{ 4\pi \frac{L_c}{L_s} \right\}^2 \quad (3.15)$$

where  $L_s = 2\pi u_\infty / (gs)^{1/2}$  is the wavelength of a gravity wave. From the way in which both the parameters  $\tilde{u}_1$  and  $S$  occur in the governing Eq. 3.14 it is obvious that both are of significant value in shaping the temperature perturbation profiles in the city. The term involving  $\partial^2 \tilde{u}_1 / \partial \tilde{z}^2$  introduces the effect of wind shear into the governing equation. The parameter  $S$  denotes the interaction between the conduction profile and the gravity wave.

The solution to Eq. 3.12 is obtained with a sinusoidal surface temperature distribution of the form

$$\theta(\tilde{x}, 0) = \text{Real} \{ \exp(i k \tilde{x}) \} = \cos K \tilde{x} \quad (3.16)$$

in a manner similar to Olfe and Lee. Then the governing Eq. 3.12 should have solutions proportional to

$$\text{Real} \{ \exp(m\tilde{z} + i K \tilde{x}) \} \quad (3.17)$$

Substitution of Eq. 3.17 into Eq. 3.12 yields a characteristic equation for  $m$  of the following form,

$$\tilde{u}_1 m^4 - m^2 (iKu_1^2 + a_1) + iK (a_1 u_1 - S) = 0 \quad (3.18)$$

Equation 3.18 is quadratic in  $m^2$  and can be solved for the four  $m$  roots. Imposing the condition that the perturbations should decrease to zero as  $z$  tends to  $\infty$ , two roots are selected that have negative real parts,

$$m_1 = - \frac{1}{(2\tilde{u}_1)^{\frac{1}{2}}} \{r_1^{\frac{1}{2}} (\cos \beta_{1/2} + i \sin \beta_{1/2})\}$$

$$m_2 = - \frac{1}{(2u_1)^{\frac{1}{2}}} \{r_2^{\frac{1}{2}} (\cos \beta_{2/2} + i \sin \beta_{2/2})\} \quad (3.19)$$

The values  $r_1$ ,  $r_2$ ,  $\beta_1$ , and  $\beta_2$  are defined in terms of the known quantities as below:

$$a_1 = \partial^2 \tilde{u}_1 / \partial z^2$$

$$r = \{(a_1^2 - K^2 \tilde{u}_1^4)^2 + K^2 (4S\tilde{u}_1 - 2a_1 \tilde{u}_1^2)^2\}^{\frac{1}{2}}$$

$$\beta = \tan^{-1} \left\{ \frac{4S\tilde{u}_1 - 2a_1 \tilde{u}_1^2}{a_1^2 - K^2 \tilde{u}_1^4} \right\}$$

$$c = a_1 + r^{\frac{1}{2}} \cos \beta/2 \quad ; \quad c_1 = a_1 - r^{\frac{1}{2}} \cos \beta/2$$

$$d = K\tilde{u}_1^2 + r^{\frac{1}{2}} \sin \beta/2 \quad ; \quad d_1 = K\tilde{u}_1^2 - r^{\frac{1}{2}} \sin \beta/2$$

$$r_1 = (c^2 + d^2)^{\frac{1}{2}} \quad ; \quad r_2 = (c_1^2 + d_1^2)^{\frac{1}{2}} \text{ and}$$

$$\beta_1 = \tan^{-1} (d/c) \quad ; \quad \beta_2 = \tan^{-1} (d_1/c_1) .$$

With the roots given by Eq. 3.19, the solution for the non-dimensional temperature perturbation becomes,

$$\tilde{\theta}(\tilde{x}, \tilde{z}) = \text{Real} \{ [A \exp(m_1 \tilde{z}) + B \exp(m_2 \tilde{z})] \exp(iK\tilde{x}) \} \quad (3.20)$$

where A and B are constants to be determined from boundary conditions. The two boundary conditions to be used are:

- (1) temperature at the surface given by Eq. 3.16, and
- (2) zero normal velocity at the surface.

Imposition of condition 1 into the general solution given by Eq. 3.20 yields the relation

$$A + B = 1 \quad (3.21)$$

The perturbed vertical velocity  $w'$  can be obtained from the energy equation 3.5. After imposing the approximation, Eq. 3.10 and non-dimensionalization in a manner similar to that for the temperature equation,

$$\frac{w'}{u_\infty} = \left(\frac{T_s}{T_0}\right) \frac{1}{sL_1} \frac{\partial^2}{\partial \tilde{z}^2} - \tilde{u}_1 \left\{ \frac{\partial}{\partial \tilde{x}} \right\} \tilde{\theta} \quad (3.22)$$

After substituting for  $\tilde{\theta}$  and performing the differentiations and equating  $w'$  at  $\tilde{z} = 0$  to zero, the relation

$$\text{Real} [A m_1^2 + B m_2^2] = 0 \quad (3.23)$$

follows.

Equations 3.21 and 3.23 when solved simultaneously yield

$$A = \frac{-r_2 (\cos \beta_2)}{r_1 \cos \beta_1 - r_2 \cos \beta_2} \quad \text{and} \quad B = \frac{r_1 \cos \beta_1}{r_1 \cos \beta_1 - r_2 \cos \beta_2}$$

The vertical perturbation velocity  $w'$  is obtained by the substitution of Eq. 3.20 into Eq. 3.22:

$$\frac{w'}{u_\infty} = \left( \frac{T'_S}{T'_O} \right) \frac{1}{sL} \left\{ \text{Real} \left[ \left\{ \frac{Ar_1}{2\tilde{u}_1} \exp(i\beta_1 + m_1 \tilde{z}) + \frac{Br_2}{2\tilde{u}_1} \exp(i\beta_2 + m_2 \tilde{z}) \right\} \right. \right. \\ \left. \left. \exp(iK\tilde{x}) \right] - \tilde{u}_1 \text{Real} \left[ \left\{ A \exp(m_1 \tilde{z}) + B \exp(m_2 \tilde{z}) \right\} \right. \right. \\ \left. \left. iK \exp(iK\tilde{x}) \right] \right\} \quad (3.24)$$

The horizontal perturbation velocity  $u'$  may be obtained by substituting the value of  $w'$  given by Eq. 3.24 into Eq. 3.2 and integrating the resultant quantity with respect to  $x$  :

$$\frac{u'}{u_\infty} = - \left( \frac{T'_S}{T'_O} \right) \frac{1}{sL} \left\{ \text{Real} \left[ \left( Am_1^3 \exp(m_1 \tilde{z}) + B m_2^3 \exp(m_2 \tilde{z}) \right) \frac{\exp(iK\tilde{x})}{iK} \right] \right. \\ \left. - \tilde{u}_1 \text{Real} \left[ \left( Am_1 \exp(m_1 \tilde{z}) + B m_2 \exp(m_2 \tilde{z}) \right) \exp(iK\tilde{x}) \right] \right\} \quad (3.25)$$

The Fourier transform technique is now used to obtain solutions for the perturbed temperature and velocities. This involves the superposition of sinusoidal solutions using a Fourier cosine transform of the form

$$\tilde{\theta}(\tilde{x}, 0) = \int_0^\infty g(K) \cos K\tilde{x} dK \quad (3.26)$$

$$\text{where } g(K) = \frac{2}{\pi} \int_0^\infty \tilde{\theta}(\tilde{x}, 0) \cos K\tilde{x} d\tilde{x} \quad (3.27)$$

Equation 3.20 gives the solution for perturbed temperature for each wave number. The total solution is given by

$$\tilde{\theta}(\tilde{x}, \tilde{z}) = \int_0^\infty g(K) \text{Real} \{ [A \exp(m_1 \tilde{z}) + B \exp(m_2 \tilde{z})] \exp(iK\tilde{x}) \} dK \quad (3.28)$$

similarly the total solution for the vertical perturbation velocity is given by

$$\frac{w'(\tilde{x}, \tilde{z})}{u_\infty} = \int_0^\infty g(K) (\text{R.H.S. of Eq. 3.24}) dK \quad (3.29)$$

and the horizontal perturbation velocity by

$$\frac{u'(\tilde{x}, \tilde{z})}{u} = \int_0^{\infty} g(K) \text{ (R.H.S. of Eq. 3.25) } dK \quad (3.30)$$

The method of solution is to assume a surface temperature distribution to determine the weighting function  $g(K)$  and substitute it in the Eqs. 3.28, 3.29 and 3.30 to obtain the perturbed temperature, vertical velocity and horizontal velocity respectively. The two surface temperature distributions considered are:

(1) Mountain function -

$$\begin{aligned} \theta(\tilde{x}, 0) &= 1/[1 + (\pi\tilde{x}/2)^2] \\ g(K) &= (2/\pi) \exp(-2K/\pi) \end{aligned} \quad (3.31)$$

(2) Square function -

$$\begin{aligned} \tilde{\theta}(\tilde{x}, 0) &= 1, \quad 1 - \tilde{x} \leq 1 \\ \theta(\tilde{x}, 0) &= 0, \quad 1 - \tilde{x} > 1 \\ g(K) &= (2/\pi) (\sin K/K) \end{aligned} \quad (3.32)$$

The main characteristics of these surface temperature distributions are that

$$\begin{aligned} (1) \quad \tilde{\theta}(0, 0) &= 1 \quad \text{and} \\ (2) \quad \int_0^{\infty} \tilde{\theta}(\tilde{x}, 0) d\tilde{x} &= 1 \end{aligned} \quad (3.33)$$

### 3.3 Three-dimensional model - General solutions

A three dimensional model for a circular heat island may be constructed by superposing the two-dimensional solutions of Section 4.2 at varying angles  $\alpha$  to the uniform flow direction in a manner similar to Scorer (1956) and Olfe and Lee (1971). It will be convenient

to use the cylindrical coordinate system  $(r, z, \phi)$  for this model where  $\phi = 0$  denotes the freestream direction. The variables are now re-defined as:

$$\begin{aligned}\tilde{x}_c &= \frac{r}{L_c} \cos(\phi + \alpha) \\ S_c &= \frac{4gskL_2}{(u_\infty \cos\alpha)^3} \\ \tilde{z}_c &= \left\{ \frac{u_\infty \cos\alpha}{kL_2} \right\}^{1/2} z\end{aligned}\tag{3.34}$$

where  $r$  is the distance along the radius,

$L_2$  is the effective half-width of the circular heat island, and the suffix  $c$  denotes the variable for a circular heat island.

Integration of the two-dimensional total solutions with respect to  $\alpha$  between the limits  $-\pi/2$  and  $+\pi/2$  yields the distributions for the three-dimensional heat island. The form of the solution will be:

$$\begin{aligned}\theta(r, z, \phi) &= \frac{1}{\pi} \int_{-\pi/2}^{\pi/2} \left[ \int_0^\infty g(K) \operatorname{Real} \{ [A \exp(m_1 \tilde{z}_c) + B \exp(m_2 \tilde{z}_c)] \right. \\ &\quad \left. \exp(iK\tilde{x}_c) \} dK \right] d\alpha\end{aligned}\tag{3.35}$$

Solutions for  $w'$  and  $u'$  are obtained in a similar manner. The following sections are concerned with the specific calculations based on the above linearized solutions and their comparison with Olfe and Lee's solutions and field observations. Numerical integrations were performed using the CDC 6400 computer at Colorado State University.

### 3.4 Solutions for specific cases

3.4.1 Two dimensional model - The linear solution developed in the previous sections was applied for a specific case to test the validity and to compare with other results. Parameters used by Olfe and Lee (1971) to describe the heat island of New York City were used to develop solutions for the perturbed temperatures.

Representative length of the heat island - 6.87 km

Reference wind velocity (at  $z = 100$  m) -  $3 \text{ m sec}^{-1}$

Constant stability factor,  $s$  -  $10^{-4} \text{ m}^{-1}$

Variable eddy diffusivity is assumed to be of the form

$$L = k_0 u_* z \quad (3.36)$$

where  $k_0$  is the Kármán constant,  $u_*$  is the shear velocity and  $z$  is the height above the surface. A shear velocity of 60 cm/sec estimated for Tokyo (Jones et al., 1971) was assumed. An average eddy diffusivity for the height of a typical urban boundary layer of 1700 feet (Davenport, 1960) was used for computing the conduction length  $L_c$ . A logarithmic type mean velocity was assumed with a roughness length  $z_0$  of 1 meter. A reference mean wind speed of 3 meters/sec at a reference height of 100 meters was used for the calculations.

The solutions obtained with the parameters mentioned above for the perturbed temperature profile at the city center along is shown in Fig. 3.1. The shaded area in the figure represents the urban temperature excess observed by Bornstein (1968) for New York City during different days. The profile for the present model was found to have a gradient less than that for Olfe and Lee. This may be the effect of the introduction of a boundary layer type velocity profile into the model. The

negative perturbations are of the same order of magnitude as observed in the field.

The non-dimensional perturbed temperature profiles at different downwind distances is shown in Fig. 3.2. They indicate the height of the base of the elevated inversion to increase with downwind distance, a feature observed both in the field and in the laboratory. The perturbations decrease rather slowly near the center of the heat island with steeper gradients near the edge. All the profiles converge at a height of about 200 meters beyond which the cooling due to the drifting of the rural air dominates.

The distribution of non-dimensional perturbed vertical velocity  $w'/u_\infty$  with height at different distances along the heat island is indicated in Fig. 3.3. Positive perturbations near the center and negative values downwind are found to be the effects of the heat island. The distribution of non-dimensional longitudinal perturbed velocity,  $u'/u_\infty$  with height is shown in Fig. 3.4. Positive perturbations are maximum near the center at lower levels with the longitudinal wind velocity decreasing at higher levels. This phenomena has been observed in the field and in the laboratory. The increase in the longitudinal velocity at lower levels is due to the drifting of cold air from the rural area towards the core of the city. Another interesting feature observed in the above figure is the lessening of the positive perturbations and increase in negative values near the downwind periphery of the heat island. The increase in negative perturbations may be due to the presence of the counter-gradient flow.

A comparison of the vertical profiles of non-dimensional perturbed temperatures for two different surface temperature distribution is

shown in Fig. 3-5. The profile with the surface temperature distribution defined by a square function has higher values of perturbations, both positive and negative at any given height. Base of the elevated inversion was found to be the same for both cases.

3.4.2 Three dimensional model - Superposition of two dimensional solutions to solve for a three-dimensional case is shown in Fig. 3.6 for a mountain function surface temperature distribution and with a value of  $L_2 = 0.433L$  as was assumed by Olfe and Lee. The solution for the three-dimensional case indicates lesser cross-over heights. This feature was also observed by Olfe and Lee. Predicted results compare with the observed ones better for a three-dimensional model.

## Chapter IV

## EXPERIMENTAL EQUIPMENT AND DATA COLLECTION

Experiments were conducted in the meteorological wind tunnel of Colorado State University. The tunnel is located in the Fluid Dynamics and Diffusion Laboratory at the Engineering Research Center. A view of this wind tunnel and the location of the experimental arrangement inside the wind tunnel is shown in Fig. 4.1. The performance characteristics of this wind tunnel are given in Table 4.1. The capability of this wind tunnel to simulate stratified atmospheric boundary layers has been discussed by Cermak et al., (1966). The experimental equipment, techniques used for measuring different variables, the mode of atmospheric simulation and data collection are discussed in the following sections.

#### 4.1 Physical arrangement of the experiment

The experimental arrangement was located at a horizontal distance of 59.5 feet from the beginning of the test section of the wind tunnel and 20.5 feet from the beginning of the aluminum floor. This distance facilitated the development of a boundary layer to the required height at the point of interest. Figure 4.2 shows the plan and sectional views of the experimental arrangement. It consisted essentially of three electrical heaters 2 feet x 6 feet with the longer side along the direction of the wind. A line source 5 feet long was placed across the wind tunnel at a horizontal distance of 2 feet upwind from the beginning of the heater. A false floor made up with aluminum plates was provided around the heaters and the line source to ensure a level floor. Care was taken to give long ramps at the beginning and at the end of

the experimental arrangement to assure smooth air flow. The detailed description of the different components of the experimental arrangement is given in the following paragraphs.

4.1.1 Electrical heater plates - Commercial heaters used were made with nickel-chromium resistance wire wound on premium mica with an aluminized steel sheath material. The base of the heater was insulated with an asbestos sheet 1/8 inch thick in order to prevent heating the aluminum plate of the experimental setup on which it rested. Holes were made in the edges to screw down the heaters onto the false floor. The total thickness of each heater was 3/16 inch. Provision was made to individually heat each heater by means of a variac assembly. The typical cross section of a heater and the photograph of the variac assembly are indicated in Figs. 4.3 and 4.4 respectively. The 2 feet x 6 feet heater was used to simulate a rectangular urban heat island. A rectangular heater 6 feet long and 2 feet wide was chosen instead of a square one for two main reasons:

- (1) to avoid measuring three dimensional profiles in the region of the developing internal boundary layer of the roughness over the heater and
- (2) to provide for a sufficient buffer zone in the rear of the area of measurement so as to minimize the end effects.

4.1.2 Line source of tracer gas - The three-dimensional effects introduced by the presence of a heater with finite width can be brought forth better with the use of a two-dimensional line source rather than using a point source. Hence it was decided to introduce a two-dimensional, continuous, line source upwind of the heat island, level with the top of the heater. The cross-section of the line source assembly (5 inches wide and 5 feet long) is shown in Fig. 4.5. It consisted of two

rectangular copper tubes held together 3 in. apart by two brass plates soldered to them, one at the top and the other at the bottom. Series of holes were drilled in both the tubes but were staggered to reduce the velocity of the incoming source gas. The diameter of the holes in the top of the copper-brass box was 1/16 in. and the spacing was 1/2 in., thus providing for a series of small jets. The exit velocity was reduced to the minimum value practicable. In order to ensure uniformity of the source in the lateral direction of the wind tunnel, source gas was supplied through a supply cylinder onto five equally spaced entry points in the back of the source. The horizontal distance of the source from the heater was selected such that it achieved a two-dimensional distribution of concentration in front of the heater.

#### 4.2 Measurements

The variables measured or observed during the experiment were:

- (1) mean and fluctuating components of longitudinal velocity.
- (2) mean and fluctuating temperatures,
- (3) surface mean temperatures,
- (4) mean concentrations of the radioactive tracer gas released from a continuous line source located upwind of the heat island and several point sources located in and around the heat island and
- (5) the flow pattern in, above and around the heat island.

(This was observed by flow visualization technique and recorded by still and motion pictures).

The instruments and the methods used to measure the foregoing variables are described in the following paragraphs.

4.2.1 Mean velocity and turbulence - The freestream velocity selected for the experiment from the considerations of model similarity

was 4.5 ft/sec. The accuracy of the pressure reading instruments were of the same order as this velocity thus eliminating the possibility of using pitot tube for mean velocity measurements. Smoke wire techniques developed in the Fluid Dynamics Laboratory at Colorado State University, could not be used because of the extreme mixing near the heat island and the amount of time required to measure three-dimensional profiles. Hence, the only alternative was to use a hot-wire anemometer. Whereas the use of a hot-wire anemometer in constant temperature air is fairly simple, it becomes highly complicated in a thermally stratified air flow. This is due to the variation in heat transfer from the hot-wire with the variation of the ambient air temperature. The temperature compensated hot-wire probe - DISA 55 E 30 was used for the thermally stratified flows in this study along with a DISA 55 D01 constant temperature anemometer. This probe had two sensors, a velocity sensor consisting of a 1.2 millimeter long, 5 micrometer diameter point plated tungsten wire and a temperature sensor made up of a tungsten wire coil. The prongs and the coil leads were embedded in the ceramic probe shank and the probe had two leads into the anemometer--one for velocity measurement and the other for temperature compensation. The constant-temperature anemometer gave voltage output after compensating for the temperatures. The details of this probe are shown in Fig. 4.6. Technical data for the temperature compensated hot-wire probe is given in Table 4.2 in the Appendix.

The probe was calibrated in a Thermo-System calibrator modified to suit the purpose. A line diagram indicating the details of the calibration is shown in Fig. 4.7. Since the maximum frequency of the airflow for this study was within 100 hertz, the velocity-fluctuation data

measured by the temperature compensated hot-wire probe were fairly accurate. Moreover, sufficient time was allowed at each station to allow for the temperature compensation reaction time. Mean velocities were measured by integrating the output voltage from the anemometer over a sufficiently long time. A Hewlett-Packard model 2401 C integrating digital voltmeter was used. The fluctuating component of the velocity was measured directly with a DISA 55 D 35 r.m.s. meter and also was recorded on a magnetic tape for a few positions of interest. Some of the instruments used to measure the mean and turbulent components of velocity are shown in Fig. 4.8. A General Radio wave analyzer was used to analyze the instantaneous air-velocity data for the energy spectrum. Measurements for constant temperature airflow were made with the conventional hot-wire anemometer.

4.2.2 Surface temperature - An attempt was made to find the surface temperature of the heater by installing two thermocouples one over the other at a finite vertical distance apart inside the heater. Since the overall thickness of the heater was  $3/16$  inch and the thickness after allowing for an insulation layer was barely  $1/16$  inch, the distance provided between the two thermocouples was of the order of  $1/50,000$  in. making it very difficult to obtain a reliable estimate of the surface temperature. Measuring the surface temperature with the help of thermocouples resting on the surface will cause serious errors due to the presence of air gaps. Hence it was decided to use an infrared pyrometer that does not have to be in contact with the surface and had high resolution. A Williamsen Corporation model 600 battery powered infrared pyrometer was used. The principle of operation of the pyrometer was as below: infrared energy from the target is focussed by a plano

convex quartz lens onto a lead sulphide photoconductor. Interposed between the lead sulfide cell and the lens are two elements - (1) a 2.3 micron filter - used to reduce the sensitivity of the instrument to a visible light and near visible light and (2) a revolving segmented disk, which alternately blocks and passes the infrared energy from the target is used to generate pulses of the infrared energy for driving the lead sulphide cell. This is done so that the electrical output from the photoconductor will be an ac signal.

The instrument was calibrated with the help of a calibration source built into the system. The calibration system was an aged filament lamp operated at a fixed infrared output used as a calibrating reference. The lamp voltage is adjusted until the lamp output had an effect on the system equivalent to a black-body target at a factory set level. Corrections for the change in emissivity of the heater surface and the aluminum blocks was made. An overall view of the instrument is shown in Fig. 4.9. The pyrometer was held at a vertical distance of one foot from the target and the temperature of an area 0.75 in. in diameter was measured.

Surface temperatures of the wind-tunnel floor around, upwind and downwind of the heaters were measured by the copper-constantan thermocouples installed at about 1/16 in. from the surface of the 7/8 in. thick aluminum floor.

4.2.3 Mean and fluctuating temperatures - Mean and fluctuating temperatures for the first part of the experiment were measured with a cold-wire probe using a constant current anemometer. Copper-constantan thermocouples were used to measure the mean temperatures for the latter part of the experiment.

(a) Measurement of the mean and fluctuating temperatures with the cold-wire - A DISA 55 D01 anemometer was used in constant-current mode for temperature measurements. Tungsten wire 0.00035 in. in diameter was used as the temperature sensor probe. The probe resistance was measured directly with the change in ambient temperature. A special oven designed for this purpose was used for calibration. A typical calibration curve is shown in Fig. 4.10. The calibration curve can be expressed by the equation

$$R_T = R_O [1 + \alpha_w (T - T_O)] \quad (4.1)$$

where  $R_T$  is the wire resistance at temperature  $T$ ,

$R_O$  is the wire resistance at temperature  $T_O$ , and

$\alpha_w$  is the thermal coefficient of resistance of the wire material.

Having determined  $\alpha_w$  from the calibration curve, the corresponding resistance changes were calculated for the desired temperature measuring range. The mean temperature was measured by integrating the voltage output of the anemometer over a specified time. Hewlett-Packard model 2401 C integrating digital voltmeter was used along with an electronic time counter. The fluctuating temperatures were measured by a 55 D 35 DISA r.m.s. meter.

(b) Measurement of the mean temperatures by copper-constantan thermocouples - Twenty five copper-constantan thermocouples mounted on a rake and controlled by a multiple-switch were used to measure the mean temperatures. Care was taken to allow for the reaction time of the thermocouples before taking measurements. The thermocouple reference was always maintained at 32°F. The output of the thermocouple was integrated over a specified time if it showed large fluctuations with the help of an integrating digital voltmeter. A typical calibration curve of a copper-constantan thermocouple is shown in Fig. 4.11.

4.2.4 Mean mass concentrations - In addition to the line source described in Section 4.1.2 several point sources were used at different places in and around the heaters. The purpose of using the point source was to quantitatively follow the movement of air in, above and around the heater and verify the results obtained by the flow visualization. Radioactive Krypton 85 was used for the sources and the gas flow rate was monitored by flow meters. The wind tunnel was flushed after each run to reduce the background concentrations to the minimum.

Sampling rakes were set up at the required locations over the model and were drawn by vacuum pressure from the wind-tunnel through 1/8 in. internal diameter flexible tubing and collected in glass bottles by the displacement of water. The details of the sampling system are shown in Figs. 4.12 and 4.13. This arrangement enabled collection of 25 samples at the same time. Each sample was then transferred into a cylindrical jacket around Geiger-Mueller (G.M.) tube by applying a positive pressure to the reservoir. The radioactivity of the sample after transfer to the G.M. tube was counted by a Nuclear-Chicago ultrascaler. After counting the sample, water was used to flush the sample out from the cylindrical jacket of the G.M. tube and a fresh sample transferred and counted. A photograph of the experimental arrangement and a close-up view of the roughness elements are shown in Fig. 4.14.

4.2.5 Flow visualization - For the different cases of this study, flow visualization formed an important part of the experiment. Smoke generated by titanium tetrachloride was used to visualize the flow pattern induced by the three-dimensional heat island. Black and white still pictures and color motion pictures were taken with the smoke source at the positions of interest.

### 4.3 Similarity criteria

Cermak et al. (1966) presented comprehensive guidelines for the simulation of atmospheric motion by wind-tunnel flows. The simulation of stratified flows requires facilities in the wind tunnel specifically designed to reproduce magnitudes of stability and stratification as found in the atmosphere. The wind tunnel used for this study had the capability of simulating the atmospheric conditions regarding temperature stratification as can be seen from the performance characteristics shown in Table 4.1.

The mechanical energy of turbulence is associated with vertical wind shear,  $d\bar{u}/dz$  through an eddy stress  $\tau_0$  where  $\bar{u}$  is the mean velocity in the longitudinal  $x$  direction and  $z$  is measured in the vertical direction. In the presence of a diabatic lapse rate, turbulent energy is also strongly affected by buoyancy forces. Richardson (1920) proposed a dimensionless number as a criterion to signify the influence of buoyancy in enhancing or damping turbulent motion in a thermally stratified flow. This dimensionless number  $Ri$  has been given his name and has the following form:

$$Ri = \frac{\text{rate of consumption of turbulent energy by buoyancy forces}}{\text{rate of production of turbulent energy by wind shear}}^{-1} \quad (4.2)$$

A second form of the Richardson number is expressed as a gross parameter that will describe the condition of the atmospheric layer with respect to stability and is known as a flux Richardson number,  $R_f$ . Batchelor (1953) has shown the Richardson number to be the only criterion for the similarity of mean velocities near a rough boundary in a thermally stratified flow. Moreover, the non-dimensionalization of the linearized

equations for the stratified flow over a heat source indicated Richardson and Reynolds numbers as the governing parameters in Chapter III. Hence, for the current study the Richardson number was chosen as the modeling parameter to simulate the flow conditions upwind of the heaters. The objective was not to simulate the flow conditions existing over any particular urban area but to obtain a general Richardson number that will be typical of a rural area upwind of a city. Several field velocity and temperature profiles that have been measured and reported were considered before arriving at a representative flux Richardson number  $R_f$ . The vertical temperature gradients near the ground observed in the atmosphere upwind of some of the cities are given below:

- |   |                              |
|---|------------------------------|
| (1) Idaho Falls (Weather Bureau Observations) | 4°F/100 feet                 |
|   | (De Marrais, 1961)           |
| (2) New York City                             | 4.5°F/100 feet               |
|   | (Bornstein, 1968)            |
| (3) Palo Alto                                 | 11°F/100 feet                |
|   | (Duckworth & Sandberg, 1954) |

The temperature gradient observed in Palo Alto was considered to be a special case and not typical. Wind speed at 100 feet height in the atmosphere was assumed to be about 9 ft/sec as the one that may be typical of an anticyclonic pressure system. Richardson number based on the equation, (Cermak and Peterka, 1966)

$$R_f = \frac{g \left( \frac{d\theta}{dz} \right)}{\theta \left( \frac{\partial \bar{u}}{\partial z} \right)^2} \quad (4.3)$$

with a temperature gradient of 4°F/100 feet was calculated to be approximately equal to 0.25. This value of Richardson number was used as a guide in selecting a free-stream wind speed of 4 ft/sec, free stream temperature of 110°F and surface temperatures around, downwind, and upwind of the heaters as 35°F for the wind-tunnel simulation of a typical three-dimensional urban heat island.

The criterion adopted for the similarity of the heat sources was based on the non-dimensional length  $z/L'$  where  $z$  is the height above the surface and  $L$  is Monin-Obukhov's length characteristic of the surface layer in the atmosphere. Monin-Obukhov's length is given by

$$L' = \frac{u_*^3}{k_o (g/T_A)} \frac{c_p}{H}$$

where  $u_*$  is the shear velocity,

$k_o$  is von Kármán constant

$g$  is the gravitational acceleration,

$T_A$  is the average potential temperature of air,

$c_p$  is the specific heat of air at constant pressure, and

$H$  is the eddy heat flux.

With the relation

$$\left(\frac{z}{L'}\right)_p = \left(\frac{z}{L'}\right)_m$$

where  $p$  and  $m$  denote the prototype and the model conditions respectively and eliminating the parameters having equal value for the atmosphere and the wind tunnel, the above equation becomes

$$\frac{z_p H_p}{u_{*p}^3 T_{Ap}} = \frac{z_m H_m}{u_{*m}^3 T_{Am}}$$

which reduces to

$$\frac{H_p}{H_m} = \frac{z_m}{z_p} \frac{T_{Ap}}{T_{Am}} \frac{u_{*p}^3}{u_{*m}^3} \quad (6)$$

Following values were assumed for the prototype and the model to represent the meteorological conditions existing over a typical city near the surface:

$$T_{A_p} = 20^\circ\text{C} \quad u_{*p} = 30 \text{ cm/sec}$$

$$T_{A_m} = 75^\circ\text{C} \quad u_{*m} = 20 \text{ cm/sec}$$

From the considerations of the thickness of the boundary layer over the heat island in the wind tunnel and the corresponding urban boundary layer over a city, one meter of the model roughly represented 1300 meters in the prototype. With the above values in Eq. 6

$$\frac{H_p}{H_m} \approx .002 \quad \text{or the heat output in the model}$$

should be about 500 times that in the prototype. Estimates of the heat output from a moderate size city showed the heat energy to be of the order of  $10^9$  calories/minute (Sekiguti, 1970). Assuming an area of 75 square kilometers for this city, the corresponding estimate for heat output per unit area will be about  $7 \times 10^{-8}$  KW/cm<sup>2</sup>. In order to satisfy the  $z/L'$  criterion, the laboratory model should have a heat output of about  $4 \times 10^{-8}$  KW/cm<sup>2</sup>. The electrical input for the heaters was determined based on this value.

#### 4.4 Data collection

The experiment was divided into 12 different cases. Measurements of the variables indicated in Section 4.2 were made for three different approach flows for the heater under neutral and unstable conditions with and without roughness. Roughness consisted of aluminum blocks one inch x one inch x 1/4 inch thickness arranged in mutually perpendicular street patterns. Three different approach flows considered were:

- (1) Neutral
- (2) Stable stratified with ground based inversion
- (3) Elevated inversion.

The free-stream wind speed and the heat source were maintained constant for the entire experiment. The following table classifies and names different cases that were studied:

<u>Case No.</u>	<u>Approach</u> <u>Flow (AF)</u>	<u>Heat</u> <u>with respect to</u> <u>temperature</u>	<u>Island Condition</u> <u>with respect to</u> <u>roughness</u>
I	Neutral	Neutral	without roughness
II	Neutral	Unstable	without roughness
III	Stable	Neutral	without roughness
IV	Stable	Unstable	without roughness
V	Elevated inversion	Neutral	without roughness
VI	Elevated inversion	Unstable	without roughness
VII	Neutral	Neutral	with roughness
VIII	Neutral	Unstable	with roughness
IX	Stable	Neutral	with roughness
X	Stable	Unstable	with roughness
XI	Elevated inversion	Neutral	with roughness
XII	Elevated inversion	Unstable	with roughness

The data were analyzed by the CDC 6400 digital computer at Colorado State University.

## Chapter V

### DISCUSSION OF EXPERIMENTAL RESULTS

The results of the laboratory measurements for different cases of airflow over the heat island are presented in this chapter. Comparison of the theoretical predictions of perturbed temperatures over the heat island with the experimental wind tunnel results are given. In addition, temperature and wind profiles and the relevant mechanisms as observed in the field in general are compared with the results from the wind tunnel.

#### 5.1 Flow visualization

Visualization of air flow over the heat island with the help of titanium oxide smoke formed an important part of the study to understand the predominant mechanisms of a three-dimensional heat island. The qualitative results obtained by flow visualization checked very closely with the quantitative measurements. Some of the interesting features of airflow over a three-dimensional urban heat island are presented and discussed in this section. Footage index of the motion picture is given in the Appendix.

The unperturbed air motion for the neutral approach flow over a smooth, neutral heat island is shown in Fig. 5.1. In contrast, the perturbations induced on the stable flow by an unstable heat island is shown in Fig. 5.2. The negative vertical velocities near the upwind edge of the heat island was predicted by the theoretical model and observed in the field by several investigators. With the buoyancy forces becoming predominant, there was vertical upward motion over the middle portions. The effect of an unstable heat island in causing the

convergence of flow towards the heater is shown in Figs. 5.3 and 5.4. This convergence was mainly due to the buoyancy forces lifting the air above the heat island and causing the cold air from the sides to rush in. The cold air that converged into the heat island, became heated and raised as can be seen in Fig. 5.5 with the help of a ground level smoke source on one side. The increase in instability and the vortices created by the roughness elements can be observed in Fig. 5.6.

Laminar type unmixed flow was visualized in Fig. 5.7 for the stable flow over a neutral rough heat island. With heating, the amount of mixing and the magnitude of buoyancy forces that are brought into action can be seen in Fig. 5.8. The "urban heat island plume" generated by the heat island and discussed in the following sections is also seen in the above photograph.

The nature of airflow near the downwind edge of the heat island for a stably stratified flow over an unheated heater surface is shown in Fig. 5.9. Once the heater was heated, air over the heat island became unstable and a plume moving well above the downwind ground surface was generated as one of the many effects of the heat island. This in turn created a reverse flow near the downwind edge as can be seen in Fig. 5.10. The strength of the reverse flow depended on the intensity of the heat island and the surface temperature difference. The reverse flow diffused more for a rough heat island as shown in Fig. 5.11. Presence of the longitudinal vortices at the edges of the heat island is visualized in Fig. 5.12 for the stable flow over an unstable rough heat island.

## 5.2 Mean temperature distributions

The results of the mean temperature measurements for various cases are presented in this section. They are arranged in three subdivisions, the first one regarding the surface temperature distributions both longitudinal and lateral and mean temperature profiles along the center line, the second part consisting of the mean temperature distributions along the width of the heat island and the third one comprising the mean temperature contours.

### 5.2.1 Surface temperature distributions and mean temperature profiles along the centerline -

(a) Neutral approach flow - The distribution of surface temperatures of the heater for neutral flow over an unstable rough heat island is given in Fig. 5.13 (top). An average temperature of 270°F was maintained. The variation of surface temperature along the centerline was due to the difference in the density of nichrome heating wires at the edges of each of the three heaters used for this study. This difference in the surface temperature amounting to approximately 8 percent at the edges in the longitudinal direction was not expected to affect the accuracy of the results appreciably. The surface temperature distribution along the width of the heat island showed a similar temperature difference approximating a mountain function. This was given due consideration in the data analysis and in the theoretical prediction of perturbed temperatures.

Mean temperature profiles along the centerline for neutral flow over an unstable rough heat island are shown in Figs. 5.13 and 5.14. Steep temperature gradient near the heater surface to a depth of one in. is indicated in Fig. 5.13 (bottom).

The details beyond  $z = 1$  in. over the heat island are shown in the temperature profiles in Fig. 5.14. Overall temperature profiles can be formed with the help of the surface temperatures shown in Fig. 5.13. The absence of even weak elevated inversions is worth noting. In fact the mean temperatures became isothermal at a finite height. This height increased along the heat island in the downwind direction varying from about 3 in. at the beginning of the heater, to about 9 in. near the end ( $x = 69$  feet). Another interesting aspect was the formation of a weak inversion downwind of the heater. This is due to the presence of a low-level heated plume passing over an unheated surface.

(b) Stable approach flow - Mean temperature profiles for the stably stratified flow with ground based inversion over an unstable heat island for rough and smooth cases are given in Fig. 5.15 and Fig. 5.16. The surface temperatures for the rough case showed a slight increase over that for the smooth ones presumably due to larger surface area and more efficient heat transfer. In general, the average temperature for the stable flow was about  $260^{\circ}\text{F}$ , about 4 percent lesser than that for the neutral case. This reduction was probably due to the decrease in mixing over the heater as compared to the neutral approach flow. The mean temperature profiles in the vertical direction along the centerline in Fig. 5.15 (bottom) and Fig. 5.16 show certain interesting features and are discussed in the following paragraph.

The vertical profile at  $x = 62$  feet characterizes the mean temperature of the two-dimensional stably stratified approach flow. The profile at  $x = 63$  feet (beginning of the heat island) indicated the effect of the heater in the upwind direction. There was an increase in the mean temperatures by 15 percent for the smooth case and 5 percent for the

rough case. Lesser increase for the rough case was due to the more intense mixing caused by the roughness elements. A definite but weak elevated inversion could be seen over the heat island at successive profiles. Although temperatures for the rough case were lesser than that for the smooth case in general, the difference was found to diminish as the air moved along the heater and became approximately equal over the downwind half of the heat island at lower levels. The temperature profile at the downwind edge of the heat island ( $x = 69$  feet) indicated the temperatures for the smooth case to be lesser than that for the rough case. This was due to the fact that for the smooth case, the reverse flow that took place at the downwind edge of the heater was stronger than that for the rough surface and can be seen from the photographs presented in the Section 5.1. The mean temperature profile downwind of the heater ( $x = 70$  feet) shows a similar effect at the upper levels. The base of the elevated inversion was seen to increase in height with distance from the beginning of the heat island. The approaching stably stratified temperature profile was found to reoccur downwind of the heat island.

(c) Elevated inversion approach flow - The surface temperature distribution for the elevated inversion approach flow over an unstable rough heat island is shown in Fig. 5.17 (top). Average surface temperature for this case was approximately  $250^{\circ}\text{F}$ . The vertical profiles of the mean temperature along the centerline are shown in Figs. 5.17 and 5.18. The two-dimensional elevated inversion approach flow was characterized by the mean temperature profile at  $x = 63$  feet with the base of the elevated inversion about 1.5 in. from the surface. The basic nature of the vertical distribution of temperature was essentially the

same as for the stably stratified flow, but the temperature gradients were steeper for the latter case.

5.2.2 Mean temperature distributions along the width of the heat island - Mean temperature vertical profiles at different distances along the width of the heat island at  $x = 66$  feet is shown in Fig. 5.19 for the ground based and elevated inversion approach flows over an unstable rough heater. The temperature gradients became steeper as the lateral distance from the edge of the heat island increased with the maximum temperature recorded at  $y = 0$ . The elevated inversion was persistent along the width although the height of its base from the surface decreased with the maximum at  $y = 0$  in. and the minimum at  $y = 12$  in. Temperature profiles beyond  $y = 12$  in. were stably stratified. Fig. 5.20 indicates the symmetrical, dome shaped three-dimensional distribution of the base of the elevated inversion for stable flow over the rough heated island. Temperature inversion structure similar to this has been observed in the field. Spangler and Dirks (1972) in their study at St. Louis, Missouri indicate the base of the inversion to be at 1500 m over the downtown area dropping down to about 1000 m over the periphery of the city.

The three-dimensional effect for a neutral flow over an unstable rough heat island is shown in Fig. 5.21. The distribution of temperature over the middle portion of the heater was approximately two-dimensional with the temperatures decreasing to the constant temperature of approach flow at  $y = 13$  in. Three-dimensional effects were observed for 40 percent of the width of the heater whereas outside the edge of the heater flow over only one in. (or a width equivalent to about 8 percent of the

heater) width was affected. At about 6 in. above the surface the temperature of the flow was uniform across the width.

In contrast to the neutral approach flow, stably stratified flow with ground based inversion over a rough heated island showed certain interesting features as can be seen from Fig. 5.22. The temperatures started decreasing from  $y = 6$  in. attaining minimum values approximately at  $y = 14$  in. and then remaining uniform. The zone of influence increased with about 50 percent of the air flowing over the heater affected by the cold air drawn in. There was a "horizontal cross over" in the nature of the temperature profile around  $y = 10$  in. (inside the heat island) at which the unstable vertical temperature profile changed into a stable one. The lateral extent to which the cold air moved over the heat island could be inferred from the position at which the temperatures at different levels began decreasing.

The mean temperature distribution at different elevations along the width of the heater at  $x = 65.5$  feet for an approach flow with elevated inversion over an unstable rough heat island is shown in Fig. 5.23. The general pattern was essentially the same as for the ground based stable approach flow with the "horizontal cross over" occurring at about  $y = 10$  in.

A comparison of the lateral distribution of mean temperatures over an unstable, rough heat island for the three different approach flows is shown in Fig. 5.24 at  $x = 66$  feet at an elevation of 0.5 in. The stable flow had the maximum temperatures near the center of the heat island with the elevated inversion approach flow having the next higher temperatures. Maximum temperature difference between the heat island

and the surrounding area occurred for the ground-based stable approach flow at this height.

5.2.3 Mean temperature contours - Since the temperature contour lines represent flow paths closely, mean temperature contours in the longitudinal and lateral directions are plotted and discussed in this section.

Temperature contours along the centerline in x-z plane for a stable flow over neutral, smooth heat island is shown in Fig. 5.25. The constant temperature lines show a wavy pattern (gravity waves) as would be expected for a stable flow with no disturbance superimposed. This waviness was also observed in diffusion measurements under similar conditions and is reported in Section 5.7 of this chapter.

The temperature contours for the neutral flow over an unstable, rough heat island is given in Fig. 5.26. The reverse flow at the downwind edge of the heat island was perceptible from the contour lines. Constant temperature lines for the stable flow over an unstable, smooth heat island is shown in Fig. 5.27. The temperature contours indicated a large volume of reverse flow downwind of the heat island. The perturbations introduced by the heat source of the heater was appreciable as compared to the orderly flow seen in Fig. 5.25. Mean temperature contours for the stable flow over an unstable rough heat island in Fig. 5.28 indicated the degree of mixing and reduction of the temperatures above the heat island induced by the roughness elements.

Elevated inversion approach flow over a rough heat island for the neutral and unstable cases are shown in Figs. 5.29 and 5.30 respectively. Air flowing over the heated plate (heated to create elevated inversion) suddenly encounters the cold heater and decelerates and this may be

the reason for the big hump at  $x = 65$  feet in Fig. 5.29. Downwind of this position contour lines are fairly straight. The mean temperature contours for the elevated inversion approach flow over an unstable heat island at  $x = 66$  feet is shown in Fig. 5.31. Constant temperature lines for the stable flow over an unstable heat island with and without roughness at  $x = 66$  feet is shown in Figs. 5.32 and 5.33 respectively. Steeper gradient of the contour lines towards the heat island indicates large influx of cold air. The temperature contours for an elevated inversion approach flow over an unstable, rough heat island at  $x = 66$  feet is shown in Fig. 5.34. The flow had essentially the same features as for the ground based stable approach flow.

### 5.3 Development of different boundary layers over the model

The average thicknesses of the momentum boundary layers observed over the model for different conditions of the approach flow and the heat island are listed in Table 5.1. Thickness of the momentum boundary layer was calculated from the consideration that  $\bar{u}_\delta / u_\infty = 0.99$  where  $u_\delta$  was the mean wind speed at a height equal to the thickness of the boundary layer and  $u_\infty$  was the free stream velocity.

There was a substantial variation in the momentum boundary layer thickness, with the minimum observed for the stable approach flow over a smooth, neutral heat island which approximated a laminar flow. The maximum was found for an approach flow with an elevated inversion over a rough, unstable heat island. The difference in thickness between the stably stratified and elevated inversion approach flows amounted to about 25 percent of that of the former. Thickness of the momentum boundary layer was found to be fairly constant over the downwind half of the length of the heat island for all the cases studied.

Thermal boundary layer growths for the stable and elevated inversion approach flows over an unstable rough heat island are shown in Fig. 5.35 along with the internal boundary layer. Thickness of the thermal boundary layer was found to be about 50 percent of the corresponding momentum boundary layer. The thermal boundary layer thickness was determined from a similar consideration to that for the momentum boundary layer as indicated above. The average thickness of the internal boundary layer caused by the presence of aluminum blocks was about six times the height of the roughness elements and leveled off within two ft from the leading edge of the heat island.

A typical distribution of the wind speed across the wind tunnel is shown in Fig. 5.36. The thickness of the wall boundary layer on either side was found to be about 9 inches at a free stream velocity of four ft/sec. The distribution of air velocity across with wind tunnel was closely two-dimensional without the roughness and the heat island.

#### 5.4 Mean velocity distributions

The distribution of mean wind speed in the longitudinal direction is presented in this section. For ease in discussion this section is subdivided, each concerned with different aspects of mean velocity distribution.

5.4.1 Mean velocity profiles along the centerline - Distance along the vertical direction ( $z$  axis) was normalized with the thickness of the momentum boundary layer and the mean velocities were normalized with the free-stream velocity which varied from 4 to 4.5 feet per second for different runs. In the following discussion "neutral heat island" represents the heater not heated and the "unstable heat island" indicates the heater in operation.

(a) Neutral approach flow

The non-dimensional velocity profiles at different distances along the centerline for the case of neutral, smooth heat island is shown in Fig. 5.37. All the profiles tend to be similar. The corresponding velocity profiles for the case of neutral, rough heat island is indicated in Fig. 5.38 which also have a similar tendency. A comparison of these curves for the smooth and rough cases is shown in Fig. 5.39 which indicates the lessening of the wind speed in the lower layers of the boundary layer due to the presence of roughness.

For the case of an unstable heat island, the velocity profiles at different locations along the centerline do not match as can be seen from Fig. 5.40. The velocity profile at  $x = 64$  ft (one foot upwind of the heat island) indicates smaller shear and is similar to the one obtained in Fig. 5.37. The profile at  $x = 64$  ft (one foot inside the heat island) shows a slight decrease in the velocities at upper levels and there is no significant difference at lower levels. The decrease in the longitudinal velocity component at upper levels may be due to the downward flow of the air at the beginning of the heat island. This downward flow was photographed and presented in Section 5.1. The profile at  $x = 66.3$  ft indicates a sharp increase in wind speed near the ground due to the convergence of cool air from the sides.

The mean velocity profiles for the neutral approach flow over an unstable, rough heat island is shown in Fig. 5.41. But for the smaller velocities in general due to the presence of roughness, they indicate the same trend as for the smooth case.

(b) Stable approach flow

Mean velocity profiles observed along the centerline for a stably stratified approach flow with ground based inversion over a neutral, rough heat island are given in Fig. 5.42. They tend to fall into a single curve due to the similarity of profiles and exhibit smaller shear near the surface than that for neutral approach flow.

The different dimensionless mean velocity profiles encountered along the centerline for a stably stratified approach flow over an unstable, rough heat island are shown in Figs. 5.43 and 5.44. This approach flow incorporated the common features observed in the field. The mean velocity profiles observed for this case in the model showed several interesting aspects of the urban heat island. The profile at  $x = 62$  ft is the one that represented the approaching two-dimensional stably stratified flow. Two distinct levels with respect to the wind speeds are indicated by the velocity profiles at  $x = 63$  ft and at  $x = 69$  ft the lower level ( $0 < z/\delta < 0.05$ ) and the upper level ( $z/\delta > 0.05$ ). Due to the strong buoyancy forces set up by the heat island, the air flowing over the heat island raised and to make up for this mass of air, cold air from the sides converged into the heat island, was heated, moved upward and downwind as a plume commonly known as an "urban heat island plume." This feature of the heat island was photographed and presented at Section 5.1. At the lower level, the mean velocity progressively increased downwind over the heat island but started decreasing near the downwind edge of the heat island. The conditions were different at the upper level. The mean wind speeds at the beginning of the heat island ( $x = 64$  ft) were higher than the approaching flow, but became smaller at middle and downwind portions. This may have been due to the

fact that at the beginning of the heat island the volume of cold air influenced by the heat island was greater than that near the downwind portions. The additional volume of cold air drawn into the heat island was from the area upwind of the heat island itself. Near the intersection of the heat island and the downwind cold (rural) area, the air motion slackened with the maximum reduction occurring at about one foot ( $x = 70$  ft) and had certain interesting features observed in rural areas downwind of the heat island. The wind speed was logarithmic with height at lower levels, uniform for a height equal to about 50 percent of the momentum boundary layer thickness and then sharply increased to the maximum velocity observed over the heat island in a relatively small vertical distance. The height at which there was a sharp increase in the mean velocity indicated the position of the base of the urban heat island plume. The decrease in the wind speed at the lower level was associated with the reverse flow at the downwind edge of the heat island.

(c) Approach flow with elevated inversion

Non-dimensional mean velocity profiles for an approach flow with an elevated inversion (height of the base at 1.5 in.) over a neutral, smooth heat island is shown in Fig. 5.45. As for the previous cases with the neutral heater, the velocity profiles tend to be similar. The mean velocities for the rough case indicated slight reduction in wind speed in the lower layers as can be seen from Fig. 5.46. For the air-flow over an unstable, smooth heat island, the mean velocities had the same trend as for the ground based stable approach flow case except that approaching velocities were themselves relatively higher due to the presence of an elevated inversion.

The mean velocity profiles for the unstable heat island without and with roughness are indicated in Figs. 5.47 and 5.48, respectively. Flow over unstable, rough surface with elevated inversion approach flow had certain features different from that with a ground based stable approach flow. The mean velocities increased throughout the height over the heat island. At the downwind edge, mean velocity started decreasing at higher levels. The reason for the increase of the wind speed at the lower levels near the downwind edge of the heat island may have been due to the more diffused heat island plume and the higher elevation of the plume itself as compared to that with a stable approach flow.

A comparison of the effect of the three different approach flows on the center line mean velocity of the air flow over an unstable, rough heat island is presented in Fig. 5.49. As discussed in the above paragraphs the one with the neutral approach flow had the smallest mean velocities with the elevated inversion and stably stratified approach flows having greater values in that order. The reason for the stable approach flow causing highest velocities was due to the greater volume of cold air surrounding the heater as compared to the elevated inversion approach flow.

#### 5.4.2 Mean velocity profiles along the width of the heat island -

The mean velocity profiles measured along the width of the heat island have been plotted as profiles in the vertical direction in Fig. 5.50 for stable approach flow over unstable heat island for smooth and rough cases. Contrary to the effect usually expected for a rough surface to reduce the wind speeds, there was an increase in the mean velocity for the rough case over that for the smooth surface. This may be the effect

of the aluminum blocks causing more heat transfer and hence more convergence of air into the heat island. The surface temperatures showed an increase for the rough heat island. This increase in the mean velocity of air increased towards the edge of the heat island ( $y = 12$  in.). Bornstein et al. (1972) have observed such an increase in wind speeds over New York City.

The mean velocity profiles along the width of the heat island for different cases at  $x = 66$  ft and  $y = 0.5$  in. are shown in Fig. 5.51. Comparison of stably stratified flow over a neutral, smooth heater with that over an unstable, smooth heat island indicated the increase in mean velocity due to heating. The mean wind speeds beyond  $y = 11$  in. did not show any difference for the two cases indicating the boundary of the drifting cold air over the heat island.

Considering the other three cases, stably stratified flow over an unstable rough heat island had the maximum mean velocities which was consistent with the results reported in the previous section. The value at  $y = 10.5$  in. showed a peak indicating the region of accelerating flow. This peak was also observed for the neutral approach flow but of smaller magnitude at  $y = 11.5$  in. and at  $y = 13.5$  in. (the edge of the heater was at  $y = 12$  in.). The observations for the elevated inversion approach flow showed a peak at  $y = 11$  in. of still smaller magnitude. This may have been due to the fact that in the process of heating the aluminum plate upstream of the heater to create an elevated inversion, the aluminum plates on both sides of the heater were heated (to a smaller extent) and hence had temperatures slightly greater than that for a neutral approach flow. Although this was not desirable for an ideal elevated inversion approach flow, it simulated field conditions

for a three-dimensional urban heat island to a greater extent. The distribution of mean velocities near the centerline of the heater was found to be essentially two-dimensional.

Mean velocity distributions along the width of the heat island for a stably stratified flow over an unstable, rough heater at  $x = 65$  ft for different elevations are shown in Fig. 5.52. There was a general increase in the mean velocity at all levels near the edge of the heat island. In addition, presence of the accelerating flow was indicated by the peaks in the air speed at various elevations. The mean velocity has a two-dimensional distribution near the centerline and at about 4 inches outside the edges of the heater. Three-dimensionality introduced by the heater was found only for a width of about 6 to 8 in. approximately centered over the periphery of the heat island. An elevated inversion approach flow over an unstable rough heat island shown in Fig. 5.53 indicates essentially the same characteristics.

### 5.5 Turbulence profiles

The variation of the root-mean-square values of the longitudinal velocity fluctuations normalized with the respective mean velocities is discussed in this section. Vertical profiles of the turbulence level at different distances along the centerline for the stable flow over an unstable, rough heat island is shown in Fig. 5.54. The profile at  $x = 62$  ft represents the turbulence of the approaching flow. The non-dimensional turbulence was observed to increase at higher levels as the air moved along the heat island. At lower levels it was fairly constant for all distances. This may have been due to the corresponding increase in the mean velocity with downwind distance over the heat island. There was an increase in the turbulence level (about 7 times that of the

approaching flow) over the heat island at  $z/\delta \approx 0.05$  continuing to increase downwind attaining its maximum at  $x = 69$  ft (downwind edge of the heat island). The turbulence level downwind of the heater ( $x = 70$  ft) reduced to about 3 times the approach flow value near the surface but increased at higher levels to magnitudes greater than that observed over the heat island. This may have been due to the presence of the heat island plume.

The turbulence level profiles for the elevated inversion approach flow over an unstable rough heat island is given in Fig. 5.55 which indicates the turbulence level to increase with increasing distances along the heat island. Since the approach flow itself had a high turbulence level, the maximum observed over the heat island was only about 2 times that of the approaching wind. The vertical profile one foot downwind of the heater showed the same characteristics as for the ground based stable approach flow discussed above.

A comparison of the vertical profiles of turbulence level for different approach flows over the neutral, and unstable, rough heat islands is shown in Fig. 5.56 at the downwind edge of the heater along the centerline ( $x = 69$  ft). Minimum turbulence was observed for the ground based stable flow over a neutral heat island. Changing the approach flow to that of an elevated inversion increased the turbulence level by 6 times. The maximum turbulence found for the stable flow over an unstable heat island was about 1.5 times that observed for the elevated inversion approach flow at lower levels. The increase in the volume of reverse flow at the downwind edge of the heat island for the ground based stable approach flow may have been the main reason for the high values of turbulence level. In fact, in other regions of the

heater stable approach flow had lesser turbulence levels than those observed for the other two cases.

Turbulence level along the lateral direction for the flow over an unstable, rough heat island for the conditions of neutral, stable and elevated inversion approach flows are given in Figs. 5.57 and 5.58 and 5.59 respectively. Similar characteristics were observed except that for the neutral flow the effect of the temperature discontinuity at the edge of the heater on turbulence level was not found far inside the heat island. For the other two cases, the turbulence level started decreasing from the center of the heater itself. This might have occurred because of the effect of relatively cool air drifting into the heat island. All the profiles showed a dip over the edge of the heater ( $y = 12$  in.) indicating the position of the longitudinal vortex.

A comparison of the lateral distribution of the turbulence level for different approach flows at  $x = 65$  ft and  $z = 0.6$  in. is made in Fig. 5.60. It indicated the values for stable approach flow to be about 50 percent of the values for the other two cases. This may have been due to the rapid cooling of the air over the heat island due to convergence effects and consequent reduction in the turbulence. The lateral profiles for the neutral and elevated inversion approach flows tend to become equal over and near the edge of the heater.

#### 5.6 Temperature fluctuations

The lateral distribution of the normalized root-mean-square values of the temperature fluctuations for the stable and elevated inversion approach flows over an unstable smooth heat island is shown in Fig. 5.61. Temperature fluctuations showed essentially the same type of characteristics as that for longitudinal velocity fluctuations with a dip over

the edge of the heater. Typical vertical profiles of the non-dimensional temperature fluctuations at  $x = 68$  ft for the stable flow over neutral and unstable, smooth heat islands are given in Fig. 5.62. The distribution for the neutral case consisted of decreasing values up to a  $z/\delta$  of 0.3 and then increasing slowly up to a  $z/\delta$  of 0.6 before decreasing again. The increase in the middle portion may have been due to the zone of interaction of the warm air overlying the cold air in the lower layers. The profile for the unstable case decreased rapidly with height in the lower layers and then increased up to a  $z/\delta$  of 0.3 before decreasing to smaller values near the edge of the boundary layer. Increasing values indicated the zone of interaction of warm and cold air and the steep gradient showed the rapid interaction as compared to the flow over a neutral heat island. The magnitudes of the non-dimensional temperature fluctuations for the unstable case were approximately two to three times more than that for the neutral case.

### 5.7 Concentration distributions for the mass released from a two-dimensional continuous line source located upwind of the heat island

The results of the diffusion measurements of Krypton 85, a radioactive tracer gas released from a two-dimensional, ground level continuous line source two feet upwind of the heater are presented in this section. The mean concentration distributions indicated the nature of the flow and the amount of mixing for different cases studied. Vertical growths of the plume from the source along the centerline for different conditions of the approach flow and the heat island are given in Fig. 5.63. The upper boundary of the plume was determined based on the assumption that 10 percent of the maximum concentration defined the periphery of the plume at each vertical section. Stable flow over

smooth neutral heat island created a gravity wave phenomena as was indicated by temperature contours in Section 5.2.3. There was minimum amount of mass diffusion and most of the material stayed within one inch above the surface. Unstable heater produced dispersion several times more than that observed over a neutral one. The plume boundaries also indicated the nature of development of urban heat island plume with the steepest gradient for the stable approach flow over an unstable rough heat island.

Iso-concentration lines along the centerline for the tracer gas released from the line source for a stable flow over an unstable smooth heat island is shown in Fig. 5.64. Increase in the mean concentration downwind of the heat island was due to the air flowing along both the sides and convergence towards the center downwind of the heat island. Field studies by Ackerman (1972) over St. Louis, Missouri indicated a similar flow pattern around the city. Ackerman also refers to the studies conducted by Angell, et al. (1972) in Columbus, Ohio, where a similar feature was observed. Mean concentration profiles for neutral flow over a neutral smooth heat island and stable approach flow over an unstable smooth heat island are shown in Figs. 5.65 and 5.66 respectively. Profiles for the neutral flow over a neutral heat island showed a continuously decreasing concentration whereas for the stably stratified approach flow over an unstable heater the mass diffused rapidly. Moreover, the distribution at the downwind edge of the heat island showed an increase in the concentration at  $z = 0.5$  in. indicating existence of the reverse flow. There was also a sudden increase in the mean concentrations downwind of the heat island due to the bending of air around the heater.

Lateral distribution of the mean concentration at  $x = 65$  ft for the stable flow over an unstable smooth heat island at different elevations is shown in Fig. 5.67. The profile at  $z = 1.25$  in. indicated a peak near the edge of the heat island ( $y = 11.5$  in.). This peak may be due to the positioning of the core of the longitudinal vortex over the edge of the heat island. The lateral profiles at  $x = 66$  ft at different levels also showed similar peaks as in Fig. 5.68.

### 5.8 Shear velocity and roughness length

The mean velocities for the neutral flows over a neutral heat island were logarithmic in nature. Flow over an unstable heat island followed a log-linear law. Different types of log-linear distributions were tried but the one that give the best fit for most of the mean velocity data was of the form (Lumeley and Panofsky, 1964).

$$\bar{u} = \frac{u_*}{k_0} \left[ \ln \frac{z}{z_0} + \frac{\beta' z}{L''} \right] \quad (5.1)$$

where  $\bar{u}$  is the mean velocity,

$u_*$  is the shear velocity,

$k_0$  is the Kármán constant,

$z$  is the height,

$z_0$  is the roughness length,

$\beta'$  is a constant equal to  $\beta \frac{K_h}{K_m}$  where  $K_h$  is eddy diffusivity for heat,  $K_m$  is eddy diffusivity for momentum and  $\beta$  is a constant in a similar log-linear equation for near neutral conditions with Monin-Obukhov length  $L'$  replacing  $L''$  and  $L''$  is equal to  $L' K_h / K_m$ .

The value of  $\beta'$  should be constant although several investigators have suggested different values. Deacon (1962) has mentioned a value of 4 whereas Panofsky, Blackadar and McVehil (1960) have suggested 4.5 and a value of 6 was mentioned by Taylor (1960). The value of  $\beta'$  for stable air was found to be 7 by McVehil (Lumeley and Panofsky, 1964). For the data of this study a  $\beta'$  of 4 was found appropriate. Shear velocities and roughness lengths were found using Eq. 5.1 for the unstable heat island for different approach flows. The value of  $L'$  for different cases were also found which gave an indication of the Monin-Obukhov lengths involved. The distribution of the shear velocity along the centerline is shown in Fig. 5.69 for the various approach flows and different roughness conditions. The shear velocity was seen to increase with distance along the heat island reaching a maximum near the center and then decreased. For neutral approach flow this trend was continuous for both smooth and rough cases. For stably stratified approach conditions there was an abrupt increase in the shear velocity near the downwind periphery of the heat island for the smooth and rough cases. This may have been due to the counter flow along the surface discussed in previous sections. There was an increase in the shear velocity associated with the roughness of the surface. Neutral approach flow over an unstable heat island was found to have the maximum shear velocities. The roughness lengths were seen to vary from .0005 in. for stable flow over a smooth surface to 0.15 in. for the neutral flow over an unstable rough heat island. The value of  $L'$  varied from -2 to -5 over the unstable heat island depending on the nature of approach flow.

### 5.9 Distribution of bulk Richardson numbers

Richardson numbers  $R_{i_b}$  in bulk form were computed as they reflect the gross behaviour of the flow better than the gradient Richardson numbers. They were calculated based on an equation of the form

$$R_{i_b} = \frac{g}{T_{av}} \frac{(T_h - T_o)(Z_h - Z_o)}{(u_h - u_o)^2} \quad (5.2)$$

where  $g$  is the gravitational acceleration,

$T_o$  is the temperature, at lower level,  $Z_o$ ,

$T_h$  is the mean temperature at height  $Z_h$ ,

$u_h$  is the mean velocity at  $Z_h$  and

$u_o$  is the mean velocity at  $Z_o$ .

For the present computations the lower level was taken to be at the surface so that  $T_o$  was the surface temperature and  $Z_o$  and  $U_o$  were each equal to zero. The level  $Z_h$  was selected for each temperature profile as the height at which there was a large difference in the gradient. The distribution of the bulk Richardson number for different conditions of the approach flow is shown in Fig. 5.70. For neutral flow the negative  $R_{i_b}$  increased along the heat island and attained a maximum value at the downwind edge. For stable flow  $R_{i_b}$  decreased from 0.21 to 00.4 near the downwind periphery of the heat island and then increased to a positive value lesser than that of the approach flow. The distribution for the elevated inversion approach flow had the same trend with a peak at  $x = 68$  ft. The negative  $R_{i_b}$  for elevated inversion approach flow was otherwise fairly uniform and of higher magnitude than the ground-based flow over the upwind half of the heat island. Since Richardson number is essentially the ratio of the

buoyancy to inertia forces, the region of increasing buoyancy forces was apparent from this distribution. The same trend was also indicated by the behaviour of the plume released from a continuous line source shown in Fig. 5.63. The distribution of the bulk Richardson number along the width of the heat island is indicated in Fig. 5.71. The distribution was essentially two-dimensional near the centerline and started increasing over the periphery of the heat island. The appreciable reduction in the buoyancy forces over the periphery of the heat island indicates the convergence of cool air into the heat island near the surface.

#### 5.10 Turbulent energy distribution

It will be of interest to know as to how the kinetic energy of turbulence was distributed at various frequencies for the different cases studied. Although, in real turbulence a distinct frequency is not permanently present, it is possible on the average to allocate a definite amount of the total energy to a distinct frequency. Spectral distribution of energy between the frequencies for the longitudinal turbulent velocity is presented in this section. As was mentioned in Chapter IV, the velocity fluctuations were measured with a temperature compensated hot-wire probe and the compensation element had a frequency response of only 90 hertz. Although the energy content was found to occur predominantly within 100 hertz, this limitation has to be taken into account while viewing the results presented. The results have been presented in the wave number domain of the flow since it helps to consider the spatial structure at a given instant.

In terms of the frequency  $n$  and the local mean velocity  $\bar{u}$ , the wave number is defined as

$$K = \frac{2\pi n}{\bar{u}} \quad (5.3)$$

The one-dimensional wave number density function  $E(K)$  is defined as (Hinze, 1959)

$$\int_0^{\infty} E(K) dk = 1 \quad (5.4)$$

where  $E(K) dk$  is the amount of kinetic energy within the wave number range from  $K$  to  $K + dk$  non-dimensionalized by the total kinetic energy per unit mass  $\bar{u}^2$ , mean square of the velocity fluctuations. The dimensionless kinetic energy within a wave number interval 0 to  $K$  is then given by

$$\frac{\bar{u}^2(K)}{\bar{u}^2} = \int_0^K E(K) dK \quad (5.5)$$

The frequency spectra for this study were obtained using a radio wave analyzer as was discussed in Chapter IV. Each frequency spectrum was normalized by the mean square value of output voltage corresponding to the total kinetic energy per unit mass,  $\bar{u}^2$  giving a one-dimensional frequency density function  $f(n)$ . The one-dimensional wave number energy-spectrum function  $E(k)$  is obtained as below:

$$E(k) = \frac{\bar{u}}{2\pi} f(n) \quad (5.6)$$

The wave number spectra for different cases are presented in Figs. 5.72 and 5.73 with a curve corresponding to  $K^{-5/3}$ . Spectra for different heights along the centerline for  $x = 68$  ft for neutral approach flow over a neutral, rough heat island is shown in Fig. 5.72.

Maximum energies at these heights were found to occur between the wave numbers 0.3 and 0.5 with the maximum energy content decreasing with height. The spectral distribution for  $z = 13.11$  in. indicated larger energies at higher wave numbers. The curve corresponding to  $K^{-5/3}$  appeared to provide an approximate fit to the measured spectra within the most part of the higher wave number range. It has been pointed out (Grant et al., 1962) that the Reynolds numbers for common laboratory flows are not sufficiently high for an inertial subrange to occur.

Figure 5.73 shows the wave number energy spectra for different heights at  $x = 68$  ft along the centerline for the stable approach flow over an unstable, rough heat island. Maximum energies occurred again between the wave numbers 0.3 and 0.5. The maximum energy was found to decrease with height up to about one inch and then started increasing. This may be due to the existence of an elevated inversion over the unstable heater for a ground-based stable approach flow. Correspondence with  $K^{-5/3}$  curve was found to exist only for a narrow band of wave numbers.

A comparison between Figs. 5.72 and 5.73 indicates the effect of an unstable heat island in increasing the energy content of the flow. The increase in energy was of the order of two.

#### 5.11 Diffusion from continuous point sources

This part of the experiment was principally designed to augment the results of the flow visualization discussed in Section 5.1 by providing some quantitative values. The vertical concentration profiles and surface distribution from a ground level continuous point source at  $x = 65.75$  ft on the centerline over an unstable rough heat island for a stable approach flow are shown in Fig. 5.74. The vertical profiles

indicate the degree of dilution for the ground source on a heat island (of the order of 10). The ground level concentrations also indicate the symmetry of the air flow.

The surface concentration distribution from a point source at  $x = 65.75$  ft and  $y = 13$  in. (one inch outside the heat island) is shown in Fig. 5.75 which reproduced the results indicated by the flow visualization photographs regarding the drifting of the cold air to the center of the heat island. Concentrations at one foot and 1.5 ft downwind of the source decreased with the distance downwind outside the heat island whereas those inside showed a definite increase. The peaks that occurred at both locations were at the same lateral distance from the centerline. Occurrence of the peaks inside the heat island and a general increase in the concentration with distance downwind indicated the movement of the cold air across the periphery towards the core of the heat island.

#### 5.12 Comparison of the airflow over smooth and rough heat islands

A comparison between the mean temperature profiles across the heat island for rough and smooth cases for an approach flow with inversion is shown in Fig. 5.76. The distribution tends to be similar near the center. The influence of the roughness elements in causing more efficient heat transfer and higher mean temperatures for the air flowing over the heat island could be observed across the width. Height of the base of the elevated inversion was more for the smooth case than for the rough one. This is probably due to lesser mixing associated with a smooth surface.

Mean velocity distributions shown in Fig. 5.77 indicated the wind speeds to be about 50 to 100 percent greater for the rough case as compared to the smooth one. As was discussed in an earlier section,

although the effect of the roughness alone was to decrease wind speeds, the combined effect of roughness and heating was found to result in an appreciable increase in the flow of air moving over the heat island.

The vertical variation of the turbulence levels obtained by normalizing the root mean square values of the longitudinal velocity fluctuations by the respective mean wind speeds at the center of the heat island for smooth and rough cases for an approach flow with inversion is shown in Fig. 5.78. Although the longitudinal velocity fluctuations were appreciably larger for the rough case, normalized values tend to be a little higher for the smooth case near the surface due to larger mean velocities for the former. Turbulence level for the smooth case decreased rapidly with height as compared to the rough surface. The same trend was found for the mean temperature profiles in Fig. 5.76.

Vertical mean concentration distributions of Krypton 85 released from an upwind line source along the centerline for smooth and rough cases for an approach flow with inversion are shown in Fig. 5.79. Concentrations for the smooth case were about three times higher than those for the rough surface. Maximum values occurred at a lesser height for the flow over the smooth surface. Mean concentrations for the flow over rough heat island decreased with height near the surface before reversing its trend. This may be due to the effect of the internal boundary layer developing over the roughness elements.

All the measurements of the flow parameters for the flow over smooth and rough heat islands indicated the increase in diffusion characteristics for the latter and the general predominance of the effect of heating over that of mechanical roughness.

### 5.13 Comparison of the experimental perturbed values with the theoretical results

As could be seen from the experimental measurements and the flow visualization, the heat island was approximately two-dimensional for a lateral distance of about 5 in. on either side of the centerline. Hence a comparison is made of the theoretical results of a two-dimensional model with the experimental values near the center of the heat island, 3 ft from the beginning of the heater. Logarithmic velocity profile of the form

$$\bar{u} = \frac{u_*}{k_0} \ln \frac{z + z_0}{z_0} \quad (5.7)$$

where  $\bar{u}$  is the mean velocity,

$u_*$  is the shear velocity,

$z$  is the height above the surface,

$z_0$  is the roughness length, and

$k_0$  is the Kármán constant taken to be 0.4

is assumed. The parameters to be defined for the theoretical model are

gravitational acceleration  $g$

constant stability factor  $s$

free stream velocity  $u_\infty$

roughness length  $z_0$

characteristic length of the heat island  $L_1$

maximum perturbation temperature  $T'_s$  and

an average unperturbed temperature  $T_0$ .

The values for the above parameters were selected based on the experimentally observed quantities. A constant eddy diffusivity was assumed based on a linear equation of the form

$$k = k_0 u_* z \quad (5.8)$$

where  $k$  is the eddy diffusivity,  
 $u_*$  is the shear velocity, and  
 $z$  is a representative height in which wind shear may be assumed constant. Assuming this height to be 3 in. for the model, with the shear velocity of 0.8 ft/sec observed for stable flow over unstable heat island in this study, an eddy diffusivity of  $0.08 \text{ ft}^2/\text{sec}$  was selected. Although the stability of the approach flow changed fairly rapidly in the laboratory, constant stability was assumed and calculated in the following manner. In Chapter III, the constant stability factor,  $x$  was shown to be related to the temperature profiles as

$$\frac{1}{T_0} \left\{ \frac{\partial T_0}{\partial z} \right\} = s + \frac{1}{T_0} \left\{ \frac{\partial T_0}{\partial z} \right\} \quad \text{adiabatic}$$

where  $T_0$  was the unperturbed temperature. For the laboratory conditions  $\left\{ \frac{\partial T_0}{\partial x} \right\}$  adiabatic is close to zero. The stability factor was then computed from the temperature profile observed for the stably stratified approach flow in the wind tunnel. In the atmosphere  $T_0$  can be assumed constant since the heights of interest are small compared to the atmospheric scaling lengths and the horizontal dimensions of the heat island. But in the laboratory such an assumption is not completely justifiable. Since the variable  $T_0$  will complicate the linear model suggested in Chapter III, constant  $T_0$  was assumed for the present and was taken to be an average value between the surface and the height at which temperatures became constant (6 in. for the present case). From the above considerations  $T_0$  was taken to be  $(110 - 40)/2$  or  $75^\circ\text{F}$  giving  $535^\circ \text{R}$ . Stability factor was calculated as

$$\frac{1}{535} \frac{(570-500)}{0.5} = 0.262 \text{ per foot .}$$

Other observed values were  $u_{\infty} = 4.5$  ft/sec.,  $Z_0 = 0.1$  in., representative length for the two-dimensional model  $L_1 = 3$  ft maximum perturbation temperature  $T_s = 250^{\circ}\text{F}$  and the gravitational acceleration  $g = 32.2$  ft/sec<sup>2</sup>. These variables gave a value for the parameter governing the flow

$$S = \frac{gskL_1}{3u_{\infty}} = 0.044$$

The value of  $S$  for the New York City with some representative values was found to be about 0.2 (Section 3.4). Since this parameter is directly proportional to the characteristic horizontal length of the heat island, a value of 0.044 may represent a city of smaller size. Mountain function surface temperature distribution of the form

$$\tilde{\theta}(\tilde{x}, 0) = \frac{1}{\left(1 + \left(\frac{\pi\tilde{x}}{2}\right)^2\right)} \quad (5.9)$$

has been assumed for theoretical calculations although there was an abrupt discontinuity in the surface temperatures at the edges of the laboratory heat island. The weighting function  $g(k)$  for this distribution was

$$g(K) = \frac{2}{\pi} \int_0^{\infty} \frac{1}{\left[1 + \left(\frac{\pi\tilde{x}}{2}\right)^2\right]} \cos K \tilde{x} \, d\tilde{x} = \frac{2}{\pi} e^{-(2K/\pi)}$$

The experimental urban temperature excesses were computed for an approach flow with inversion over a rough heat island as the difference between the mean temperature profiles at the center of the heat island ( $x = 66$  ft) and at one foot upwind of the heat island. These were then

normalized with the maximum surface excess temperature and their vertical profile compared with the theoretical profile in Fig. 5.80.

The surface temperature distribution for the heater corresponded to a distribution in between the square function and mountain function. Theoretical and experimental results agreed well for a two-dimensional mountain function surface temperature distribution up to a height of about seven inches. The negative perturbations predicted by the theoretical model were not observed. This discrepancy at higher levels may be due to the sizable departure of the approach flow from the assumption of constant stability. Mean temperatures of the approach flow remained constant above a height of seven inches. The conformity of the theoretical model with the experimental results very near the surface where large perturbations in the temperature took place is encouraging.

#### 5.14 Comparison of the wind tunnel and field experimental results

Since the objective of the present study was not to simulate the airflow over any particular city but to conduct the experiments with the general conditions of an urban heat island reproduced in a model, only qualitative comparison is possible with the field studies conducted and reported over several cities. Similarities regarding the interacting mechanisms of an urban heat island in the laboratory and the field are discussed in this section.

In order to relate and compare the experimental results with those obtained in the field a general scaling length was necessary between the model and the prototype. Davenport (1960) suggested a depth of 1700 feet for the boundary layer over the center of a typical city. Since the average boundary-layer thickness was 15 inches over the model for the stable flow over an unstable, rough heat island near the center

of the heat island, the model length scale was taken to be approximately equal to 1:1000 with the roughness blocks representing buildings of height of about 25 feet. With this length scale one can compare with the results of the field experiments more effectively.

An urban heat island induces positive perturbations in the otherwise undisturbed mean temperatures of the air flow over the urban complex. The pronounced effect of the city on the airflow will be felt only for a finite depth of the atmosphere, the effect fading off at greater height. Hence, this finite depth characteristic of maximum urban temperature excesses will, to a certain extent, define the intensity of the urban heat island. In conjunction with the mean temperatures, mean wind speeds also must show a definite trend in this region. It was found that the intensity of the heat island was maximum below a  $z/\delta$  of 0.05 in the model where  $z$  is the distance in the vertical direction and  $\delta$  is the thickness of the boundary layer over the heat island (see Section 5.4.1). This height was equivalent to a prototype elevation of about 85 feet. Bornstein (1968) found the average intensity of the New York City urban heat island based on the temperature difference between the urban and rural sites to be maximum below a depth of 82 feet.

Sekiguti (1970) on the basis of the studies conducted over different cities in Japan indicated the heights of the heat island to be fairly shallow equal to 3 to 5 times the average height of the buildings which amounted to about 75 to 125 ft in prototype. This again compared well with the laboratory model results.

Temperature cross overs have been observed in urban areas by several investigators (Duckworth and Sandberg, 1954, Bornstein 1968). The mean temperature profiles over the model showed weak cross overs above the

heat island. Weak elevated inversions have been observed over the cities in all field studies for stably stratified approach flows. The mean temperature profiles in the laboratory model for the present study showed similar results.

Chandler (1960, 1961) observed the urban heat island circulation in which cool air from the rural area near the surface moved across the fringes of an urban area towards the core of the city. Drifting of the rural air into the city due to the mesoscale circulation created by the urban rural complex was also reported by Munn (1970). This circulation causes inflow of air near the upwind edge of the city and countergradient or reverse flow near the downwind edge of the city. The convergence at the surface causes air to raise and move above the stable layer of the downwind rural region. This type of motion was observed in Cincinnati, Ohio (Clarke, 1969) as an "urban heat-island plume." Flow visualization and the quantitative measurements of the mean quantities of wind speed, temperature and mass concentration over the model indicated mechanisms similar to those observed by Chandler and Clarke.

Clarke (1969) found from his measurements over Cincinnati, Ohio that

"with a strong inversion over the rural area upwind of the city, the urban boundary layer appears to result primarily from the addition of heat within the urban area rather than from mechanical turbulence generated by the wind passing over the large roughness elements of the city."

Figs. 5.50 and 5.51 indicated a similar action taking place in the wind-tunnel model. The mean wind speed measurements over the model indicated essentially the same characteristics. Whereas the effect of the mechanical roughness was to reduce and the heating was to increase the mean

wind speed, the combined effect was to increase the wind speed indicating the predominance of heating over mechanical roughness.

Bowne and Ball (1970) based on the measurements of wind speed and mean temperature made in GT tower in the downtown area of Fort Wayne, Indiana have reported Richardson numbers less than -1.0 frequently at the lowest level and often at the upper level indicating very unstable lapse rates. The order of magnitude of the Richardson numbers observed over the heat island of the model are comparable with the values reported by Bowne and Ball.

Jones et al. (1971) have estimated the roughness length  $Z_0$  for Liverpool to be equal to 123 cm, and have reported a  $Z_0$  of 165 cm found for Tokyo by Yamamoto and Shimanuki. An average value of 0.05 in. was estimated for the model which is equivalent to a prototype value of about 162 cm based on the scaling length. Thus the model value of the roughness length is consistent with the field values.

## Chapter VI

## CONCLUSION

In the light of the foregoing discussions the following conclusions can be made:

- (1) Simulation of a three-dimensional flow over an idealized urban heat island in a wind tunnel with stratified approach flows gives results very similar to those observed in the field.
- (2) The orders of magnitude of the depth of the heat island representing the maximum effect on the airflow and the roughness length are the same as found over "typical" cities.
- (3) Flow visualisation and quantitative measurements of mean and turbulent velocities, mean temperatures and diffusion for different conditions (of stratification) of the approach flow and the heat island reveal the following significant flow characteristics of the flow pattern:

Cool air from the surrounding area near the surface moves across the periphery of the heat island towards the center due to the circulation caused by the adjoining hot and cool areas (similar to urban - rural complex). This circulation causes inflow of air near the upwind edge of the heat island and reverse (counter-gradient) flow near the downwind edge. The convergence at the surface and the buoyancy forces set up by the heat source causes air to raise and move above the cool floor (similar to rural area) downwind of the heat island as a massive plume. This plume is well defined and narrow for a stable approach flow. For an elevated inversion approach flow it becomes more diffused. The reverse flow near the downwind edge of a smooth heat island is persistent and stronger than if the surface is rough.

- (4) Longitudinal vortices are seen to exist near the fringes of the heat island as noted by flow visualisation. Measurements indicate a region of low turbulence over the edge which may be the core of the vortex.
- (5) Similarity of  $z/L'$  where  $z$  is the height above the surface and  $L'$  is Monin-Obukhov's length ensured a reasonably good simulation of the heat source for the urban heat island.
- (6) A linear model incorporating a boundary layer type velocity profile predicts the perturbed temperatures near the surface of the heat island fairly well for laboratory and field experiments. Variable stability factor for the approach flow in line with the actual conditions may improve the capability of the linear model to predict the urban excess temperatures at higher levels equally well.

## REFERENCES

- Ackerman, G. (1972), "Winds in the Ekman layer over St. Louis." Preprints from the Conference on Urban Meteorology, Philadelphia, Penn.
- Angell, J. K., Pack, D. H., Dickson, C. R., and Hoecker, W. H., (1971), "Urban influence on nighttime airflow estimated from tethered flights." J. of Applied Meteorology, vol. 10, pp. 194-204.
- Batchelor, G. K. (1958), "The conditions for dynamic similarity of motions of a frictionless perfect gas atmosphere." Q. J. Royal Meteor. Soc., vol. 79, p. 224.
- Bornstein, R. D. (1968), "Observations of the urban heat island effect in New York City." J. of Applied Meteorology, vol. 7, pp. 575-582.
- Bornstein, R. D., Lorenzen, A. and Johnson, D. S. (1972), "Recent observations of urban effects on winds and temperatures in and around New York City." Preprints from the Conference on Urban Meteorology, Philadelphia, Penn.
- Bowne, N. E. and Ball, J. T. (1970), "Observational comparison of rural and urban boundary layer turbulence." J. of Applied Meteorology, vol. 9, pp. 862-873.
- Cermak, J. E. (1970), "Air motion in and near cities - determination by laboratory simulation." Paper presented at 1970 Western Resources Conference on Urban Demands on Natural Resources, July 1970, CEP 70-71 JEC 27.
- Cermak, J. E. and Peterka, J. (1966), "Simulation of wind fields over Point Arguello, California by wind tunnel flow over a topographic model." Technical report of Fluid Dynamics and Diffusion Laboratory, Colorado State University, CER 65 JEC-JAP 64.
- Cermak, J. E., Sandborn, V. A., Plate, E. J., Binder, G. H., Chuang, H., Meroney, R. N. and Ito, S. (1966), "Simulation of atmospheric motion by wind tunnel flows." Technical report of Fluid Dynamics and Diffusion Laboratory, Colorado State University, CER 66 JEC-VAS-EJP-GJB-HC-RNM-SI 17.
- Chandler, T. J. (1960), "Wind as a factor of urban temperatures: A survey in North-East London." Weather, vol. 15, no. 6, pp. 204-213.
- Chandler, T. J. (1961), "The changing form of London's heat island." Geography, vol. 46, pp. 295-307.
- Chandler, T. J. (1967), "Nighttime temperatures in relation to Leicester's urban form." Meteorology Magazine, vol. 96, pp. 244-250.

- Chao, J. L. and Sandborn, V. A. (1964), "A resistance thermometer for transient temperature measurements." Fluid Mechanics Paper No. 1, Colorado State University.
- Chaudhry, F. H. and Cermak, J. E. (1971), "Wind tunnel modeling of flow and diffusion over an urban complex." Technical Report of Fluid Dynamics and Diffusion Laboratory, Colorado State University, CER 70-71, FHC-JEC 24.
- Clarke, J. F. (1969), "Nocturnal urban boundary layer over Cincinnati, Ohio." Monthly Weather Review, vol. 97, pp. 582-589.
- Csanady, G. T., G. R. Hilst, and N. E. Bowne (1967), "Turbulent diffusion from a cross-wind line source in shear flow at Fort Wayne, Indiana." Atmospheric Environment, vol. 1, pp. 1-20.
- Davenport, A. G. (1960), "Rationale for determining design wind velocities." Journal Structural Div., A.S.C.E., vol. 86 (ST 5) p. 39.
- Davis, M. L. (1968), "Modeling urban atmospheric temperature profiles." Ph.D. Dissertation submitted to the University of Illinois.
- Deacon, E. L. (1962), "Aerodynamic roughness of the sea." Journal of Geophysical Research, vol. 67, p. 3167.
- Delage, Y. and Taylor, P. A. (1970), "Numerical studies of heat island circulations." Boundary-Layer Meteorology, vol. 1, pp. 201-226.
- DeMarrais, G. A. (1961), "Vertical temperature difference observed over an urban area." Bulletin American Meteorological Society, vol. 42, no. 8, pp. 548-554.
- Duckworth, F. S. and Sandberg, J. S. (1954), "The effect of cities upon horizontal and vertical temperature gradients." Bulletin American Meteorological Society, vol. 35, pp. 198-207.
- Estoque and Bhumralker (1969), "Flow over a localized heat source." Monthly Weather Review, vol. 97, pp. 850-859.
- Findlay, B. F. and Hirt, M. S. (1969), "An urban-induced meso circulation." Atmospheric Environment, vol. 3, pp. 537-542.
- Grant, H. L., Stewart, R. W. and Moilliet, A. (1962), "Turbulence spectra from a tidal channel." Journal of Fluid Mechanics, vol. 12, pp. 241-263.
- Hilst, G. R. and Bowne, N. E. (1966), "A study of the diffusion of aerosols released from aerial line sources upwind of an urban complex." Final Report, Project No. 4V025001A128, Hartford, Conn., The Travellers Research Center, Inc., vol. I and vol. II.
- Hinze, J. O. (1959), "Turbulence: An introduction to its mechanism and theory." McGraw-Hill Book Co., Inc., New York.

- Jones, P. M., deLarringa, M. A. B. and Wilson, C. B. (1971), "The urban wind velocity profile." *Atmospheric Environment*, vol. 5, pp. 89-102.
- Landsberg, M. E. (1961), "City air - better or worse." *Air Over Cities*, Symposium, U. S. Public Health Service Technical Report A.62-5.
- Long, R. R. (1953), "Some aspects of the flow of stratified fluids - I: A theoretical investigation." *Tellus*, vol. 5, pp. 42-58.
- Long, R. R. (1955), "Some aspects of the flow of stratified fluids. III: Continuous density gradients." *Tellus*, vol. 7, pp. 241-357.
- Lumley, J. L. and Panofsky, H. A. (1964), "The structure of atmospheric turbulence." Interscience Publishers.
- Mitchell, J. M. (1961), "The temperature of cities." *Weatherwise*, pp. 224-229.
- Munn, R. E. (1966), "Descriptive Micrometeorology." Academic Press, New York, 245 p.
- Munn, R. E. (1970), "Airflow in urban areas." In *Urban Climates*, W. M. O. Technical Note 108, pp. 15-39.
- Myrup, L. O. (1969), "A numerical model of the urban heat island." *Journal of Applied Meteorology*, vol. 8, pp. 908-918.
- Olfe, D. B. and Lee, R. L. (1971), "Linearized calculations of urban heat island convection effects." vol. 28, pp. 1374-1388.
- Panofsky, H. A., Blackadar, A. K. and McVehill, G. E. (1960), "The diabatic wind profile." *Quarterly Journal Royal Meteorology Society*, vol. 86, p. 390.
- Pasquill, F. (1962), "Atmospheric Diffusion." D. Van Nostrand Company, Ltd., Publisher.
- Plate, E. J. and Lin, C. W. (1966), "Investigations of the thermally stratified boundary layer." *Fluid Mechanics Paper No. 5*, Colorado State University, Fort Collins, Colo.
- Preston-Whyte, R. A. (1970), "A spatial model of an urban heat island." *Journal of Applied Meteorology*, vol. 9, pp. 571-573.
- Sandborn, V. A. (1966), "Meteorology of Fluid Mechanics." Colorado State University, Fort Collins, Colo., CER 66 VAS 32.
- Scorer, R. S. (1949), "Theory of waves in the lee of mountains." *Quarterly Journal of Royal Meteorology Society*, vol. 75, pp. 41-56.
- Scorer, R. S. (1956), "Airflow over an isolated hill." *Quarterly Journal of Royal Meteorology Society*, vol. 82, pp. 75-81.

- Sekiguti, T. (1970), "Thermal situations of urban areas, horizontally and vertically." in Urban Climates, W. M. O. Technical Note 108, pp. 137-138.
- Slade, D. H. (1968), "Meteorology and Atomic Energy." U. S. Atomic Energy Commission, Division of Technical Information.
- Slade, D. H. (1969), "Wind measurement on a tall tower in rough and inhomogeneous terrain." Journal of Applied Meteorology, vol. 8, pp. 293-297.
- Spiegel, E. A. and Vernois, G. (1960), "On the Boussinesq approximation for a compressible fluid." Astrophysical Journal, vol. 131, pp. 442-447.
- Spangler, T. C. and Dirks, R. A. (1972), "Meso-scale variations of the urban mixing layer depth." Preprints from the Conference on Urban Meteorology, Philadelphia, Penn.
- Summers, P. W. (1964), "An urban ventilation model applied to Montreal." Ph.D. Dissertation submitted to McGill University, Montreal, Canada.
- Tag, P. M. (1969), "Surface temperatures in an urban environment." in Atmospheric Modifications by Surface Influences, Department of Meteorology, The Pennsylvania State University, University Park, Penn., 72 p.
- Taylor, R. J. (1960), "Similarity theory in the relation between fluxed and gradients in the lower atmosphere." Quarterly Journal of Royal Meteorology Society, vol. 86, p. 67.
- Yamada, T. (1971), "Numerical and wind tunnel simulation of response of stratified shear layers to nonhomogeneous surface features." Ph.D. Dissertation submitted to Colorado State University.

A P P E N D I X

Table 4.1  
 Performance Characteristics of the Meteorological  
 Wind-tunnel

Characteristic	Meteorological Wind Tunnel
1. Dimensions	
Test-section length	27 m
Test-section area	4 m
Contraction ratio	9.1
Length of temperature controlled boundary	12 m
2. Wind-tunnel drive	
Total power	200 Kw
Type of drive	4-blade propeller
Speed control: coarse	Ward-Leonard DC control
Speed control: fine	pitch control
3. Temperatures	
Ambient air temperature	5°C to 95°C
Temp. of controlled boundary	5°C to 205°C
4. Velocities	
Mean velocities	approx. 0 mps to 33 mps
Boundary layers	up to 50 cm
Turbulence level	low (about 0.1 percent)
5. Pressures	adjustable gradients
6. Humidity	controlled from approx. 20% to 80% relative humidity under average ambient conditions.

Table 4.2

Technical Data for the Temperature Compensated  
Probe (DISA 55E30)

## TECHNICAL DATA

Hot-wire material	Pt-plated tungsten
Temperature sensor	Tungsten
Hot-wire length	1.2 mm
Hot-wire diameter	5 $\mu$ m
Hot-wire resistance at 20°	approx. 3.5
Temperature sensor resistance at 20°C	approx. 6.3
Overheating ratio (autom.adj.)	0.8
Max. wire temperature	300°C
Max. ambient pressure	50 Kp/Cm
Max. ambient temperature	150°C
Max. velocity in air	250 m/sec
Min. velocity in air	0.1 m/sec
Upper frequency limit in without compensation	350 kHz
Frequency limit in air	90 Hz.
Temp. compensation reaction time	approx. 0.5 sec
Accuracy	$\pm$ 0.05% per °C

Table 4.3

Average Thickness of the Momentum Boundary Layer over the  
Heat Island

Approach Flow	Heat Island	Thickness of the momentum boundary layer (inches)
1. Neutral	Unheated - smooth	12.0
2. Neutral	Unheated - rough	12.5
3. Neutral	Heated - smooth	14.5
4. Neutral	Heated - rough	15.0
5. Stable	Unheated - smooth	10.0
6. Stable	Unheated - rough	11.0
7. Stable	Heated - smooth	13.5
8. Stable	Heated - rough	14.0
9. Elevated inversion	Unheated - smooth	13.75
10. Elevated inversion	Unheated - rough	14.0
11. Elevated inversion	Heated - smooth	17.0
12. Elevated inversion	Heated - rough	17.5

Table 5.1  
Footage Index of the Motion Picture

Reel No.	Footage	Approach Flow	Condition of the heat island with respect to		Position of the Smoke Source
			Temperature	Roughness	
1.	0-78	Inversion	cold	smooth	upwind 6" elevated
	78-88	-do-	-do-	-do-	left 6" elevated
	88-100	-do-	-do-	-do-	left surface
2.	0-12	-do-	-do-	-do-	at the center
	12-60	-do-	hot	-do-	upwind surface
	60-100	-do-	-do-	-do-	upwind left surface
3.	0-100	-do-	-do-	-do-	upwind elevated
4.	0-20	-do-	-do-	-do-	left surface
	20-87	-do-	-do-	-do-	two sources left surface
	87-100	-do-	-do-	-do-	over the heater
5.	0-16	-do-	-do-	-do-	two sources - one upwind and the other over the heater
	16-44	-do-	-do-	-do-	two sources - one upwind and the other downwind of the heater
	44-100	-do-	-do-	-do-	Source upwind traversed vertically
6.	0-27	-do-	cold	rough	upwind - surface
	27-37	-do-	-do-	-do-	left - surface
	37-46	-do-	-do-	-do-	at the center - surface
	46-85	-do-	hot	-do-	upwind corner - surface
	85-100	-do-	-do-	-do-	left side - surface
7.	0-57	-do-	-do-	-do-	downwind - surface
	57-75	Elevated Inversion	cold	rough	upwind - surface
	75-100	-do-	-do-	-do-	at the center - surface
8.	0-20	Elevated Inversion	hot	rough	upwind corner - surface
	20-58	-do-	-do-	-do-	at the center - surface

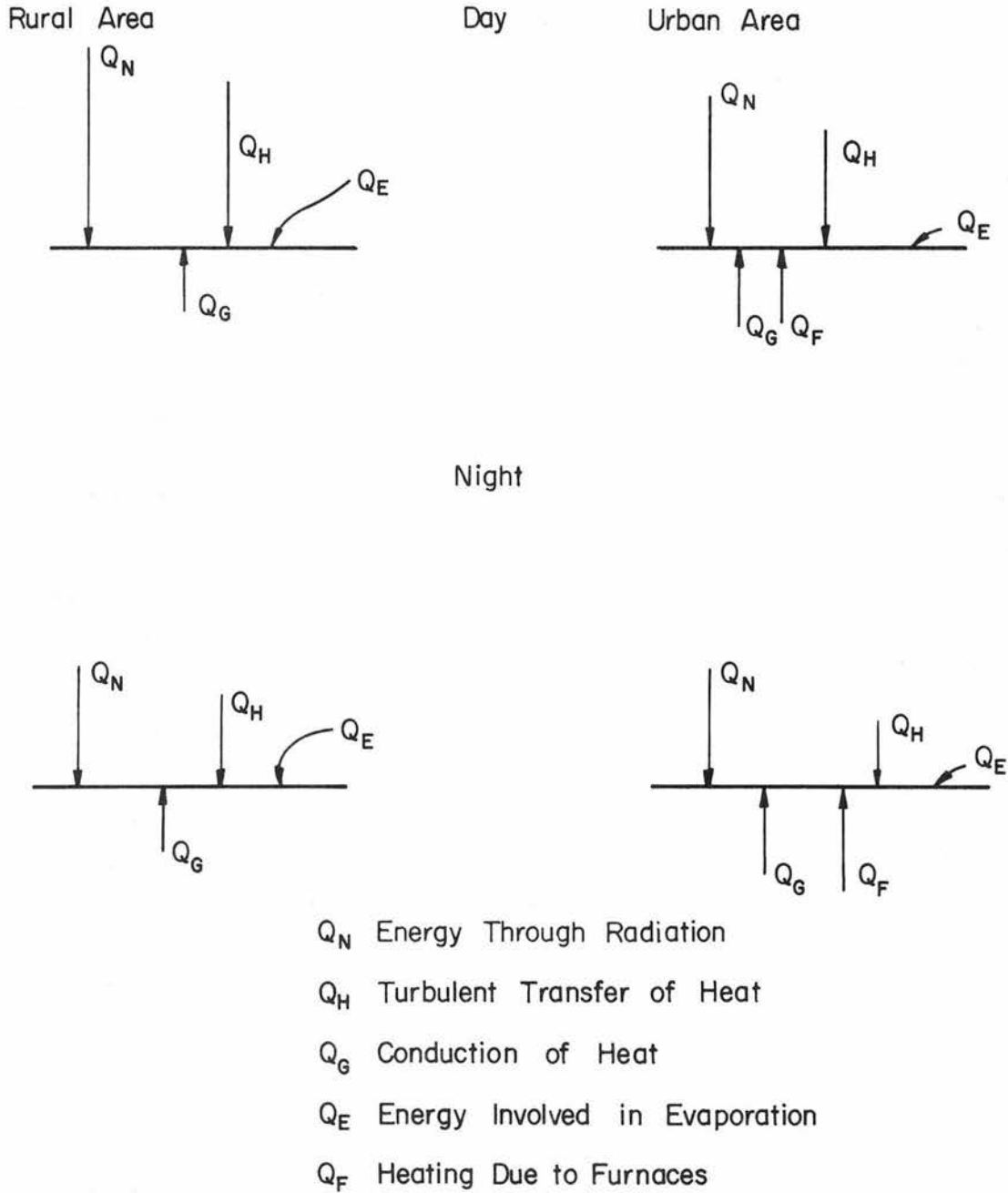


Fig. 2.1 Day and nighttime energy balances in rural and urban regions.

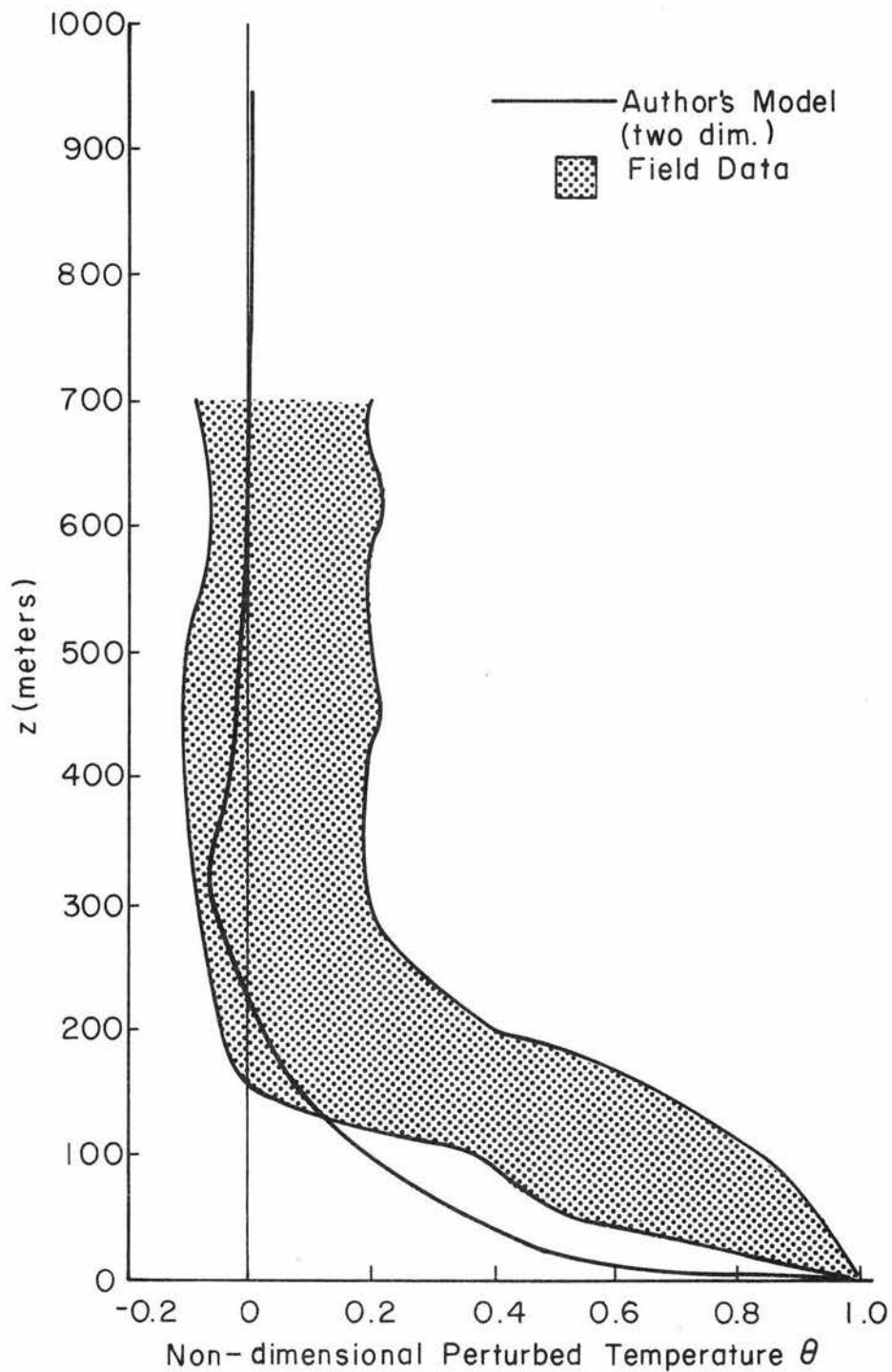


Fig. 3.1 Vertical profiles of the non-dimensional perturbed temperature of New York City center. (Mountain function surface temperature distribution was assumed for the theoretical model)

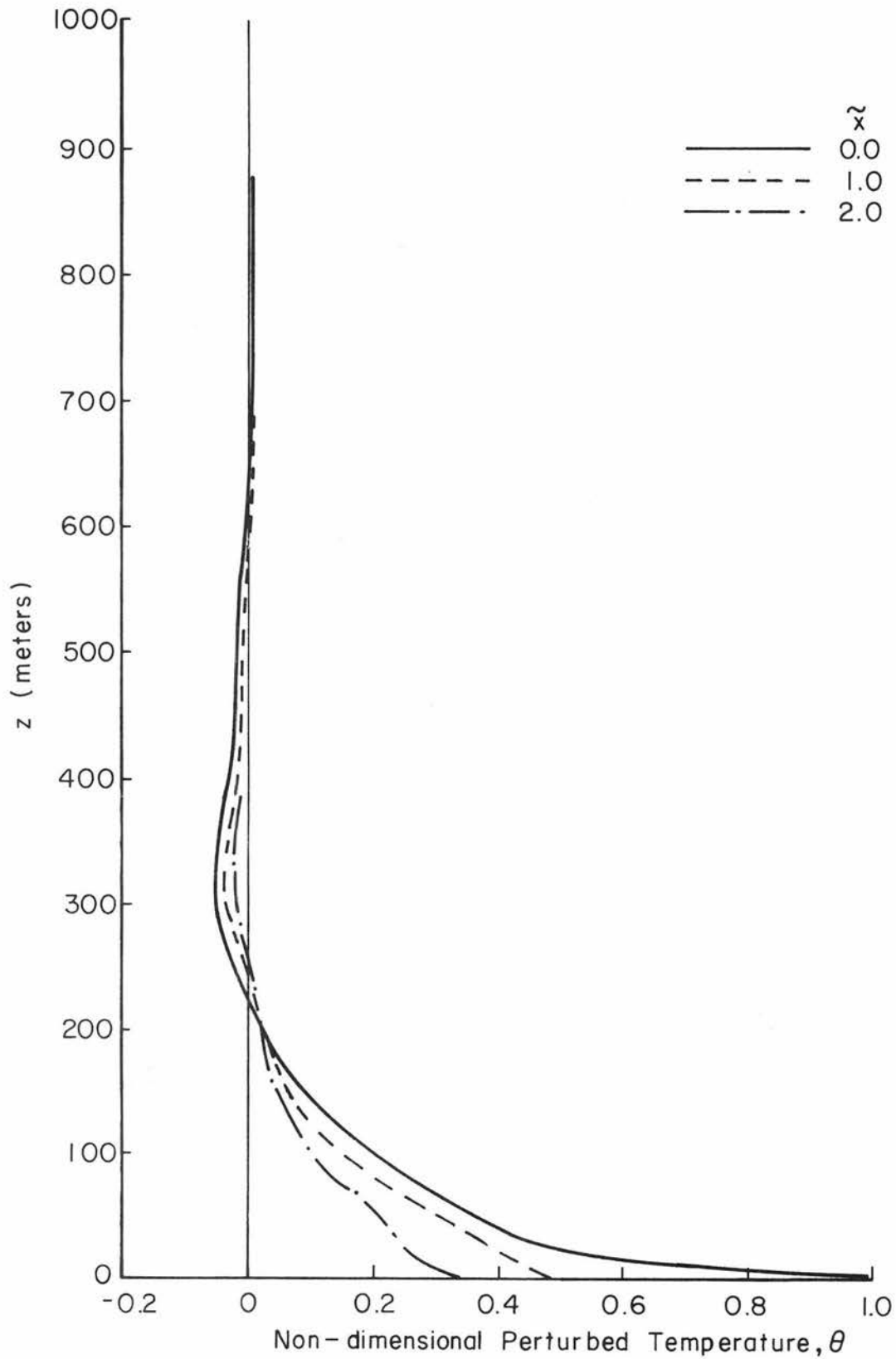


Fig. 3.2 Predicted non-dimensional perturbed temperature profiles for different downwind distances for New York City (two-dimensional model with mountain function surface temperature distribution).

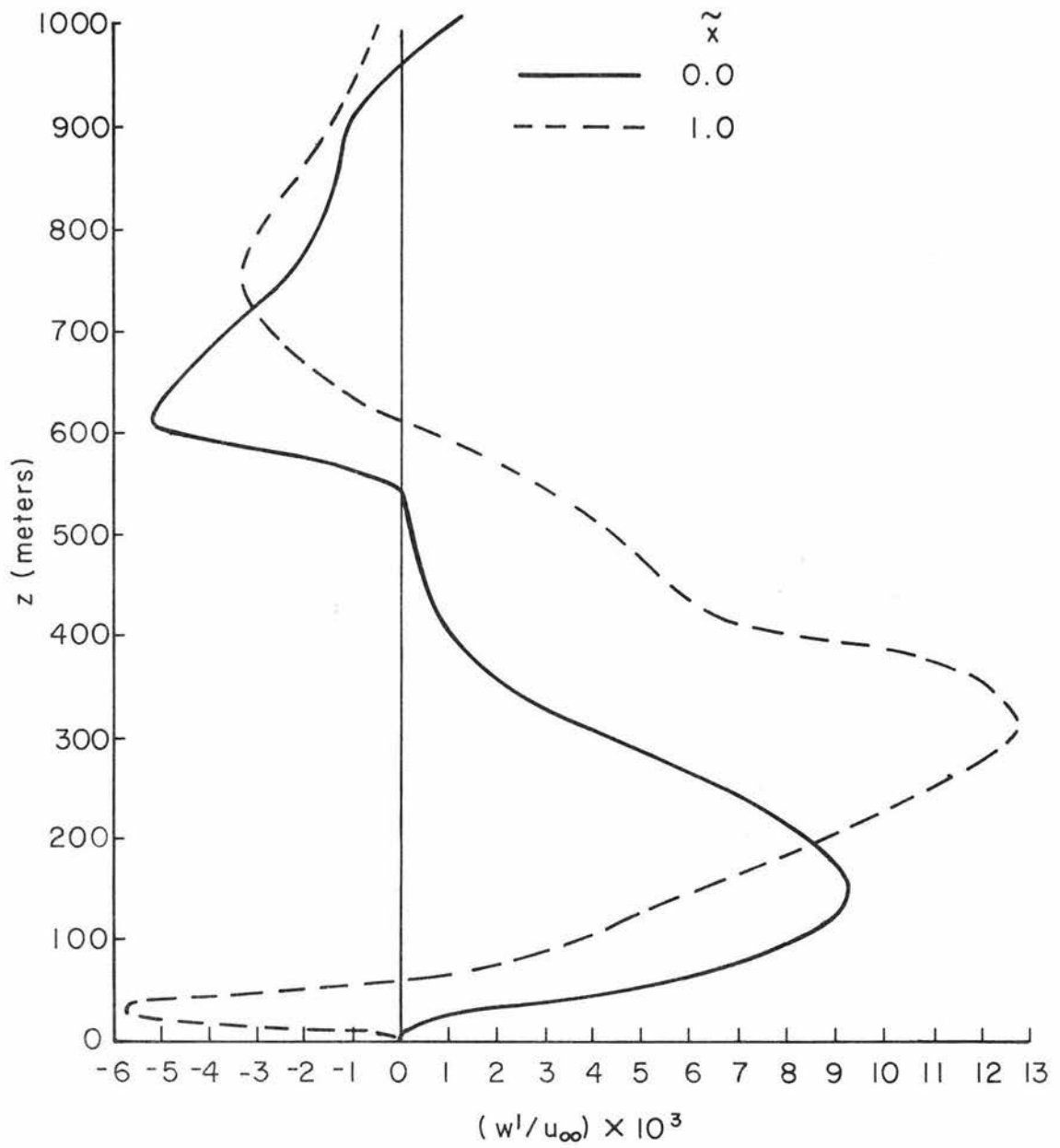


Fig. 3.3 Predicted non-dimensional perturbed vertical velocity profiles at different downwind distances for New York City (two-dimensional model with mountain function surface temperature distribution).

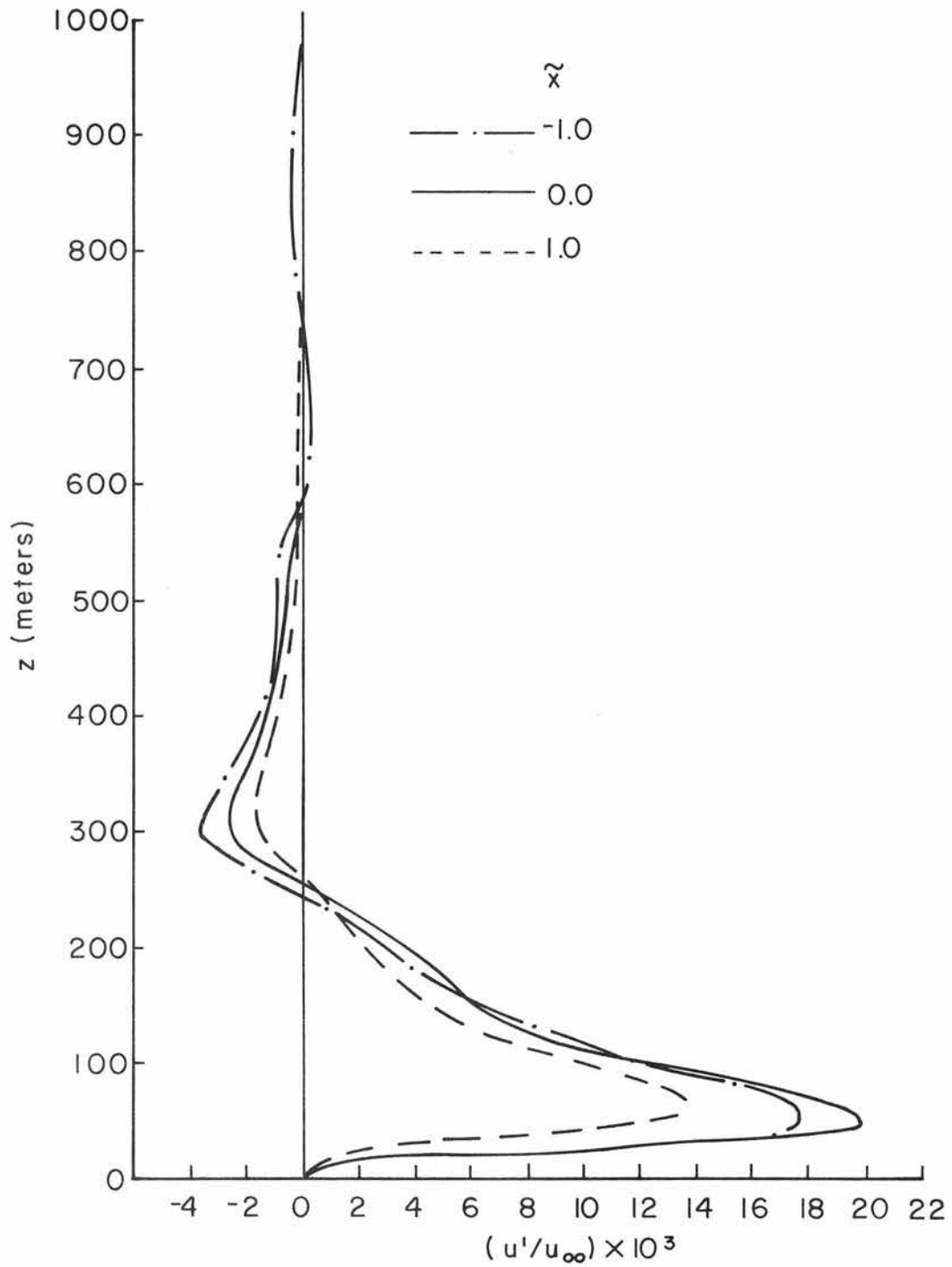


Fig. 3.4 Predicted non-dimensional perturbed longitudinal velocity profiles at different distances for New York City (two-dimensional model with mountain function surface temperature distribution).

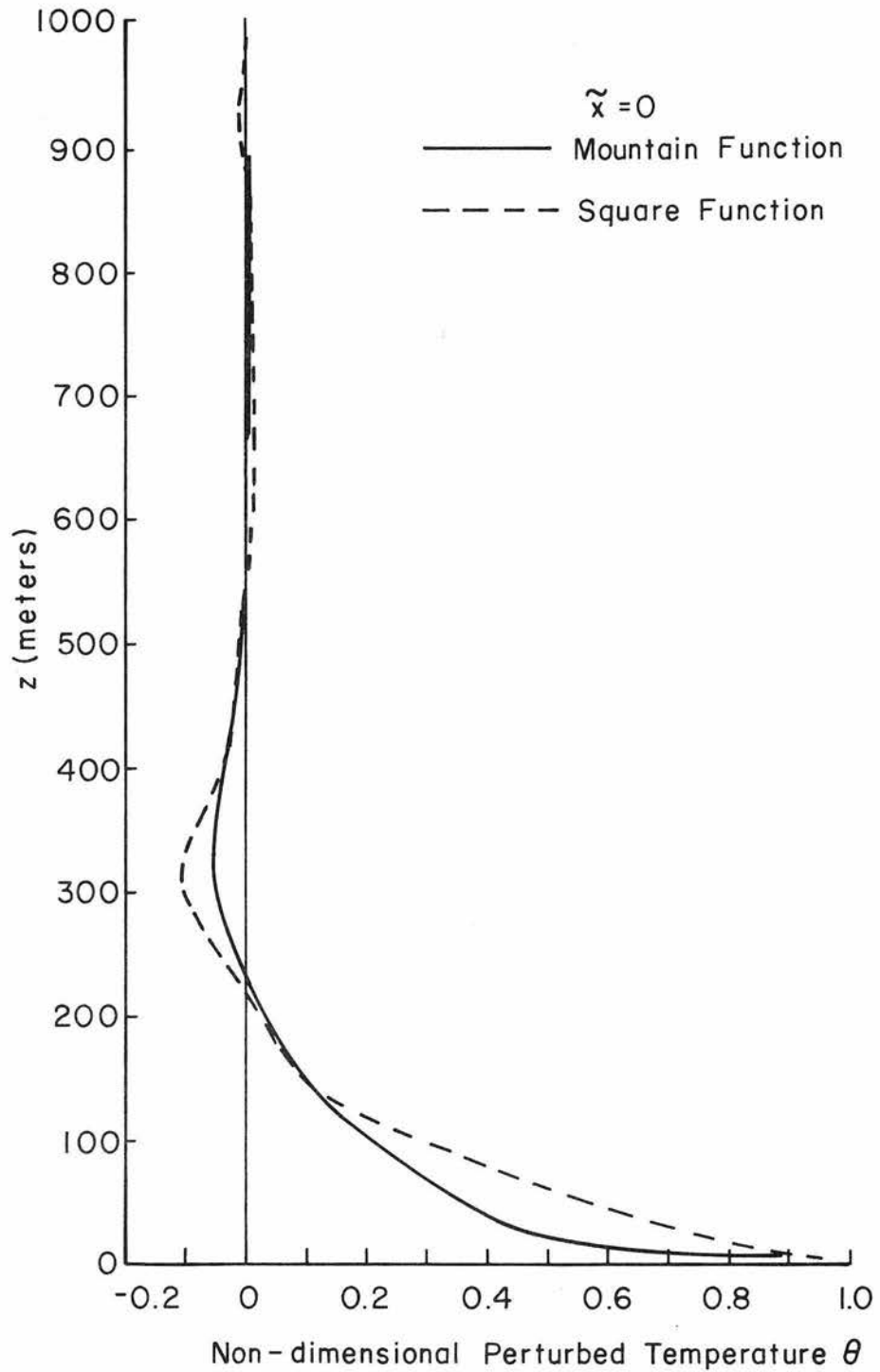


Fig. 3.5 Comparison of the predicted non-dimensional perturbed temperature profiles for different surface temperature distributions for New York City.

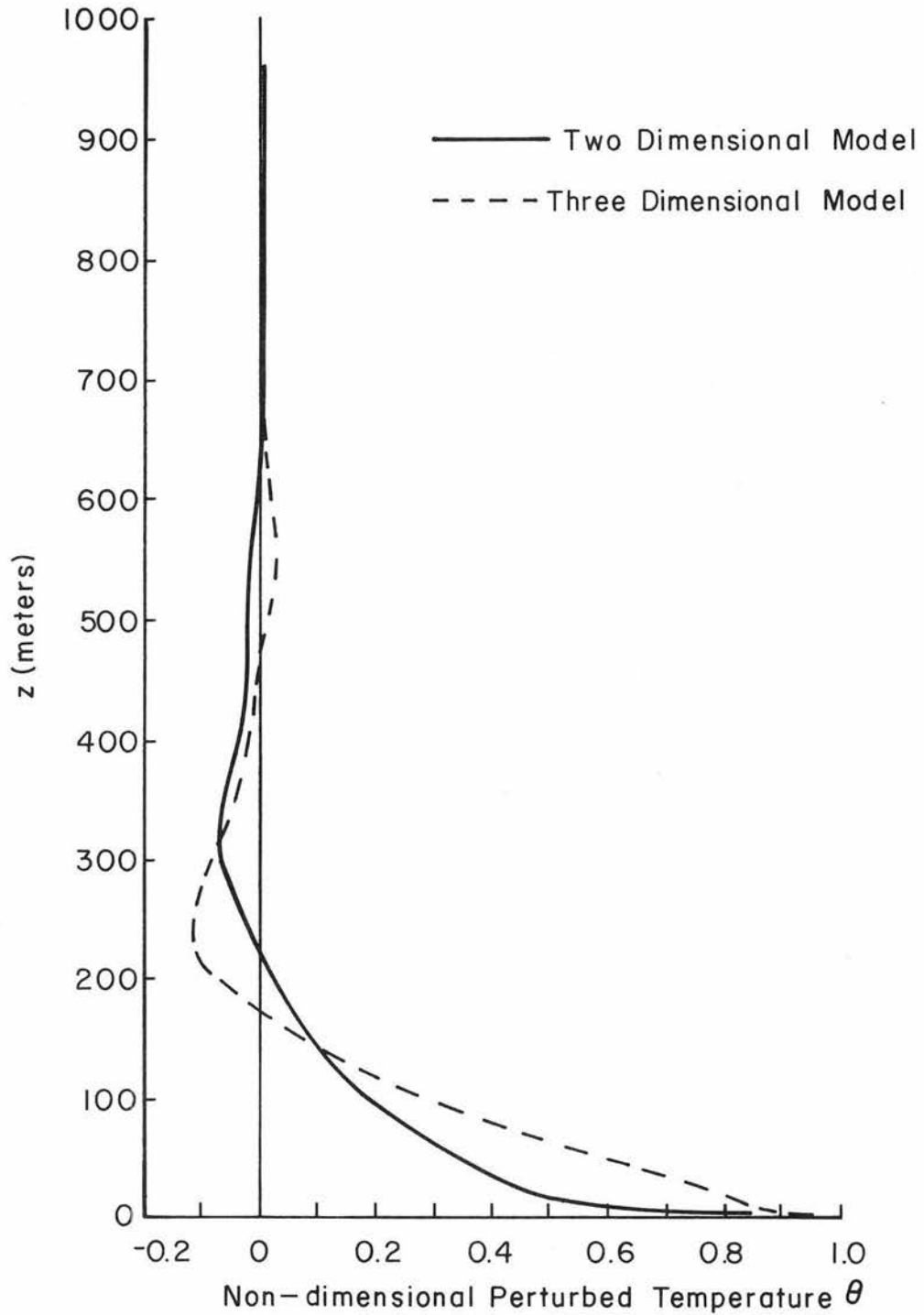


Fig. 3.6 Comparison of non-dimensional predicted perturbed temperature profiles obtained by the two-dimensional and the three-dimensional models for New York City for the mountain function surface temperature distribution.

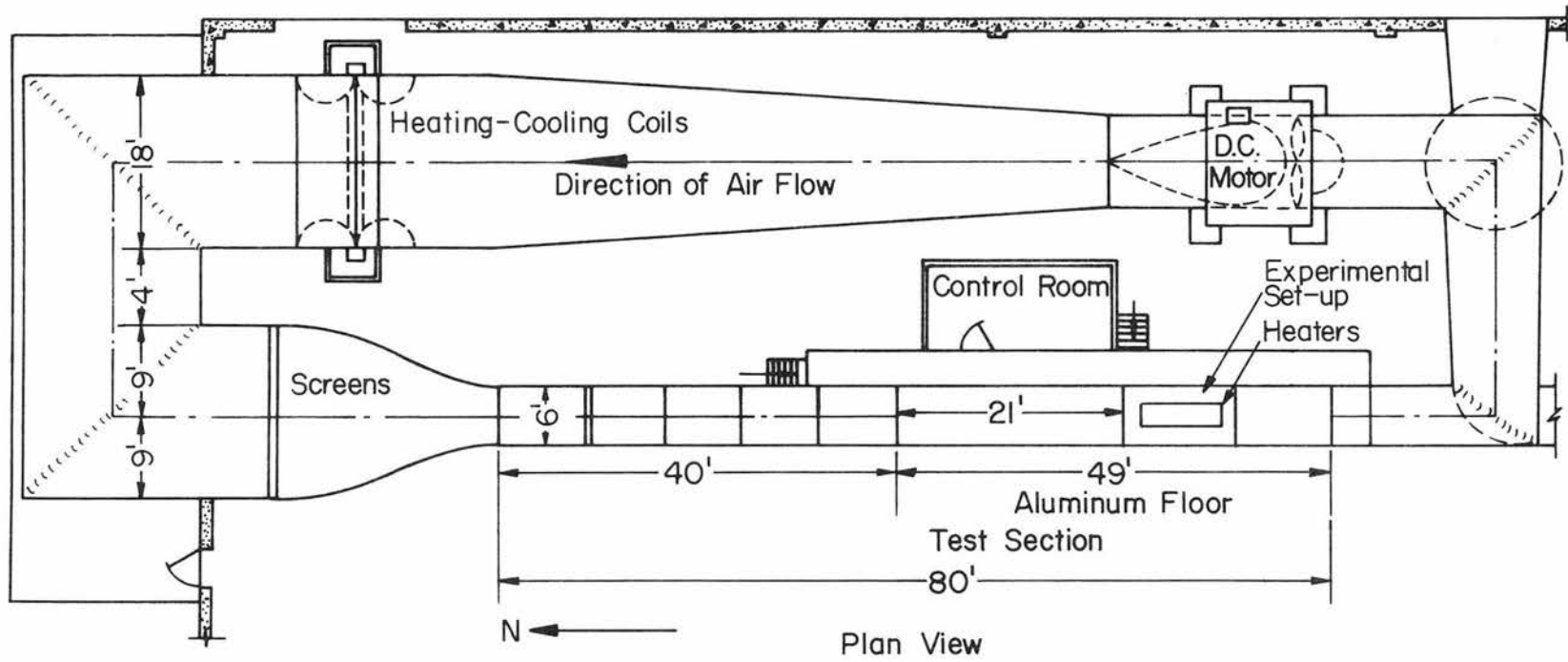


Fig. 4.1 Meteorological wind tunnel at Colorado State University.

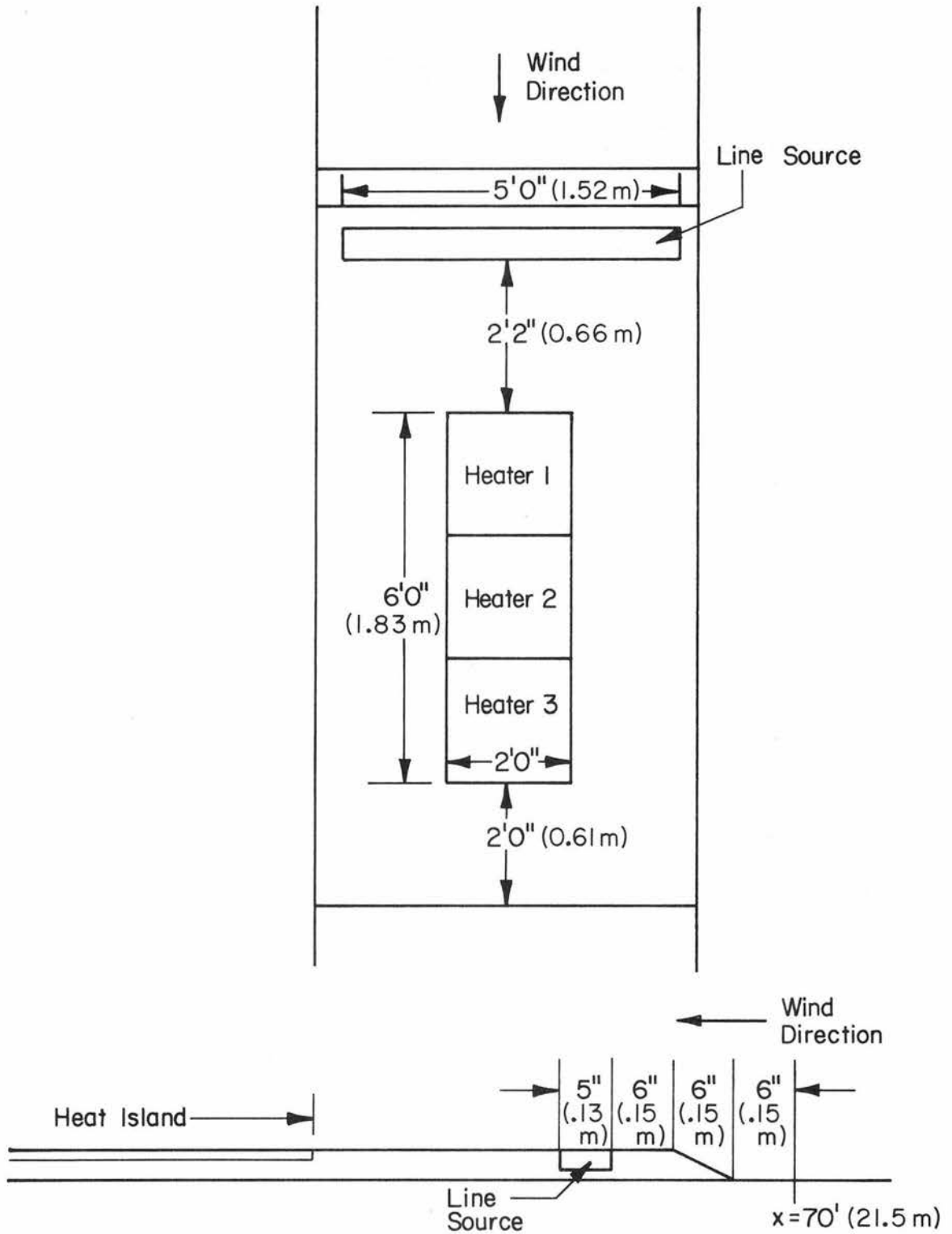


Fig. 4.2 A line sketch of the relative location of the different components of the experimental arrangement (not to scale).

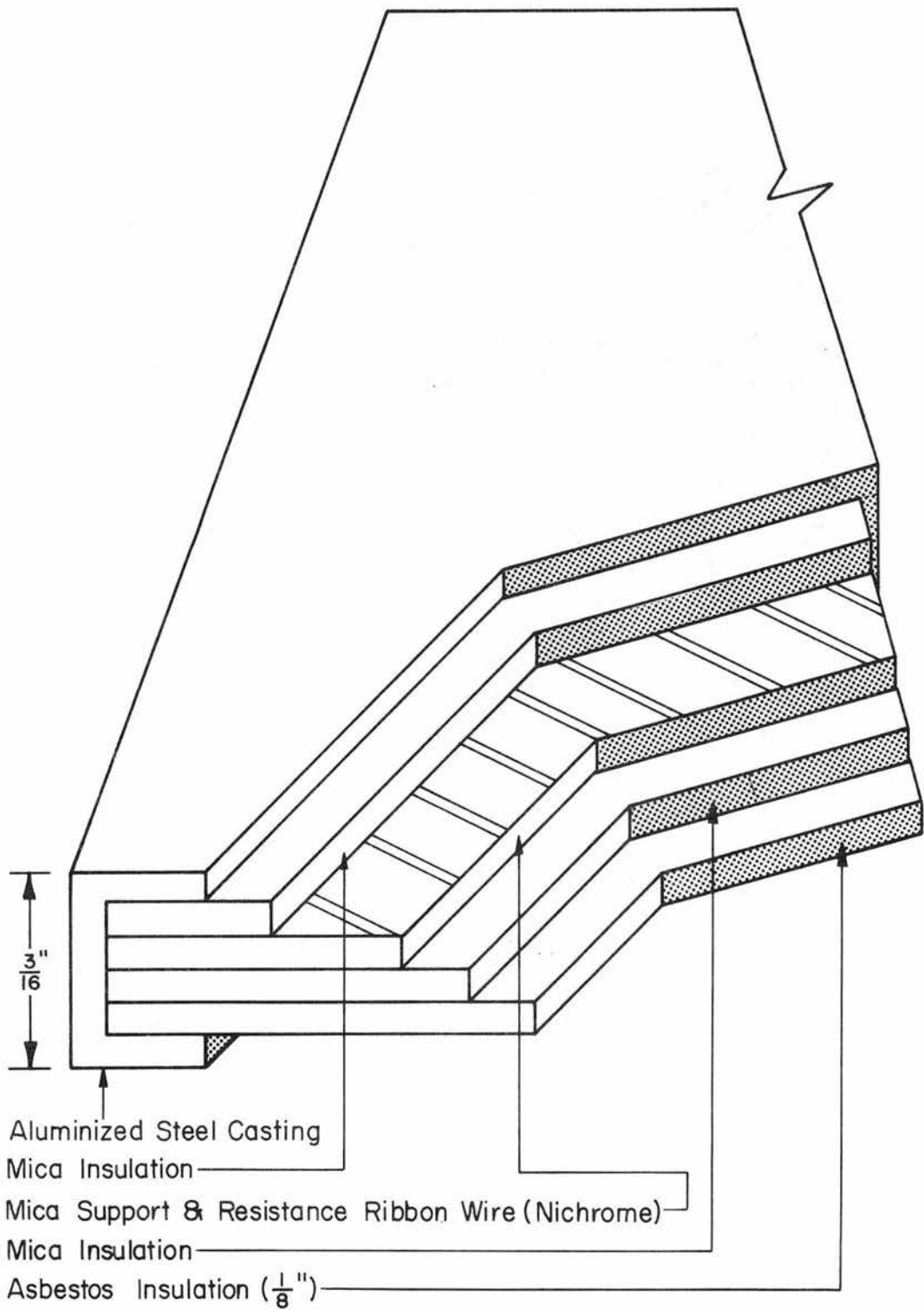


Fig. 4.3 Typical cross section of a heater.

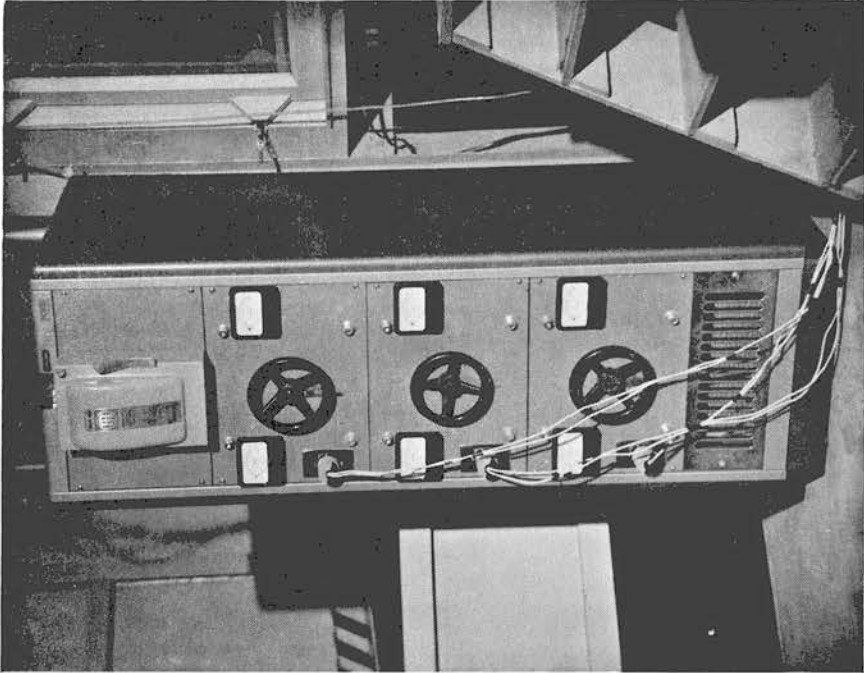


Fig. 4.4 Photograph of the variac assembly.

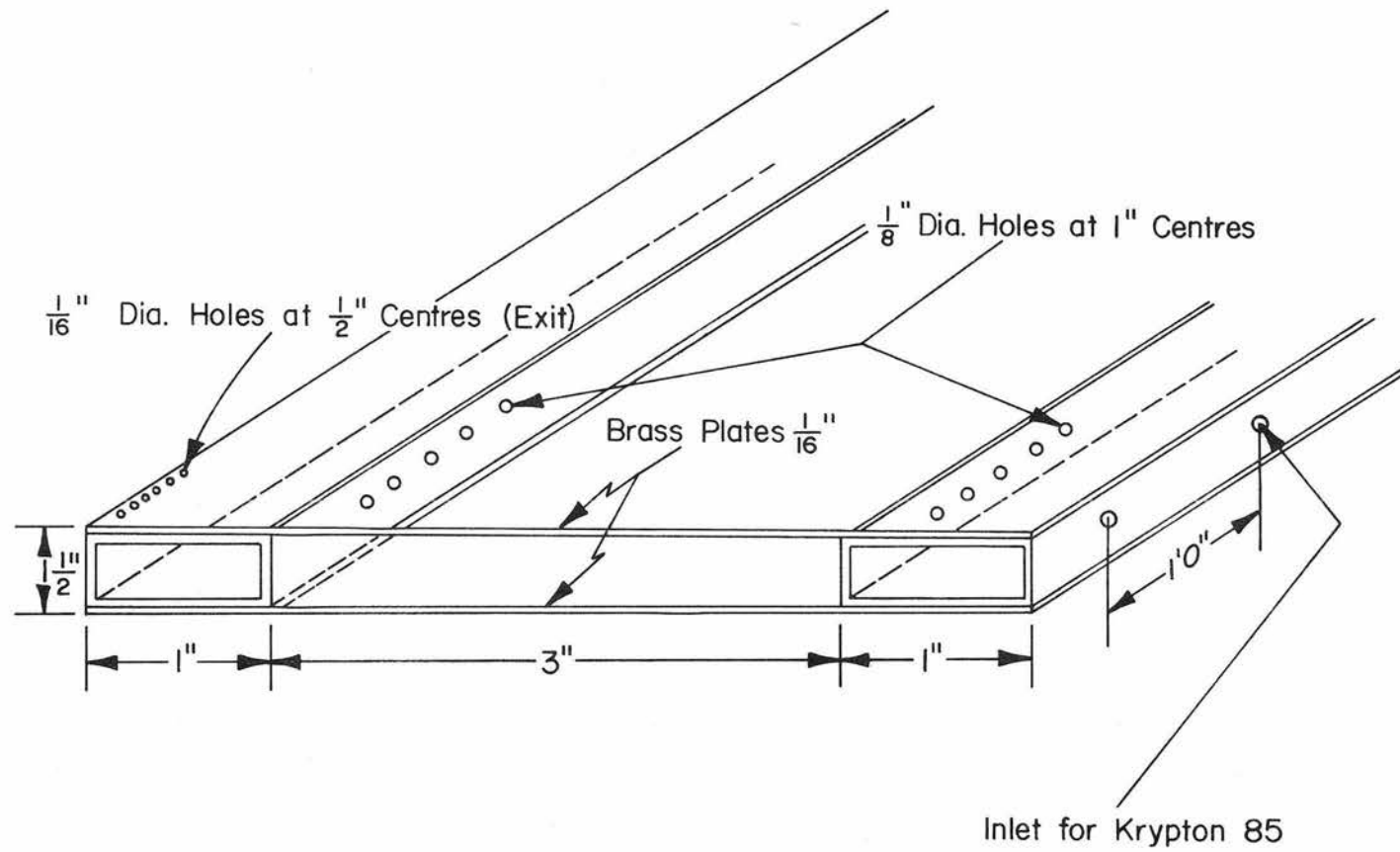


Fig. 4.5 Sectional view of the line source.

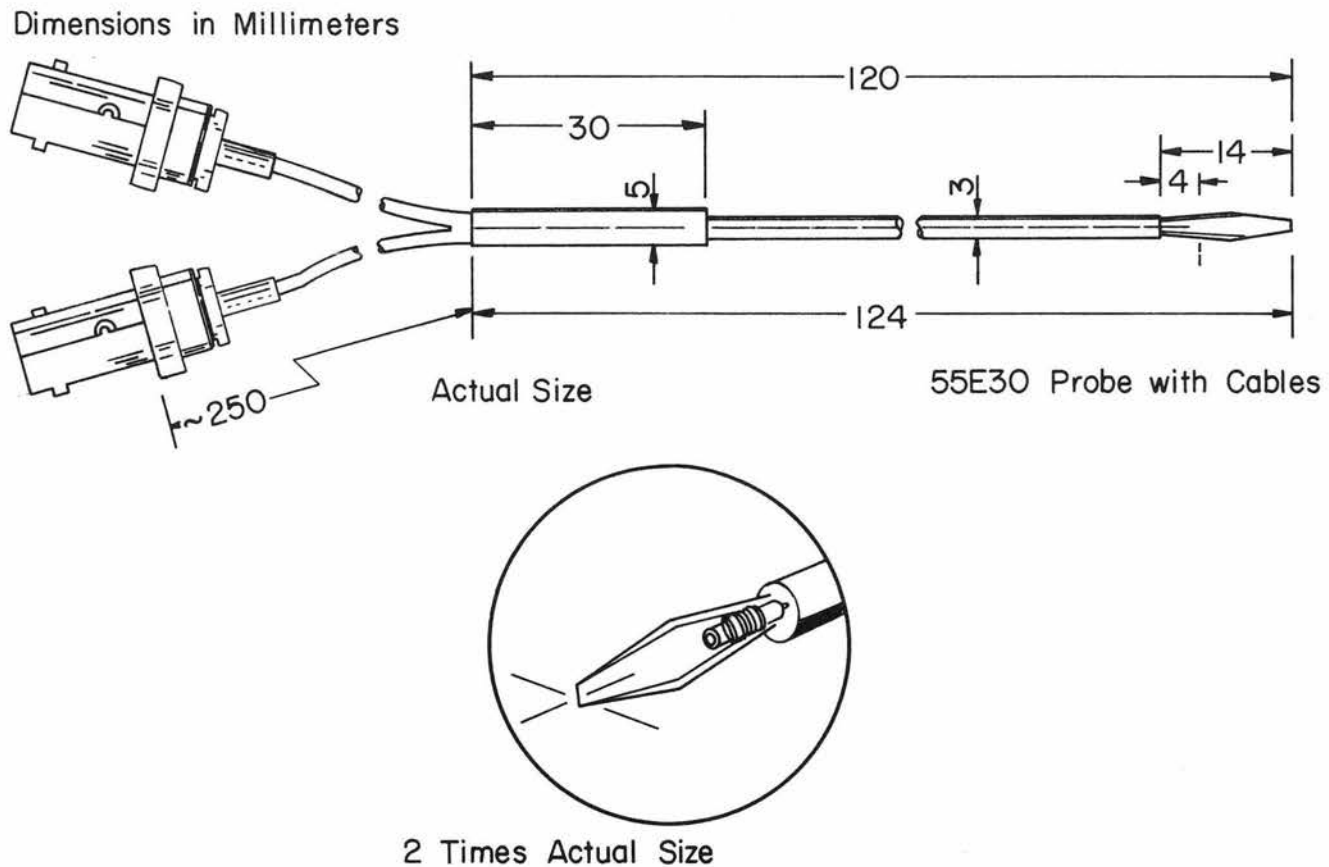


Fig. 4.6 Details of the temperature compensated hot-wire probe - DISA 55 E 30.

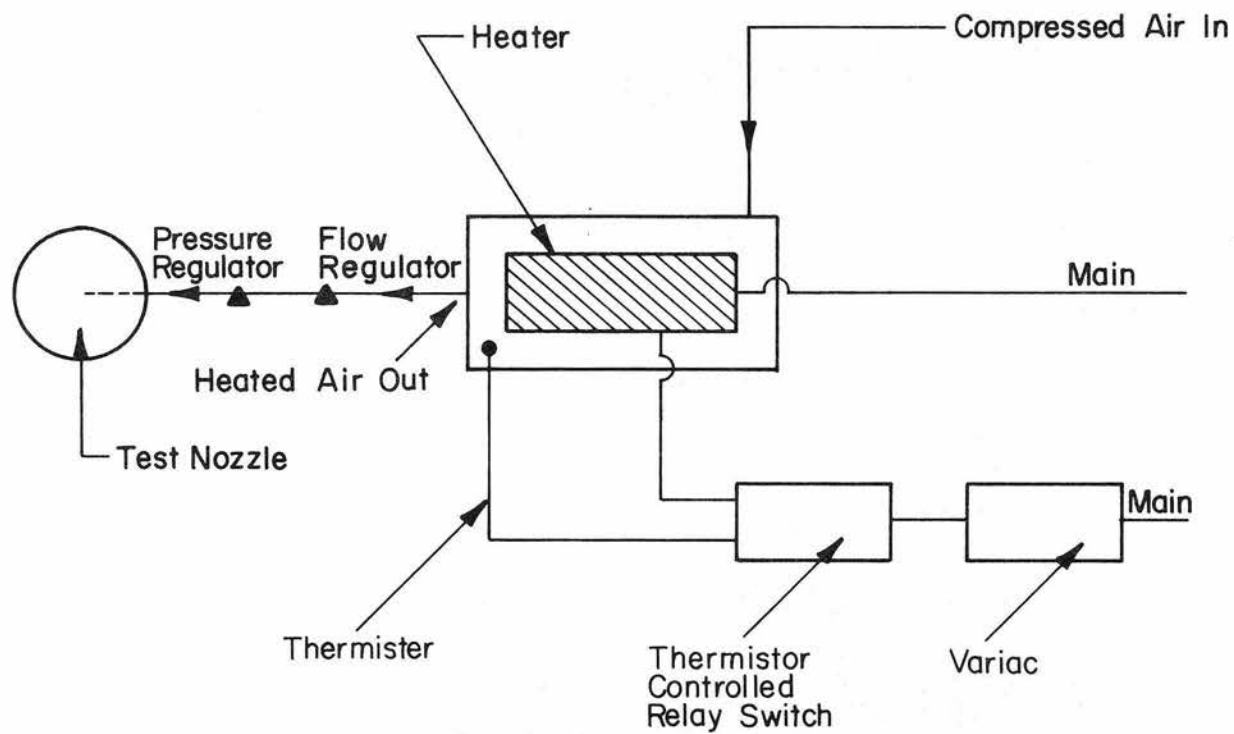


Fig. 4.7 Calibration equipment for the hot-wire.

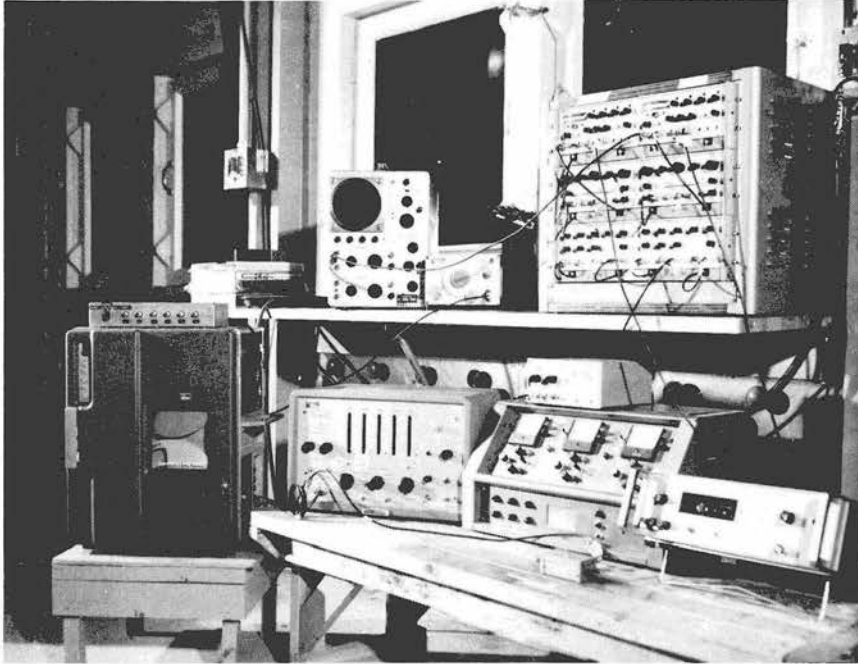


Fig. 4.8 Photograph of some of the instruments used for the experiments.

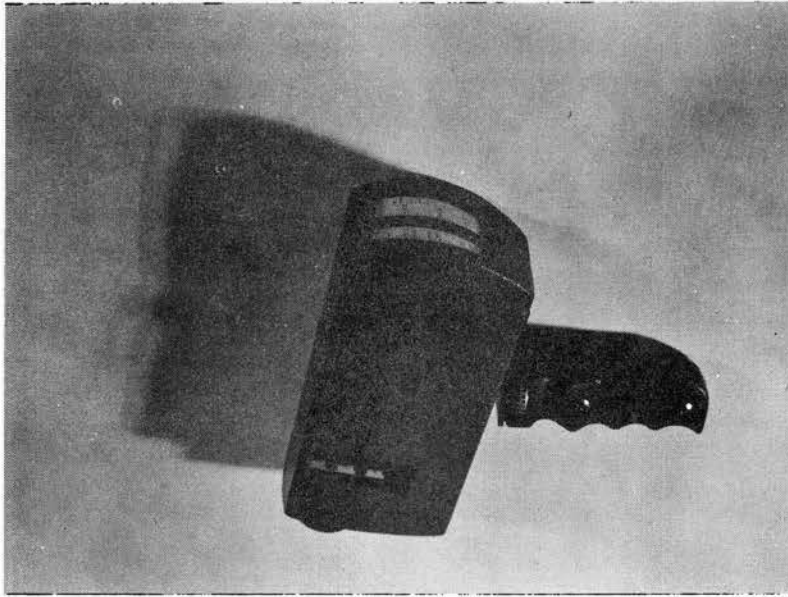


Fig. 4.9 Photograph of the infra-red pyrometer.

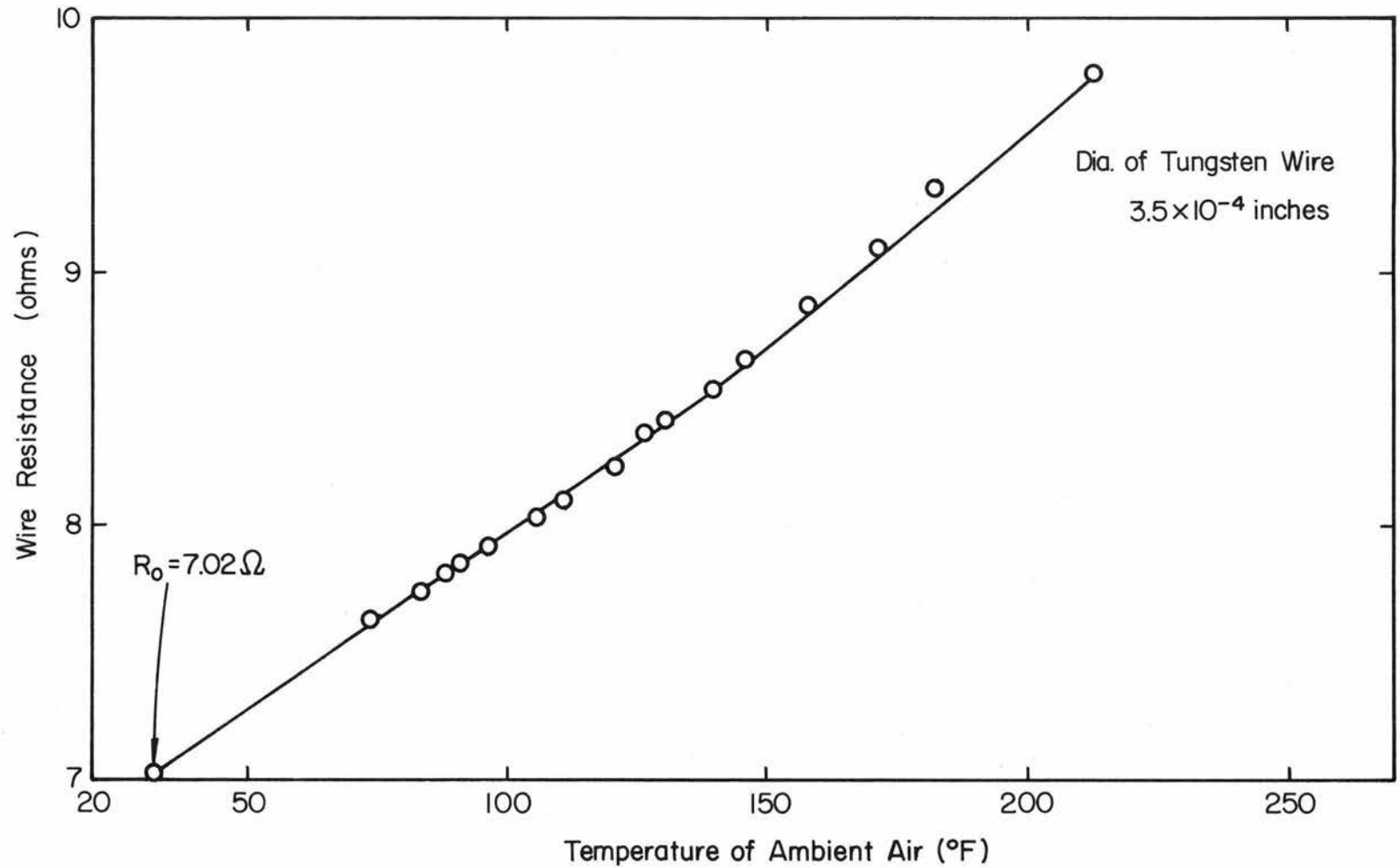


Fig. 4.10 Resistance temperature relation for a tungsten wire.

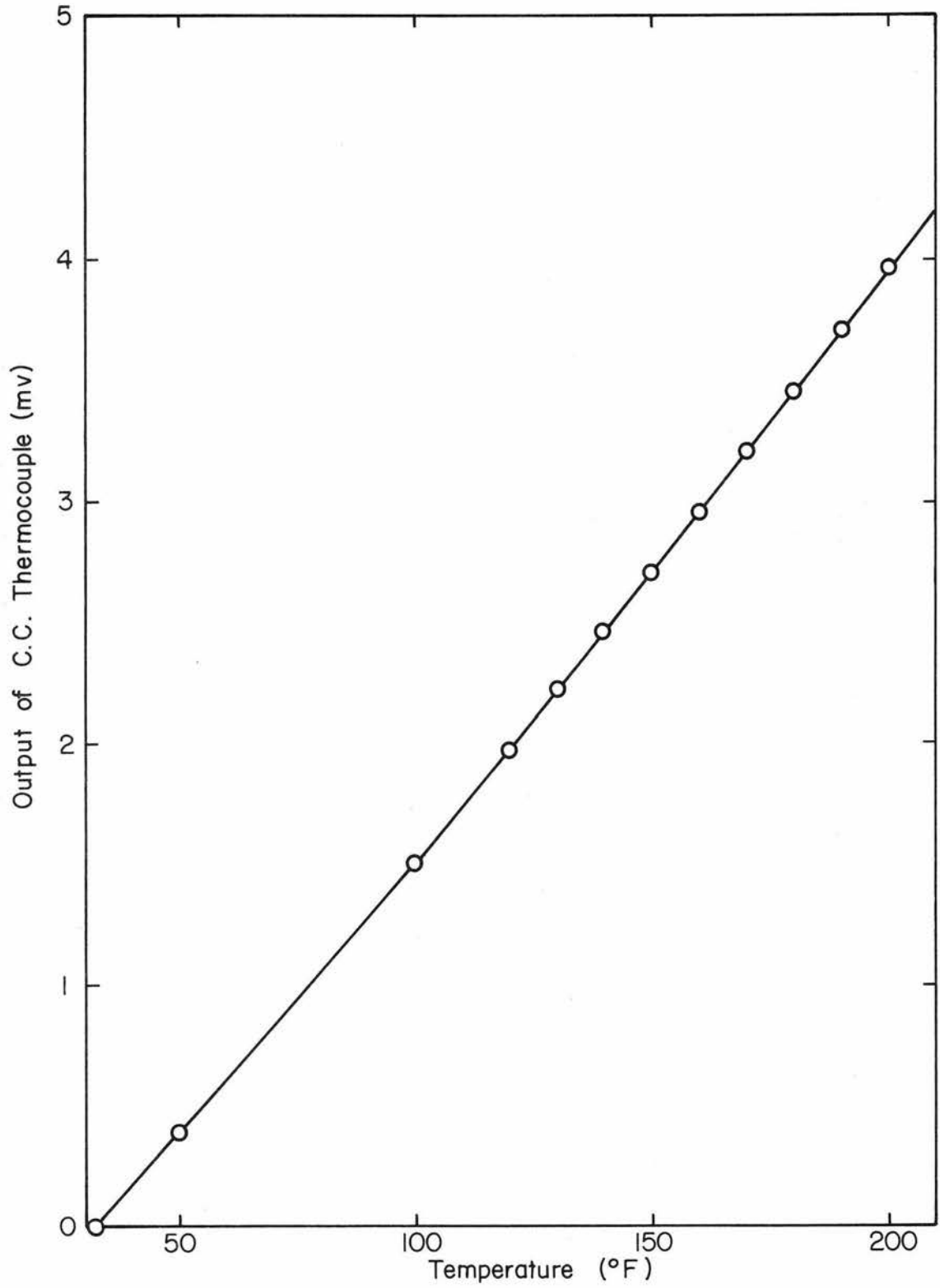


Fig. 4.11 A typical calibration curve for the Copper-Constantan thermocouple.

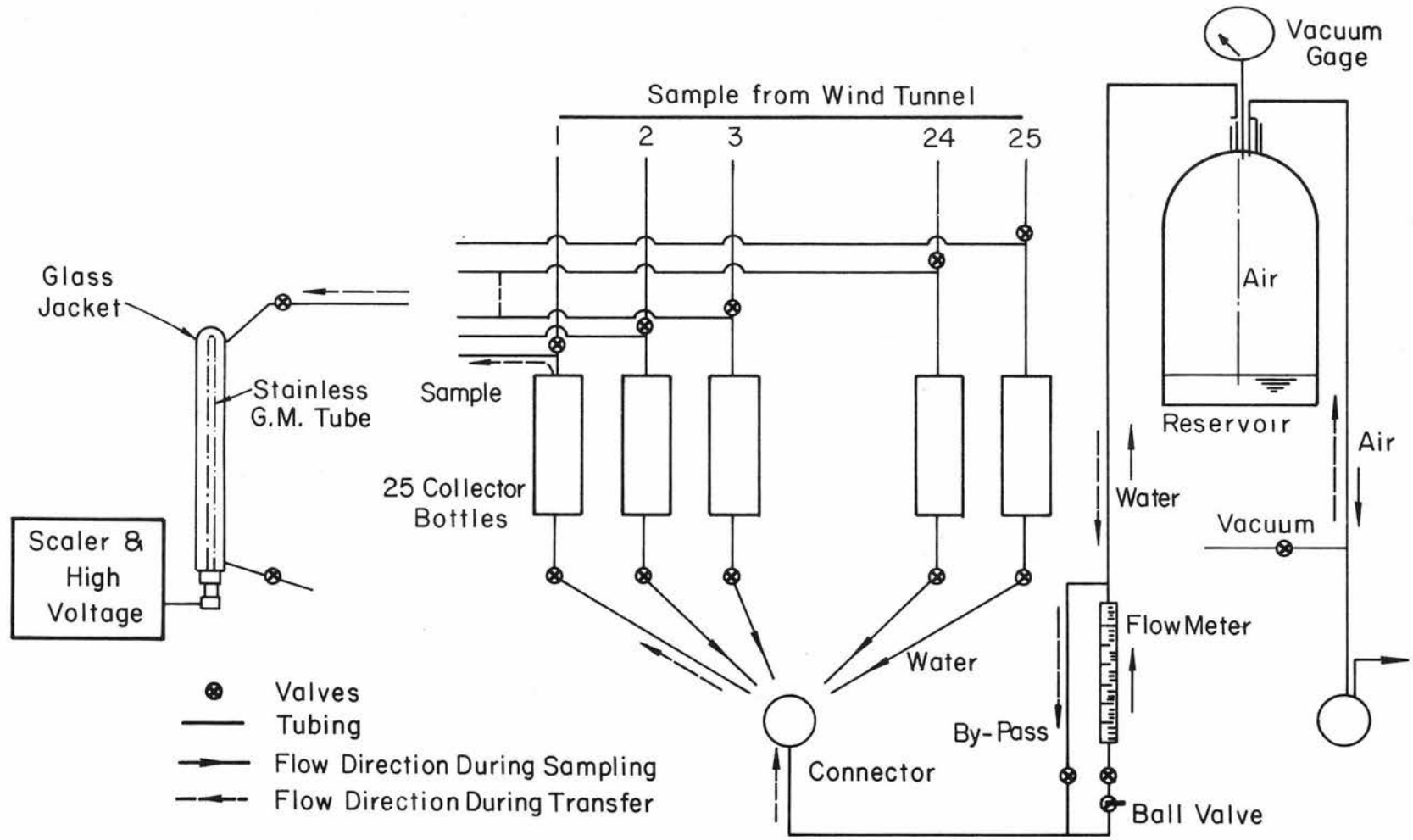


Fig. 4.12 Sampling system for diffusion experiments.

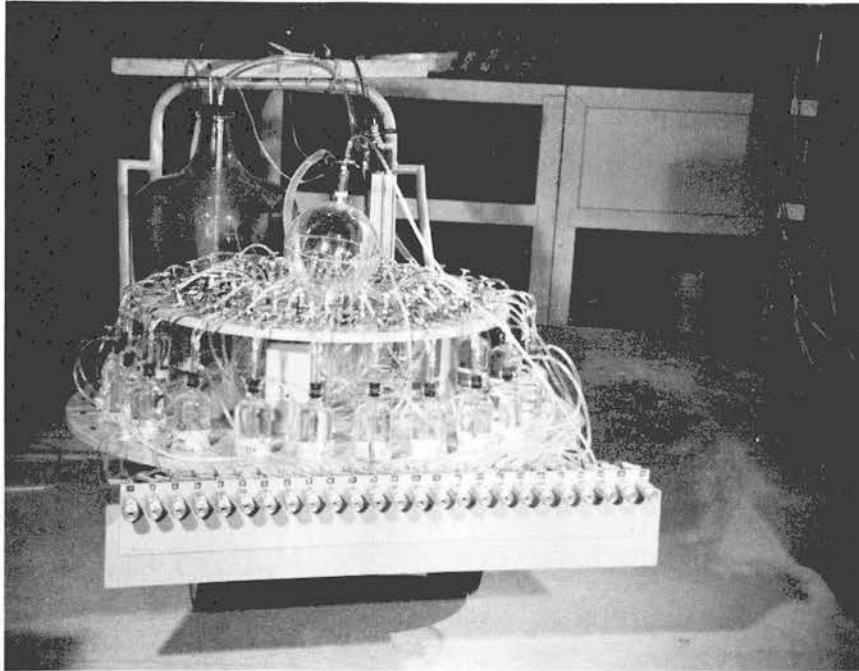


Fig. 4.13 Photograph of the diffusion sampling equipment.

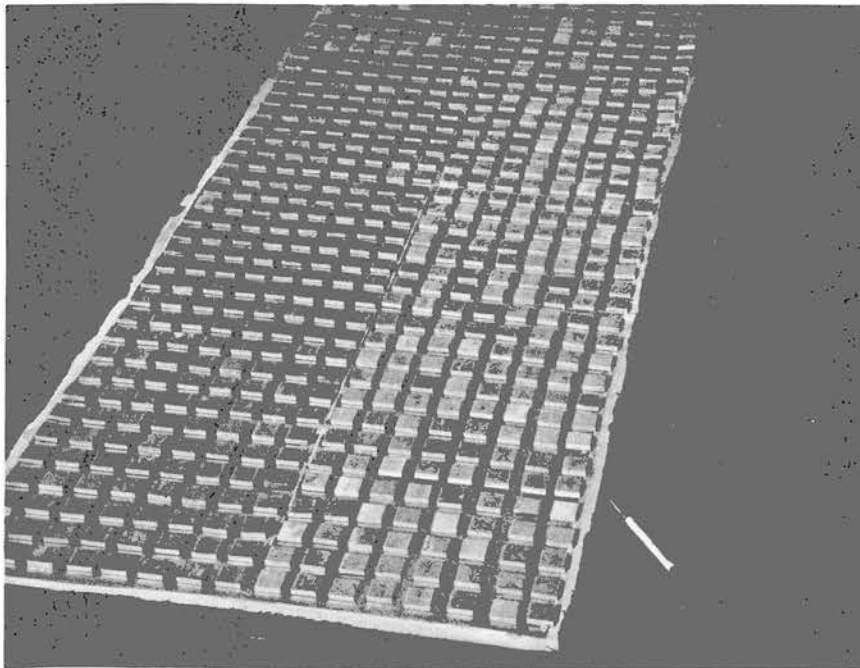
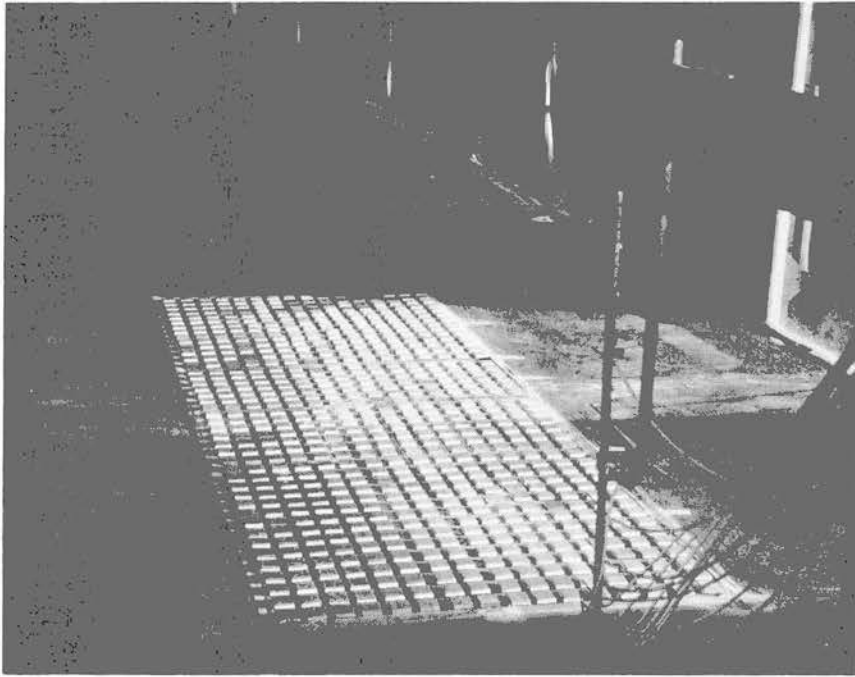


Fig. 4.14 Photographs of the experimental arrangement and a close-up view of the roughness elements.

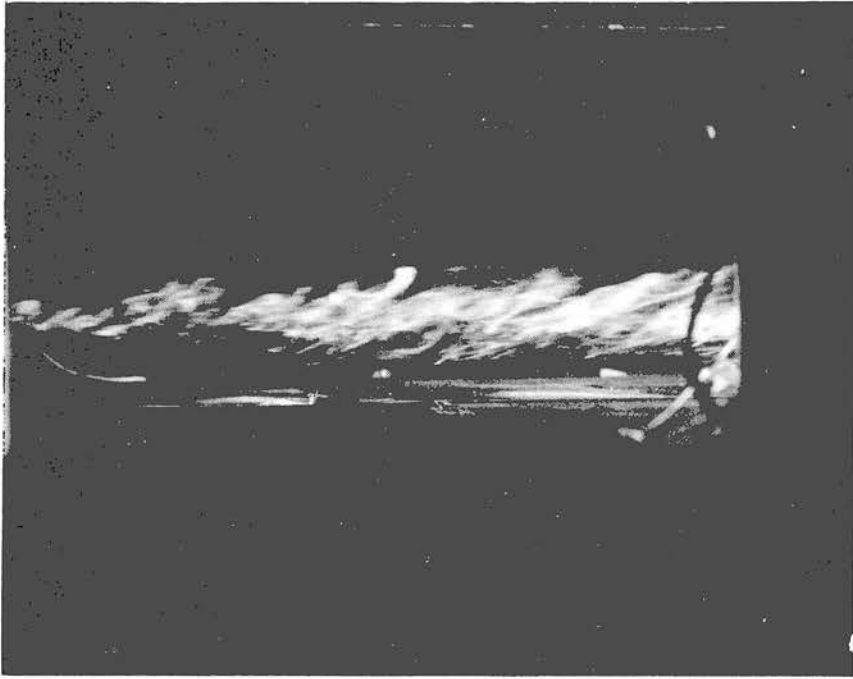


Fig. 5.1 Photograph Neutral approach flow over neutral smooth heat island-elevated smoke source upwind.

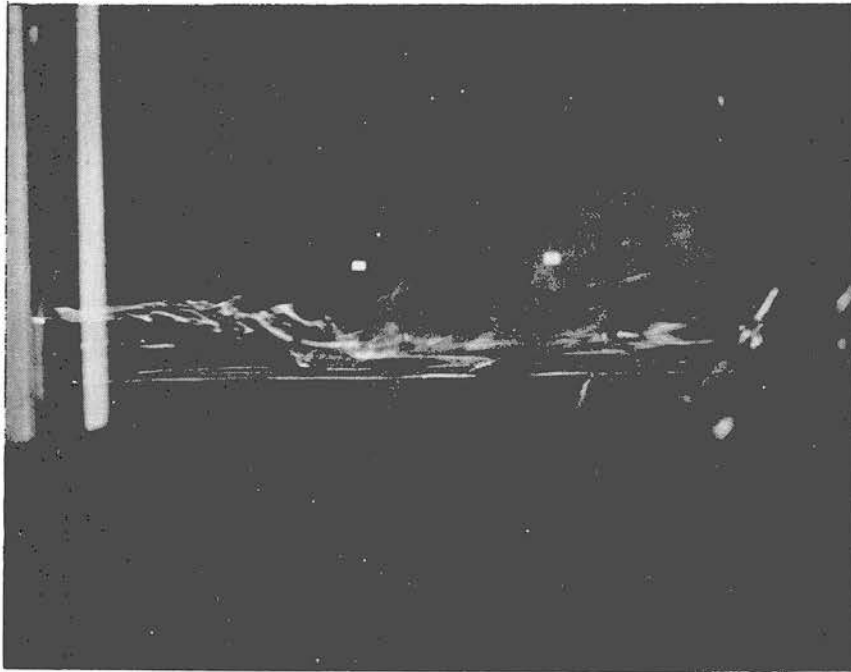


Fig. 5.2 Photograph Stable approach flow over unstable smooth heat island - elevated smoke source upwind.

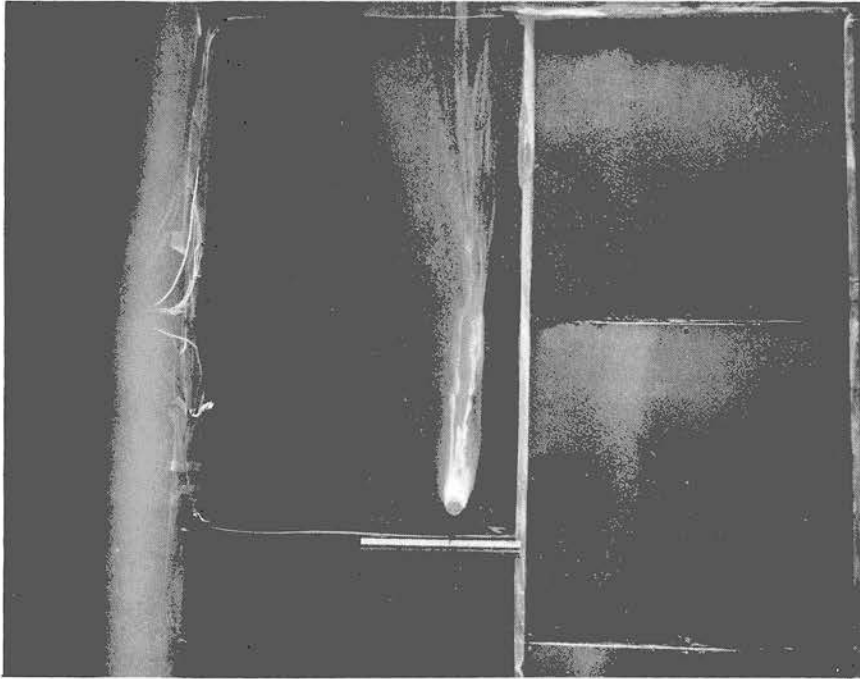


Fig. 5.3 Photograph - Stable approach flow over neutral smooth heat island - ground smoke source at left side.

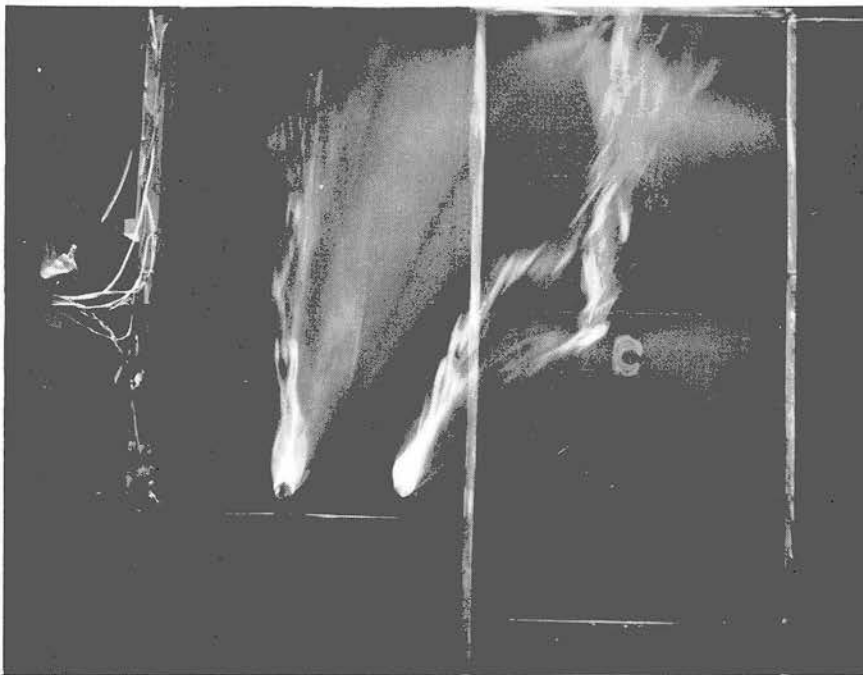


Fig. 5.4 Photograph - Stable approach flow over unstable smooth heat island - two ground smoke sources at left side.

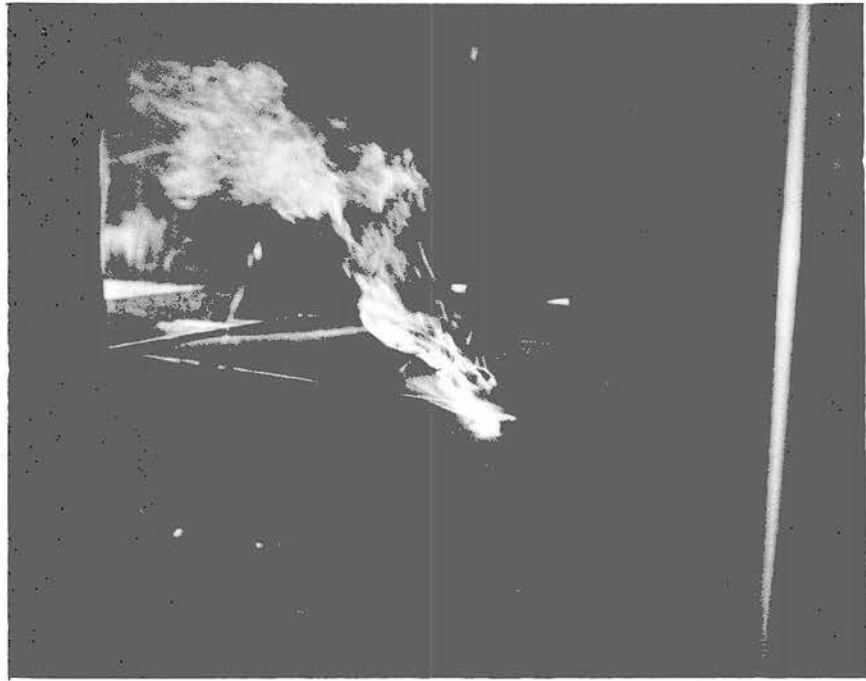


Fig. 5.5 Photograph - Stable approach flow over unstable smooth heat island - ground smoke source at left side.



Fig. 5.6 Photograph - Stable approach flow over unstable rough heat island - ground smoke source at left side.

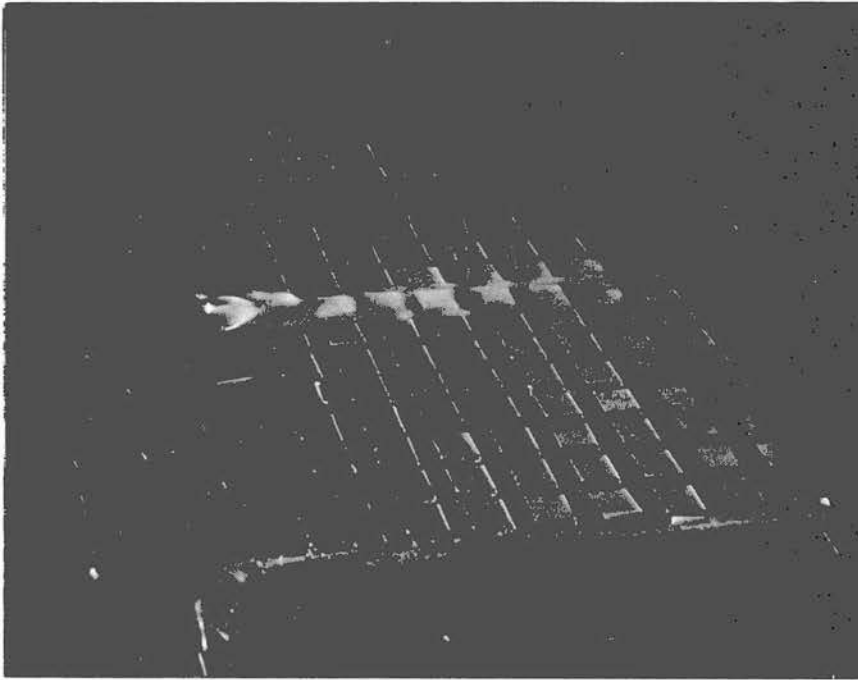


Fig. 5.7 Photograph - Stable approach flow over neutral rough heat island - ground smoke source along the centerline over the heater.

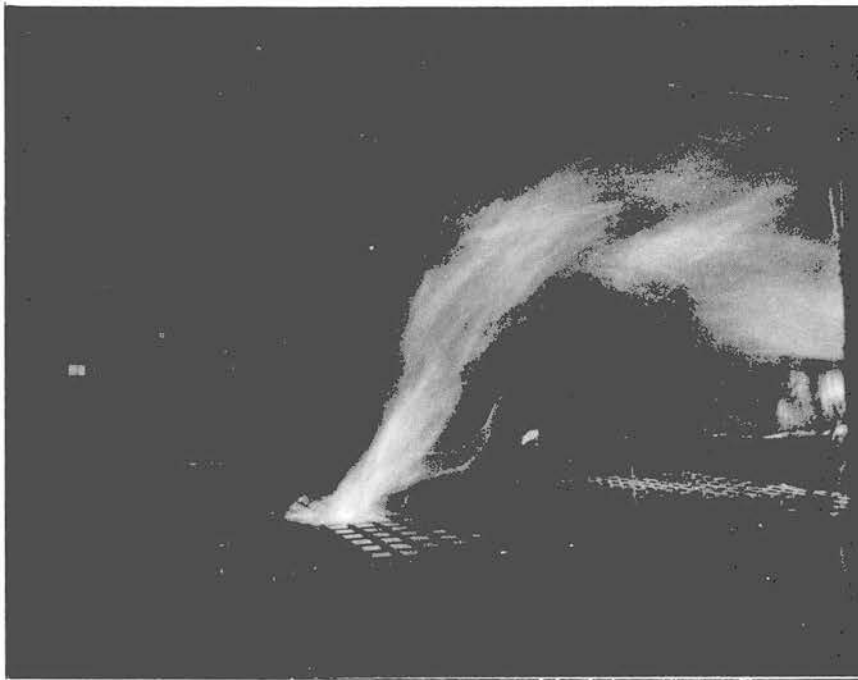


Fig. 5.8 Photograph - Stable approach flow over unstable rough heat island - ground smoke source along the centerline over the heater.

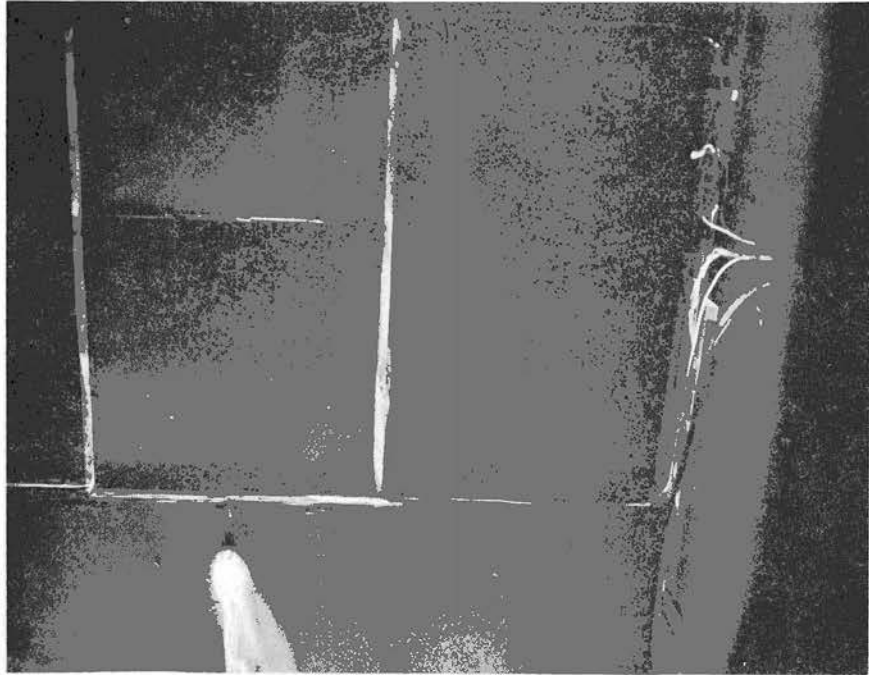


Fig. 5.9 Photograph - Stable approach flow over neutral smooth heat island - ground smoke source downwind.

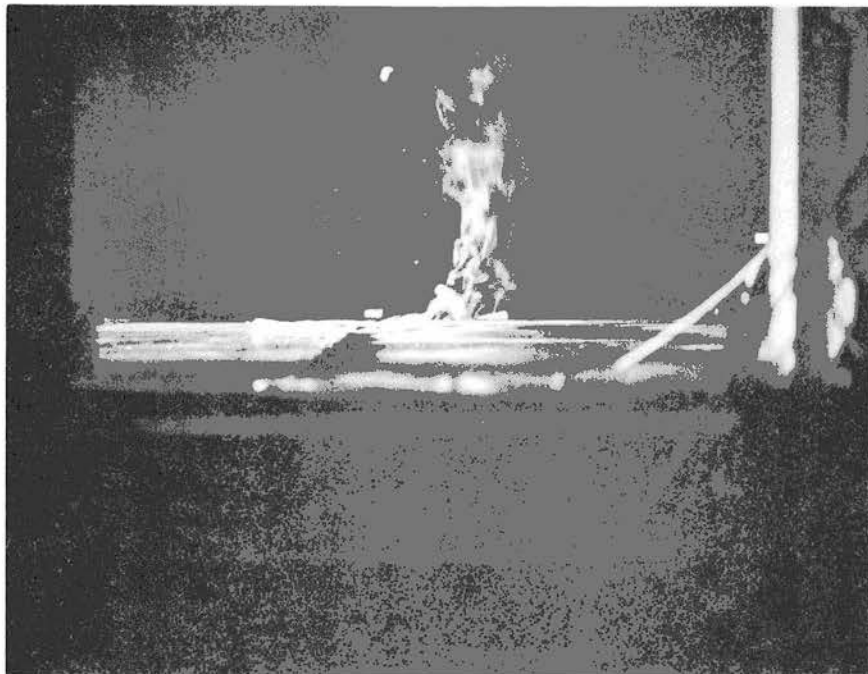


Fig. 5.10 Photograph - Stable approach flow over unstable smooth heat island - ground smoke source downwind.

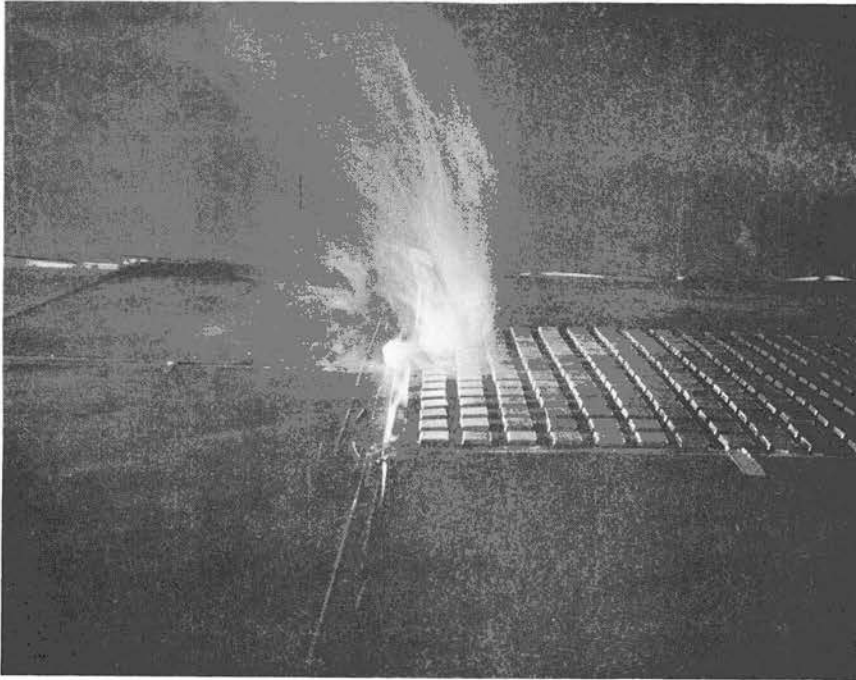


Fig. 5.11 Photograph - Stable approach flow over unstable rough heat island - ground smoke source downwind.

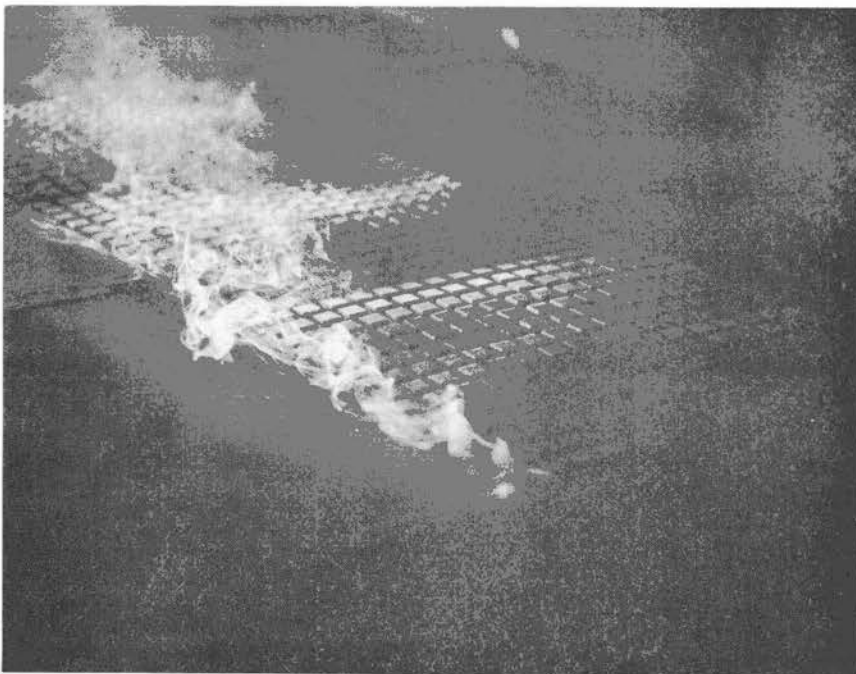


Fig. 5.12 Photograph - Stable approach flow over the unstable rough heat island - ground smoke source at upwind left corner.

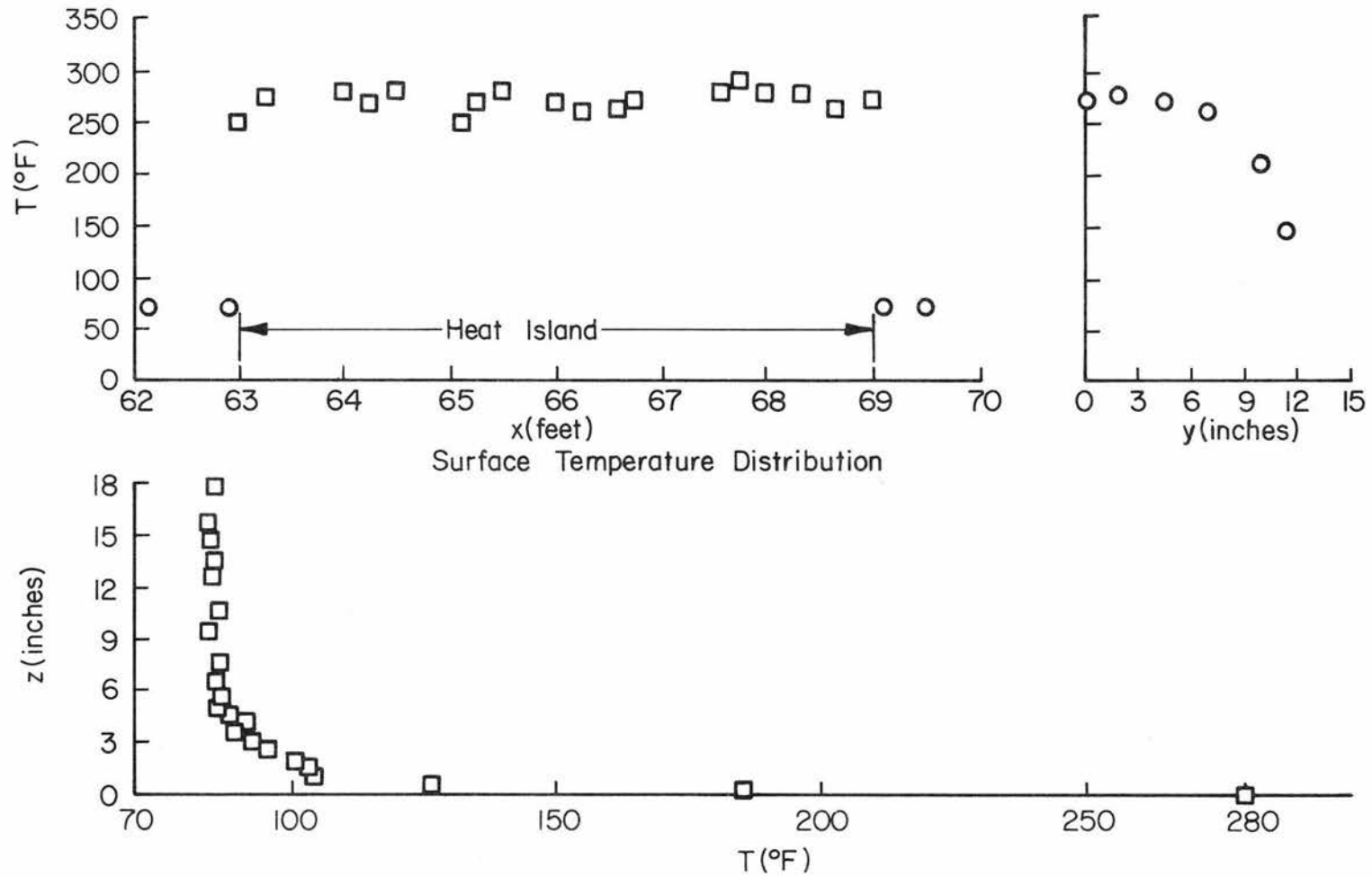


Fig. 5.13 Surface temperature distribution along the centerline for neutral flow over unstable rough heat island.  
 and  
 Mean temperature profile at  $x = 65.5$  feet and  $y = 0$  for neutral flow over unstable rough heat island indicating details near the surface.

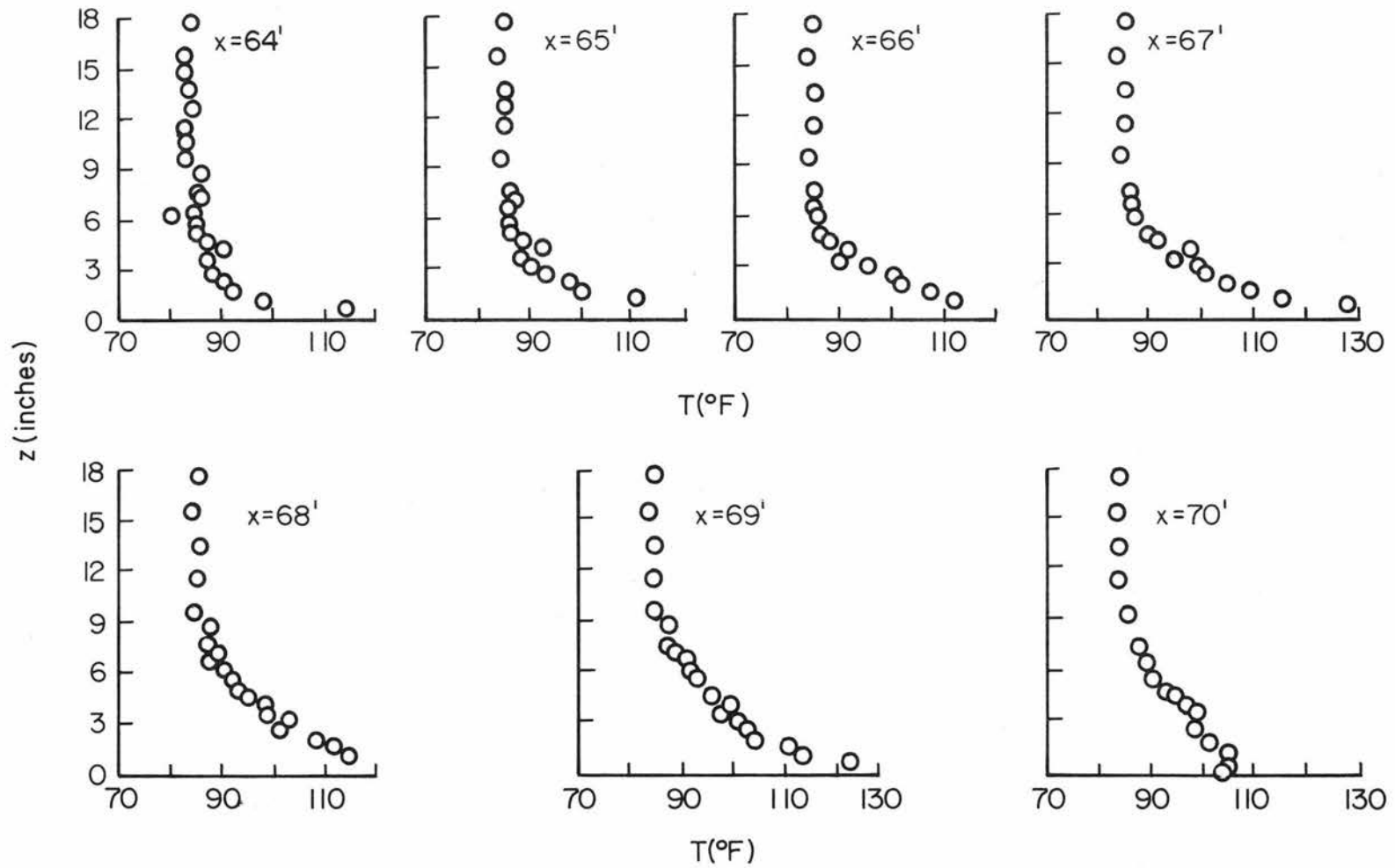


Fig. 5.14 Mean temperature profiles along the centerline for neutral approach flow over an unstable rough heat island.

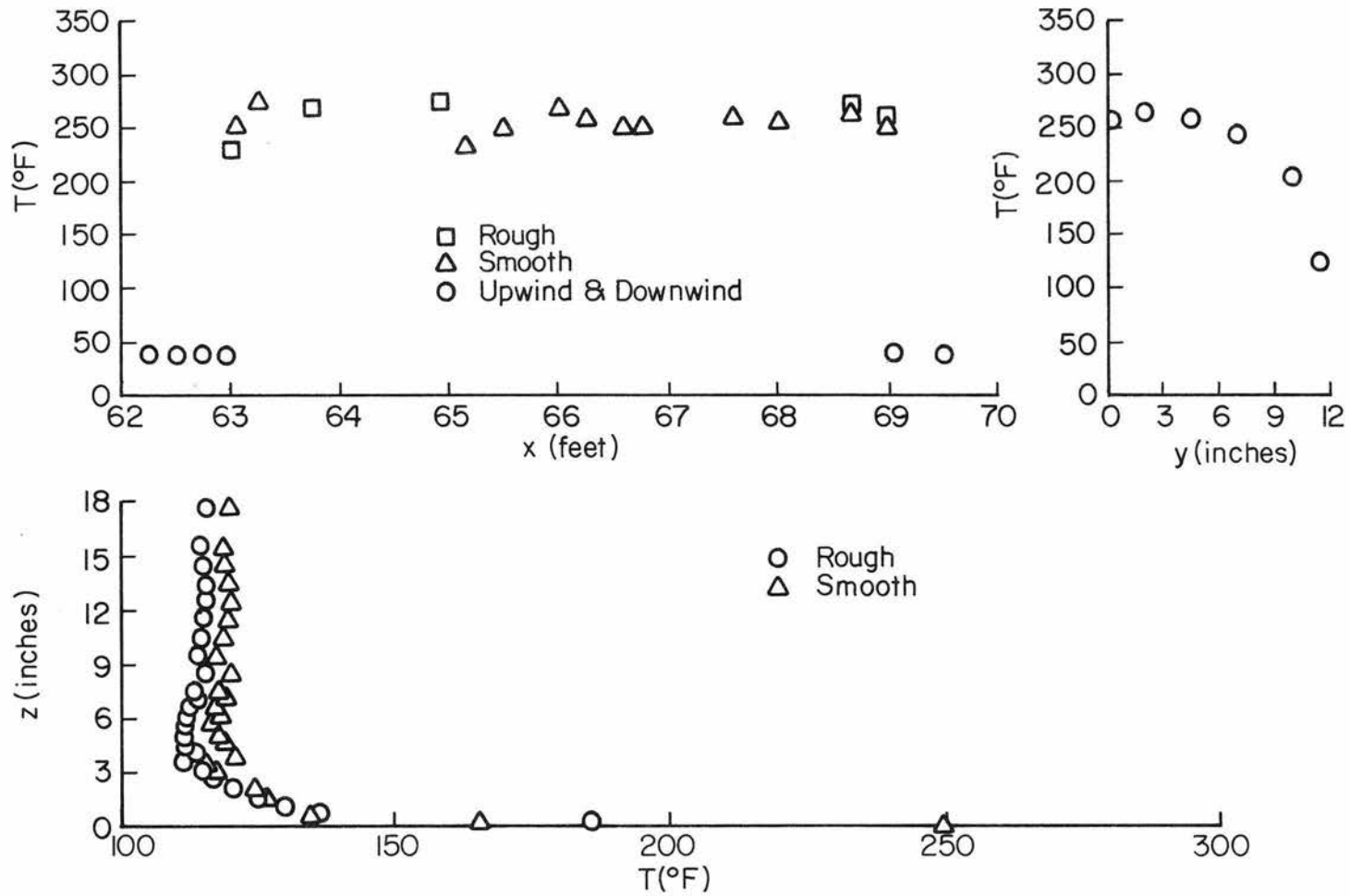


Fig. 5.15 (Top) Surface temperature distribution along the centerline for stable flow over an unstable heat island.  
 (Bottom) Mean temperature profiles at  $x = 65.5$  feet and  $y = 0$  for stable flow over an unstable heat island.

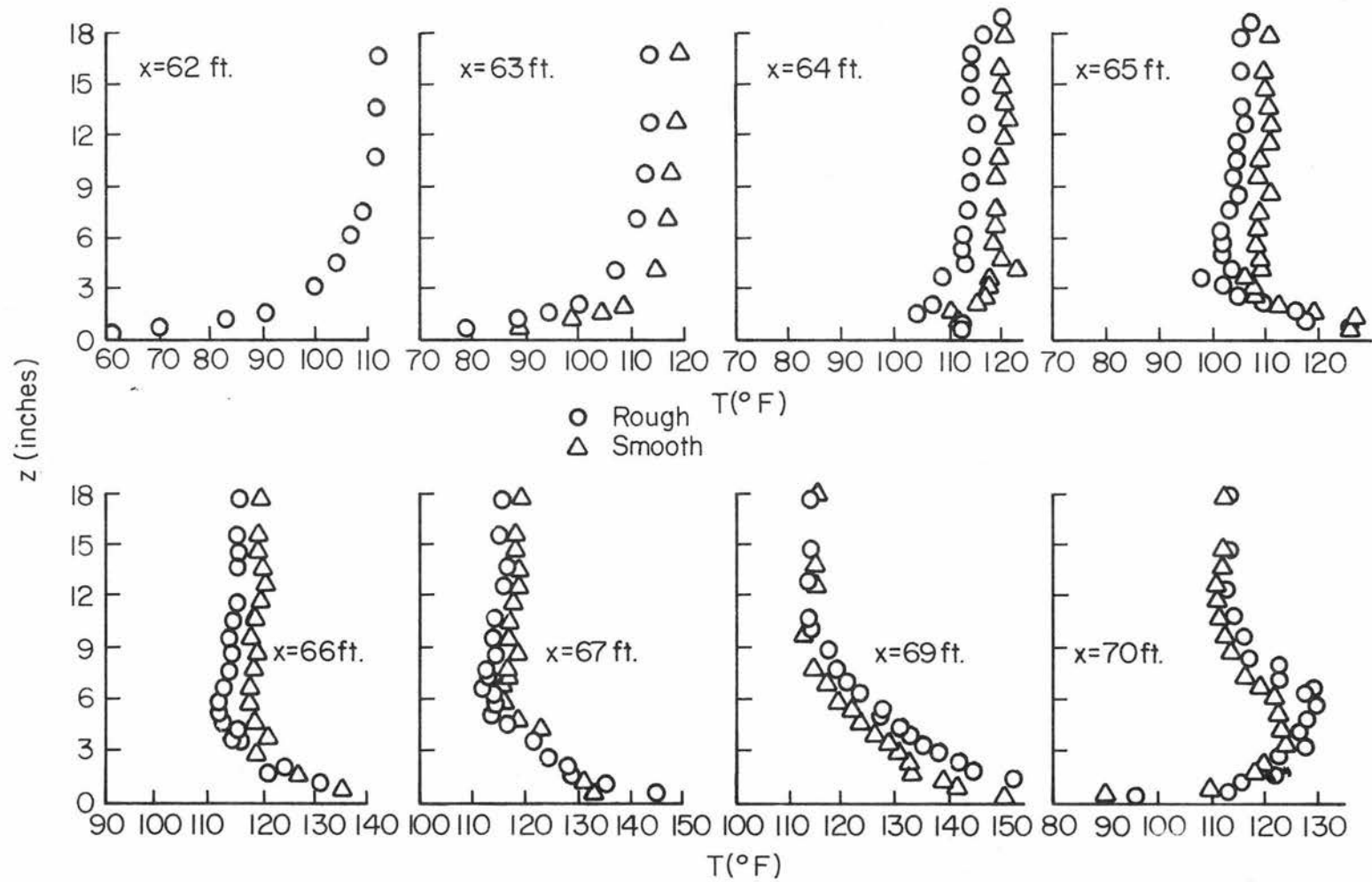


Fig. 5.16 Comparison of mean temperature profiles along the centerline for stable flow over an unstable heat island for rough and smooth cases.

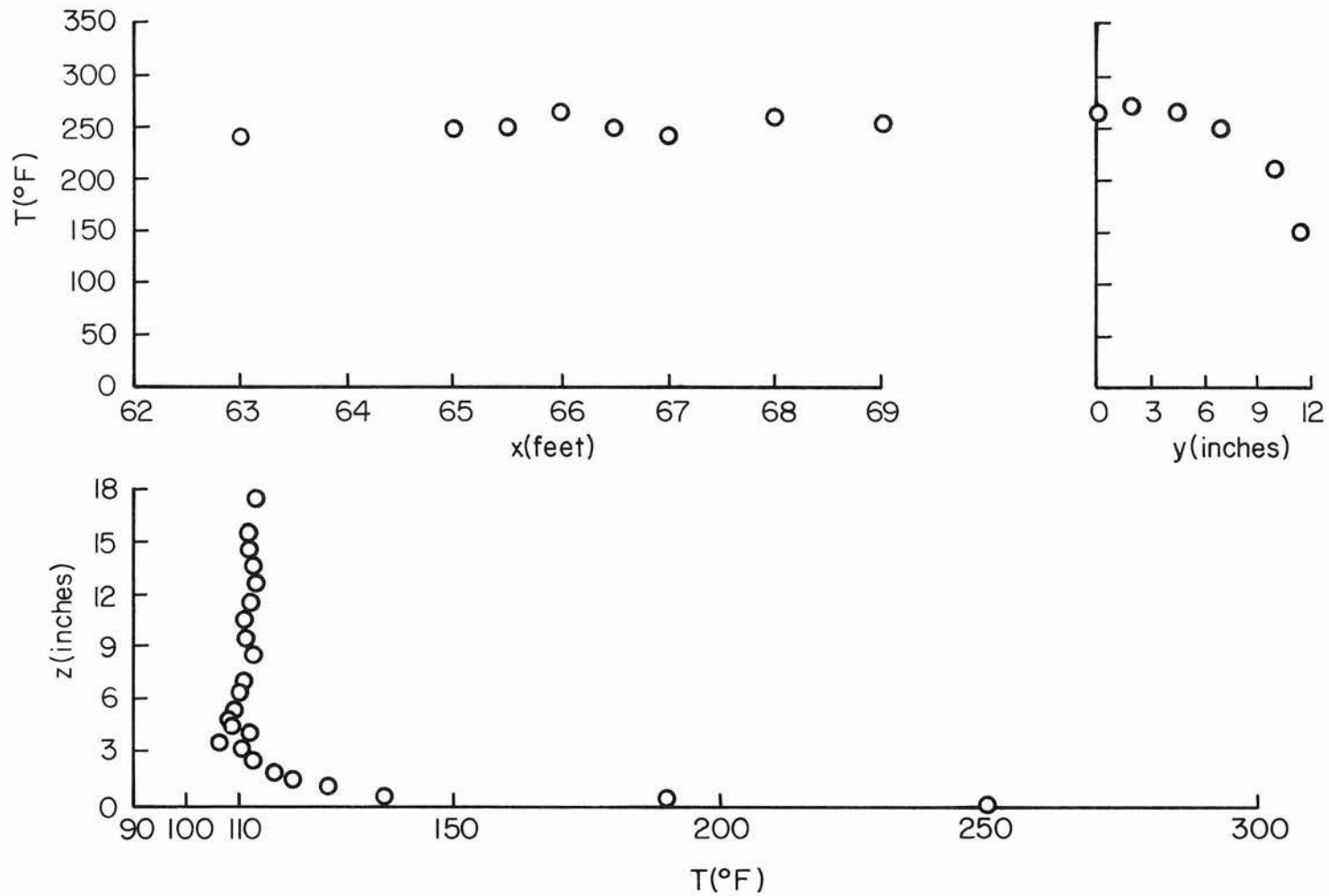


Fig. 5.17 Surface temperature distribution along the centerline for an approach flow with elevated inversion over an unstable rough heat island and Mean temperature profile at  $x = 65.5$  feet and  $y = 0$  for an approach flow with elevated inversion over an unstable rough heat island.

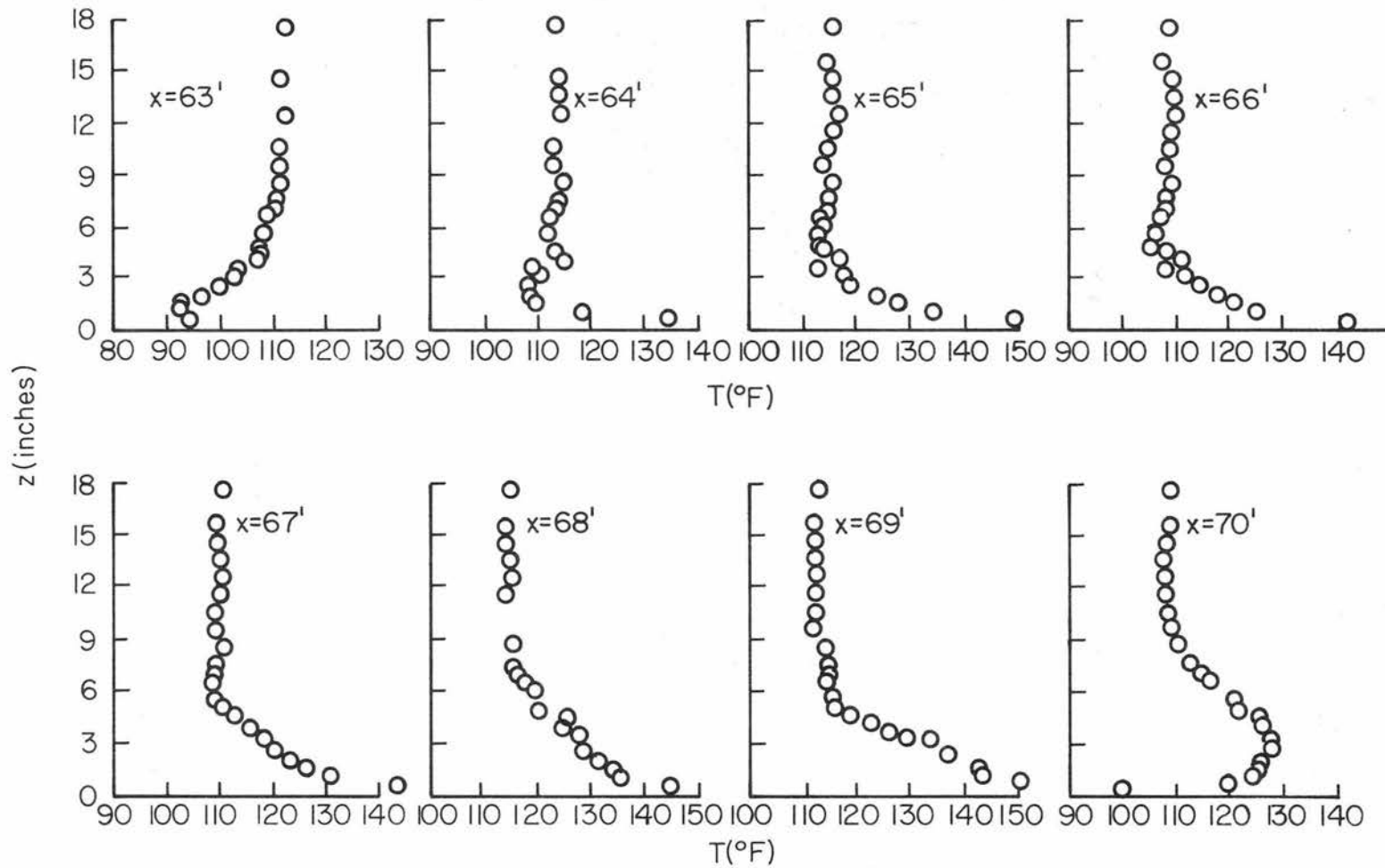


Fig. 5.18 Mean temperature profiles along the centerline for a flow with elevated inversion over an unstable rough heat island.

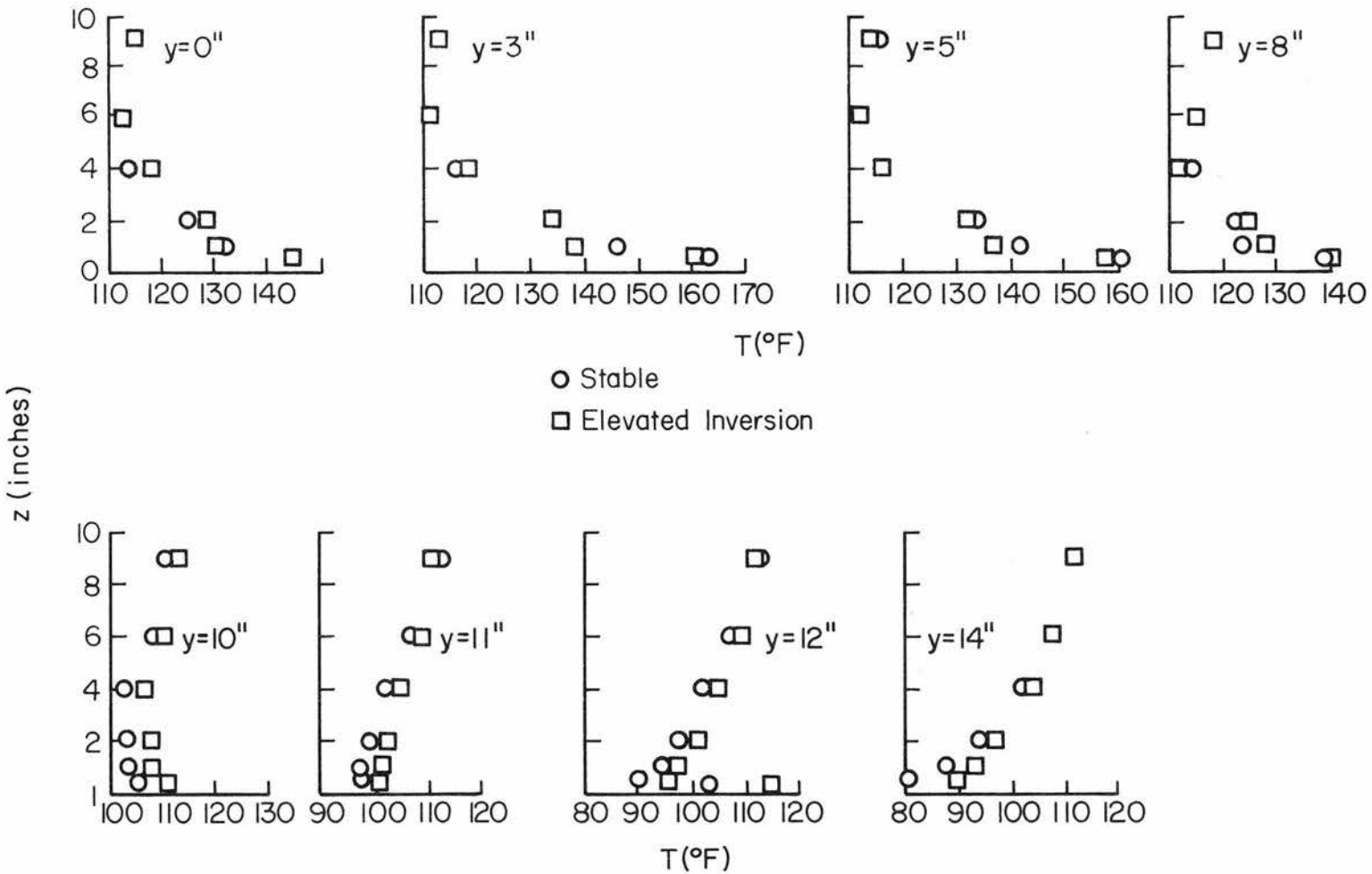


Fig. 5.19 Mean temperature profiles across the heat island for an unstable rough heat island with stable and elevated inversion approach flows.

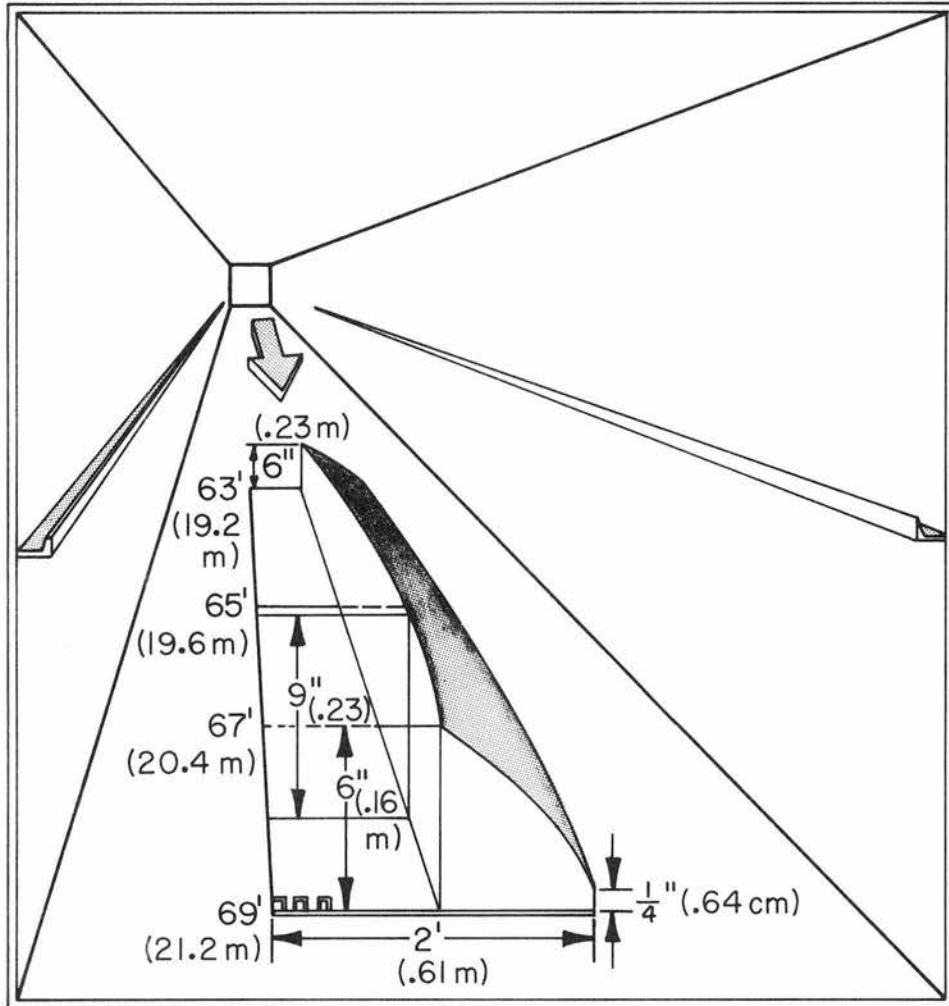


Fig. 5.20 Three-dimensional development of the base of elevated inversion for stable flow over unstable rough heat island.

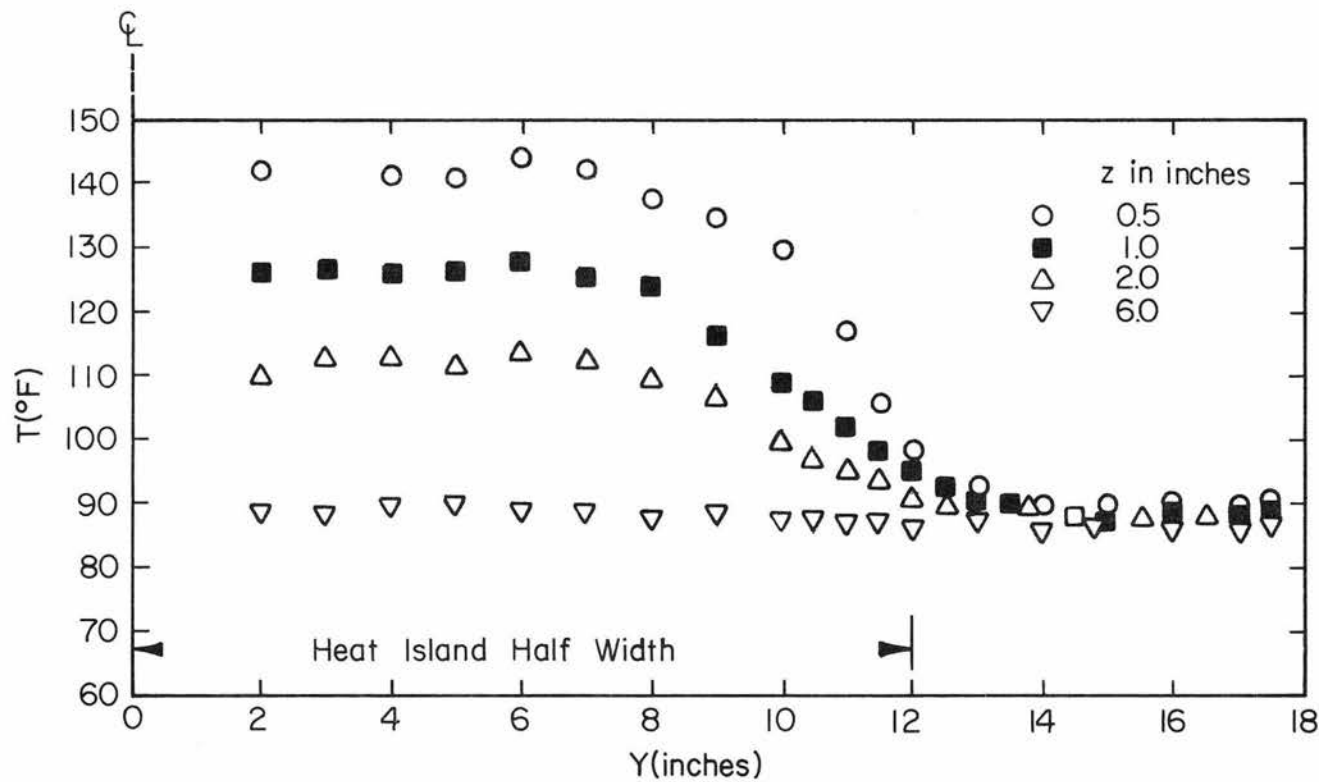


Fig. 5.21 Mean temperature distribution along the width of the heat island for neutral flow over unstable rough heat island at  $x = 65.5$  feet for different heights.

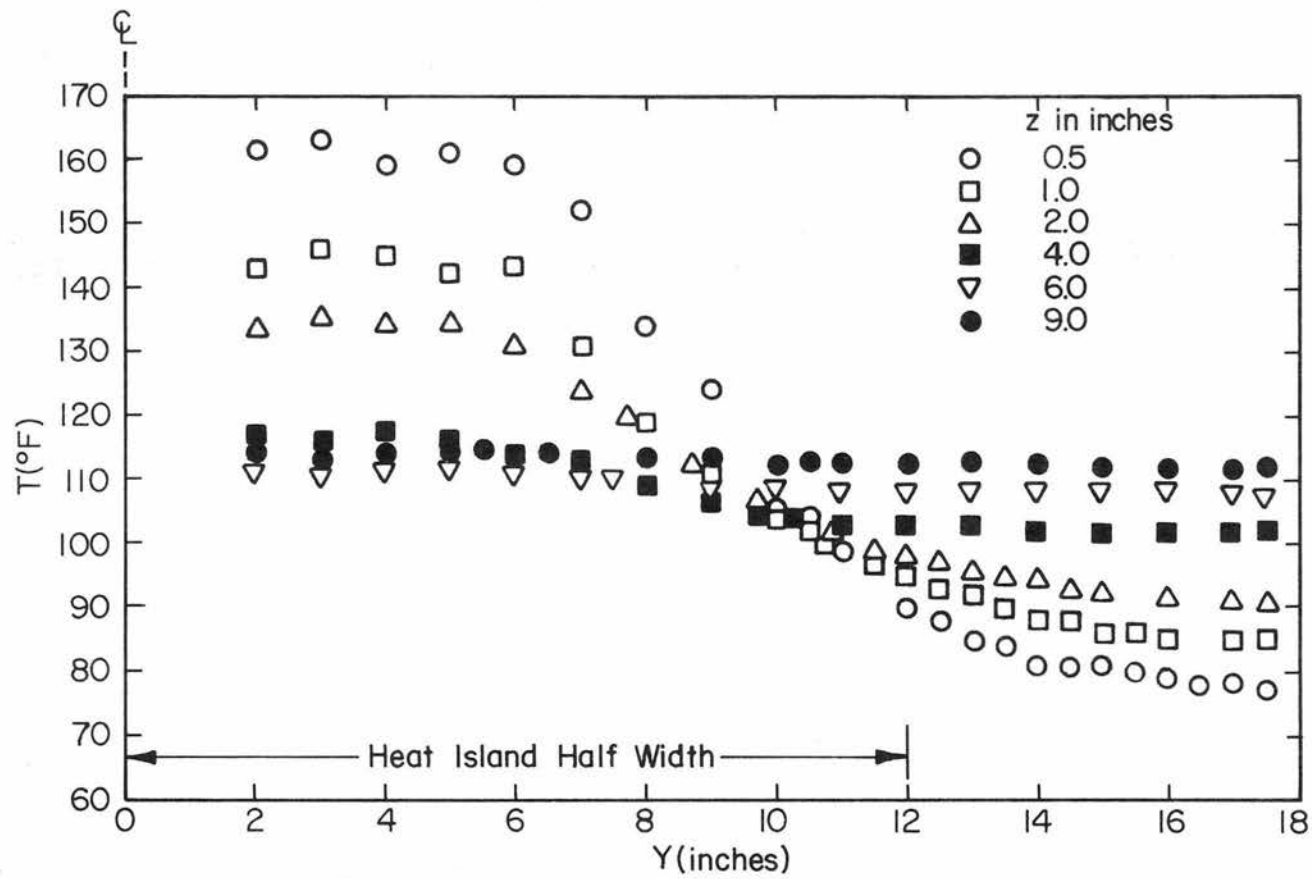


Fig. 5.22 Mean temperature distribution along the width of the heat island for stable flow over unstable rough heat island at  $x = 66$  feet for different heights.

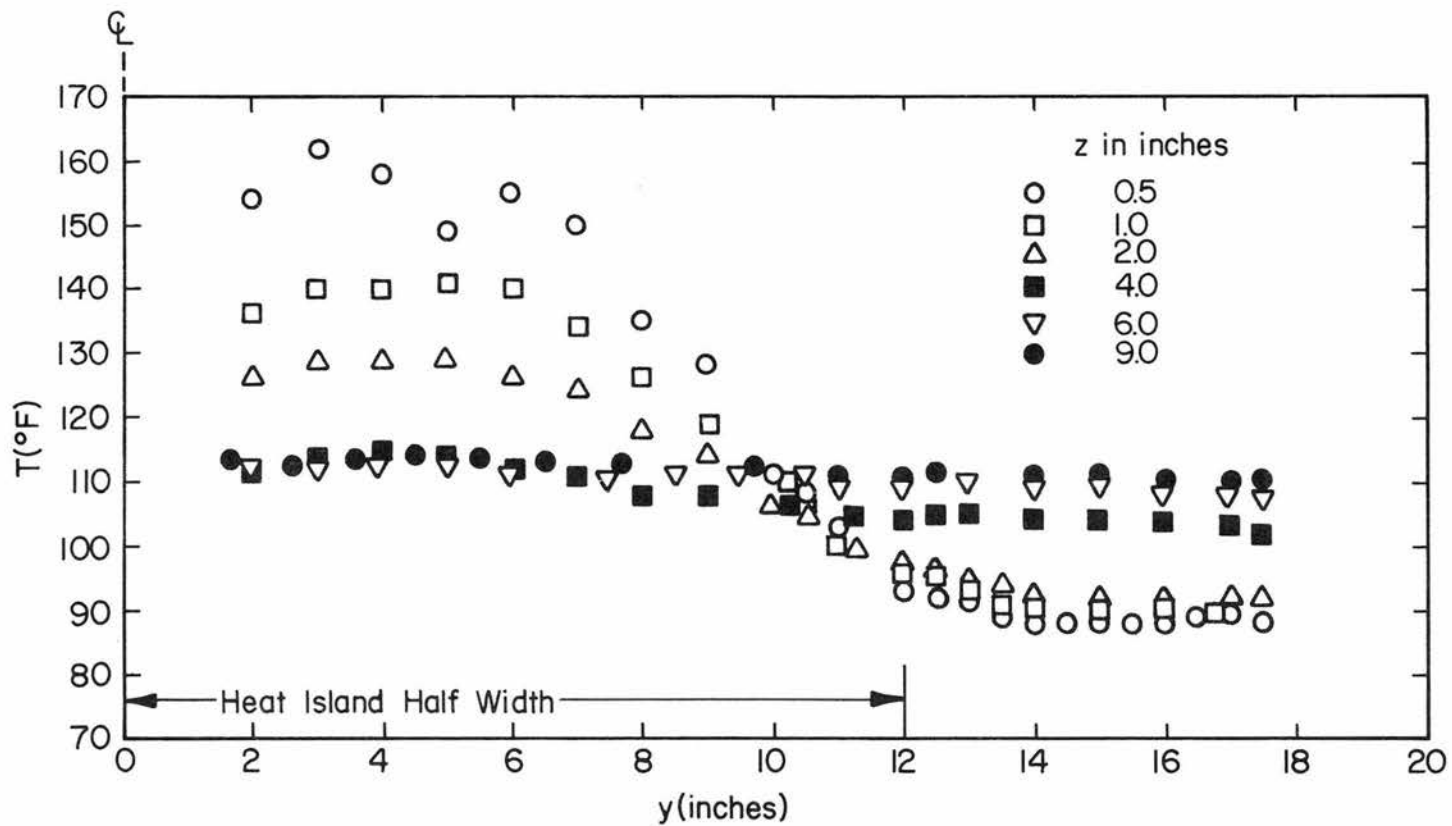


Fig. 5.23 Mean temperature distribution along the width for elevated inversion at  $x = 65.5$  feet for different heights.

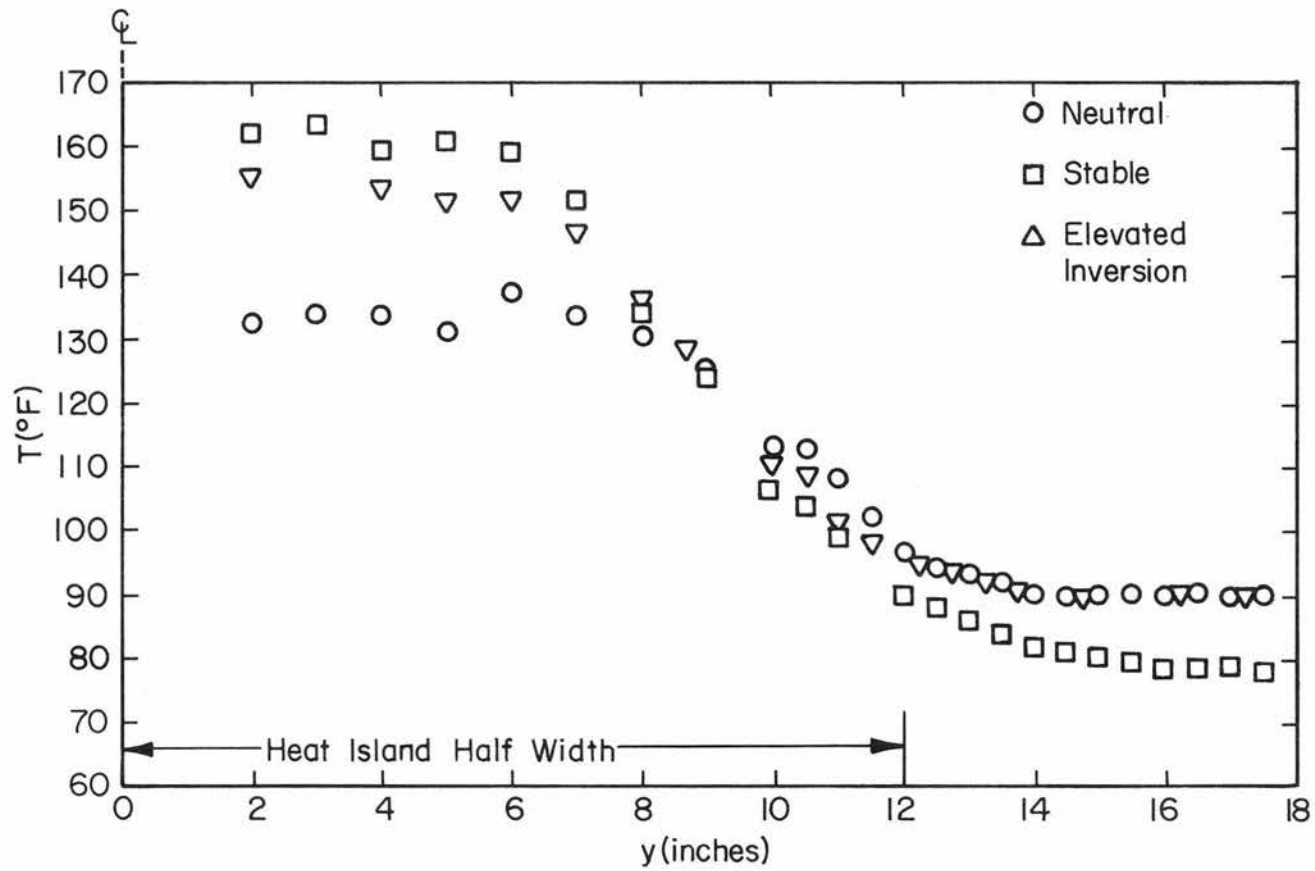


Fig. 5.24 Mean temperature distribution along the width of an unstable rough heat island for different approach flows at  $x = 66$  feet and  $z = 0.5$  in.

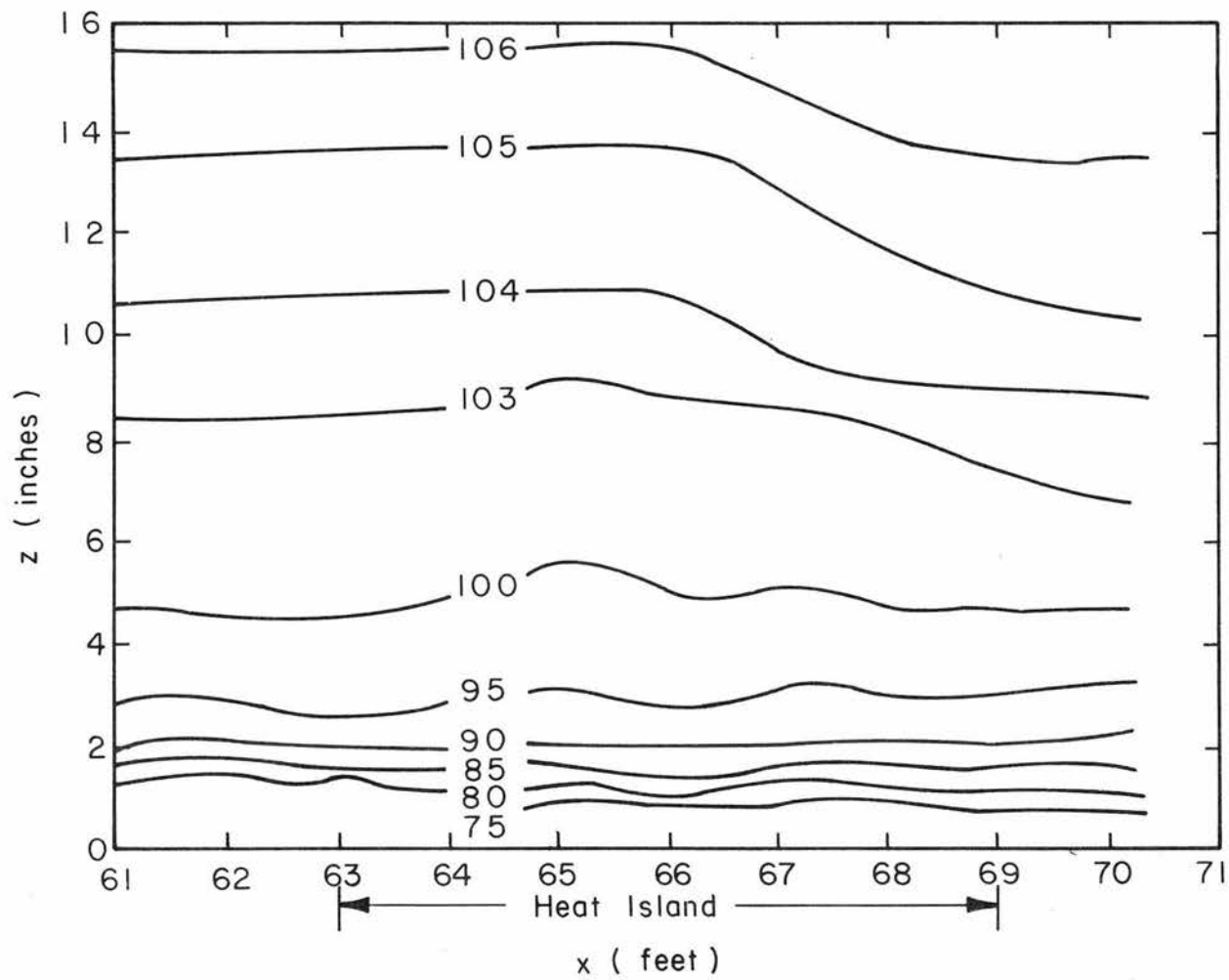


Fig. 5.25 Mean temperature contours for stable flow over a neutral smooth heat island along the centerline.

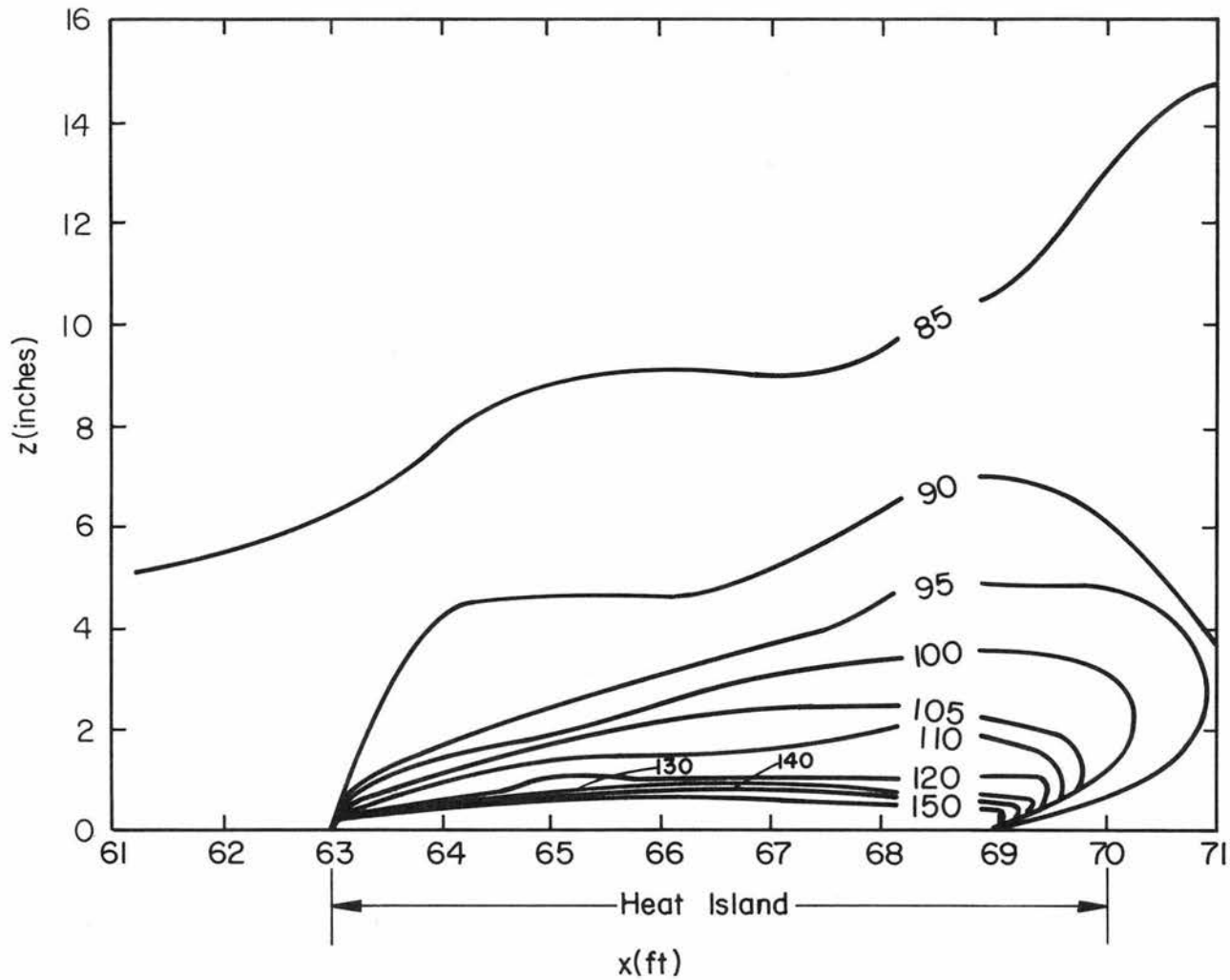


Fig. 5.26 Mean temperature contours for neutral flow over an unstable rough heat island along the centerline (temperatures in Degree F)

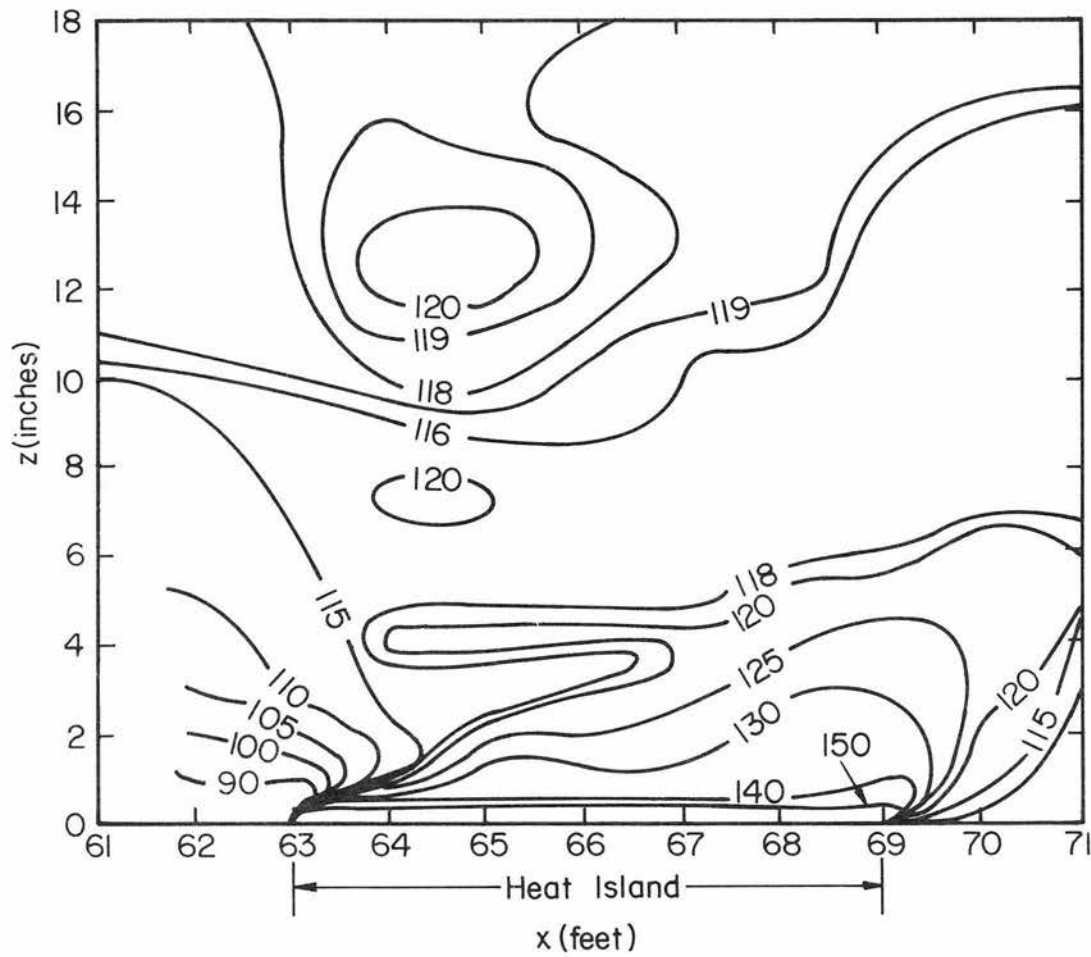


Fig. 5.27 Mean temperature contours for stable flow over an unstable smooth heat island along the centerline (temperatures in Degree F)

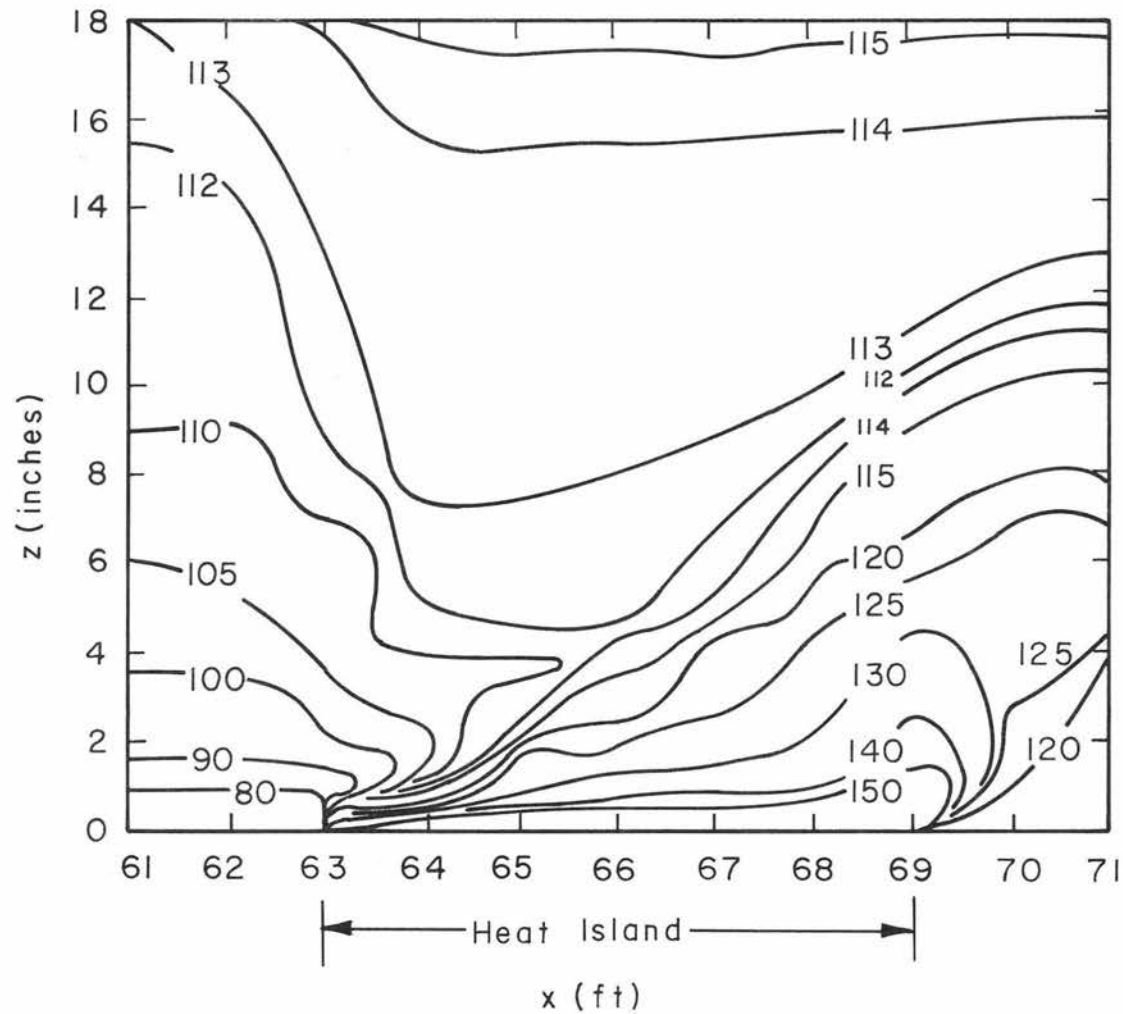


Fig. 5.28 Mean temperature contours for stable flow over an unstable rough heat island along the centerline (temperatures in Degree F)

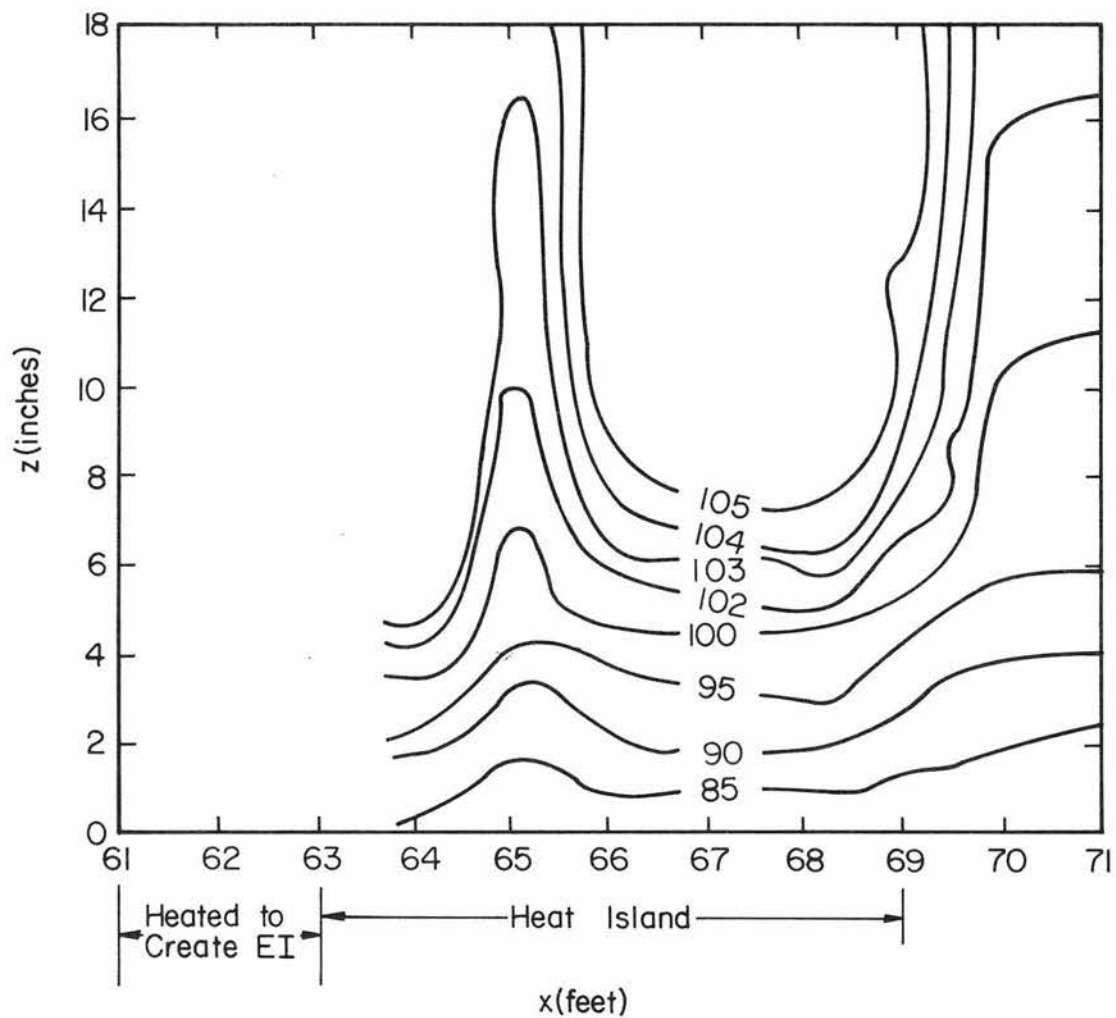


Fig. 5.29 Mean temperature contours for elevated inversion approach flow over a neutral rough heat island along the centerline (temperatures in Degree F)

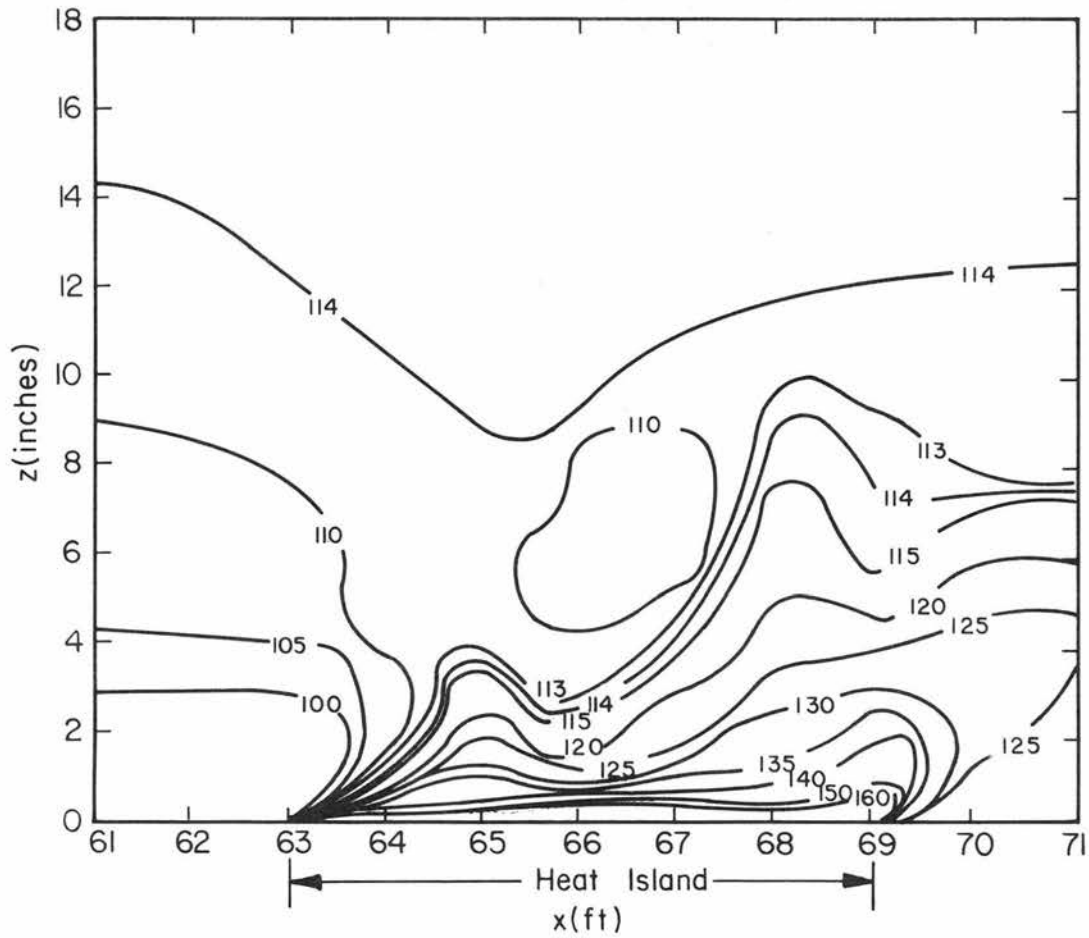


Fig. 5.30 Mean temperature contours elevated inversion approach flow over an unstable rough heat island along the centerline (temperatures in Degree F)

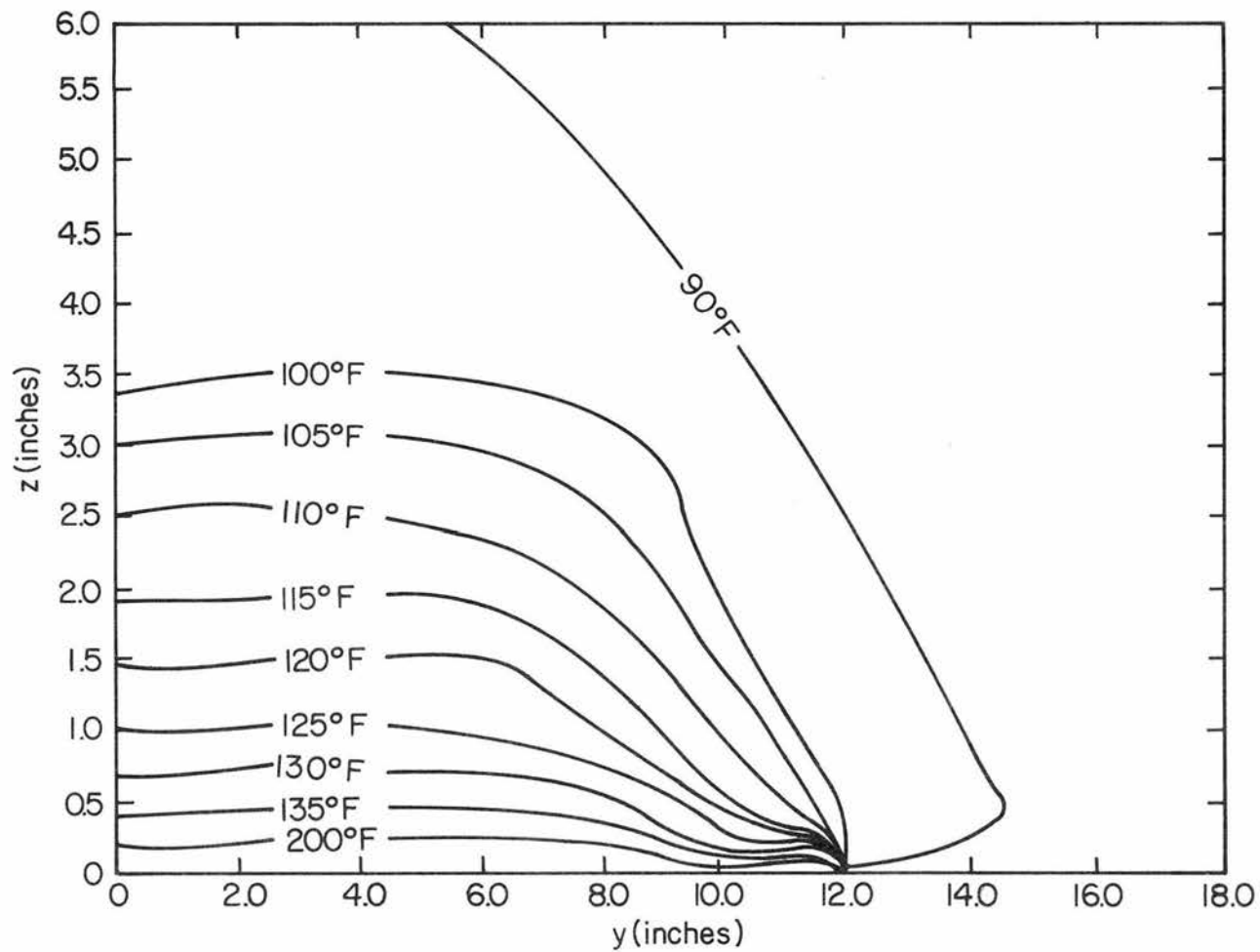


Fig. 5.31 Mean temperature contours for neutral approach flow along the width of an unstable rough heat island at  $x = 66$  feet (temperatures in Degree F)

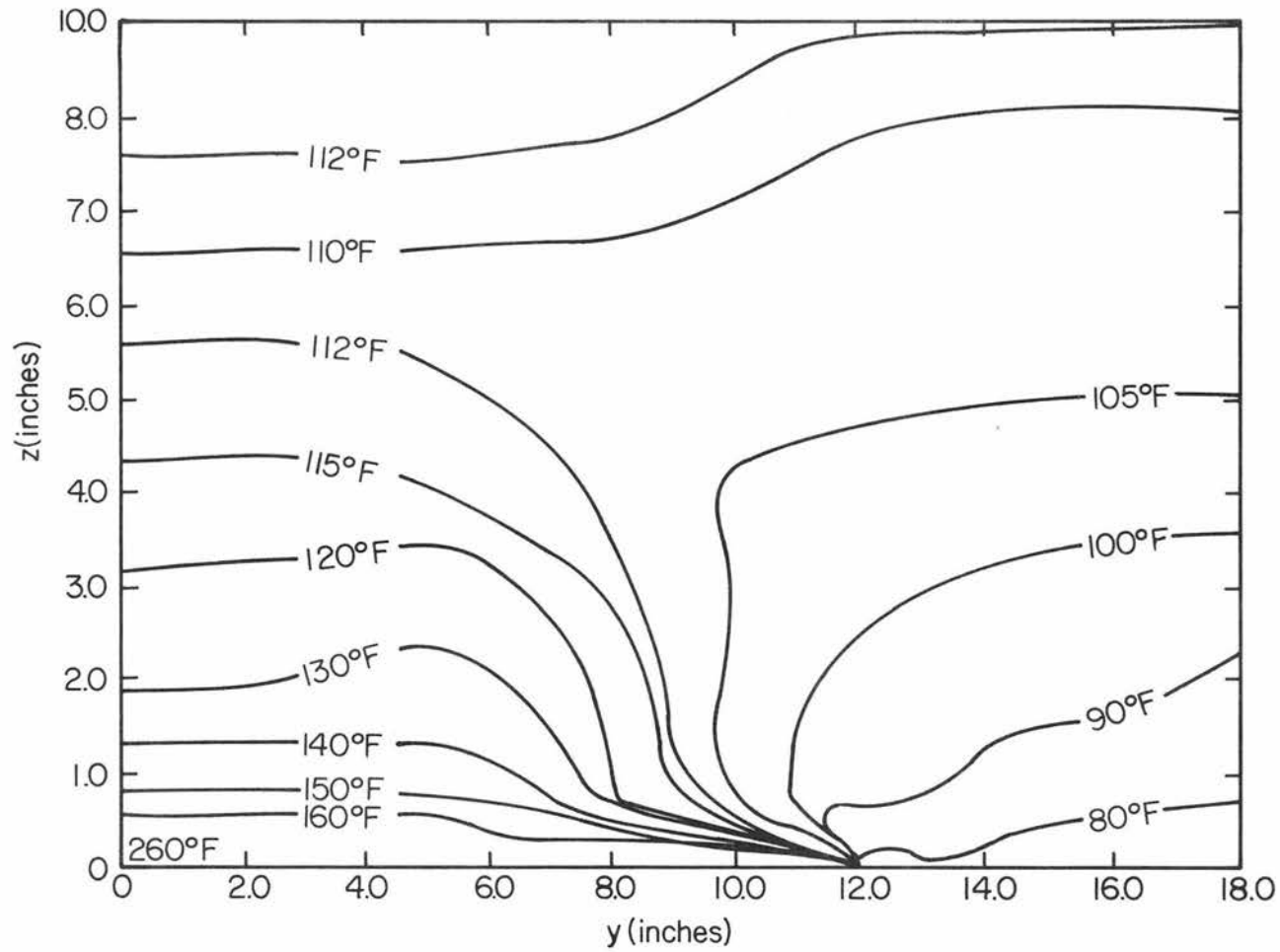


Fig. 5.32 Mean temperature contours for stable flow along the width of an unstable rough heat island at  $x = 66$  feet (temperatures in Degree F)

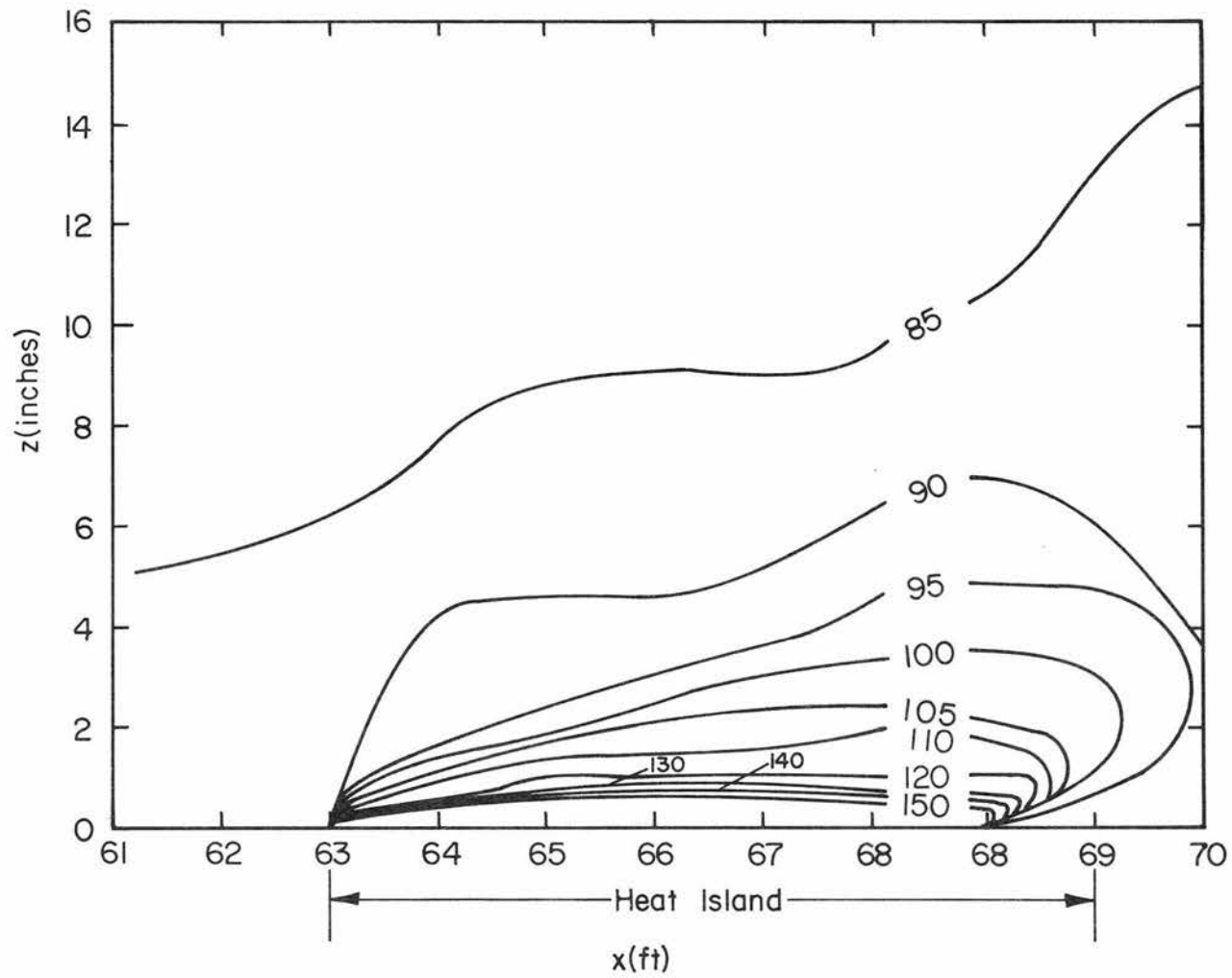


Fig. 5.33 Mean temperature contours for stable flow along the width of an unstable smooth heat island at  $x = 66$  feet (temperatures in Degree F)

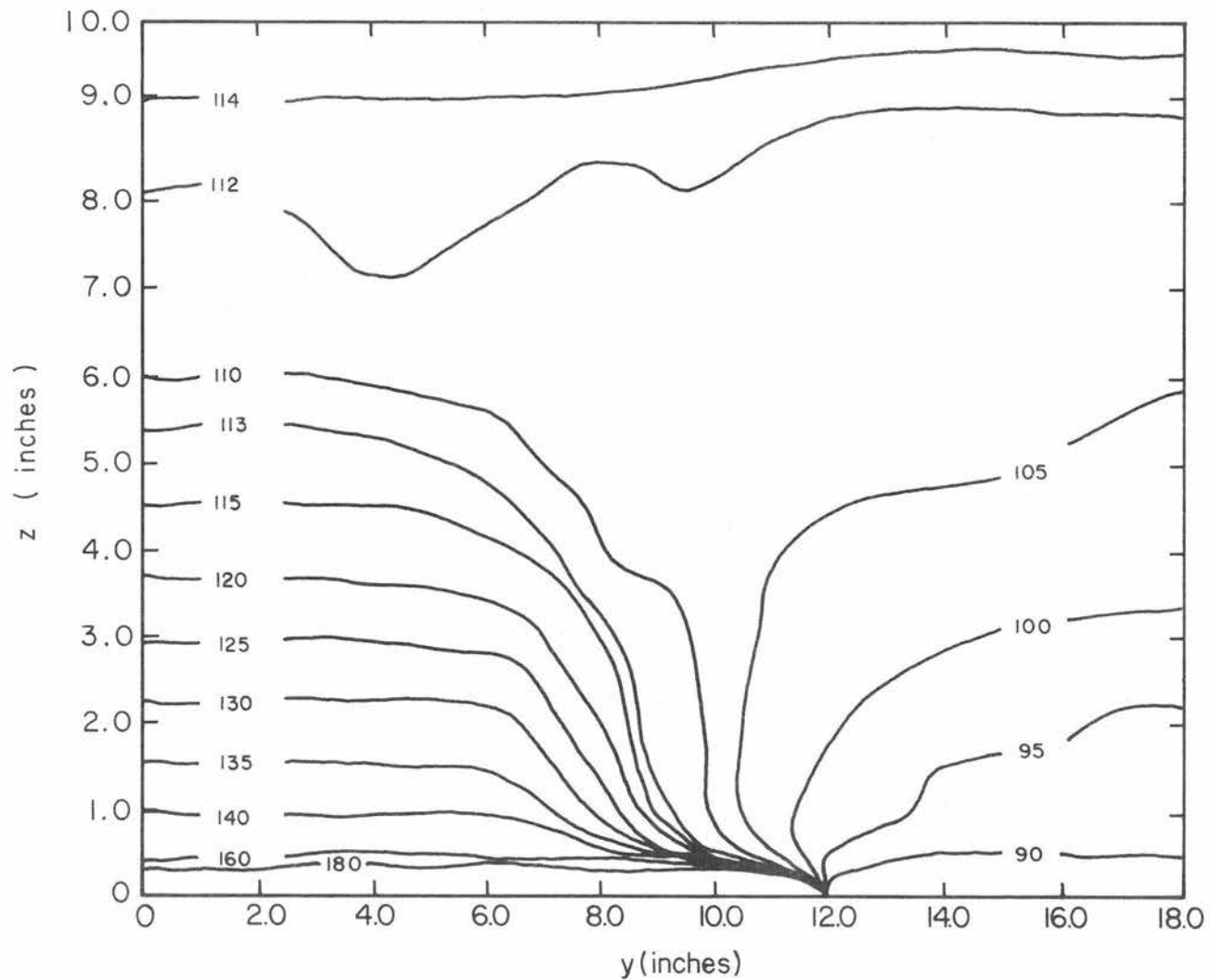


Fig. 5.34 Mean temperature contours for elevated inversion flow along the width of an unstable rough heat island at  $x = 66$  feet (temperatures in Degree F)

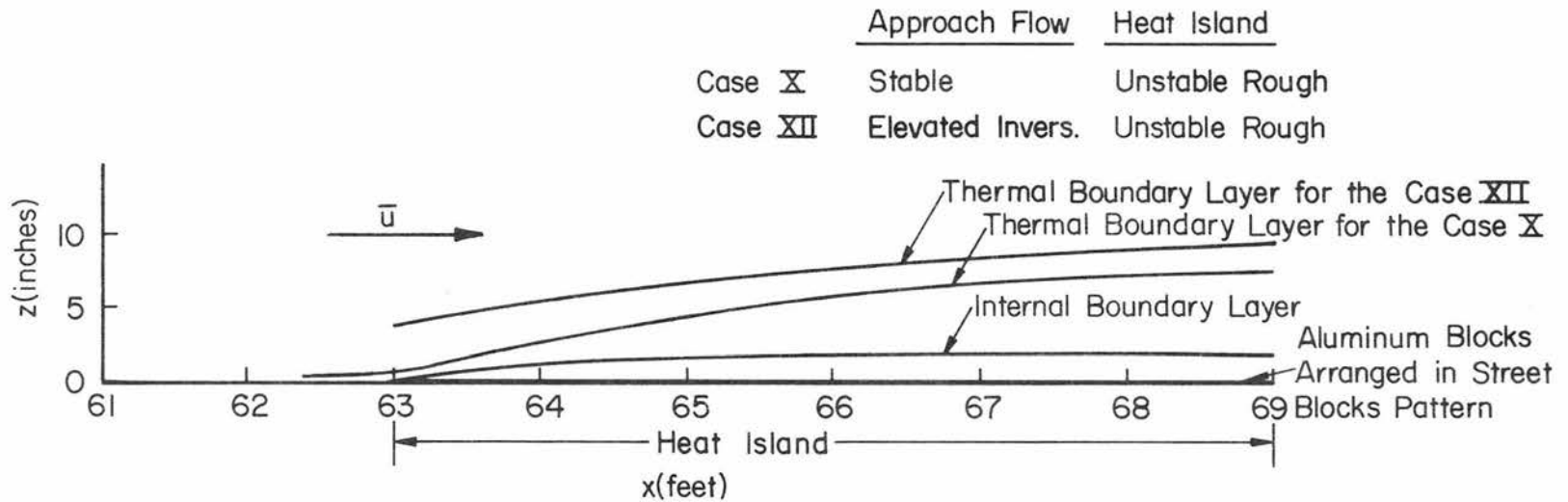


Fig. 5.35 Development of thermal and internal boundary layers over the model.

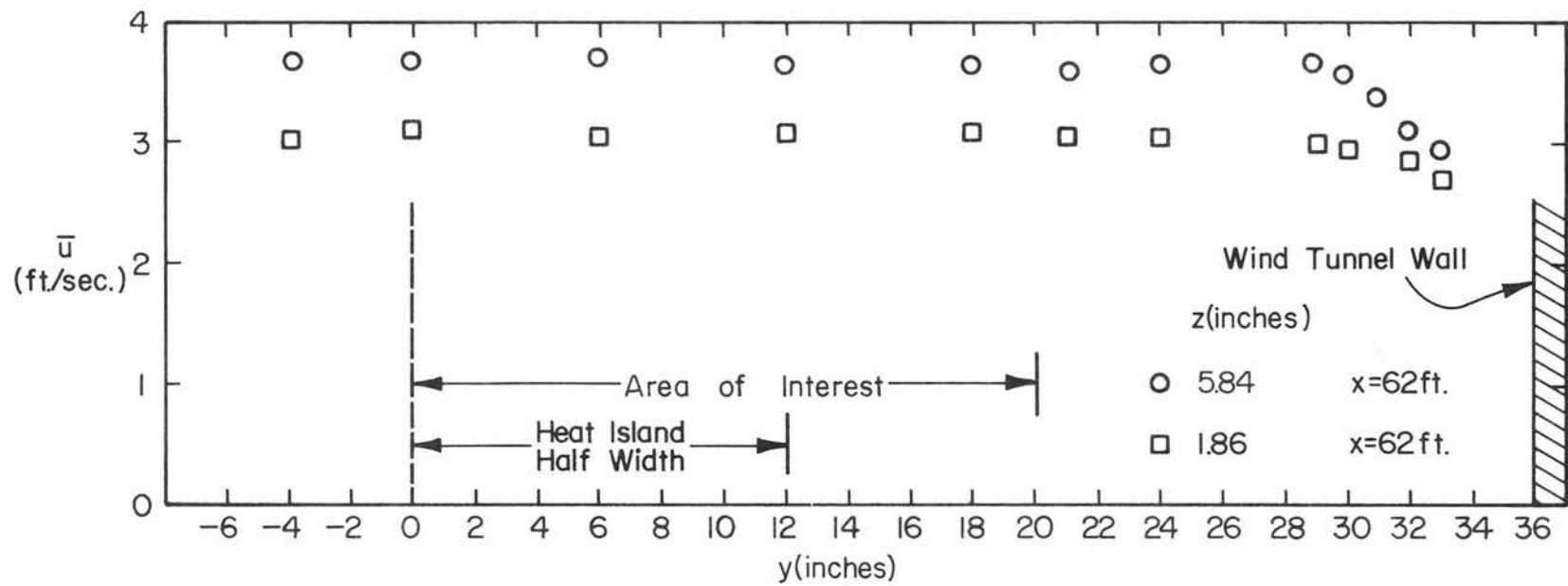


Fig. 5.36 Lateral mean velocity profiles across the wind tunnel with neutral approach flow.

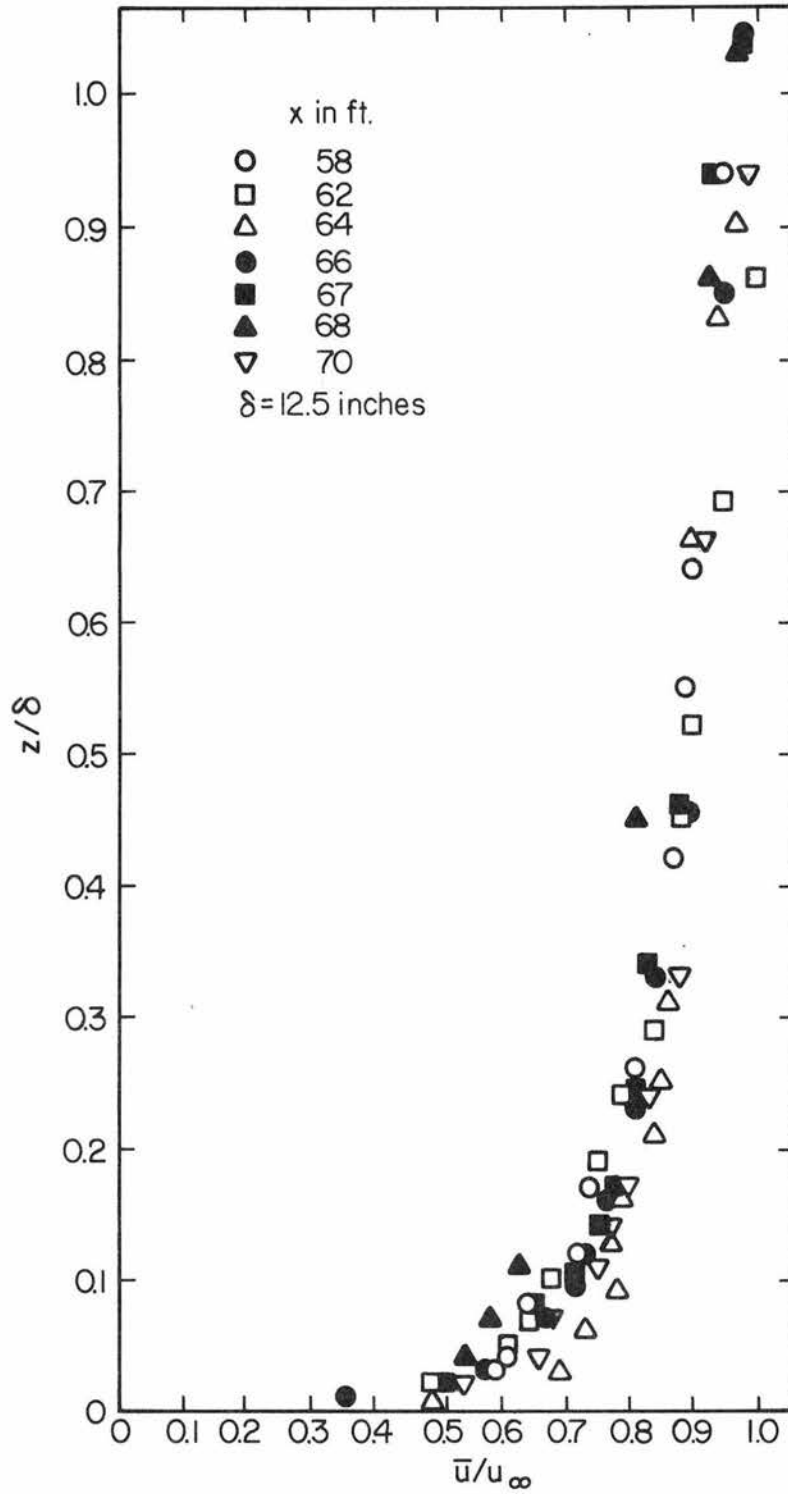


Fig. 5.37 Non-dimensional mean velocity profiles for neutral approach flow over a neutral, smooth heat island along the centerline.

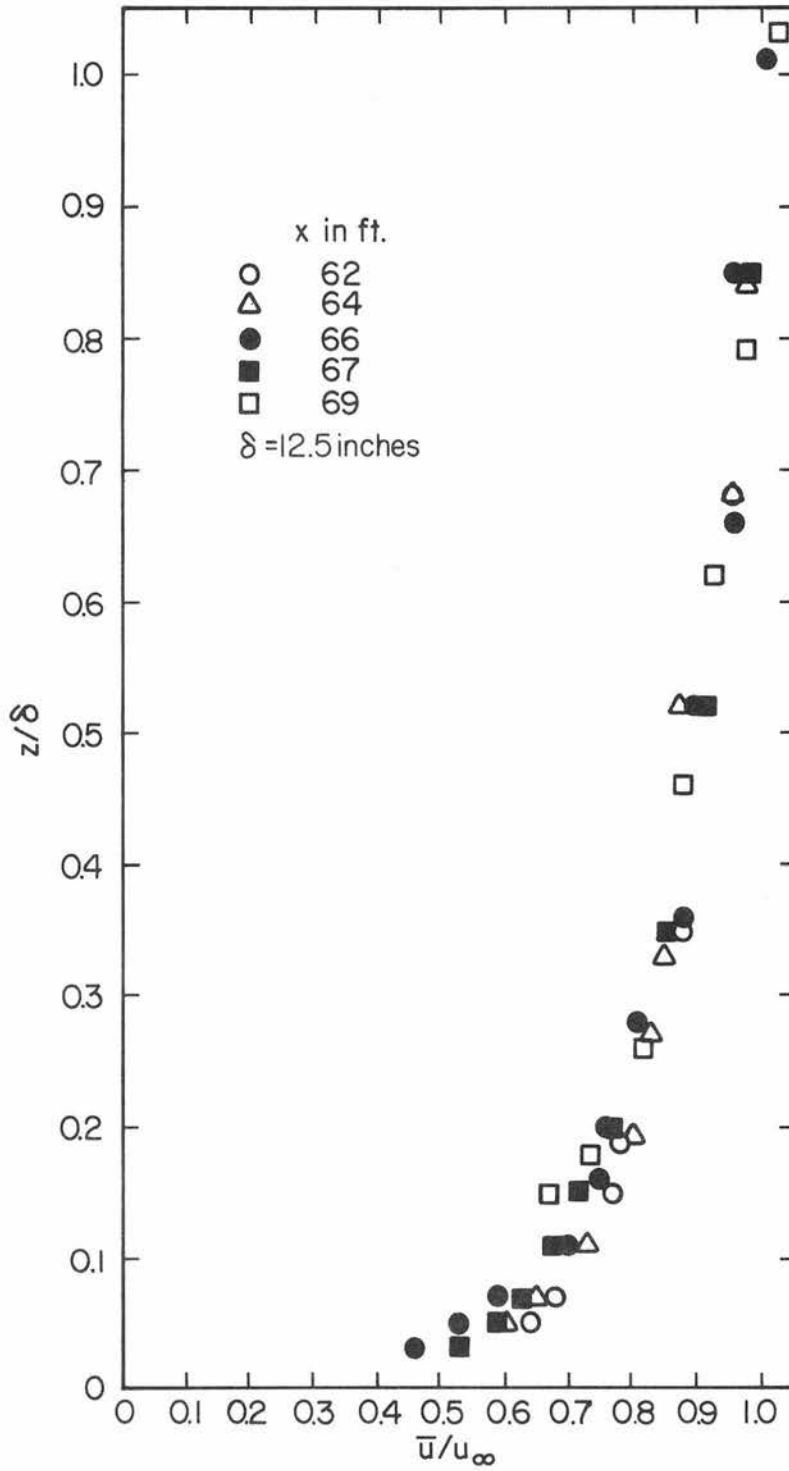


Fig. 5.38 Non-dimensional mean velocity profiles for neutral approach flow over a neutral, rough heat island along the centerline.

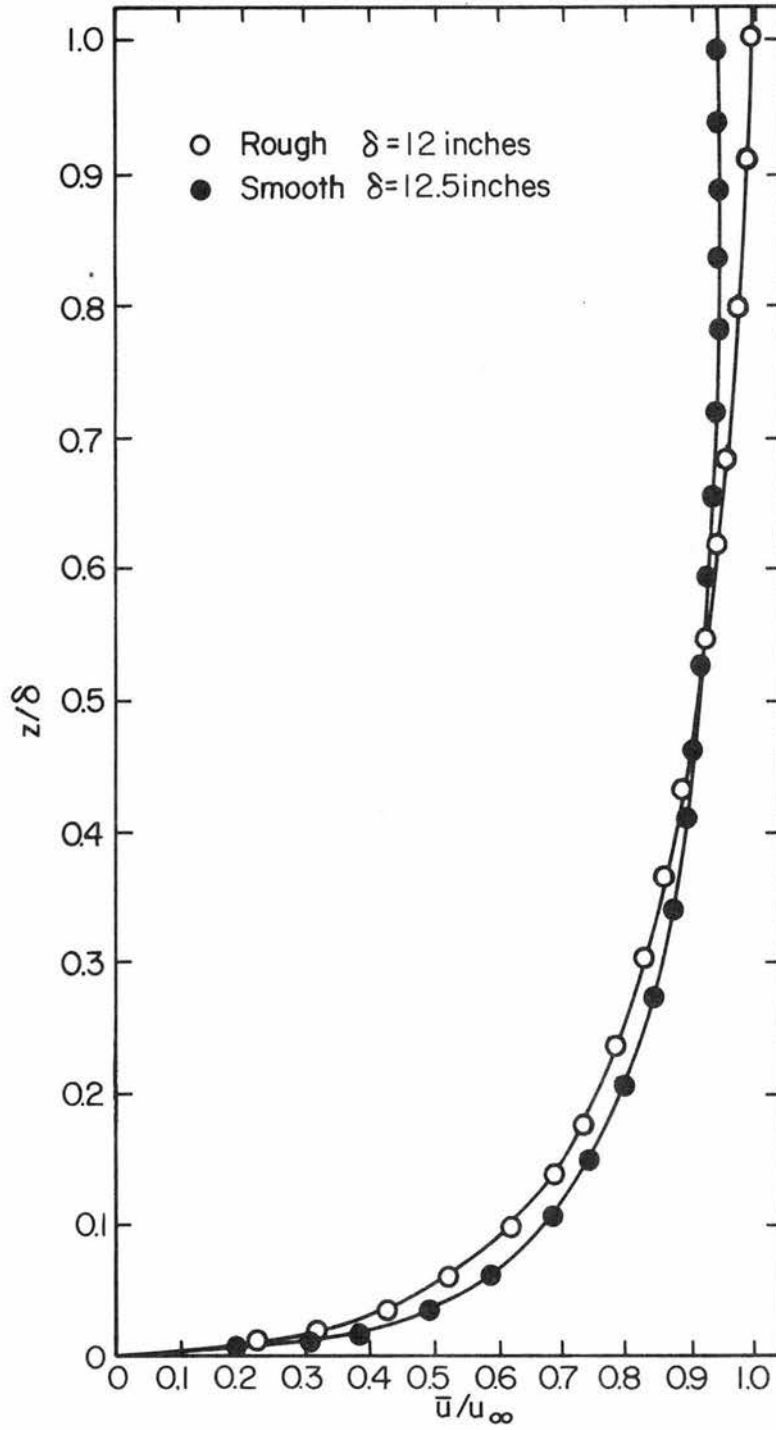


Fig. 5.39 Comparison of non-dimensional velocity profiles for neutral approach flow for smooth and rough heat island along the centerline at  $x = 66$  feet.

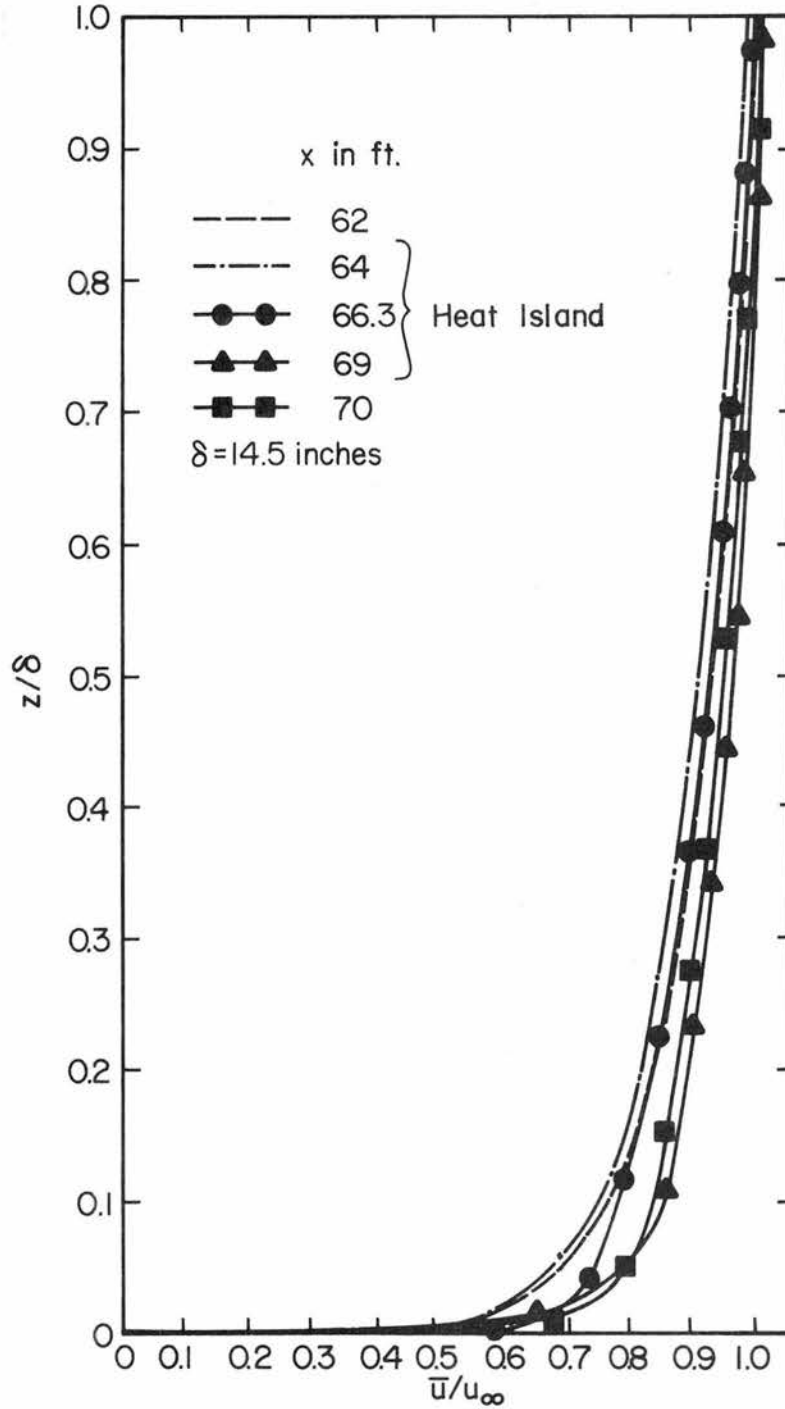


Fig. 5.40 Non-dimensional velocity profiles for neutral flow over an unstable, smooth heat island along the centerline.

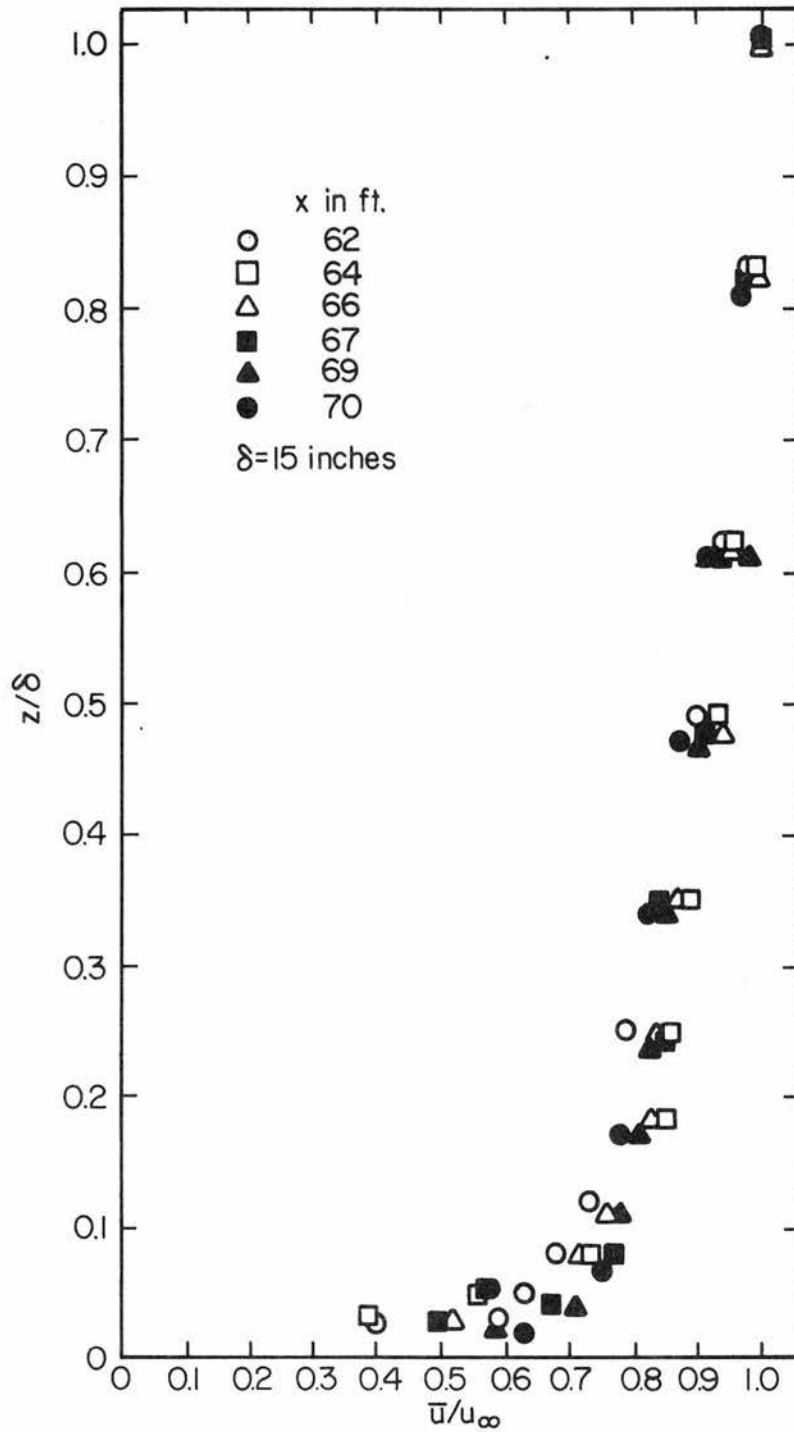


Fig. 5.41 Non-dimensional mean velocity profiles for neutral approach flow over an unstable, rough heat island along the centerline.

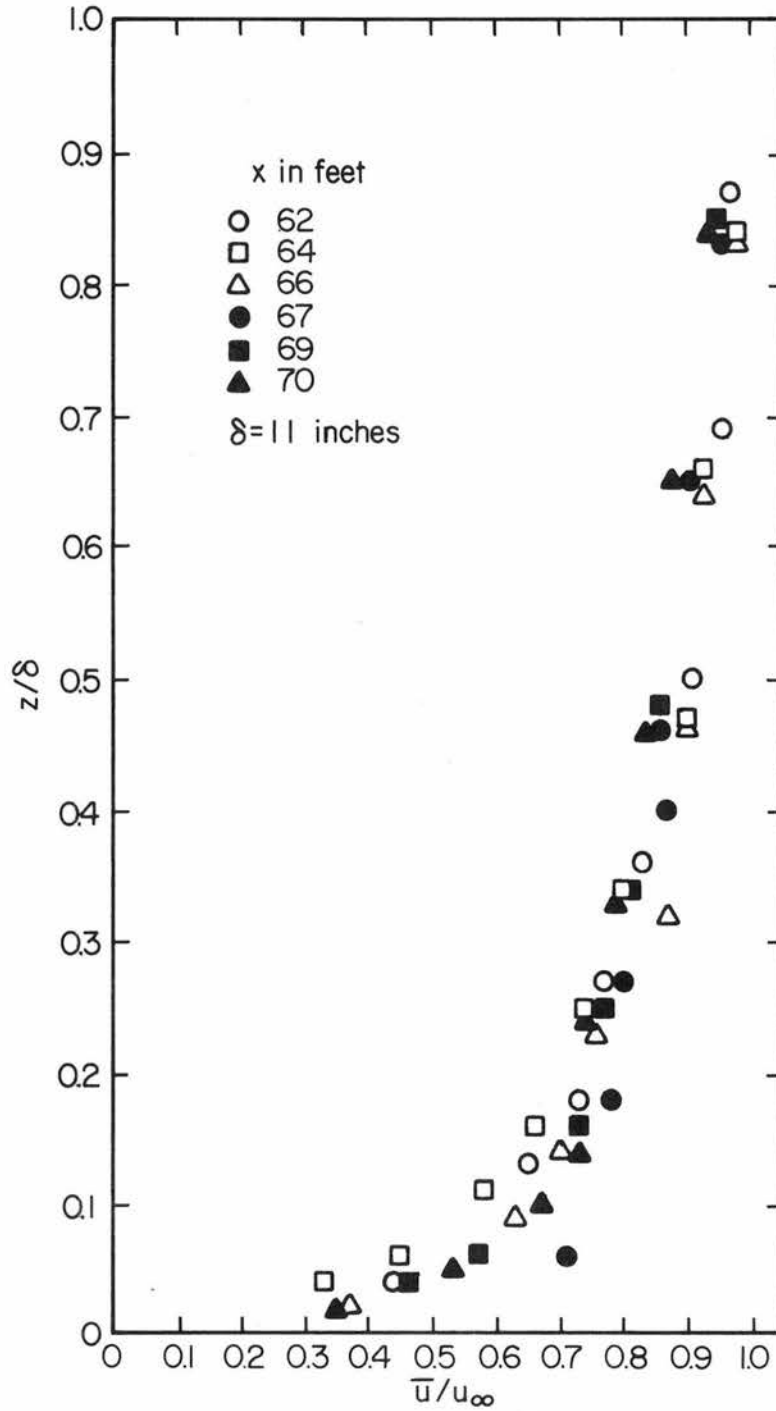


Fig. 5.42 Non-dimensional mean velocity profiles for stable approach flow over a neutral, rough heat island along centerline.

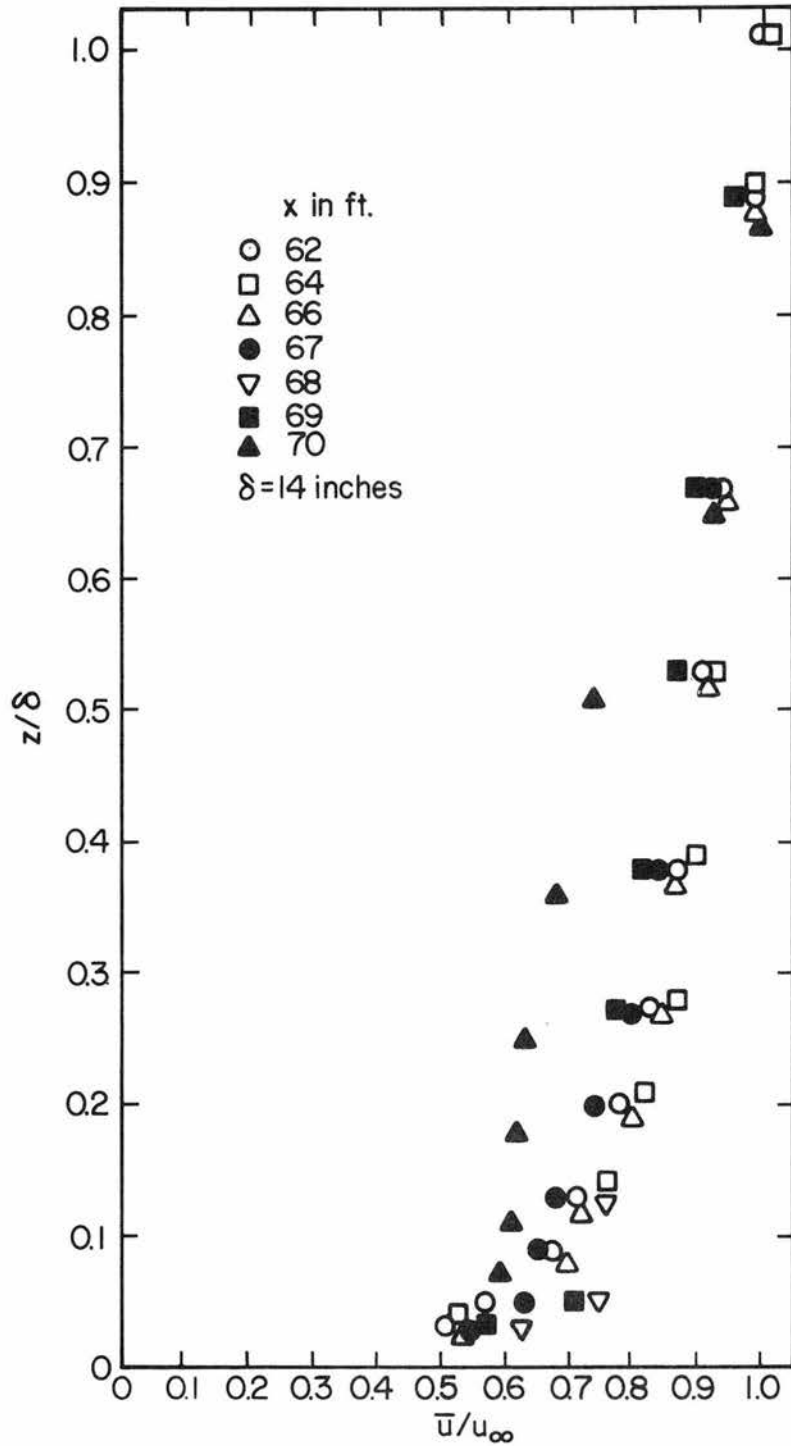


Fig. 5.43 Non-dimensional mean velocity profiles for stable approach flow over an unstable, rough heat island along the centerline.

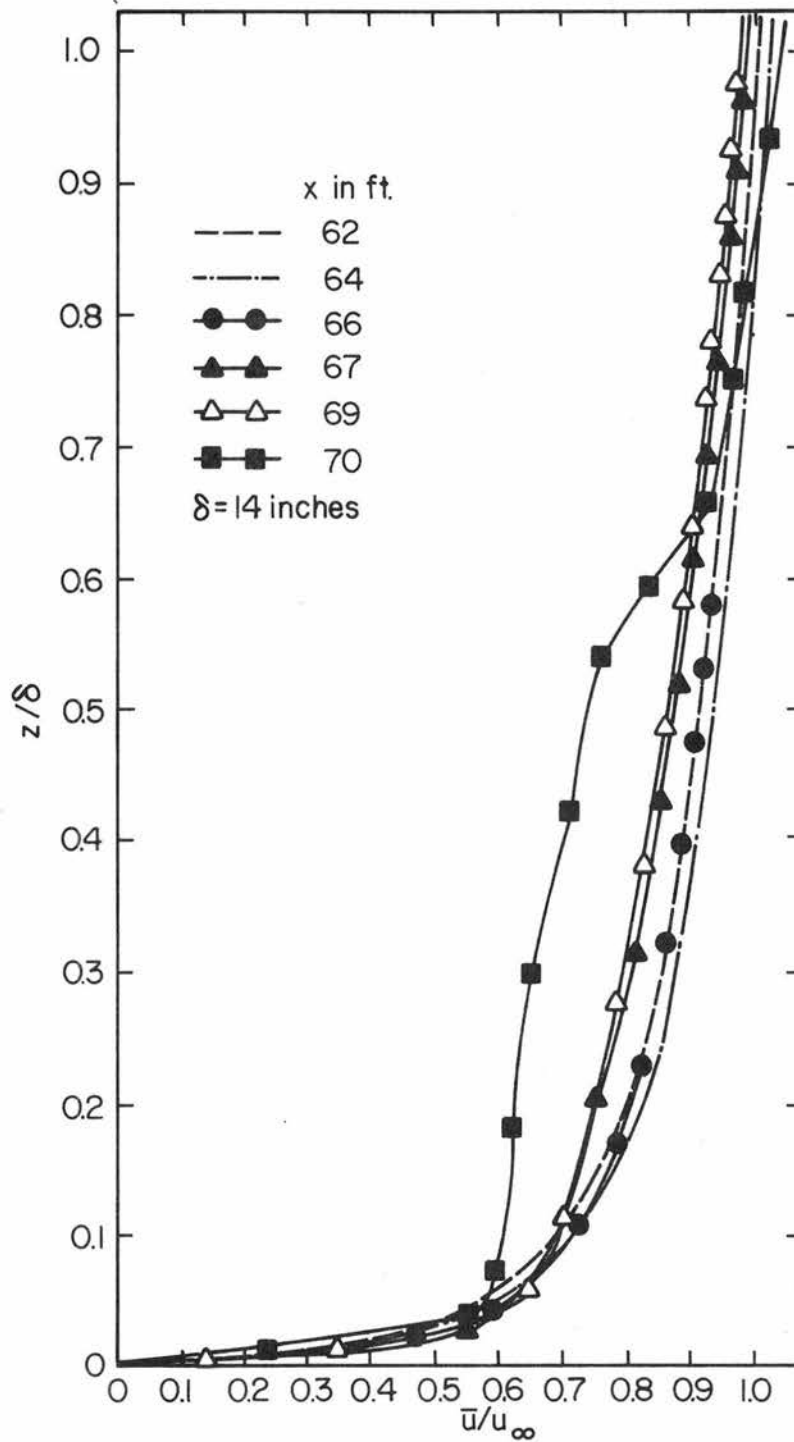


Fig. 5.44 Non-dimensional mean velocity profiles for stable approach flow over an unstable, rough heat island along the centerline.

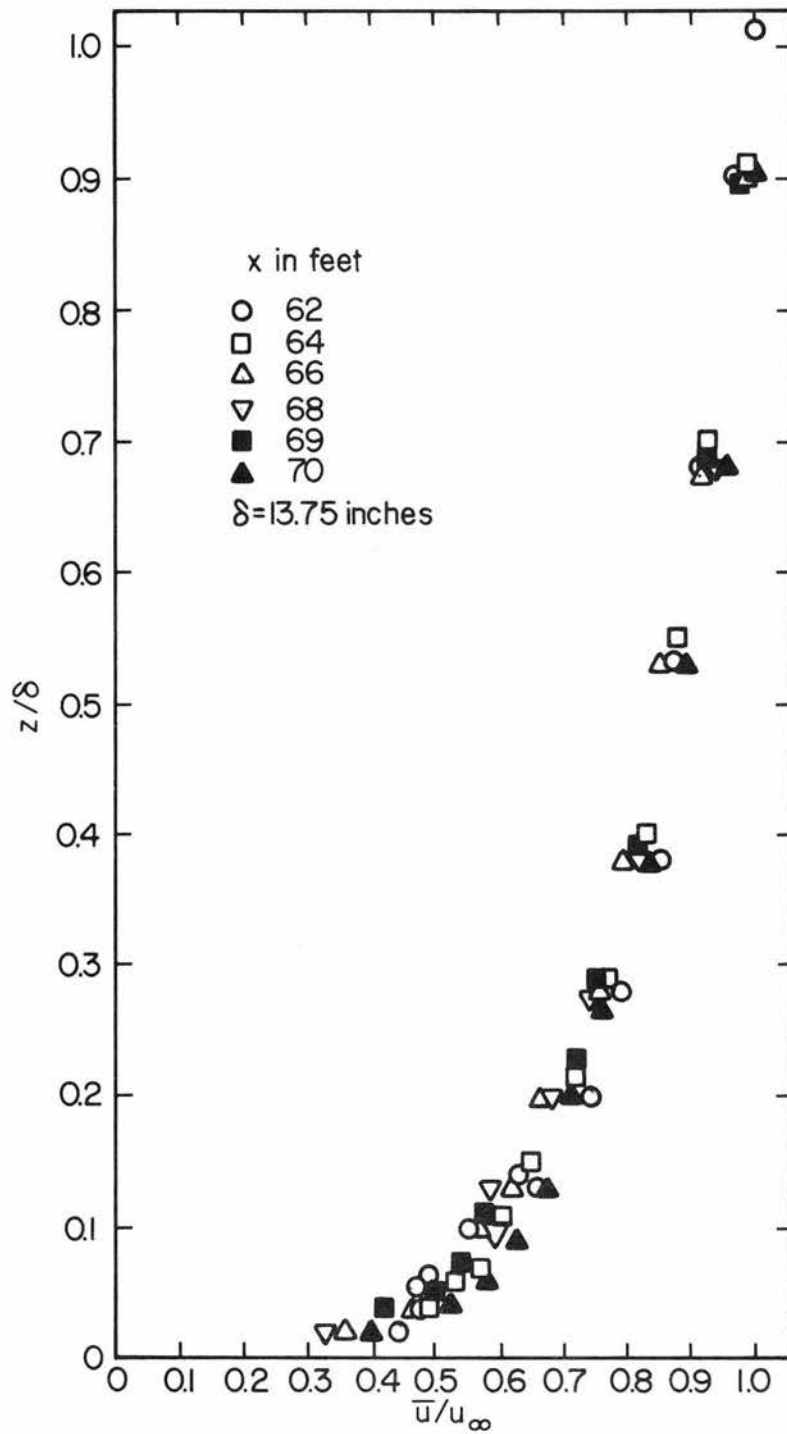


Fig. 5.45 Non-dimensional mean velocity profiles for the approach flow with elevated inversion over a neutral, smooth heat island along the center-line.

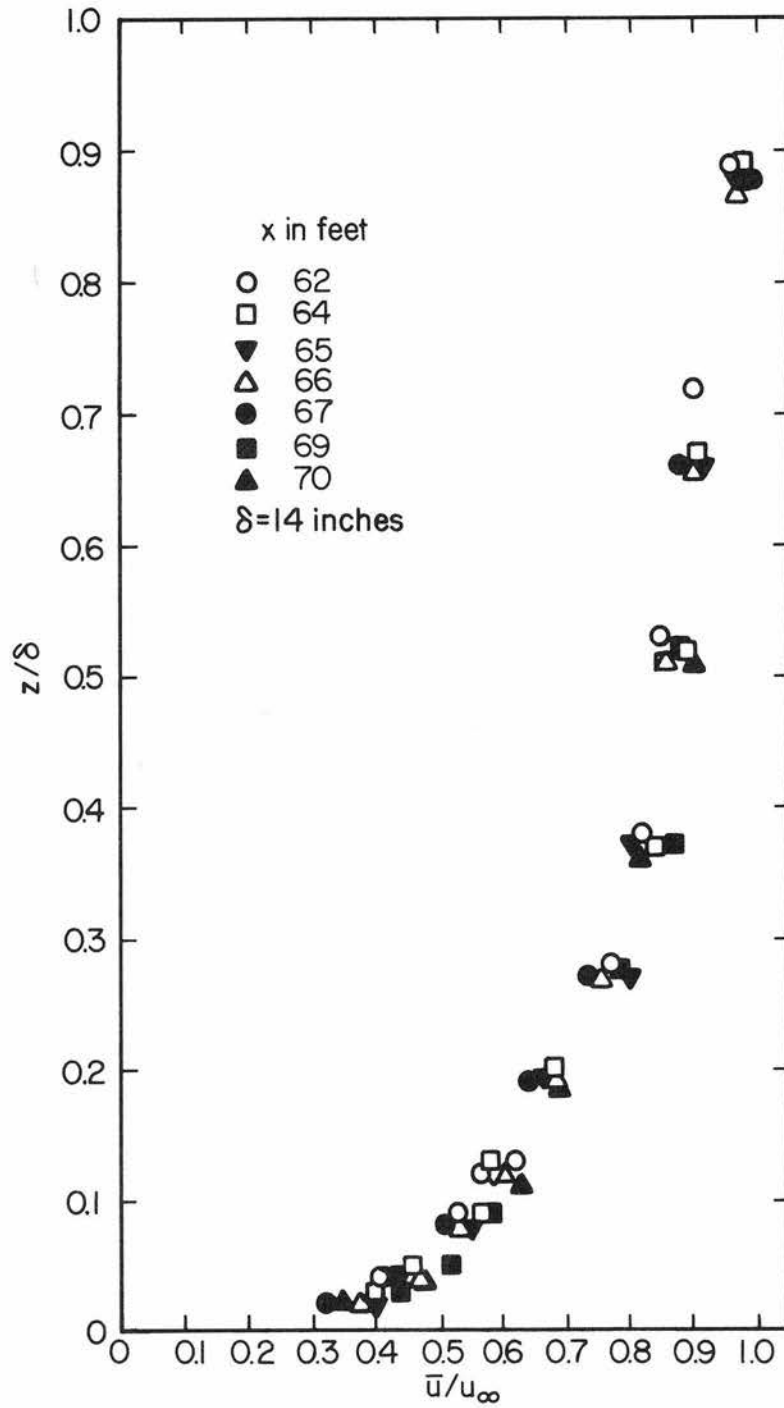


Fig. 5.46 Non-dimensional mean velocity profiles for the approach flow with an elevated inversion over a neutral, rough heat island along the center-line.

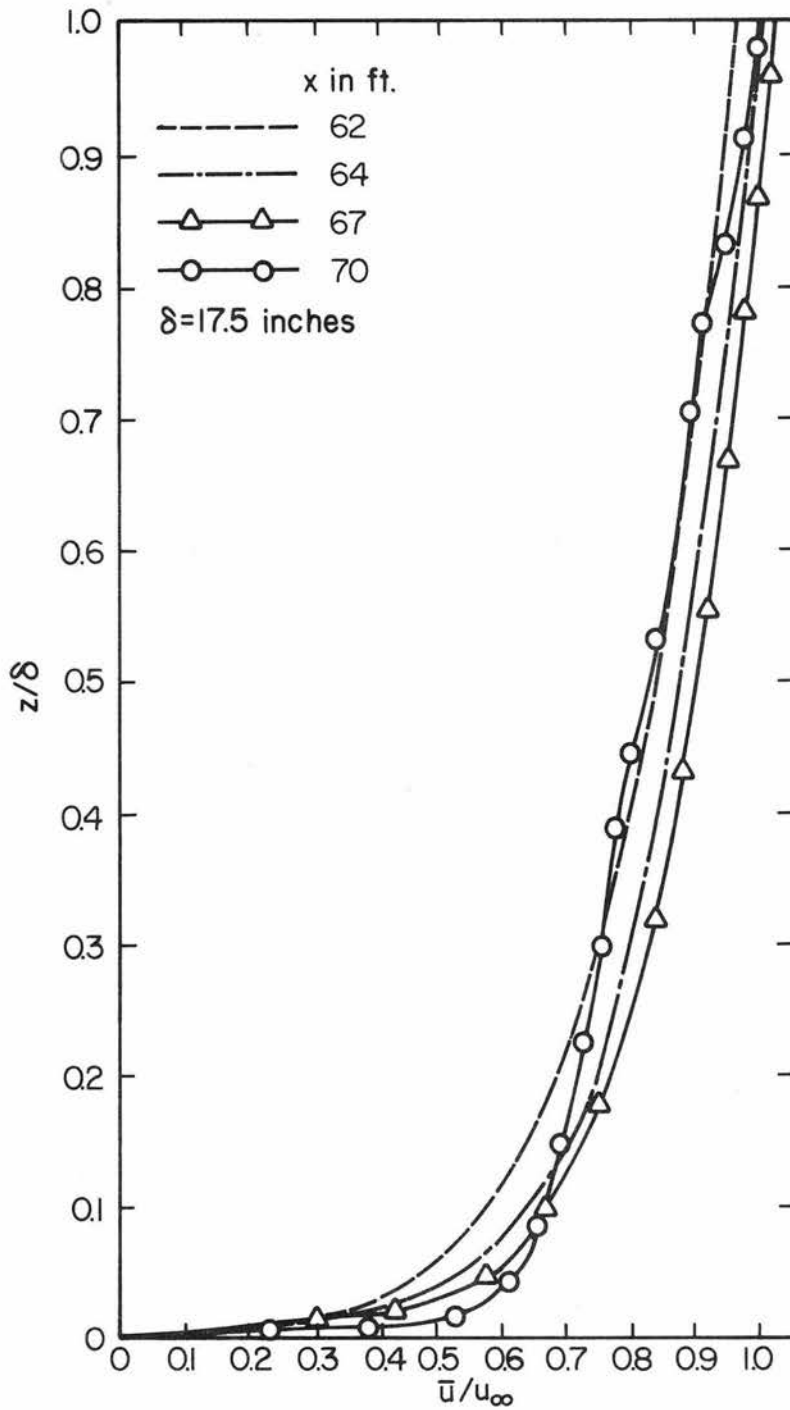


Fig. 5.48 Non-dimensional mean velocity profiles for the elevated inversion approach flow over an unstable, rough heat island along the centerline.

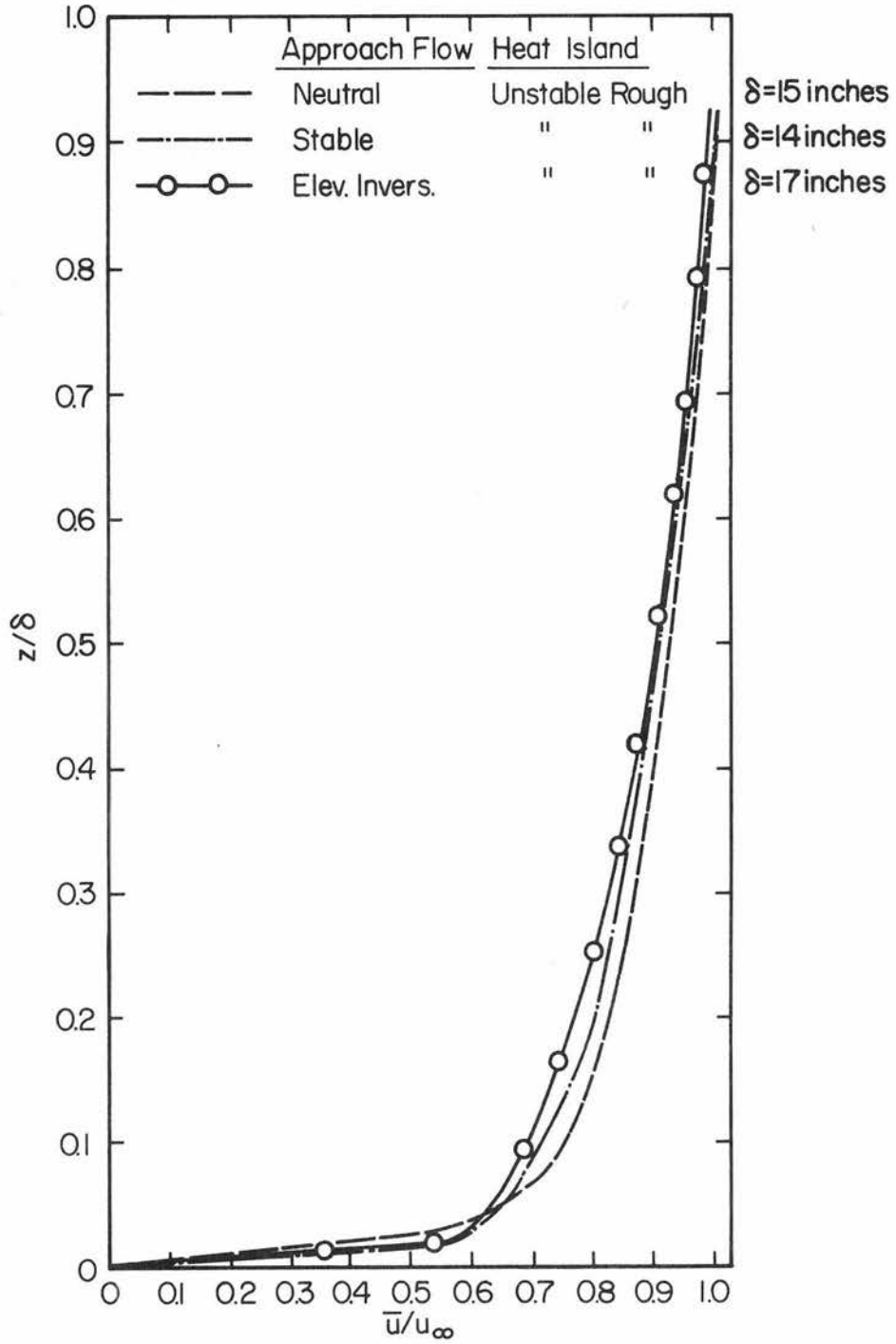


Fig. 5.49 Comparison of non-dimensional mean velocity profiles at  $x = 66$  feet and  $y = 0$  for different approach flows along the center-line.

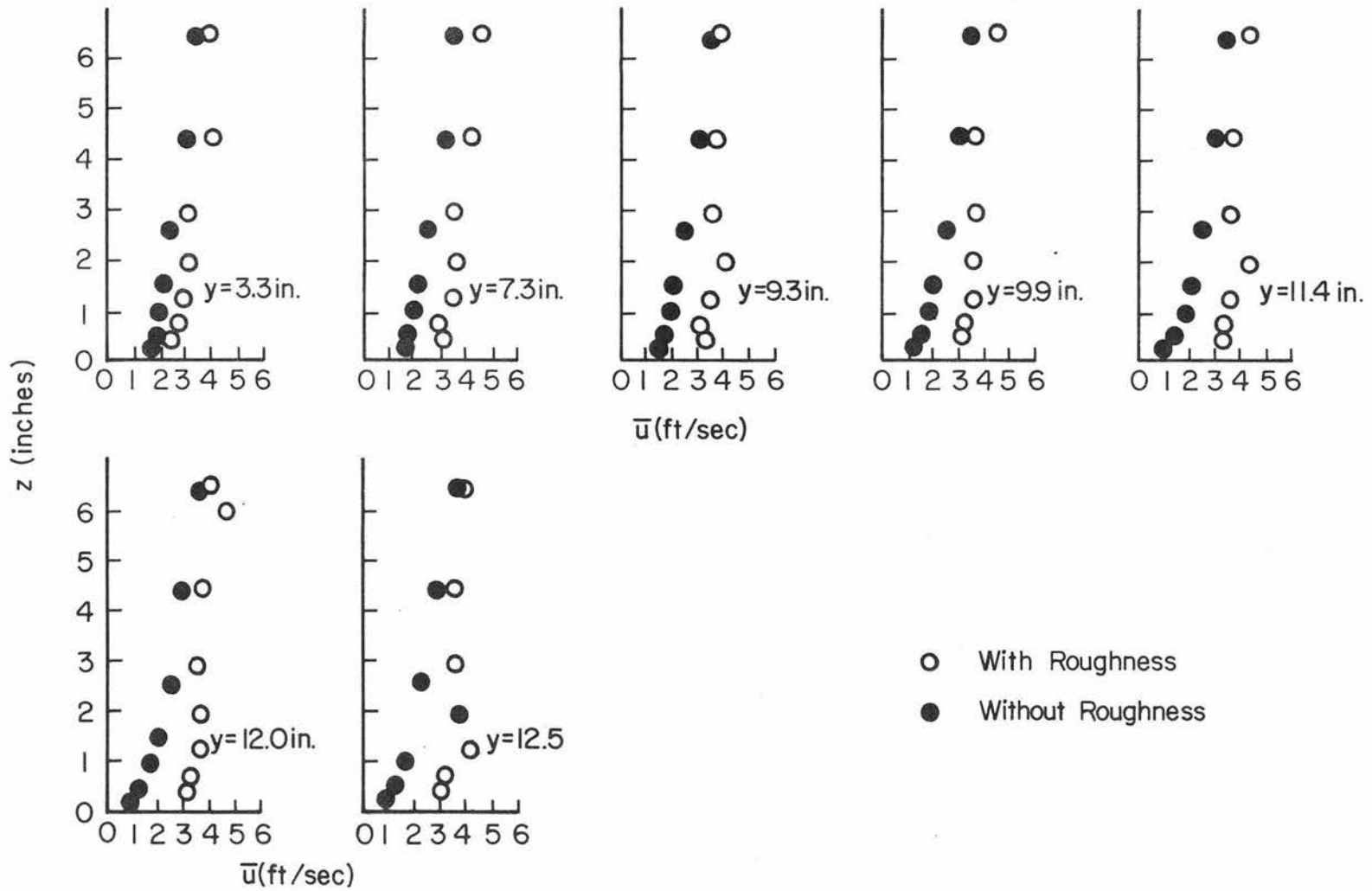


Fig. 5.50 Comparison of mean velocity profiles for stable approach flow over an unstable heat island with and without roughness along the width at  $x = 66$  feet .

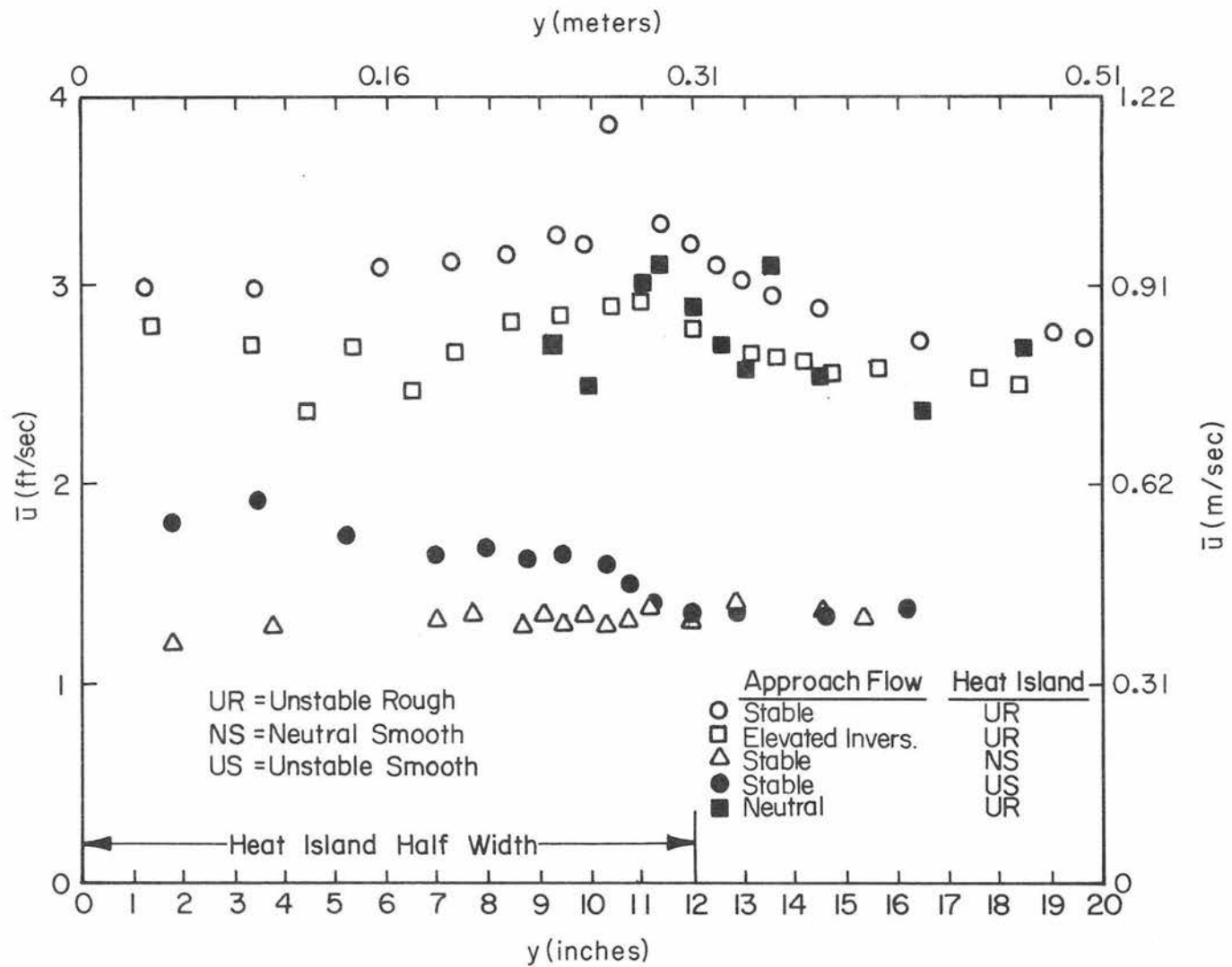


Fig. 5.51 Mean velocity distribution along the width for different cases.

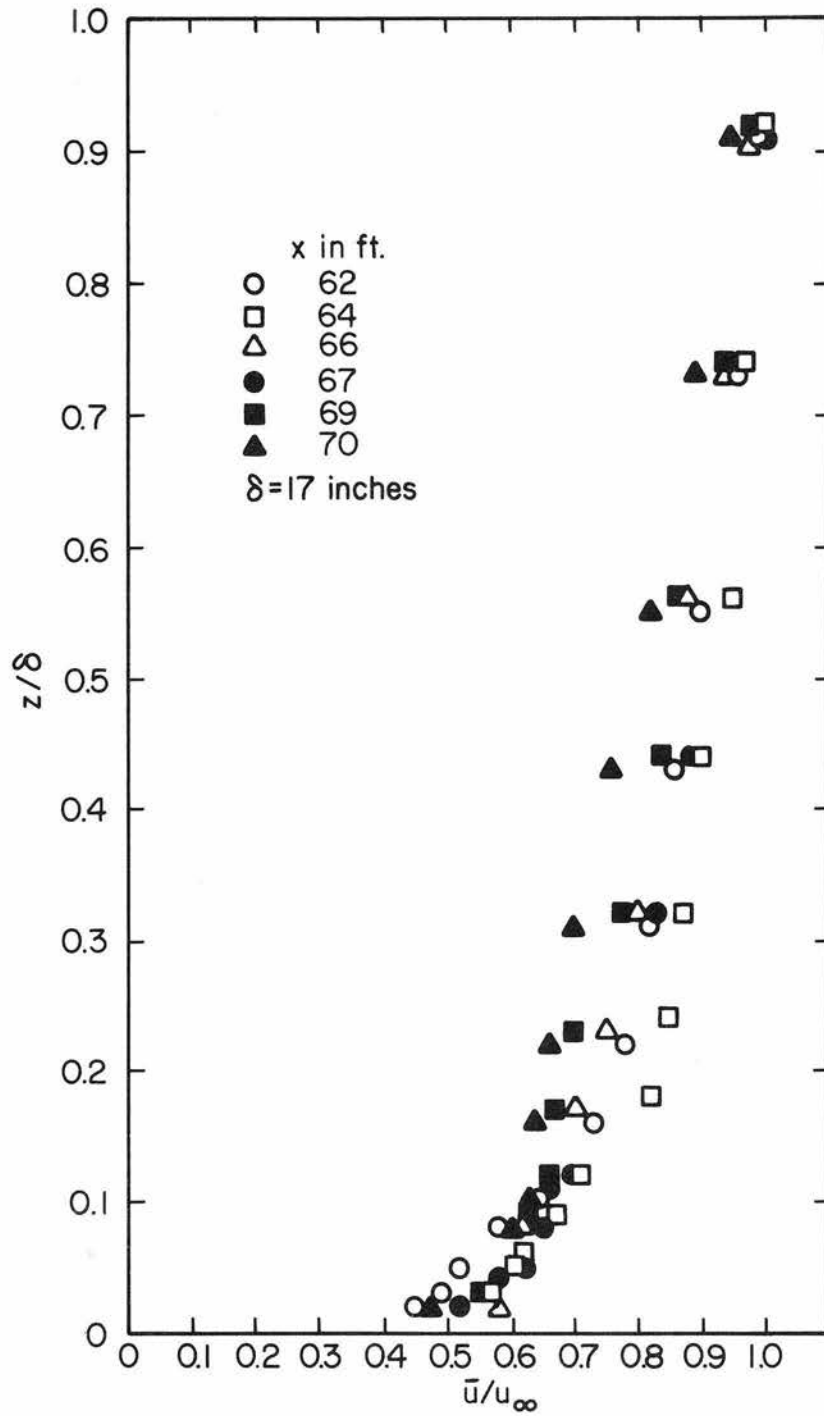


Fig. 5.47 Non-dimensional mean velocity profiles for the approach flow with an elevated inversion over an unstable, smooth heat island along the centerline.

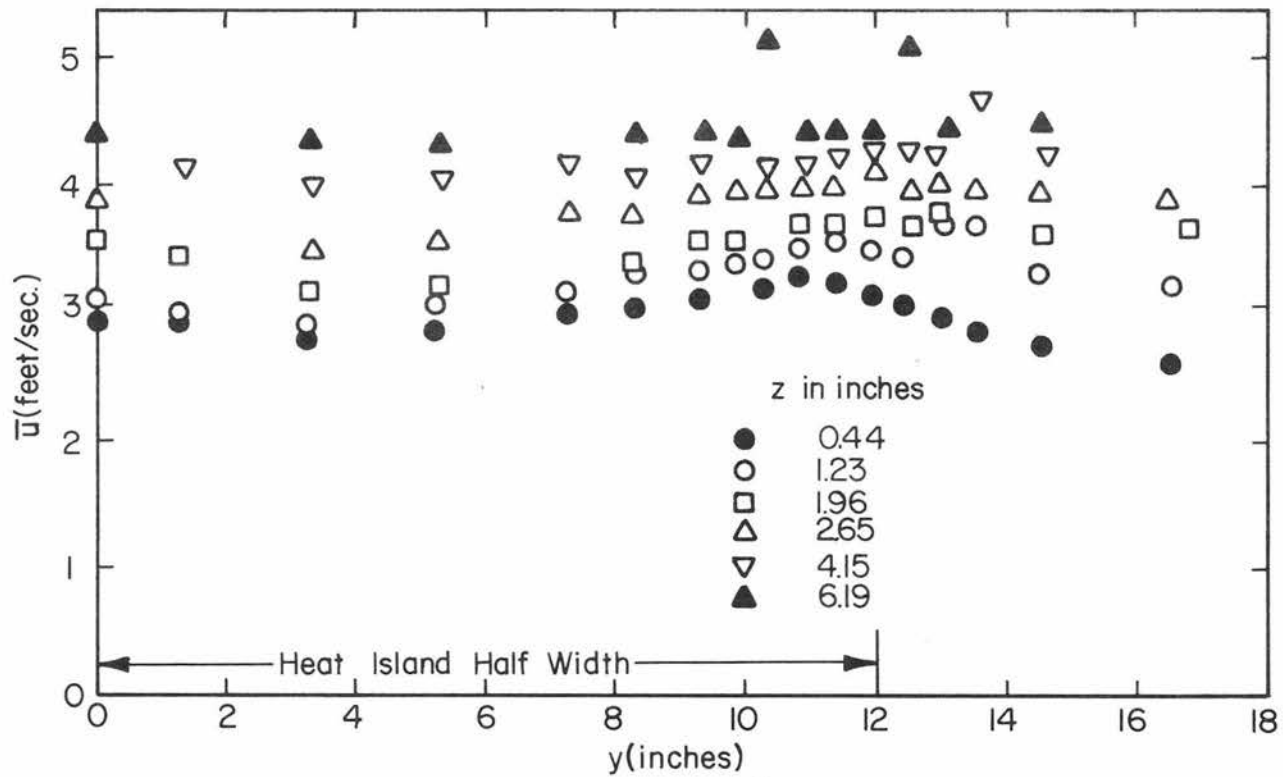


Fig. 5.52 Mean velocity distributions along the width for different heights at  $x = 65$  feet for stable approach flow over an unstable rough heat island.

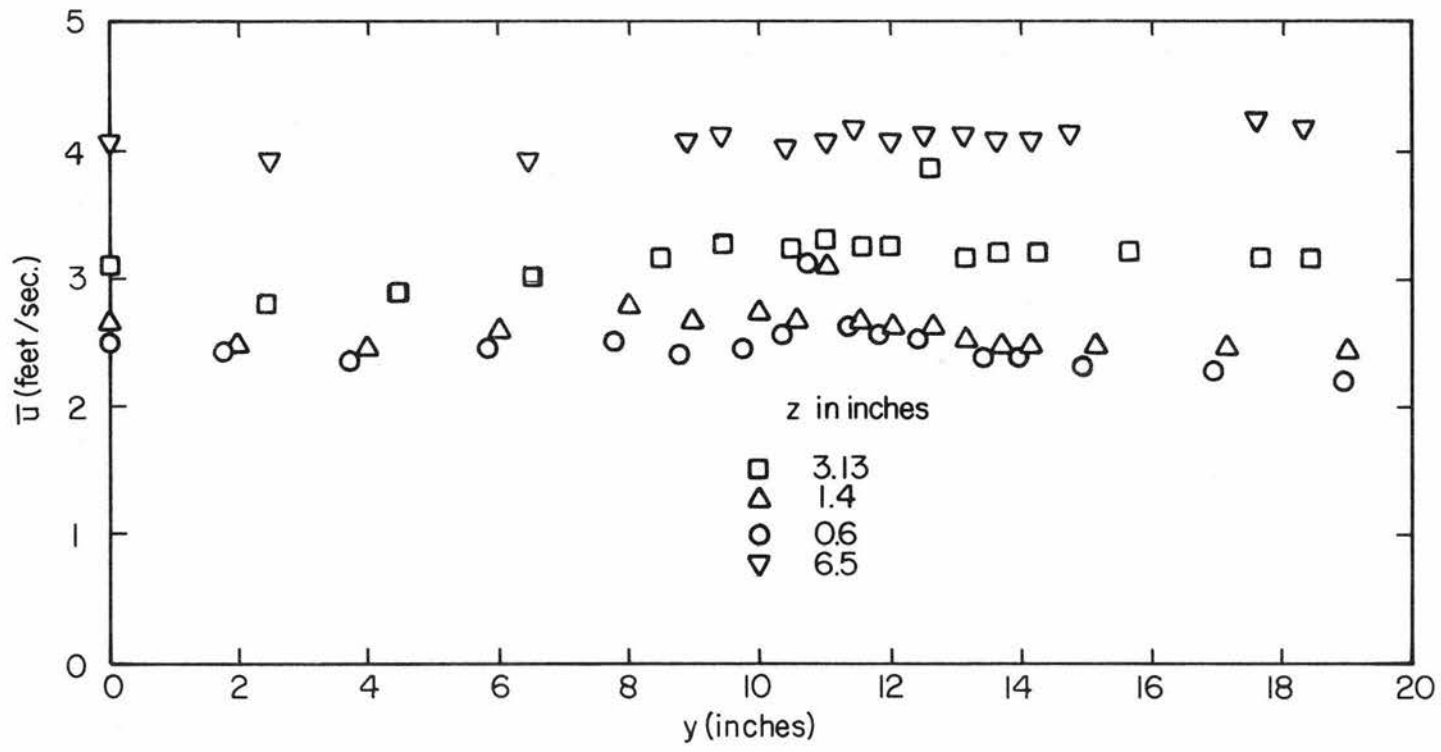


Fig. 5.53 Mean velocity distributions along the width for different heights at  $x = 65$  feet for the approach flow with elevated inversion over an unstable, rough heat island.

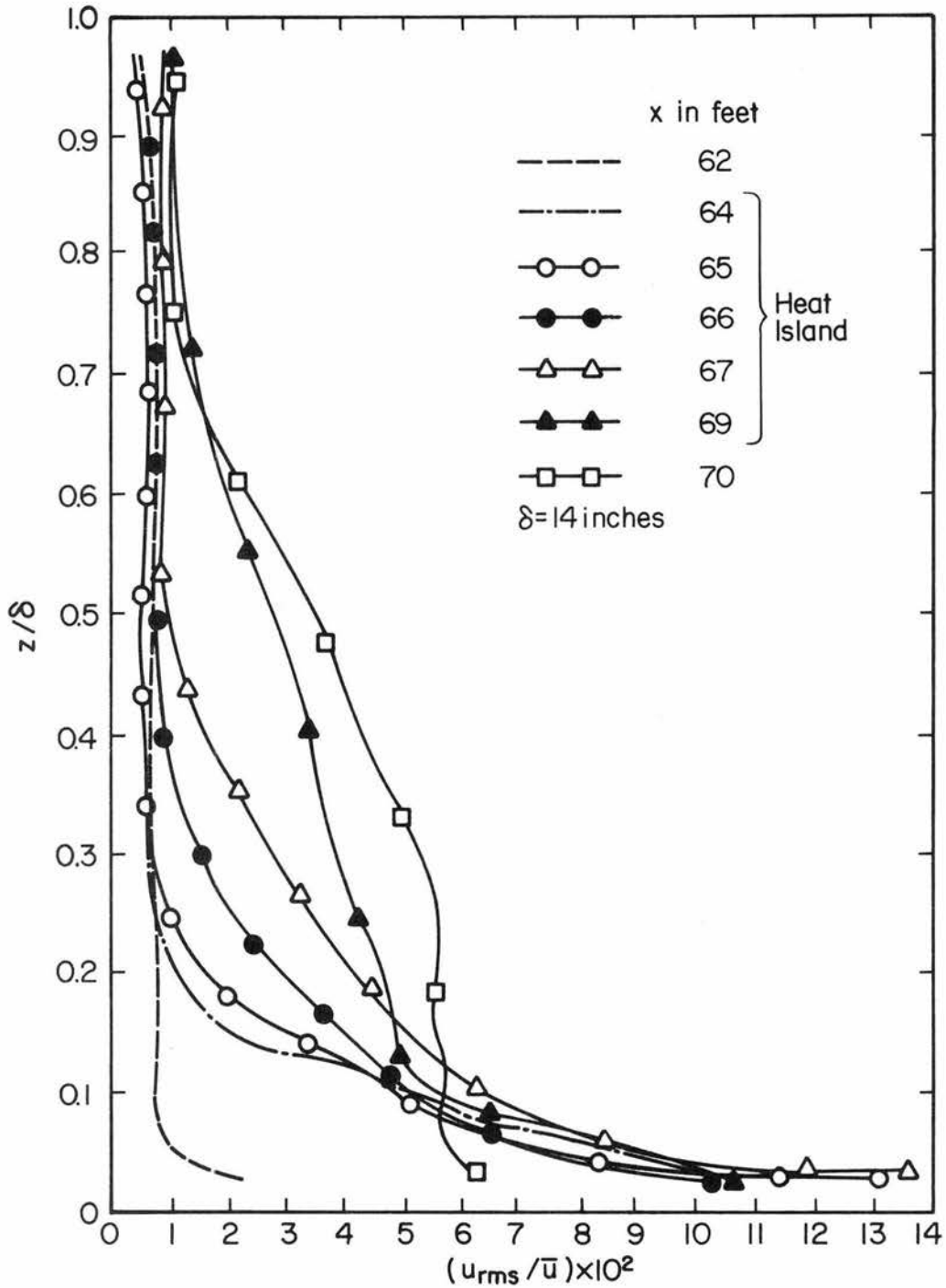


Fig. 5.54 Non-dimensional vertical profiles of longitudinal velocity fluctuations at different distances along the centerline of an unstable rough heat island for stable approach flow.

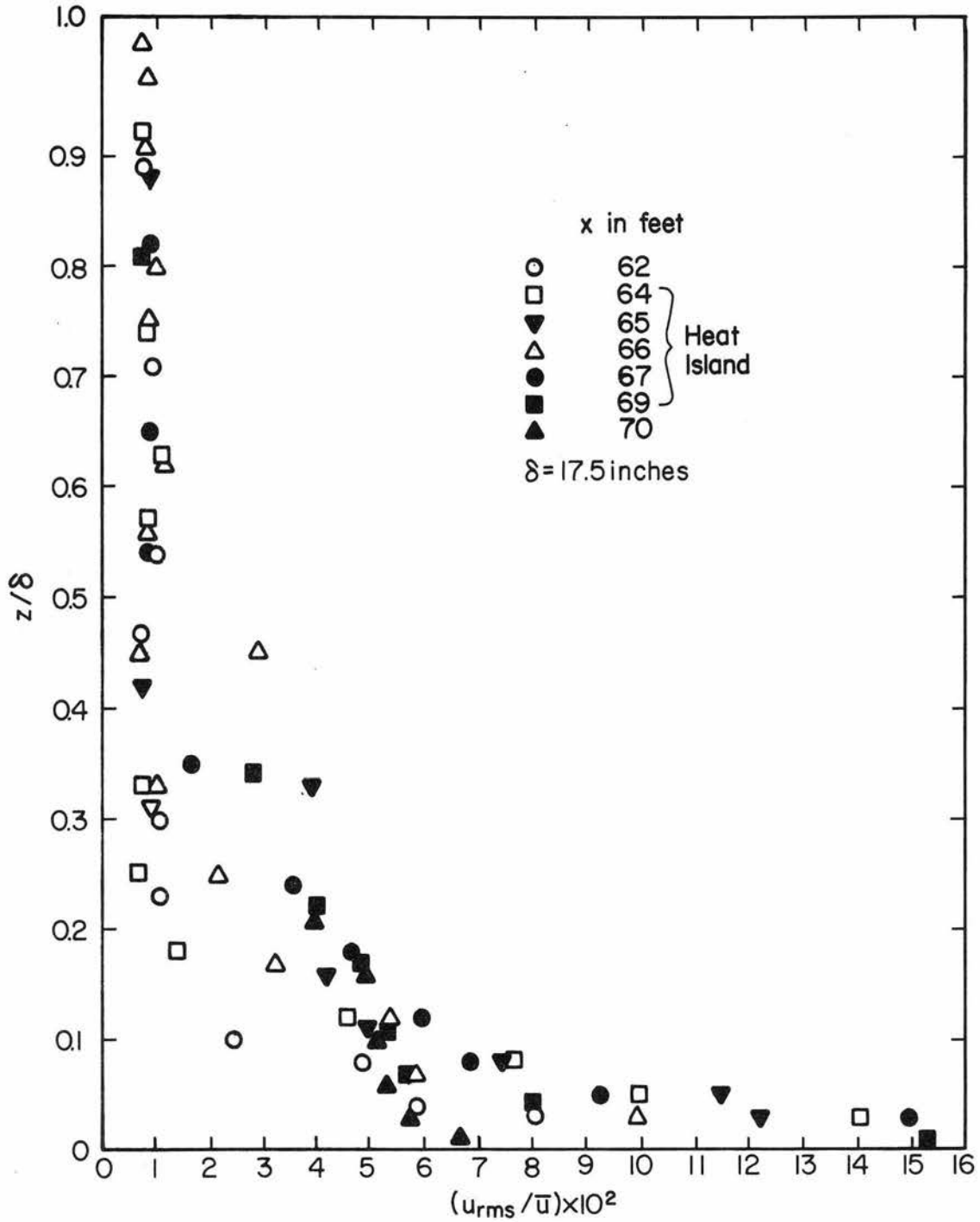


Fig. 5.55 Non-dimensional vertical profiles of longitudinal velocity fluctuations at different distances along the centerline of an unstable, rough heat island for an elevated inversion approach flow.

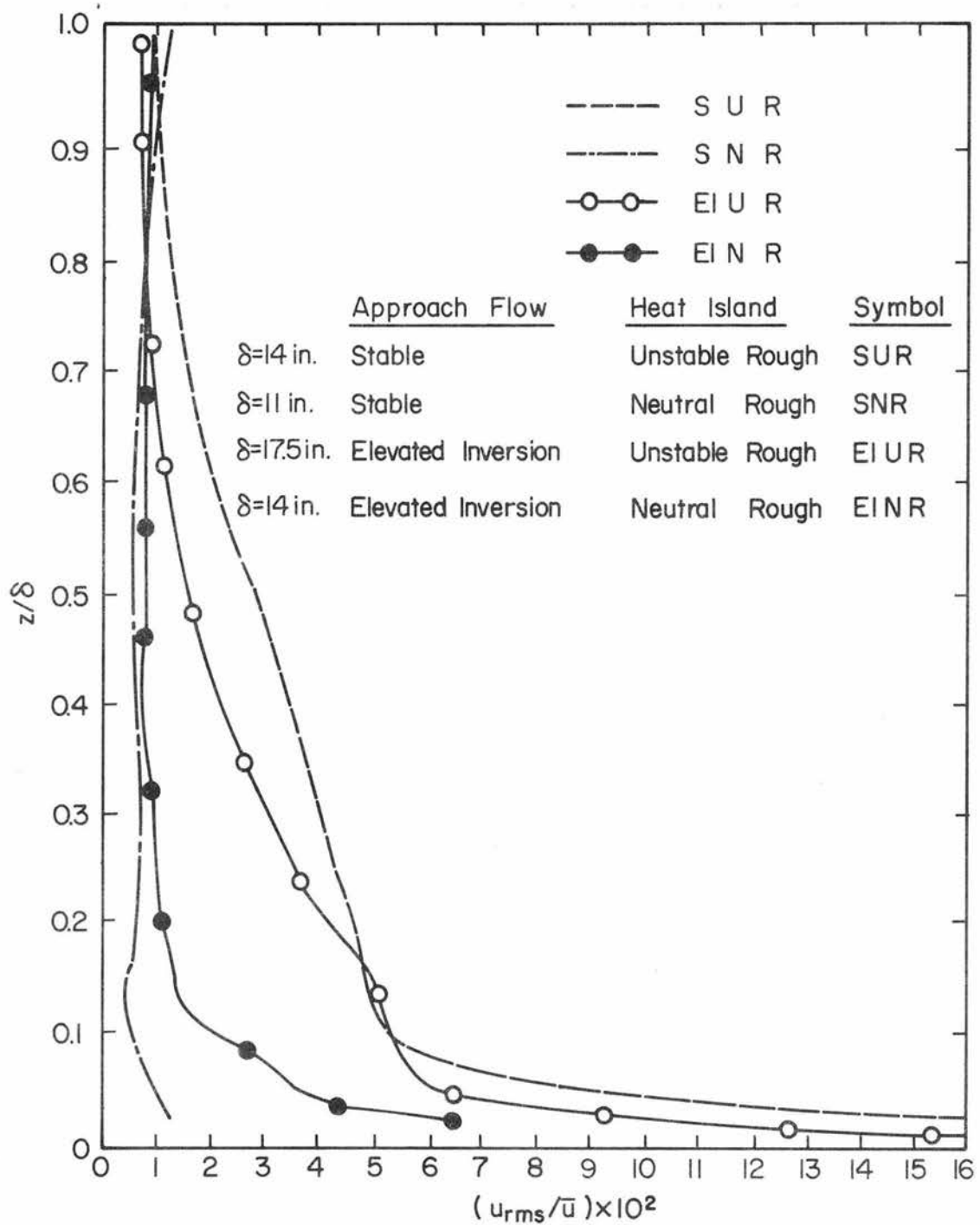


Fig. 5.56 Non-dimensional vertical profiles of longitudinal velocity fluctuations at different distances along the centerline for different cases at  $x = 69$  feet.

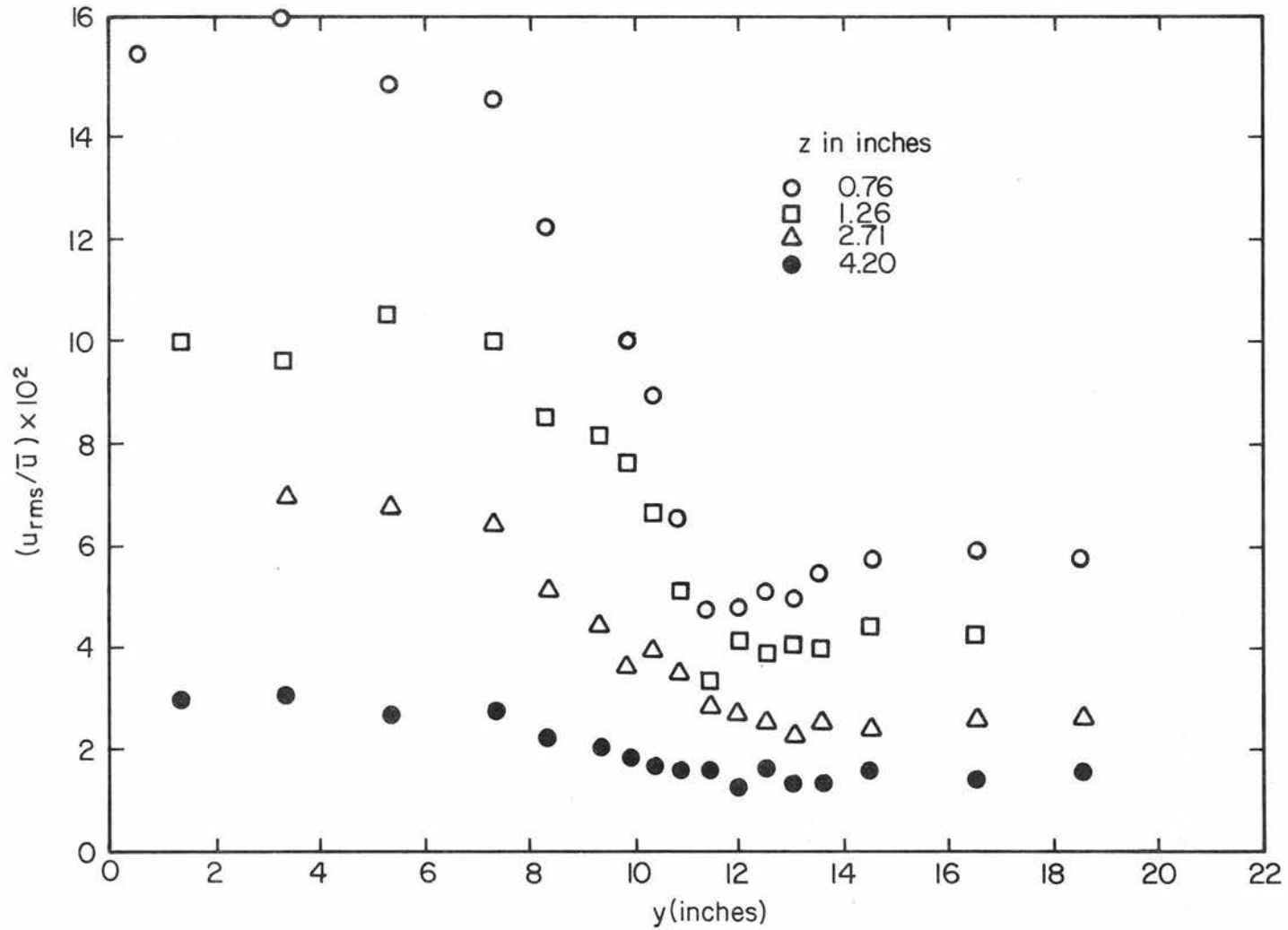


Fig. 5.57 Non-dimensional profiles of longitudinal velocity fluctuations along the width of an unstable, rough heat island for neutral flow at  $x = 66$  feet for different heights.

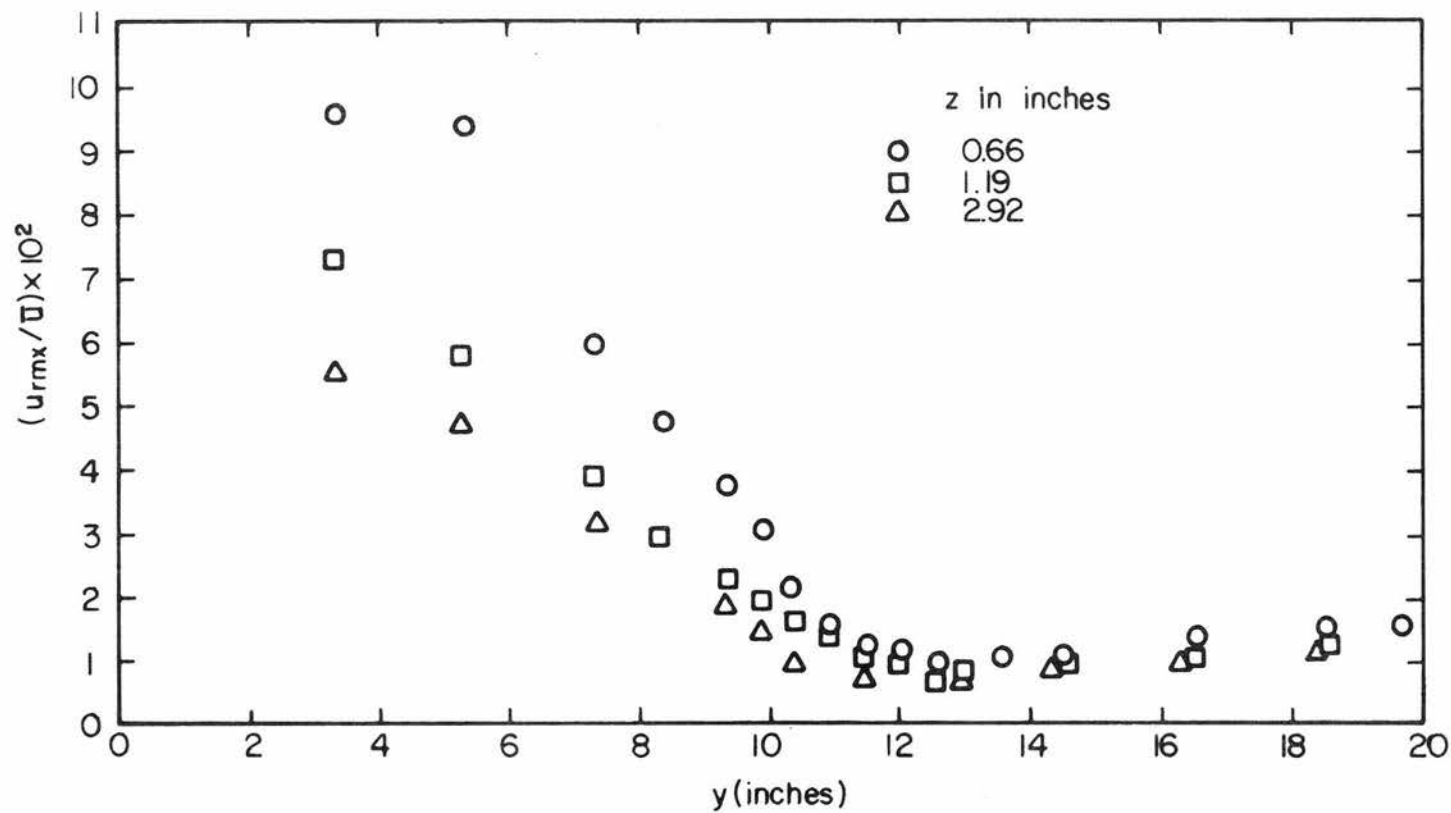


Fig. 5.58 Non-dimensional profiles of longitudinal velocity fluctuations along the width of an unstable, rough heat island for stable approach flow at  $x = 66$  feet for different heights.

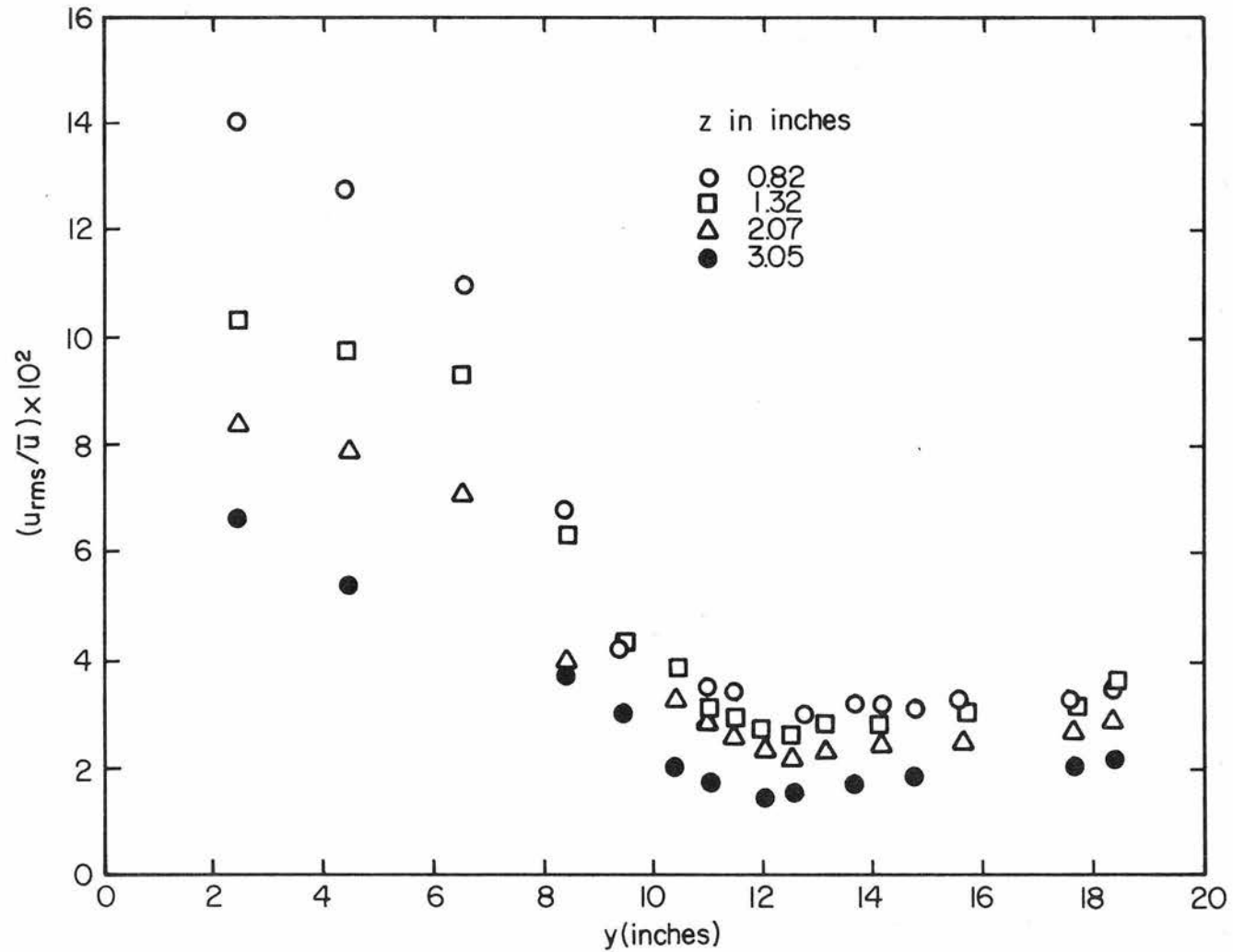


Fig. 5.59 Non-dimensional profiles of longitudinal velocity fluctuations along the width of an unstable rough heat island for elevated inversion approach flow at  $x = 66$  feet for different heights.

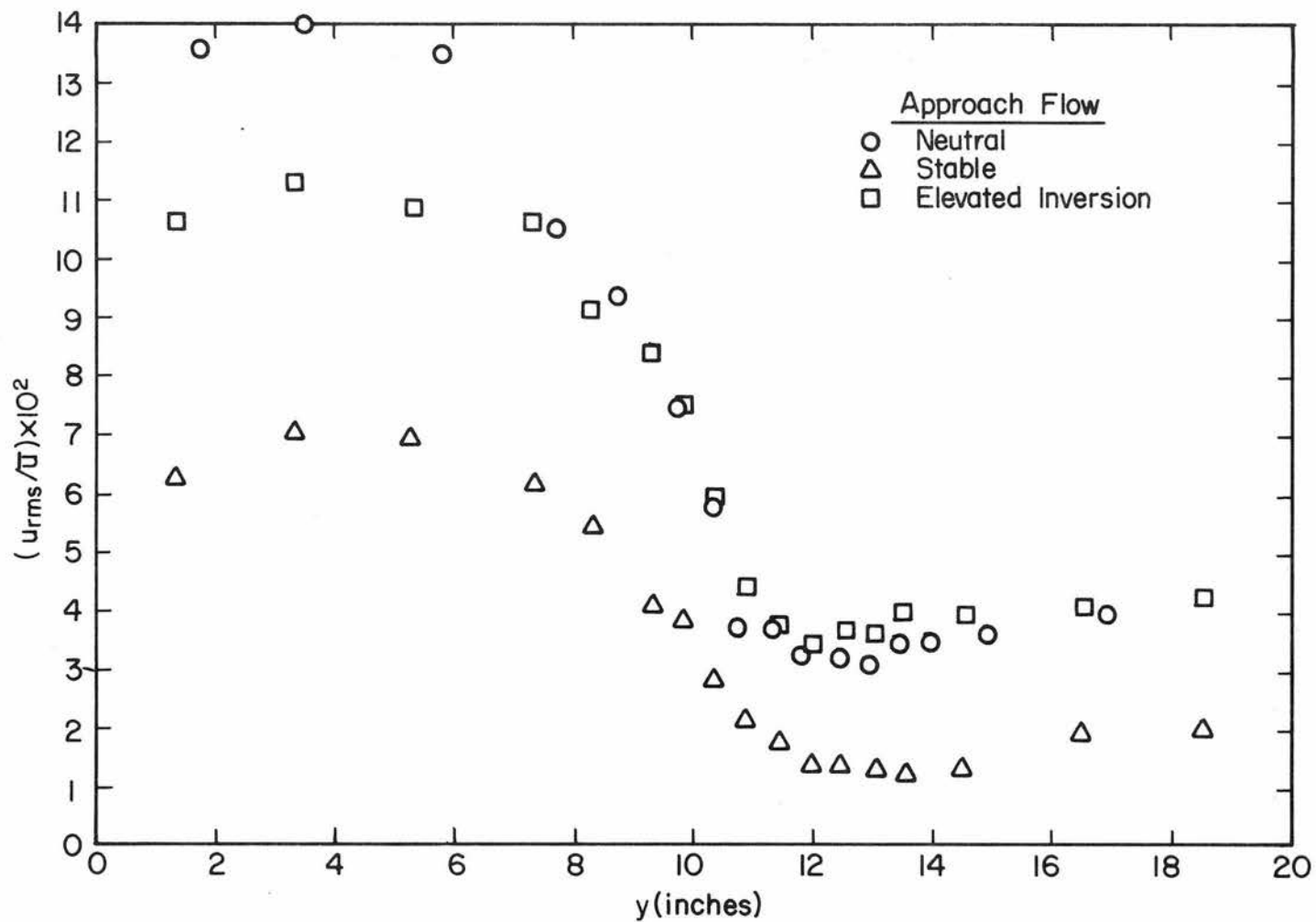


Fig. 5.60 Comparison of non-dimensional longitudinal velocity fluctuations along the width of an unstable rough heat island for different approach flows at  $x = 65$  feet and  $z = 0.6$  inch.

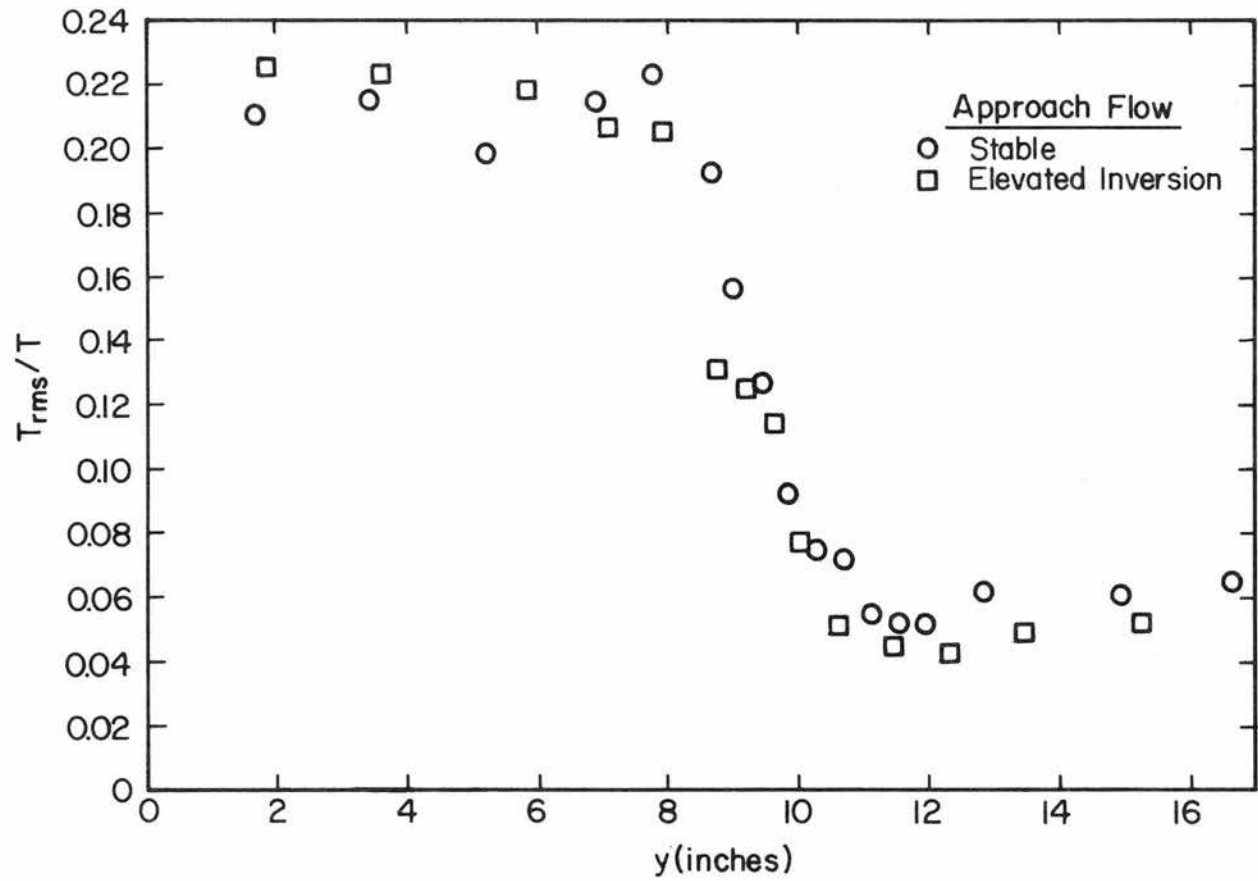


Fig. 5.61 Comparison of non-dimensional temperature fluctuations along the width of an unstable, smooth heat island for different approach flows at  $x = 65$  feet and  $z = 0.4$  inch .

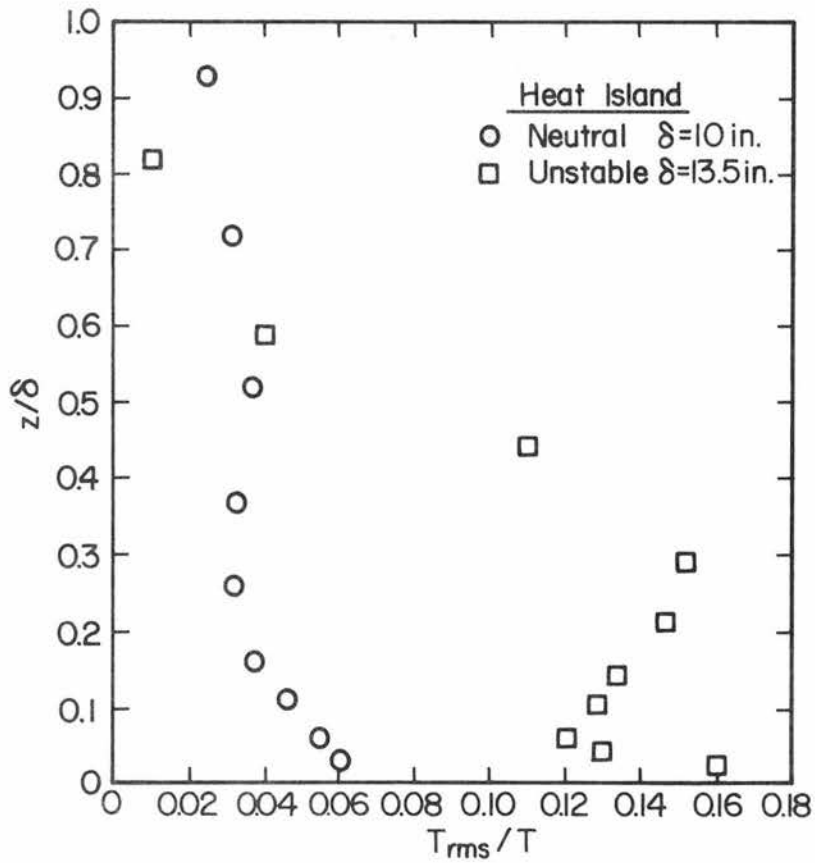


Fig. 5.62 Comparison of non-dimensional temperature fluctuations vertical profiles for neutral and unstable smooth heat islands for a stable approach flow at  $x = 68$  feet and  $y = 0$ .

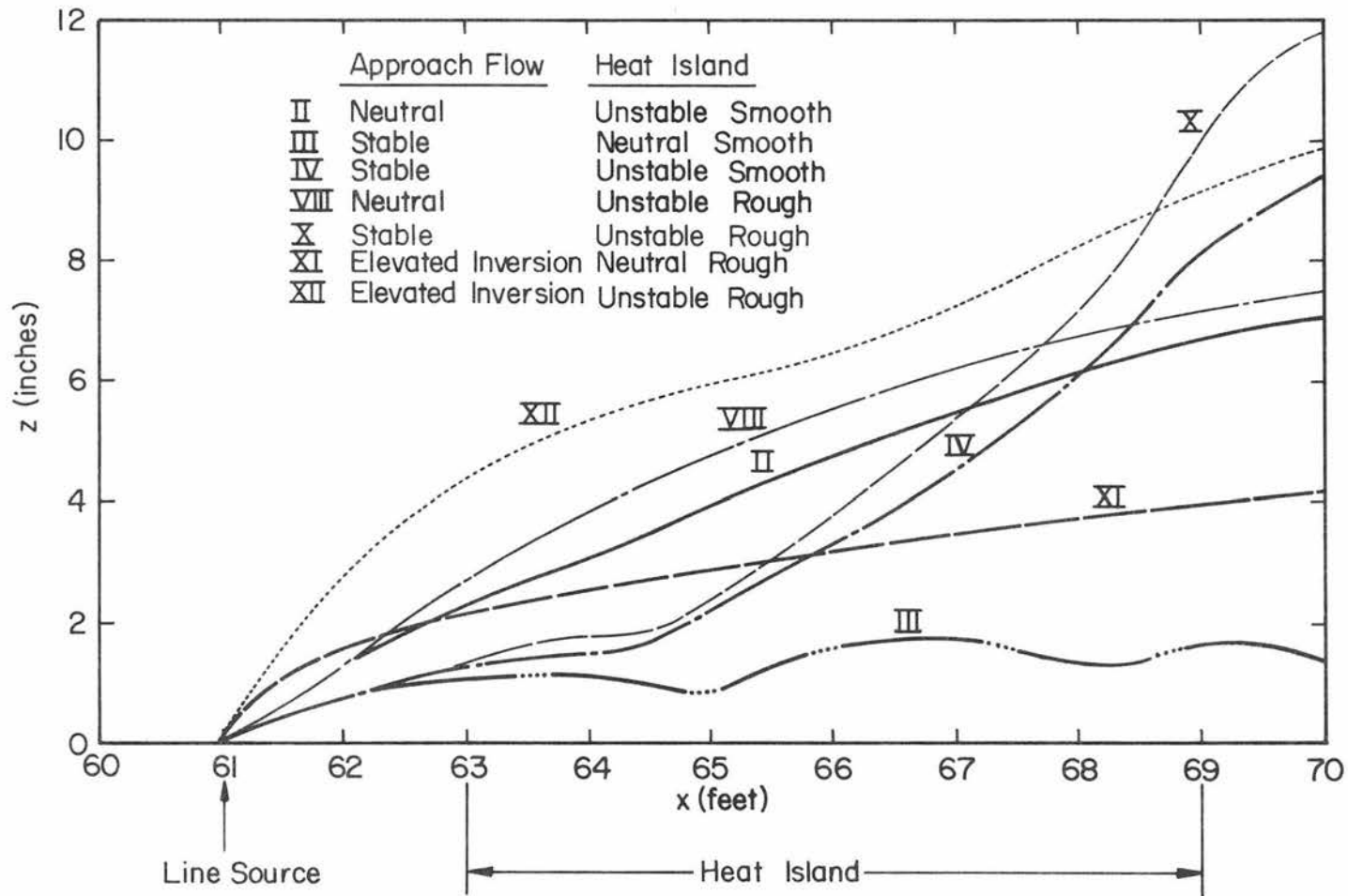


Fig. 5.63 Growth of the plume in the downwind direction based on 10 percent of the maximum concentration for different cases.

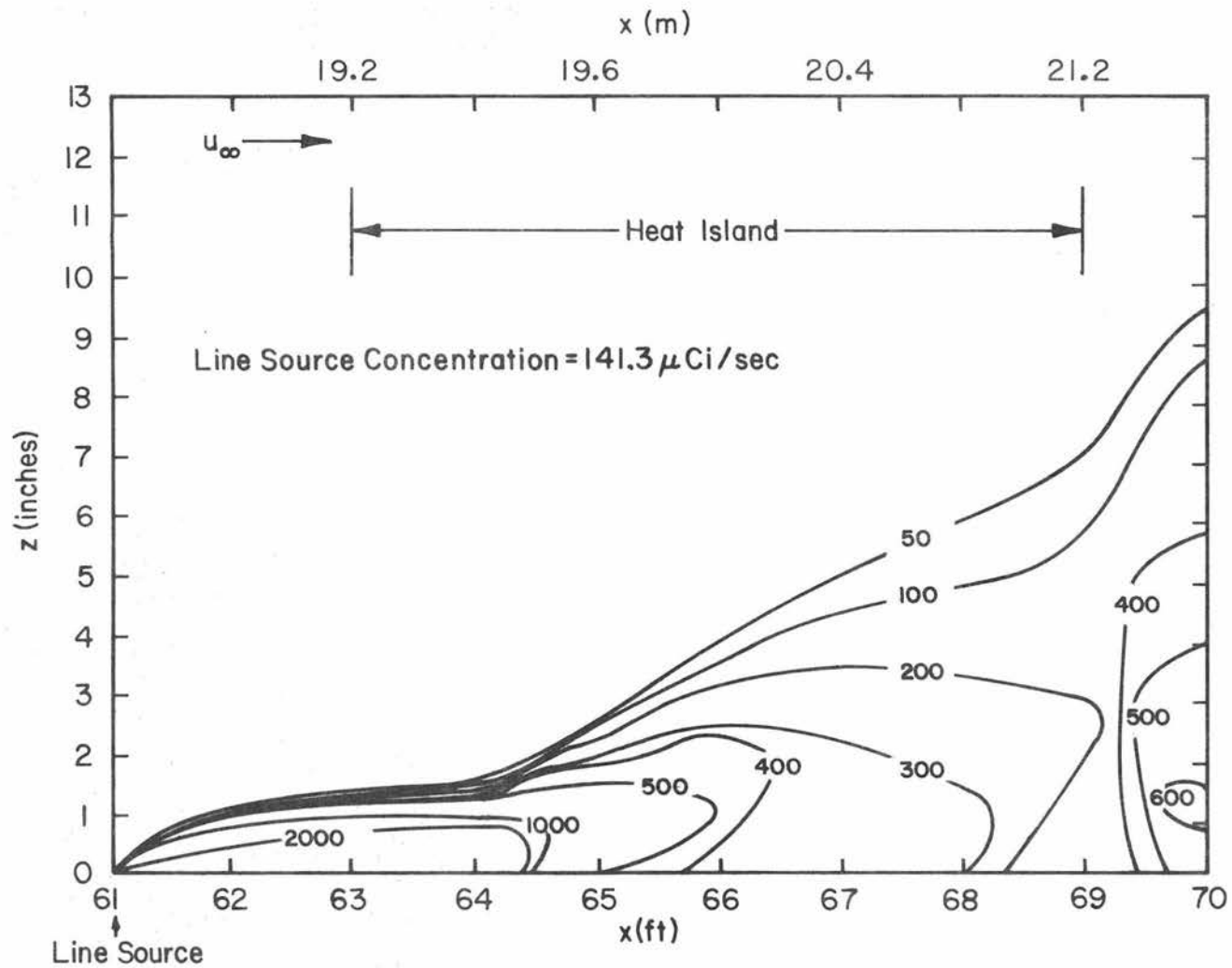


Fig. 5.64 Iso-concentration lines for the tracer gas released from the two-dimensional continuous line source for a stably stratified approach flow over an unstable smooth heat island.

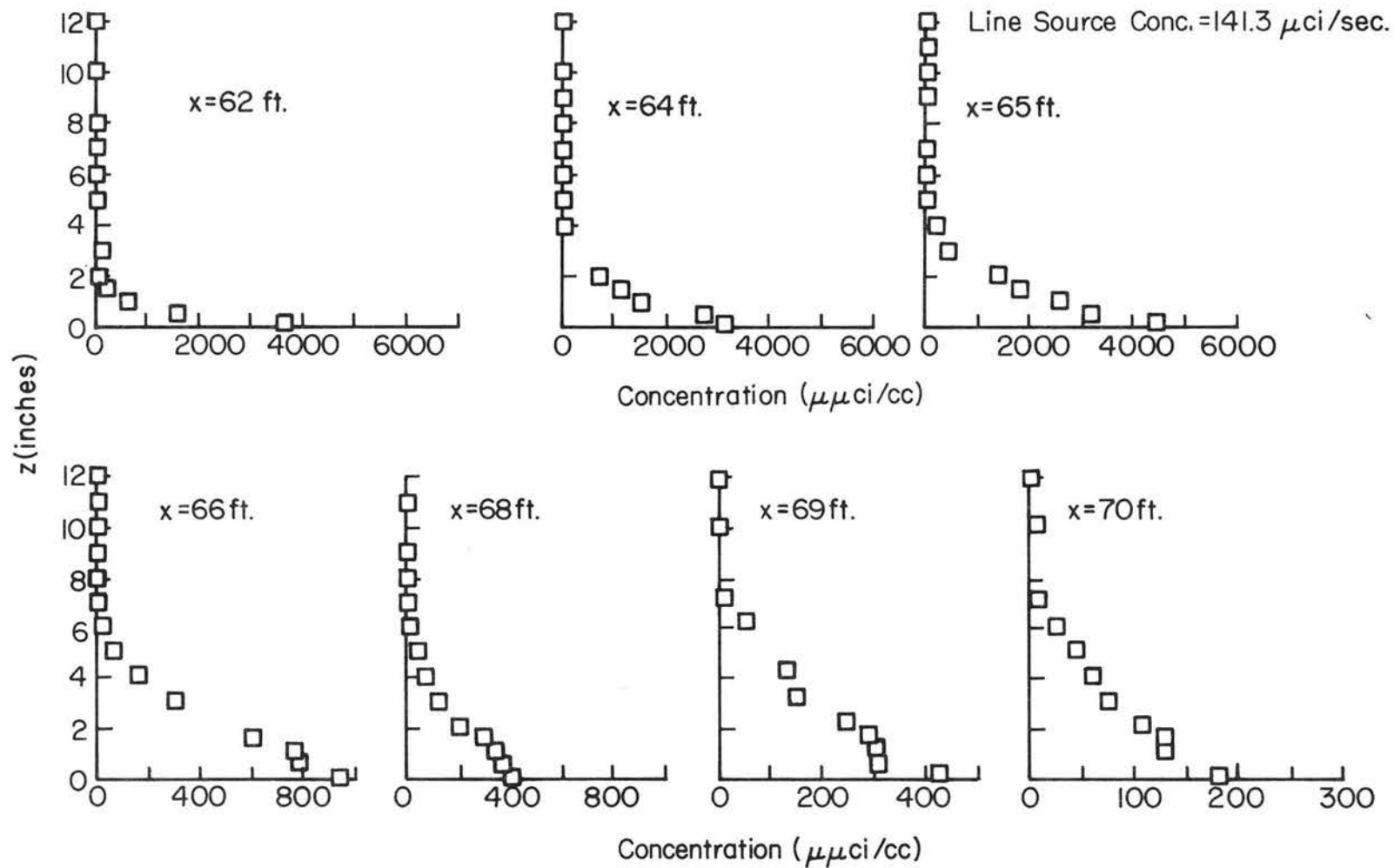


Fig. 5.65 Vertical mean concentration profiles along the centerline of a neutral, smooth heat island for neutral approach flow.

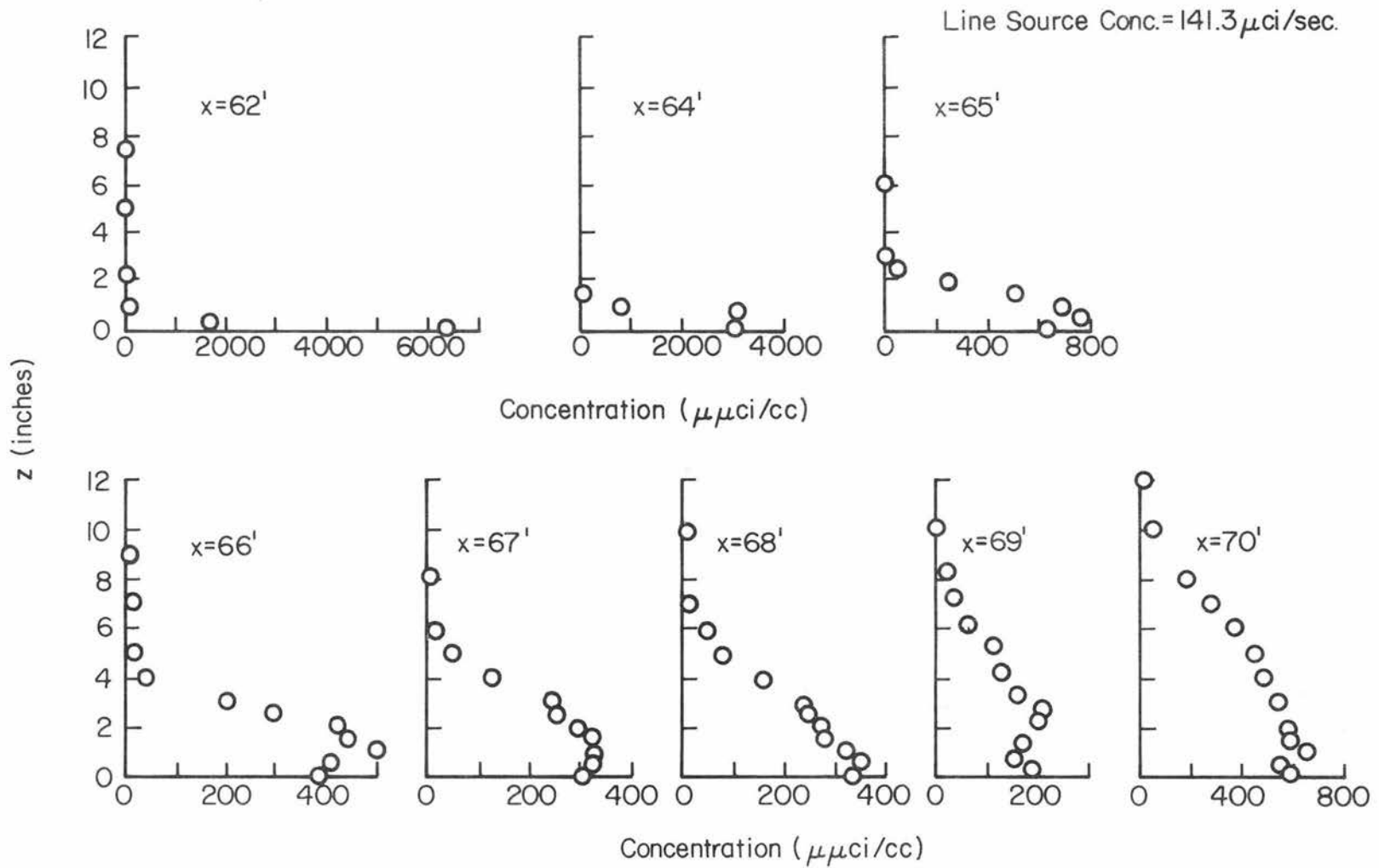


Fig. 5.66 Vertical concentration profiles along the centerline of unstable, smooth heat island for stable flow.

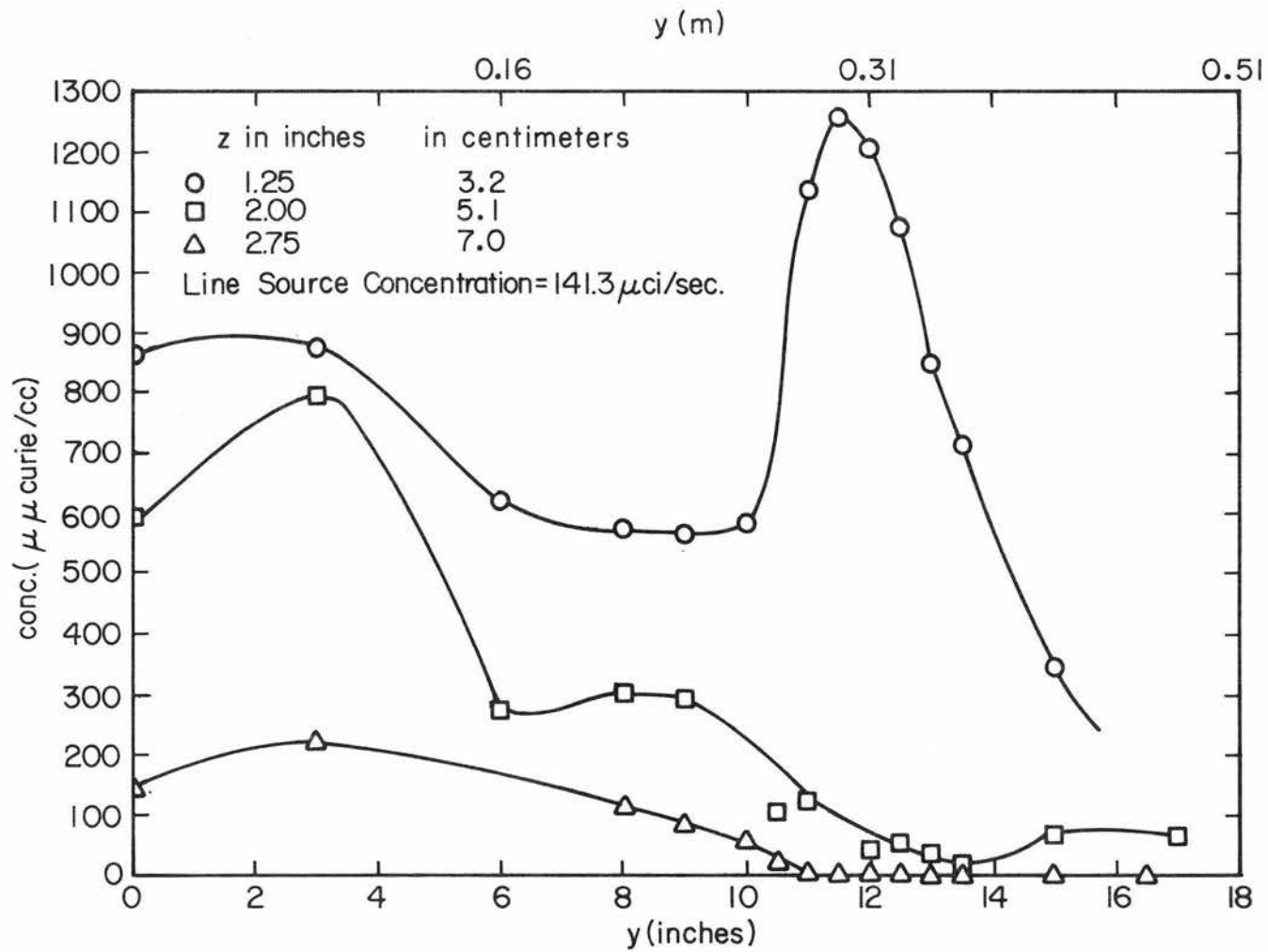


Fig. 5.67 Concentration profiles along the width of an unstable, smooth heat island for stable approach flow at  $x = 65.25$  feet for different heights.

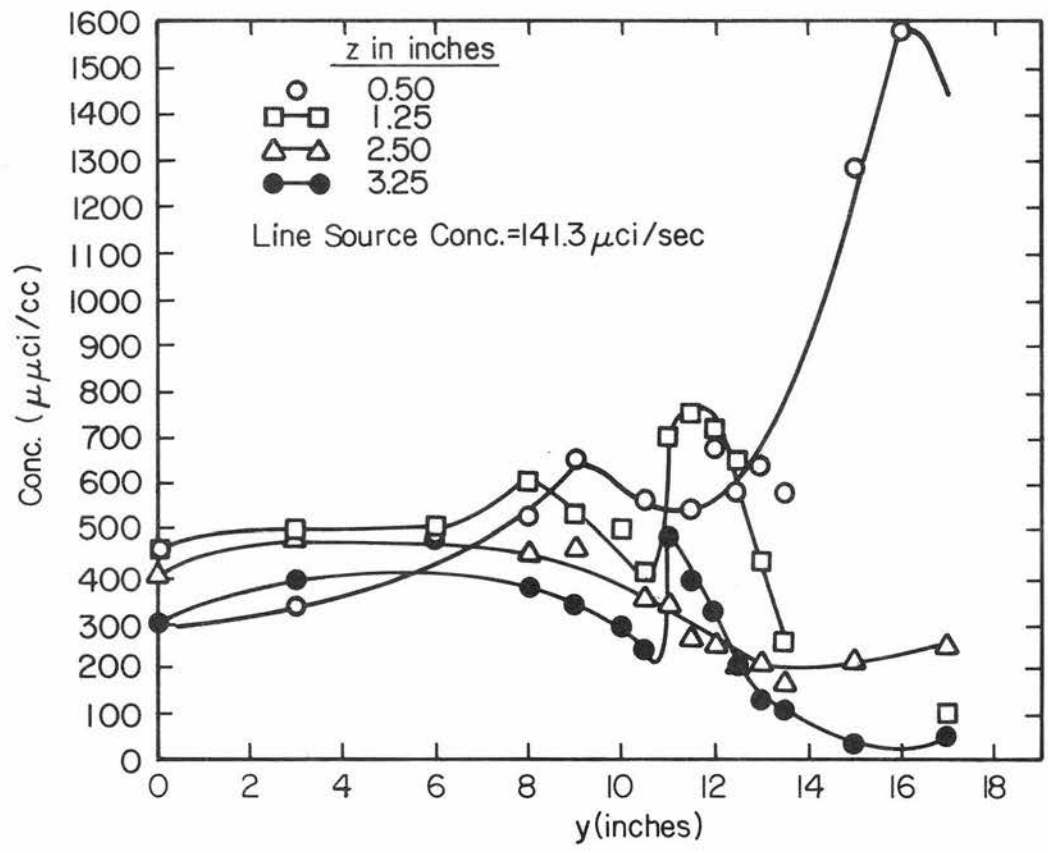


Fig. 5.68 Concentration profiles along the width of an unstable, smooth heat island for stable approach flow at  $x = 65.25$  feet for different heights.

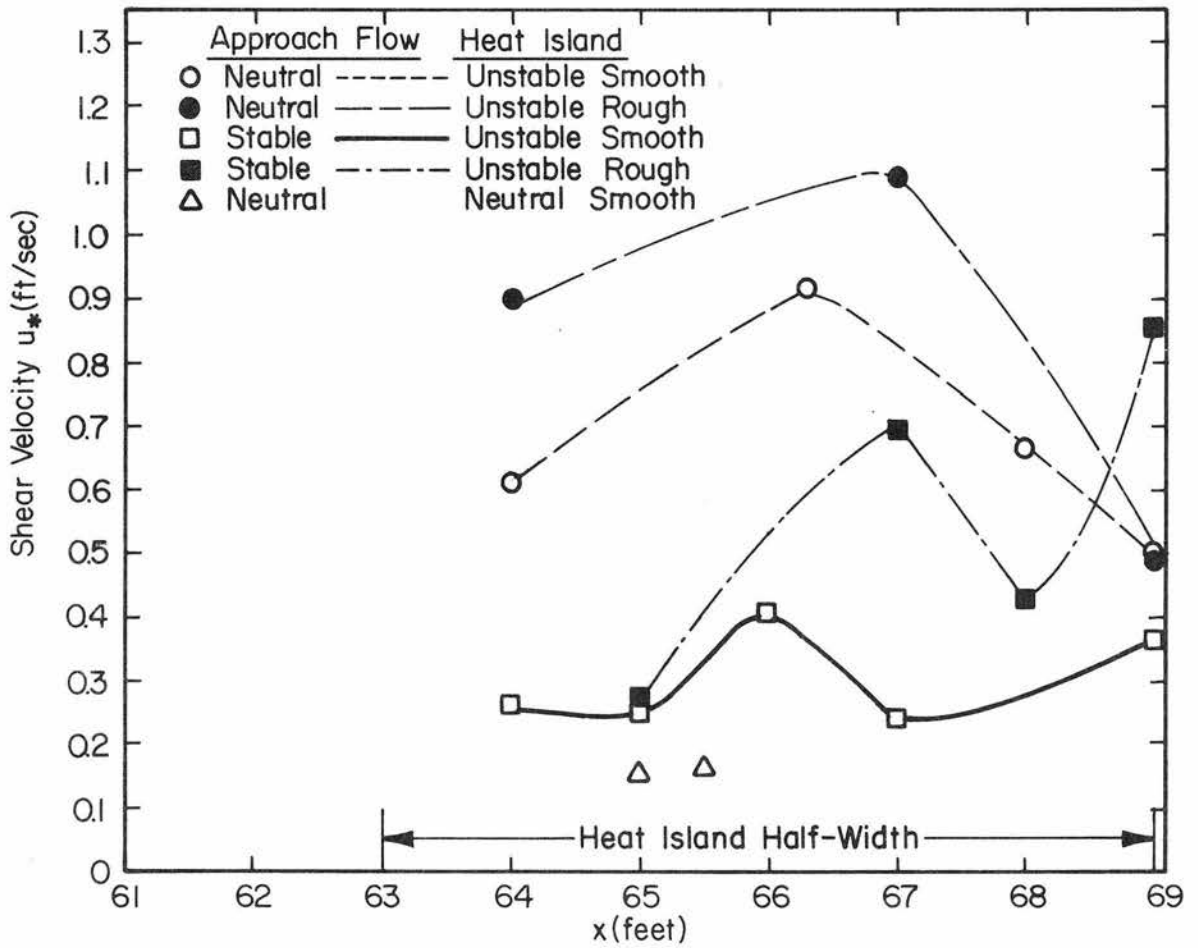


Fig. 5.69 Shear velocity distribution along the centerline for various cases.

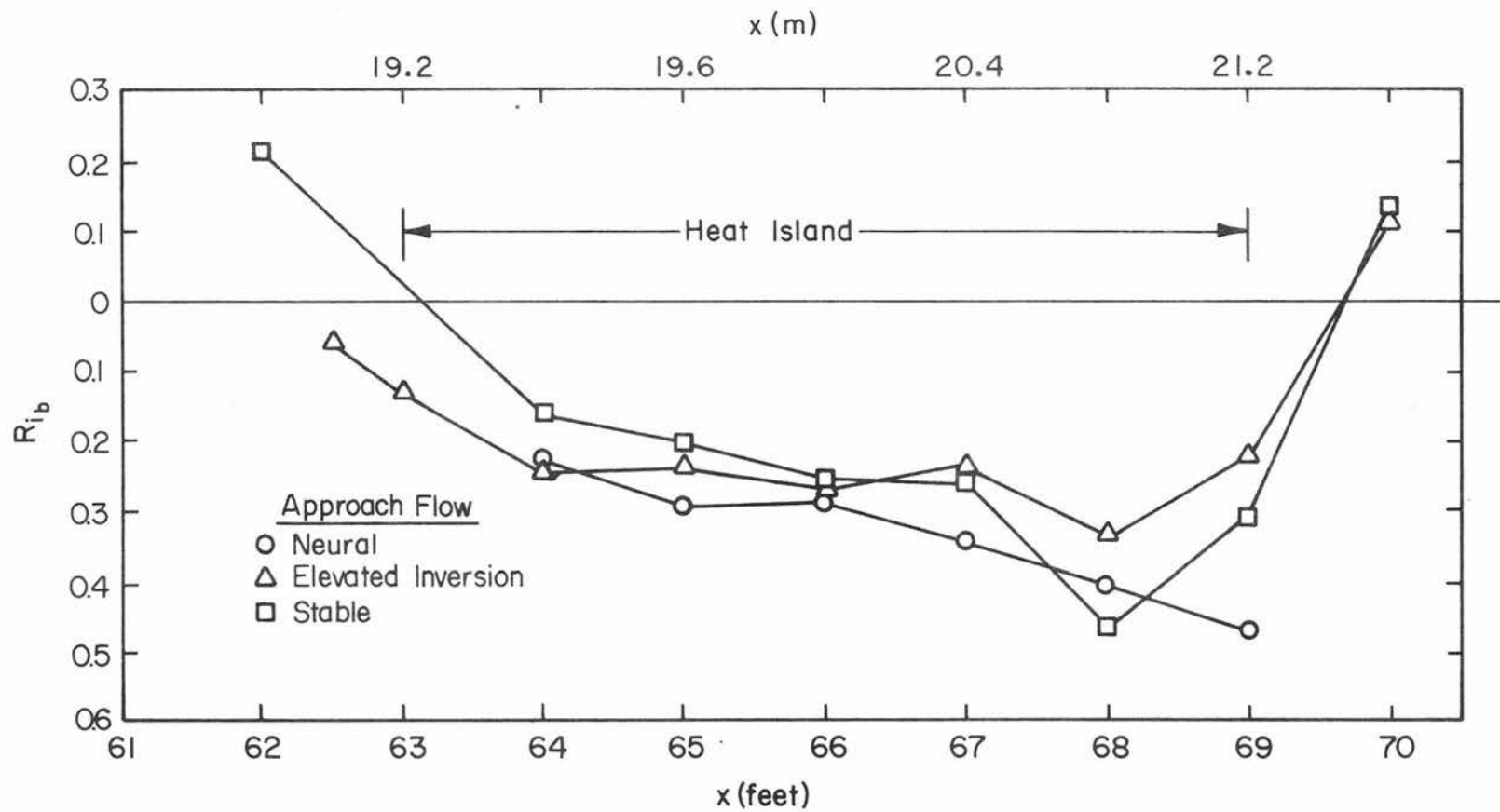


Fig. 5.70 Distribution of bulk Richardson number along the centerline over an unstable rough heat island for different approach flows.

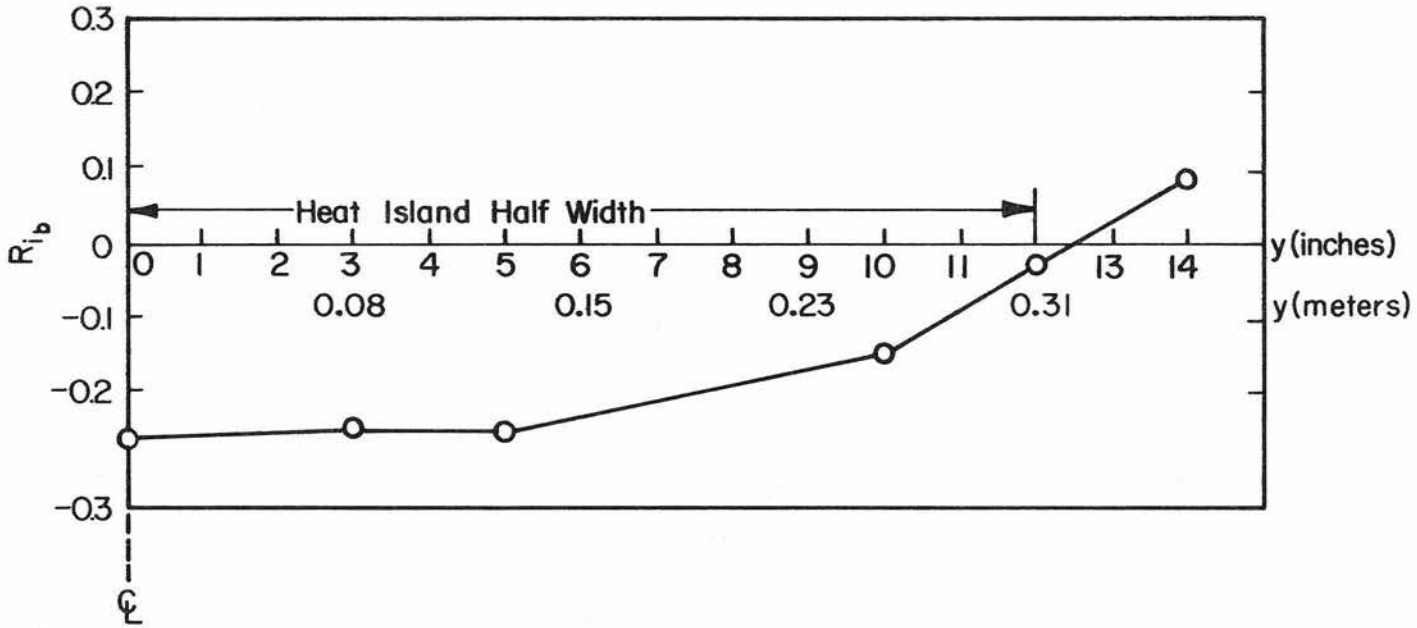


Fig. 5.71 Distribution of bulk Richardson number along the width for stable flow over unstable rough heat island at  $x = 66$  feet .

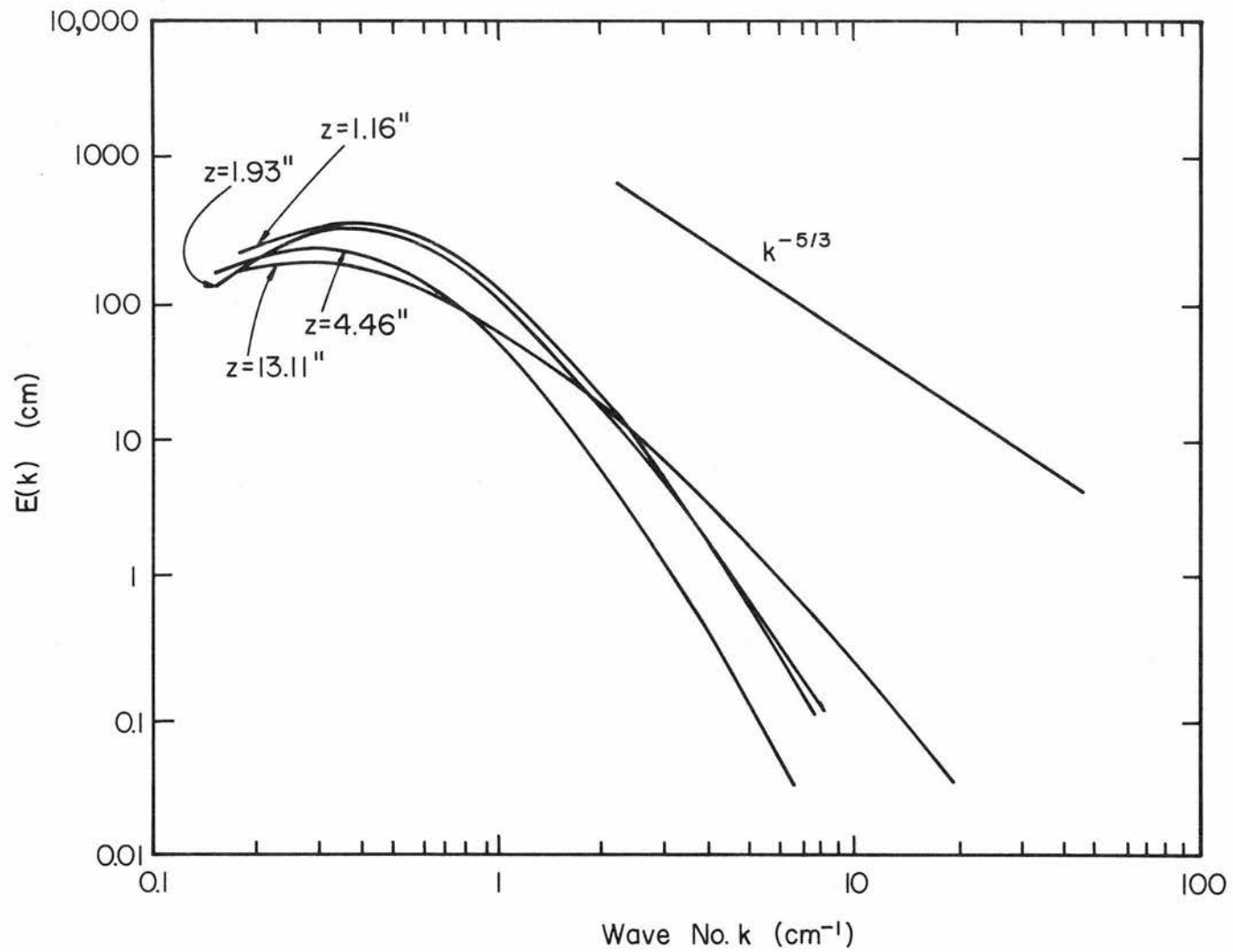


Fig. 5.72 Spectra of longitudinal component of turbulence for neutral flow over a neutral rough heat island at  $x = 68$  feet and  $y = 0$ .

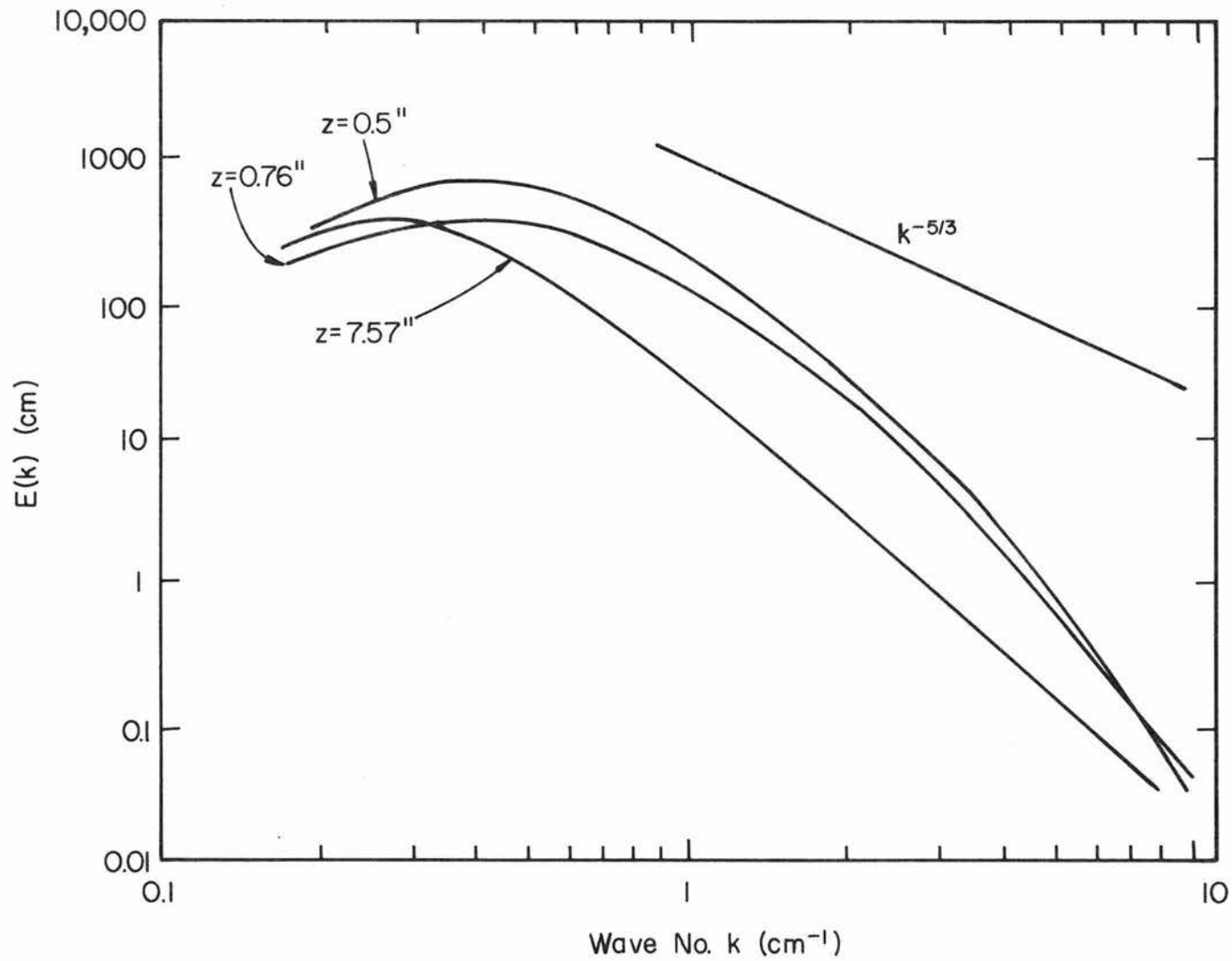


Fig. 5.73 Spectra of longitudinal component of turbulence for stable flow over an unstable rough heat island at  $x = 68$  feet and  $y = 0$ .

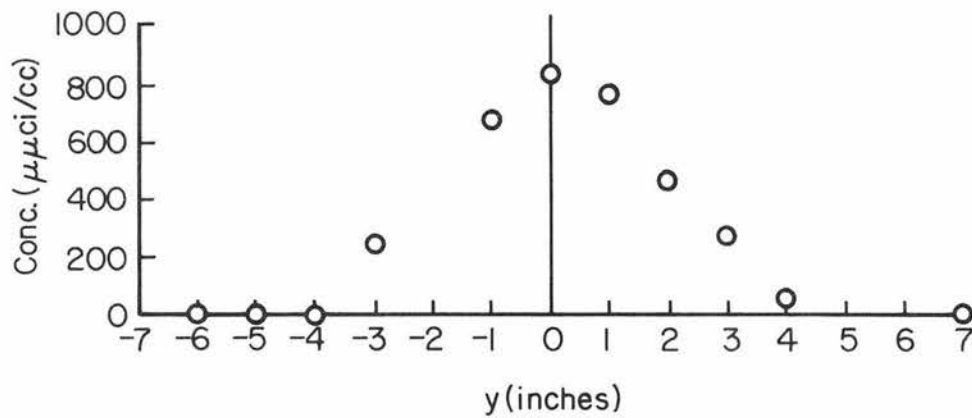
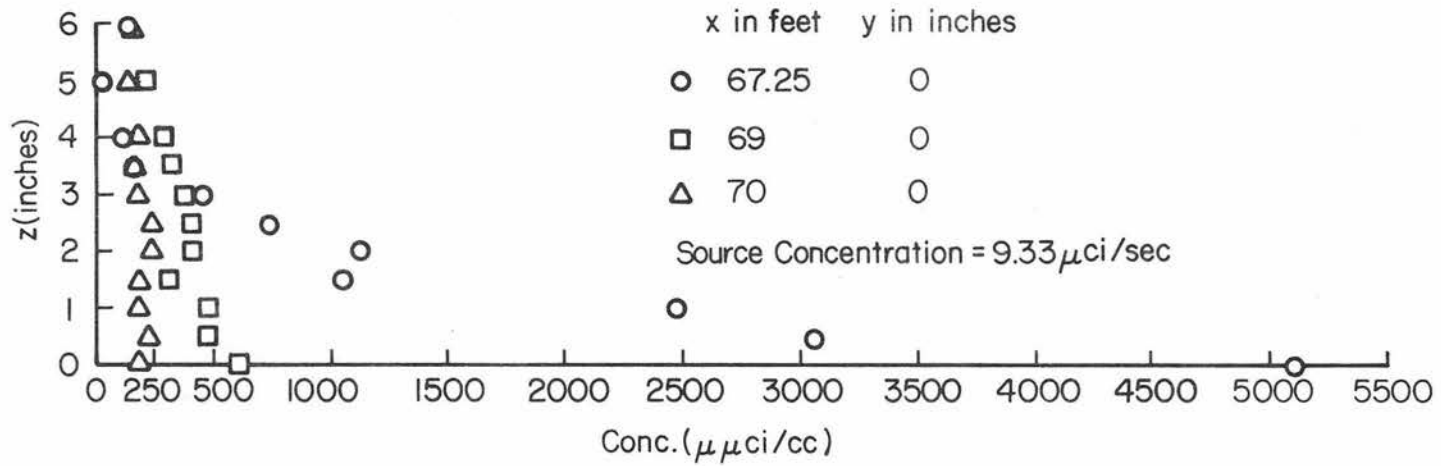


Fig. 5.74 Vertical and lateral mean concentration profiles of Kr85 released from a ground level continuous point source at  $x = 65.75$  feet and  $y = 0$  for a stable approach flow over an unstable, rough heat island.

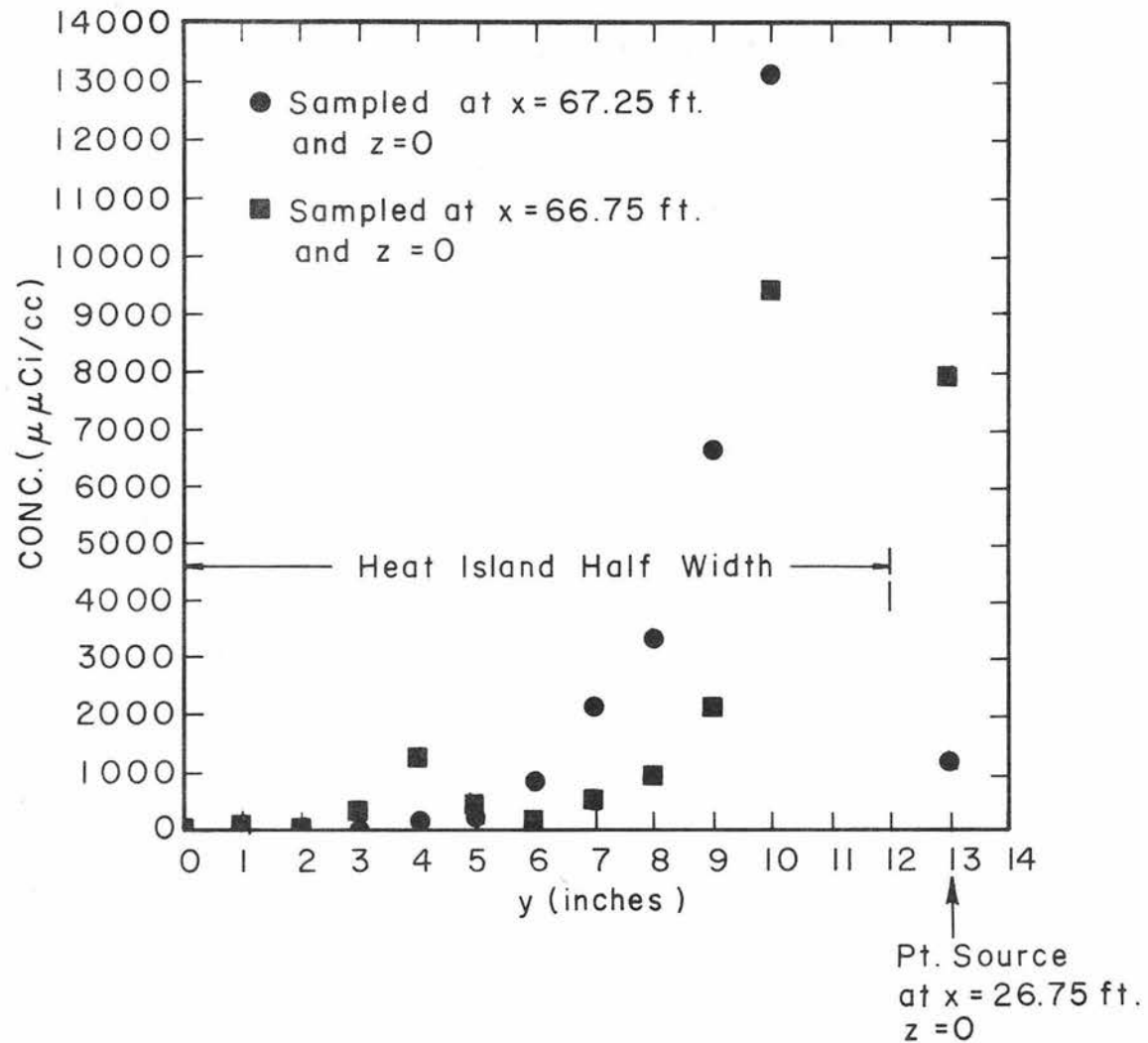


Fig. 5.75 Ground level mean concentration of Kr85 released from a ground level continuous point source at  $x = 67.25$  feet and  $y = 13$  inches for a stable approach flow over an unstable smooth heat island.

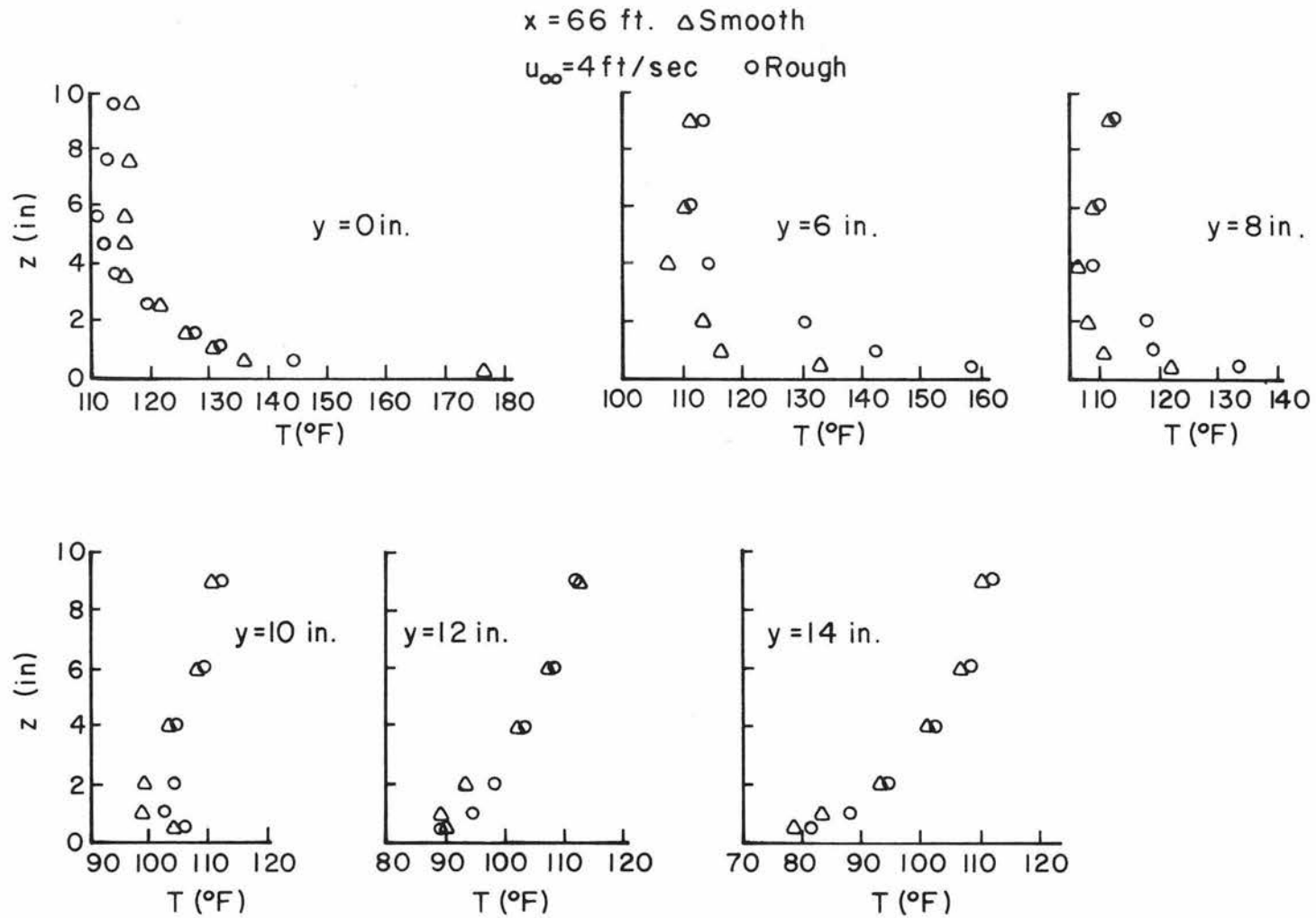


Fig. 5.76 Mean temperature profiles across an unstable heat island for a stable approach flow for smooth and rough cases.

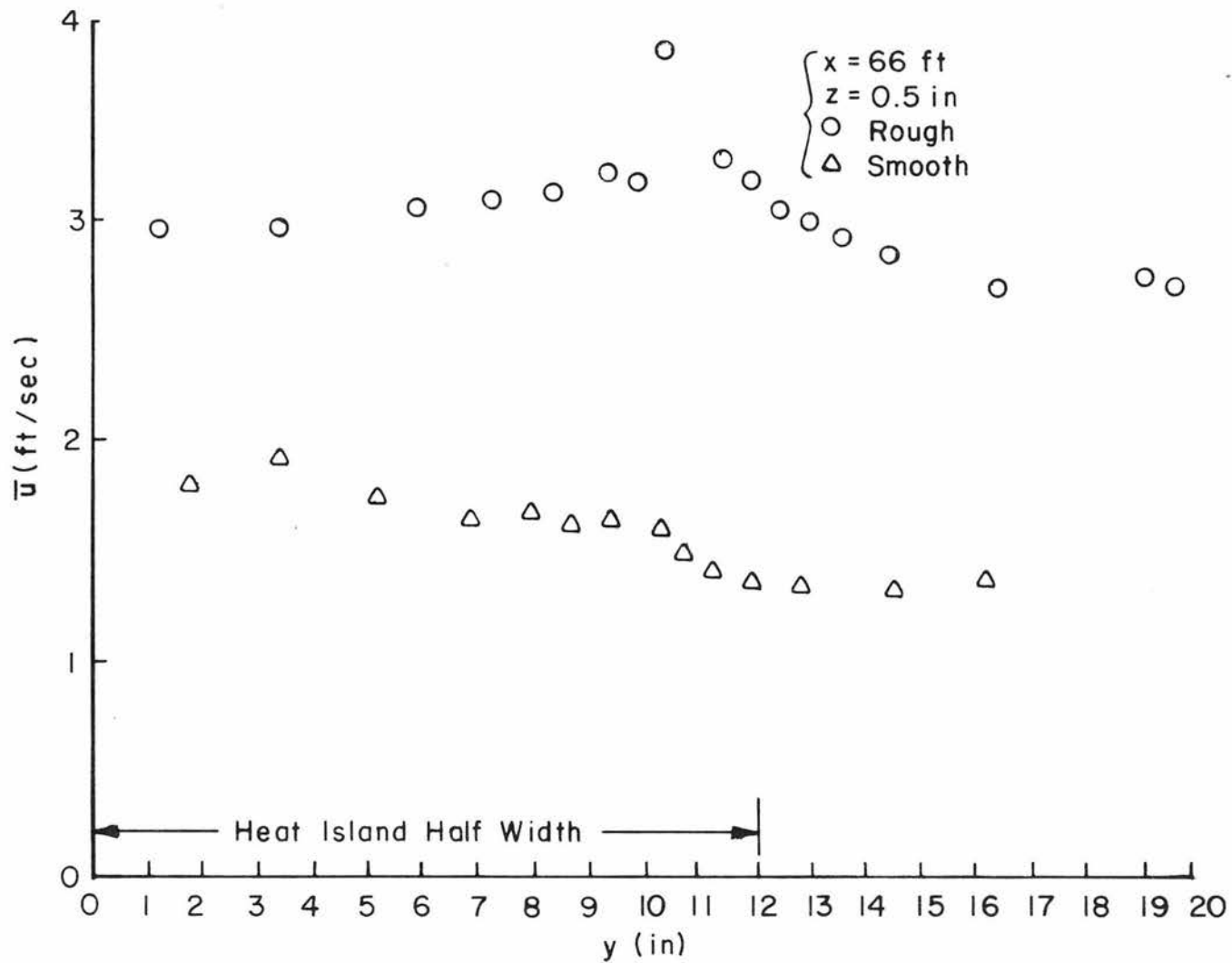


Fig. 5.77 Comparison of mean velocity distributions across an unstable heat island for a stable approach flow for smooth and rough cases.

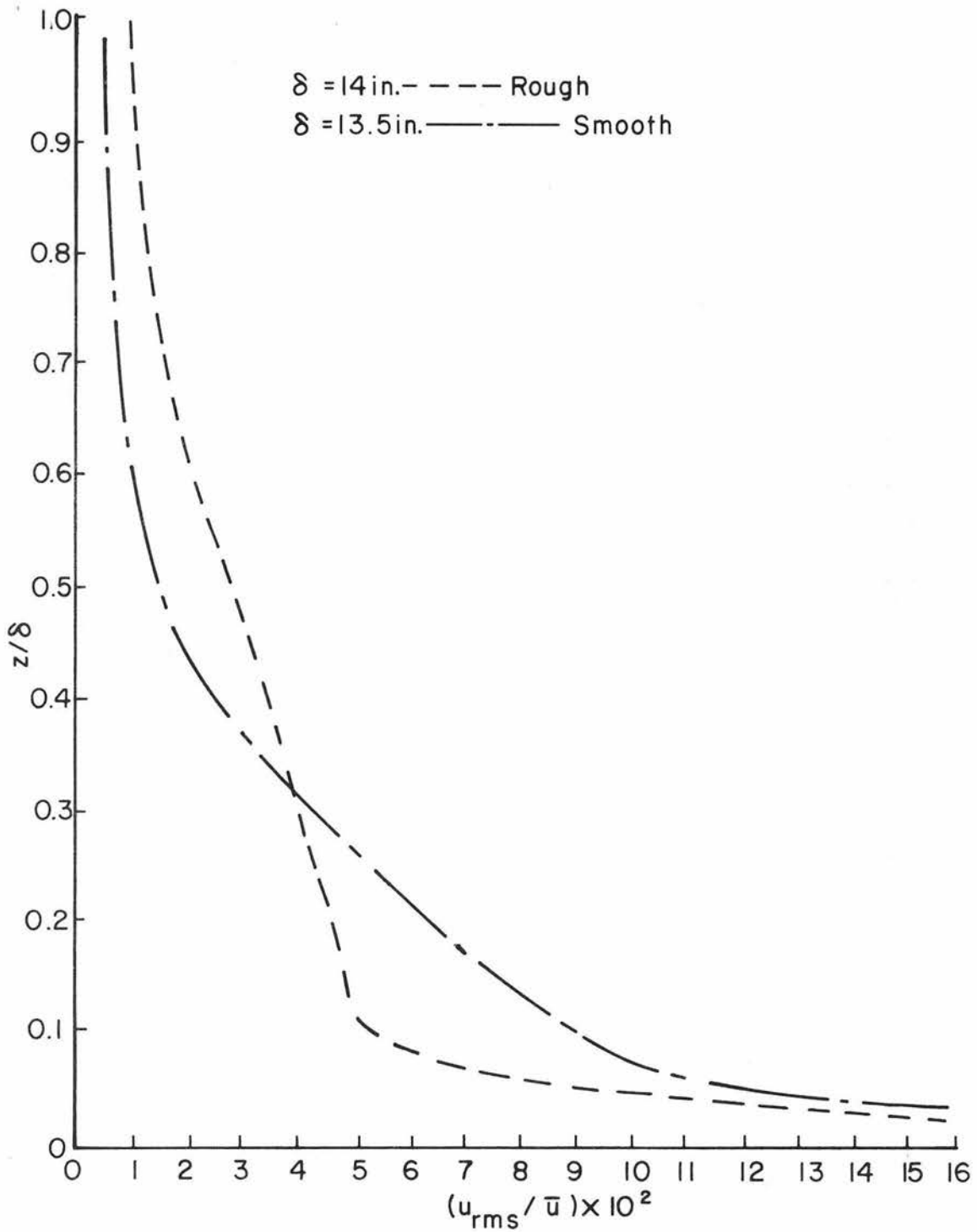


Fig. 5.78 Non-dimensional vertical profiles of longitudinal velocity fluctuations at  $x = 69$  feet and  $y = 0$  in. for stable flow over smooth and rough heated islands.

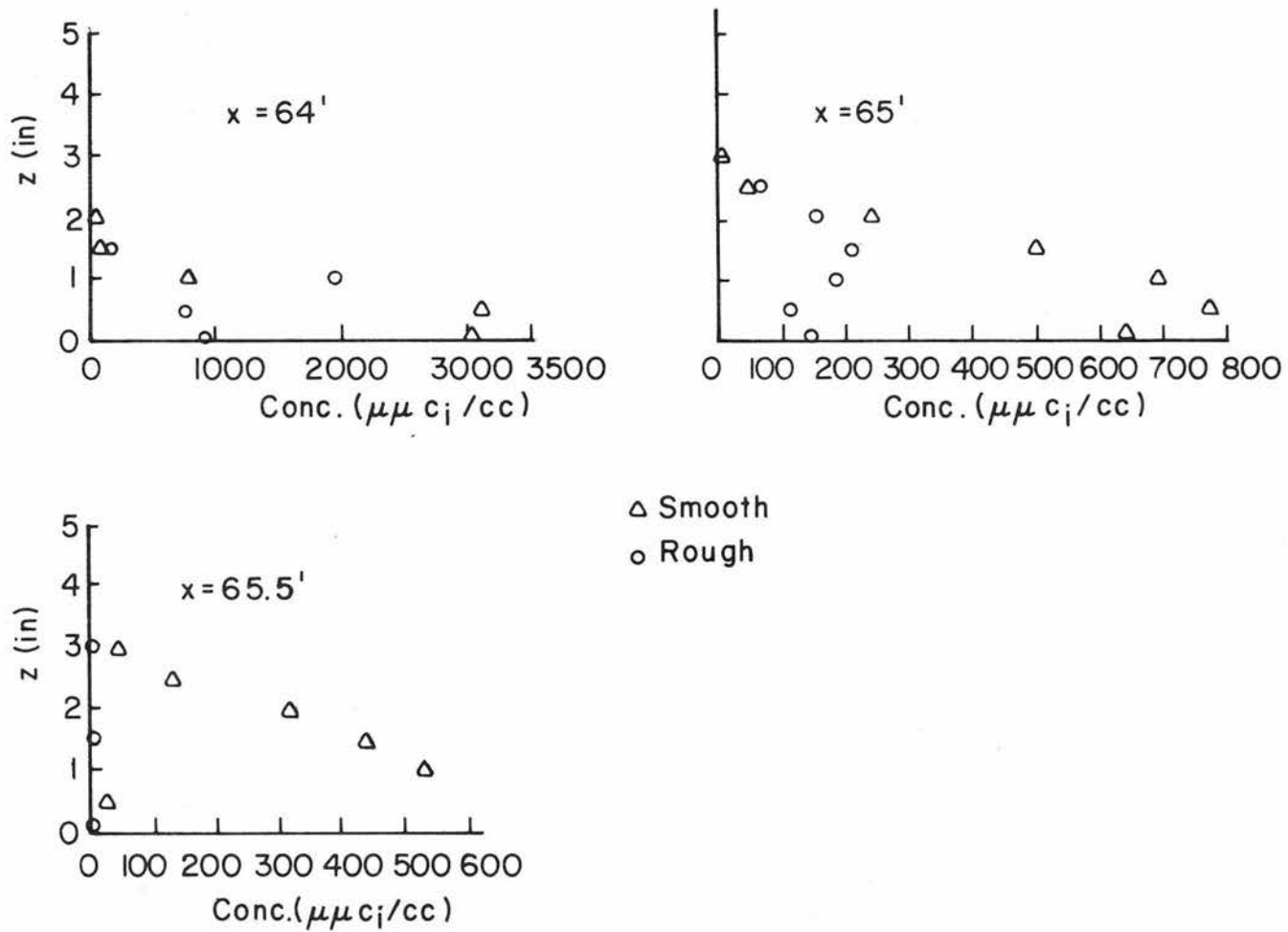


Fig. 5.79 Mean concentration profiles along the centerline for a stable flow over smooth and rough heat islands.

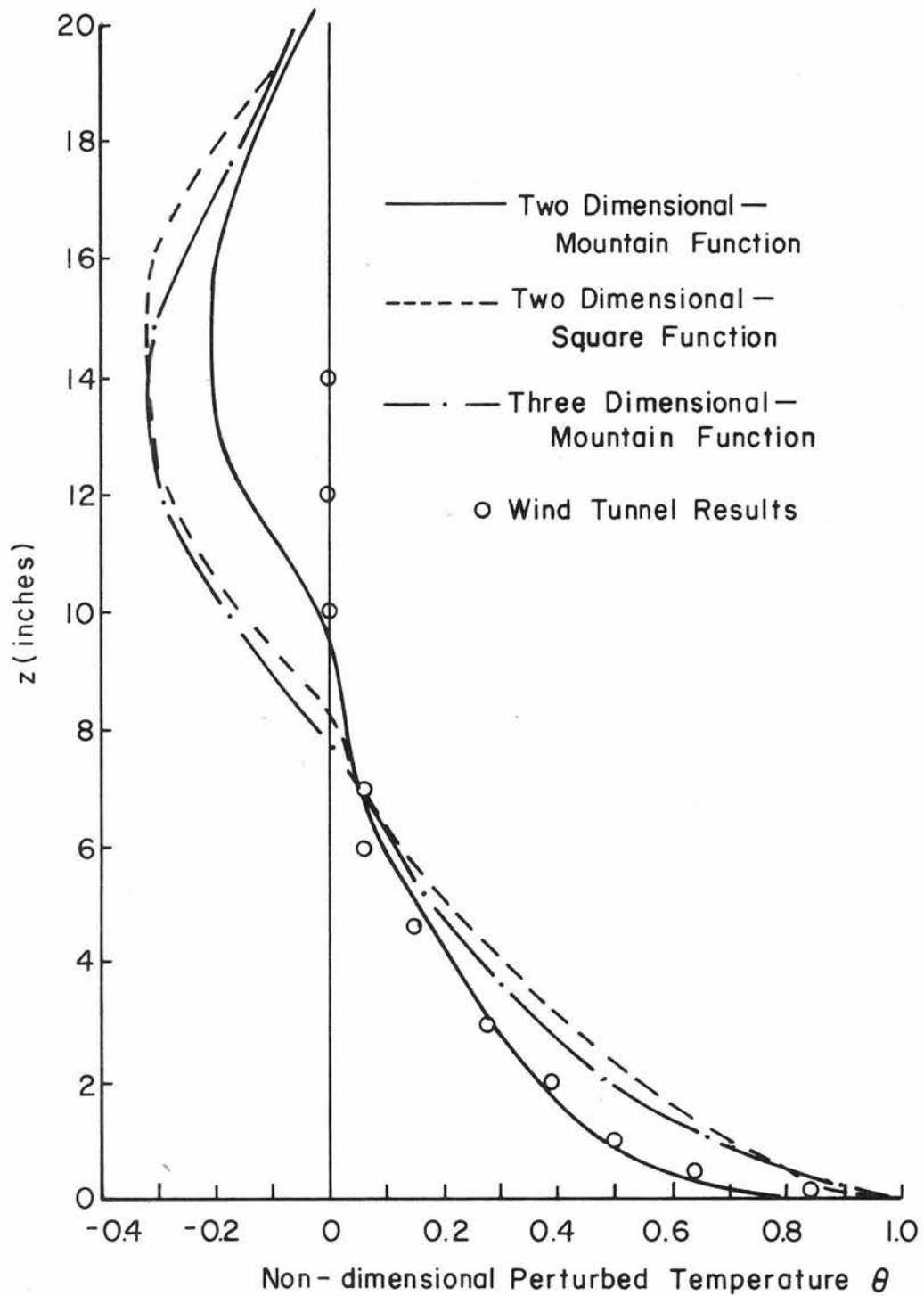


Fig. 5.80 Comparison of non-dimensional perturbed temperatures computed by the two-dimensional and the three-dimensional models with the laboratory data for an approach flow with inversion over a rough heat island.

unclassified

Security Classification

**DOCUMENT CONTROL DATA - R&D**

*(Security classification of title, body of abstract and indexing annotation must be entered when the overall report is classified)*

1. ORIGINATING ACTIVITY <i>(Corporate author)</i> Fluid Dynamics & Diffusion Laboratory College of Engineering, Colorado State University Fort Collins, Colorado 80521	2a. REPORT SECURITY CLASSIFICATION unclassified
	2b. GROUP

3. REPORT TITLE  
Stratified Shear Flows Over a Simulated Three-dimensional Urban Heat Island

4. DESCRIPTIVE NOTES *(Type of report and inclusive dates)*  
Technical Report

5. AUTHOR(S) *(Last name, first name, initial)*  
S.SethuRaman and J.E. Cermak

6. REPORT DATE August 1973	7a. TOTAL NO. OF PAGES 185	7b. NO. OF REFS 53
-------------------------------	-------------------------------	-----------------------

8a. CONTRACT OR GRANT NO. N00014-68-A-0493-0001 b. PROJECT NO. c. d.	9a. ORIGINATOR'S REPORT NUMBER(S) CER73-74SS-JEC4
	9b. OTHER REPORT NO(S) <i>(Any other numbers that may be assigned this report)</i> THEMIS Tech. Rept. No. 23

10. AVAILABILITY/LIMITATION NOTICES  
Distribution of this report is unlimited.

11. SUPPLEMENTARY NOTES	12. SPONSORING MILITARY ACTIVITY U.S. Department of Defense Office of Naval Research
-------------------------	--

Three-dimensional airflow over a rectangular heat island was studied for various conditions of approach flow in a wind tunnel. Three different thermal stratifications of the approach flow were selected for the study--neutral, ground based and elevated inversions. For each of these flows studies were conducted with and without roughness over the heat island and for the conditions with and without heating. Approach flow temperature profiles wer modeled according to atmospheric data available in the literature.

For each of the twelve cases mentioned above, measurements of mean wind velocity, longitudinal velocity fluctuations, mean temperature and temperature fluctuations were made. In addition, mean concentration measurements of a radio-active gas released from a two-dimensional, ground-level line source upwind of the heat island were made. Flow patterns were visualized for different cases with the help of a passive smoke source. Comparisons of data from the wind-tunnel measurements with the field data were made.

The mechanisms of the heat island observed in the wind-tunnel for different stratified flows were very similar to those observed in the field. The urban heat island plume that passes aloft downwind causes an appreciable reverse flow onto the heat-island. The helical vortices at the edge of the heat island cause a reduction in the turbulence level resulting in high concentrations of the mass released from a continuous line source upwind of the heat island.

A theoretical model based on linearized equations of motions incorporating a boundary layer type velocity profile has been developed to predict the urban excess temperatures and velocities. Theoretical results compare fairly well with data obtained in the laboratory and in the field.

14. KEY WORDS	LINK A		LINK B		LINK C	
	ROLE	WT	ROLE	WT	ROLE	WT
Stratified Shear Flows Thermal Stratification Urban Heat Island Three-Dimensional Airflow Helical Vortices						

INSTRUCTIONS

1. **ORIGINATING ACTIVITY:** Enter the name and address of the contractor, subcontractor, grantee, Department of Defense activity or other organization (*corporate author*) issuing the report.

2a. **REPORT SECURITY CLASSIFICATION:** Enter the overall security classification of the report. Indicate whether "Restricted Data" is included. Marking is to be in accordance with appropriate security regulations.

2b. **GROUP:** Automatic downgrading is specified in DoD Directive 5200.10 and Armed Forces Industrial Manual. Enter the group number. Also, when applicable, show that optional markings have been used for Group 3 and Group 4 as authorized.

3. **REPORT TITLE:** Enter the complete report title in all capital letters. Titles in all cases should be unclassified. If a meaningful title cannot be selected without classification, show title classification in all capitals in parenthesis immediately following the title.

4. **DESCRIPTIVE NOTES:** If appropriate, enter the type of report, e.g., interim, progress, summary, annual, or final. Give the inclusive dates when a specific reporting period is covered.

5. **AUTHOR(S):** Enter the name(s) of author(s) as shown on or in the report. Enter last name, first name, middle initial. If military, show rank and branch of service. The name of the principal author is an absolute minimum requirement.

6. **REPORT DATE:** Enter the date of the report as day, month, year, or month, year. If more than one date appears on the report, use date of publication.

7a. **TOTAL NUMBER OF PAGES:** The total page count should follow normal pagination procedures, i.e., enter the number of pages containing information.

7b. **NUMBER OF REFERENCES:** Enter the total number of references cited in the report.

8a. **CONTRACT OR GRANT NUMBER:** If appropriate, enter the applicable number of the contract or grant under which the report was written.

8b, 8c, & 8d. **PROJECT NUMBER:** Enter the appropriate military department identification, such as project number, subproject number, system numbers, task number, etc.

9a. **ORIGINATOR'S REPORT NUMBER(S):** Enter the official report number by which the document will be identified and controlled by the originating activity. This number must be unique to this report.

9b. **OTHER REPORT NUMBER(S):** If the report has been assigned any other report numbers (*either by the originator or by the sponsor*), also enter this number(s).

10. **AVAILABILITY/LIMITATION NOTICES:** Enter any limitations on further dissemination of the report, other than those imposed by security classification, using standard statements such as:

- (1) "Qualified requesters may obtain copies of this report from DDC."
- (2) "Foreign announcement and dissemination of this report by DDC is not authorized."
- (3) "U. S. Government agencies may obtain copies of this report directly from DDC. Other qualified DDC users shall request through \_\_\_\_\_."
- (4) "U. S. military agencies may obtain copies of this report directly from DDC. Other qualified users shall request through \_\_\_\_\_."
- (5) "All distribution of this report is controlled. Qualified DDC users shall request through \_\_\_\_\_."

If the report has been furnished to the Office of Technical Services, Department of Commerce, for sale to the public, indicate this fact and enter the price, if known.

11. **SUPPLEMENTARY NOTES:** Use for additional explanatory notes.

12. **SPONSORING MILITARY ACTIVITY:** Enter the name of the departmental project office or laboratory sponsoring (*paying for*) the research and development. Include address.

13. **ABSTRACT:** Enter an abstract giving a brief and factual summary of the document indicative of the report, even though it may also appear elsewhere in the body of the technical report. If additional space is required, a continuation sheet shall be attached.

It is highly desirable that the abstract of classified reports be unclassified. Each paragraph of the abstract shall end with an indication of the military security classification of the information in the paragraph, represented as (TS), (S), (C), or (U).

There is no limitation on the length of the abstract. However, the suggested length is from 150 to 225 words.

14. **KEY WORDS:** Key words are technically meaningful terms or short phrases that characterize a report and may be used as index entries for cataloging the report. Key words must be selected so that no security classification is required. Identifiers, such as equipment model designation, trade name, military project code name, geographic location, may be used as key words but will be followed by an indication of technical context. The assignment of links, rules, and weights is optional.

All addressees receive one copy unless otherwise specified

Defense Documentation Center Cameron Station Alexandria, Virginia 22314 (12 copies)	Director Office of Naval Research Branch Office 495 Summer Street Boston, Massachusetts 02210	Technical Library Naval Weapons Laboratory Dahlgren, Virginia 22448
Technical Library Naval Ship Research and Development Laboratory Annapolis, Maryland 21402	Commander Puget Sound Naval Shipyard Bremerton, Washington 98314	Computation and Analyses Laboratory Naval Weapons Laboratory Dahlgren, Virginia 22448
Professor Bruce Johnson Engineering Department Naval Academy Annapolis, Maryland 21402	Dr. Alfred Ritter Cornell Aeronautical Laboratory, Inc. P. O. Box 235 Buffalo, New York 14221	Dr. R. H. Kraichnan Dublin, New Hampshire 03444
Library Naval Academy Annapolis, Maryland 21402	Professor G. Birkhoff Department of Mathematics Harvard University Cambridge, Massachusetts 02138	Commanding Officer Army Research Office Box CM, Duke Station Durham, North Carolina 27706
Professor W. P. Graebel Department of Engineering Mechanics College of Engineering University of Michigan Ann Arbor, Michigan 48108	Professor G. F. Carrier Division of Engineering and Applied Physics Harvard University Cambridge, Massachusetts 02139	Dr. Martin H. Bloom Polytechnic Institute of Brooklyn Long Island Graduate Center Department of Aerospace Engineering and Applied Mechanics Farmingdale, New York 11735
Professor T. Francis Oglivie Department of Naval Architecture and Marine Engineering University of Michigan Ann Arbor, Michigan 48108	Commanding Officer NROTC Naval Administrative Unit Massachusetts Institute of Technology Cambridge, Massachusetts 02139	Technical Documents Center Building 315 U. S. Army Mobility Equipment Research and Development Center Fort Belvoir, Virginia 22060
Professor W. W. Willmarth Department of Aerospace Engineering University of Michigan Ann Arbor, Michigan 48108	Professor M. A. Abkowitz Department of Ocean Engineering Massachusetts Institute of Technology Cambridge, Massachusetts 02139	Professor J. E. Cermak Department of Atmospheric Sciences Colorado State University Fort Collins, Colorado 80521
AFOSR (REM) 1400 Wilson Boulevard Arlington, Virginia 22204	Professor A. T. Ippen Department of Civil Engineering Massachusetts Institute of Technology Cambridge, Massachusetts 02139	Professor O. H. Shemdin Coastal and Oceanographic Engineering Department University of Florida Gainesville, Florida 32601
Professor S. Corrsin Department of Mechanics and Materials Science The Johns Hopkins University Baltimore, Maryland 21218	Professor Phillip Mandel Department of Ocean Engineering Massachusetts Institute of Technology Cambridge, Massachusetts 02139	Technical Library Webb Institute of Naval Architecture Glen Cove, Long Island, New York 11542
Professor R. B. Couch Department of Naval Architecture and Marine Engineering The University of Michigan Ann Arbor, Michigan 48105	Professor E. W. Merrill Department of Chemical Engineering Massachusetts Institute of Technology Cambridge, Massachusetts 02139	Professor E. V. Lewis Webb Institute of Naval Architecture Glen Cove, Long Island, New York 11542
Professor L. S. G. Kovaszny Department of Mechanics and Materials Science The Johns Hopkins University Baltimore, Maryland 21218	Professor E. Mollo-Christensen Department of Meteorology Room 54-1722 Massachusetts Institute of Technology Cambridge, Massachusetts 02139	Dr. J. P. Breslin Davidson Laboratory Stevens Institute of Technology Castle Point Station Hoboken, New Jersey 07030
Professor O. M. Phillips Department of Mechanics and Materials Science The Johns Hopkins University Baltimore, Maryland 21218	Professor J. Nicholas Newman Department of Ocean Engineering Room 5-324A Massachusetts Institute of Technology Cambridge, Massachusetts 02139	Mr. C. H. Henry Stevens Institute of Technology Davidson Laboratory Castle Point Station Hoboken, New Jersey 07030
Professor M. Holt Department of Mechanical Engineering University of California Berkeley, California 94720	Commander Charleston Naval Shipyard Naval Base Charleston, South Carolina 29408	Dr. D. Savitsky Davidson Laboratory Stevens Institute of Technology Castle Point Station Hoboken, New Jersey 07030
Professor E. V. Laitone Department of Mechanical Engineering University of California Berkeley, California 94720	A. R. Kuhlthau, Director Research Laboratories for the Engineering Sciences Thorton Hall, University of Virginia Charlottesville, Virginia 22903	Dr. A. Strumpf Davidson Laboratory Stevens Institute of Technology Castle Point Station Hoboken, New Jersey 07030
Librarian Department of Naval Architecture University of California Berkeley, California 94720	Director Office of Naval Research Branch Office 536 South Clark Street Chicago, Illinois 60605	Dr. J. P. Craven University of Hawaii 1801 University Avenue Honolulu, Hawaii 96822
Professor P. Lieber Department of Mechanical Engineering Institute of Engineering Research Berkeley, California 94720	Library Naval Weapons Center China Lake, California 93555	Professor J. F. Kennedy, Director Iowa Institute of Hydraulic Research State University of Iowa Iowa City, Iowa 52240
Professor J. R. Pauling Institute of Engineering Research Department of Naval Architecture University of California Berkeley, California 94720	Professor R. V. Edwards Division of Chemical Engineering Case Western Reserve University Cleveland, Ohio 44106	Professor L. Landweber Iowa Institute of Hydraulic Research State University of Iowa Iowa City, Iowa 52240
Professor W. C. Webster College of Engineering Department of Naval Architecture University of California Berkeley, California 94720	Professor J. M. Burgers Institute of Fluid Dynamics and Applied Mathematics University of Maryland College Park, Maryland 20742	Professor E. L. Resler Graduate School of Aeronautical Engineering Cornell University Ithaca, New York 14851
Professor J. V. Wehausen Institute of Engineering Research Department of Naval Architecture University of California Berkeley, California 94720	Professor Pai Institute of Fluid Dynamics and Applied Mathematics University of Maryland College Park, Maryland 20742	Dr. Y. H. Pao Flow Research, Inc. 1819 South Central Avenue Suite 72 Kent, Washington 98031
Commander Boston Naval Shipyard Boston, Massachusetts 02129	Acquisition Director NASA Scientific and Technical Information P. O. Box 33 College Park, Maryland 20742	Dr. D. E. Ordway Sage Action, Incorporated P. O. Box 416 Ithaca, New York 14850

Professor John Miles  
c/o I.G.P.P.  
University of California, San Diego  
La Jolla, California 92038

Director  
Scripps Institute of Oceanography  
University of California  
La Jolla, California 92037

Professor A. T. Ellis  
University of California, San Diego  
Department of Aerospace and  
Mechanical Engineering Science  
La Jolla, California 92037

Dr. Coda Pan  
Mechanical Technology Incorporated  
968 Albany-Shaker Road  
Latham, New York 12110

Mr. F. Eisenberg, President  
Hydronautics, Incorporated  
8210 Pindell School Road  
Laurel, Maryland 20810

Mr. M. P. Tulin  
Hydronautics, Incorporated  
8210 Pindell School Road  
Laurel, Maryland 20810

Commander  
Long Beach Naval Shipyard  
Long Beach, California 90802

Professor John Laufer  
Department of Aerospace Engineering  
University Park  
Los Angeles, California 90007

Dr. F. H. Harlow  
University of California  
Los Alamos Scientific Laboratory  
P. O. Box 1663  
Los Alamos, New Mexico 87544

Professor J. M. Killen  
St. Anthony Falls Hydraulic Laboratory  
University of Minnesota  
Minneapolis, Minnesota 55414

Lorenz G. Straub Library  
St. Anthony Falls Hydraulic Laboratory  
University of Minnesota  
Minneapolis, Minnesota 55414

Professor J. Ripkin  
St. Anthony Falls Hydraulic Laboratory  
University of Minnesota  
Minneapolis, Minnesota 55414

Dr. E. Silberman  
St. Anthony Falls Hydraulic Laboratory  
University of Minnesota  
Minneapolis, Minnesota 55414

Superintendent  
Naval Postgraduate School  
Attn: Library  
Monterey, California 93940

Professor A. B. Metzner  
Department of Chemical Engineering  
University of Delaware  
Newark, New Jersey 19711

Technical Library  
Naval Underwater Systems Center  
Newport, Rhode Island 02840

Office of Naval Research  
New York Area Office  
207 W. 24th Street  
New York, New York 10011

Professor V. Castelli  
Department of Mechanical Engineering  
Columbia University  
New York, New York 10027

Professor H. Elrod  
Department of Mechanical Engineering  
Columbia University  
New York, New York 10027

Engineering Societies Library  
345 E. 47th Street  
New York, New York 10017

Professor J. J. Stoker  
Institute of Mathematical Sciences  
New York University  
251 Mercer Street  
New York, New York 10003

Society of Naval Architects and  
Marine Engineers  
74 Trinity Place  
New York, New York 10006

Miss O. M. Leach, Librarian  
National Research Council  
Aeronautical Library  
Montreal Road  
Ottawa 7, Canada

Technical Library  
Naval Coastal System Laboratory  
Panama City, Florida 32401

Dr. J. W. Hoyt  
Naval Undersea R & D Center  
Pasadena Laboratory  
3202 E. Foothill Boulevard  
Pasadena, California 91107

Technical Library  
Naval Undersea R & D Center  
Pasadena Laboratory  
3203 E. Foothill Boulevard  
Pasadena, California 91107

Professor A. J. Acosta  
Department of Mechanical Engineering  
California Institute of Technology  
Pasadena, California 91109

Professor H. Liepmann  
Graduate Aeronautical Laboratory  
California Institute of Technology  
Pasadena, California 91109

Professor M. S. Plesset  
Department of Engineering Science  
California Institute of Technology  
Pasadena, California 91109

Professor A. Roshko  
California Institute of Technology  
Graduate Aeronautical Laboratories  
Pasadena, California 91109

Professor T. Y. Wu  
Department of Engineering Science  
California Institute of Technology  
Pasadena, California 91109

Director  
Office of Naval Research Branch Office  
1030 E. Green Street  
Pasadena, California 91106

Naval Ship Engineering Center  
Philadelphia Division  
Technical Library  
Philadelphia, Pennsylvania 19112

Technical Library  
Philadelphia Naval Shipyard  
Philadelphia, Pennsylvania 19112

Professor R. C. MacCamy  
Department of Mathematics  
Carnegie Institute of Technology  
Pittsburgh, Pennsylvania 15213

Dr. Paul Kaplan  
Oceanics, Inc.  
Technical Industrial Park  
Plainview, New York 11803

Technical Library  
Naval Missile Center  
Point Mugu, California 93441

Technical Library  
Naval Civil Engineering Laboratory  
Port Hueneme, California 93041

Commander  
Norfolk Naval Shipyard  
Portsmouth, Virginia 23709

Dr. H. N. Abramson  
Southwest Research Institute  
8500 Culebra Road  
San Antonio, Texas 78228

Editor  
Applied Mechanics Review  
Southwest Research Institute  
8500 Culebra Road  
San Antonio, Texas 78206

Dr. Andrew Fabula  
Code 600, Building 106  
Naval Undersea R & D Center  
San Diego, California 92132

Office of Naval Research  
San Francisco Area Office  
760 Market Street, Room 447  
San Francisco, California 94102

Library  
Pearl Harbor Naval Shipyard  
Box 400, FPO  
San Francisco, California 96610

Technical Library  
Hunters Point Naval Shipyard  
San Francisco, California 94135

Librarian  
Naval Ordnance Laboratory  
White Oak  
Silver Spring, Maryland 20910

Mr. J. Enig  
Room 3-252  
Naval Ordnance Laboratory  
White Oak  
Silver Spring, Maryland 20910

Fenton Kennedy Document Library  
The Johns Hopkins University  
Applied Physics Laboratory  
8621 Georgia Avenue  
Silver Spring, Maryland 20910

Professor E. Y. Hsu  
Department of Civil Engineering  
Stanford University  
Stanford, California 94305

Dr. Byrne Perry  
Department of Civil Engineering  
Stanford University  
Stanford, California 94305

Dr. R. L. Street  
Department of Civil Engineering  
Stanford University  
Stanford, California 94305

Professor R. C. Di Prima  
Department of Mathematics  
Rensselaer Polytechnic Institute  
Troy, New York 12181

Professor J. Lumley  
Department of Aerospace Engineering  
Pennsylvania State University  
University Park, Pennsylvania 16802

Dr. J. M. Robertson  
Department of Theoretical and  
Applied Mechanics  
University of Illinois  
Urbana, Illinois 61803

Technical Library  
Mare Island Naval Shipyard  
Vallejo, California 94592

Code 438  
Office of Naval Research  
Department of the Navy  
Arlington, Virginia 22217 (3 copies)

Code 461  
Office of Naval Research  
Department of the Navy  
Arlington, Virginia 22217

Code 463  
Office of Naval Research  
Department of the Navy  
Arlington, Virginia 22217

Code 466  
Office of Naval Research  
Department of the Navy  
Arlington, Virginia 22217

Code 468  
Office of Naval Research  
Department of the Navy  
Arlington, Virginia 22217

Code 473  
Office of Naval Research  
Department of the Navy  
Arlington, Virginia 22217

Code 481  
Office of Naval Research  
Department of the Navy  
Arlington, Virginia 22217

Code 2627  
Naval Research Laboratory  
Washington, D. C. 20390 (6 copies)

Library, Code 2629 (ONRL)  
Naval Research Laboratory  
Washington, D. C. 20390 (6 copies)

Code 6170  
Naval Research Laboratory  
Washington, D. C. 20390

Code 4000  
Director of Research  
Naval Research Laboratory  
Washington, D. C. 20390

Code 8050 (Maury Center)  
Naval Research Laboratory  
Washington, D. C. 20390

Code 8040  
Naval Research Laboratory  
Washington, D. C. 20390

Code 031  
Naval Ship Systems Command  
Washington, D. C. 20360

Code 0341  
Naval Ship Systems Command  
Washington, D. C. 20360

Code 0322 (L. Benen)  
Naval Ship Systems Command  
Washington, D. C. 20350

Code 0321 (J. Schuler)  
Naval Ship Systems Command  
Washington, D. C. 20350

Code 2052  
Naval Ship Systems Command  
Washington, D. C. 20350

Code 6034  
Naval Ship Engineering Center  
Center Building  
Prince George's Center  
Hyattsville, Maryland 20782

Code 6101E  
Naval Ship Engineering Center  
Center Building  
Prince George's Center  
Hyattsville, Maryland 20782

Code 6110  
Naval Ship Engineering Center  
Center Building  
Prince George's Center  
Hyattsville, Maryland 20782

Code 6114  
Naval Ship Engineering Center  
Center Building  
Prince George's Center  
Hyattsville, Maryland 20782

Code 6120E  
Naval Ship Engineering Center  
Center Building  
Prince George's Center  
Hyattsville, Maryland 20782

Code 6136  
Naval Ship Engineering Center  
Center Building  
Prince George's Center  
Hyattsville, Maryland 20782

Dr. A. Powell (Code 01)  
Naval Ship Research & Development Center  
Bethesda, Maryland 20034

Mr. W. M. Ellsworth (Code 11)  
Naval Ship Research & Development Center  
Bethesda, Maryland 20034

Dr. W. E. Cummins (Code 15)  
Naval Ship Research & Development Center  
Bethesda, Maryland 20034

Dr. H. R. Chaplin (Code 16)  
Naval Ship Research & Development Center  
Bethesda, Maryland 20034

Mr. G. H. Gleissner (Code 18)  
Naval Ship Research & Development Center  
Bethesda, Maryland 20034

Mr. R. Wermter (Code 152)  
Naval Ship Research & Development Center  
Bethesda, Maryland 20034

Dr. W. B. Morgan (Code 154)  
Naval Ship Research & Development Center  
Bethesda, Maryland 20034

Mr. J. B. Hadler (Code 156)  
Naval Ship Research & Development Center  
Bethesda, Maryland 20034

Library (Code 5641)  
Naval Ship Research & Development Center  
Bethesda, Maryland 20034

Mr. S. F. Crump (Code 1505)  
Naval Ship Research & Development Center  
Bethesda, Maryland 20034

Dr. P. Pien (Code 1521)  
Naval Ship Research & Development Center  
Bethesda, Maryland 20034

Mr. Paul Granville (Code 1541)  
Naval Ship Research & Development Center  
Bethesda, Maryland 20034

Mr. J. McCarthy (Code 1552)  
Naval Ship Research & Development Center  
Bethesda, Maryland 20034

Dr. Nils Salvesen (Code 1552)  
Naval Ship Research & Development Center  
Bethesda, Maryland 20034

Dr. M. Strasberg (Code 1901)  
Naval Ship Research & Development Center  
Bethesda, Maryland 20034

Code 03  
Naval Air Systems Command  
Department of the Navy  
Washington, D. C. 20360

AIR 5301  
Naval Air Systems Command  
Department of the Navy  
Washington, D. C. 20360

AIR 604  
Naval Air Systems Command  
Department of the Navy  
Washington, D. C. 20360

Code ORD 05  
Naval Ordnance Systems Command  
Department of the Navy  
Washington, D. C. 20360

Code ORD 035  
Naval Ordnance Systems Command  
Department of the Navy  
Washington, D. C. 20360

Code ORD 05413  
Naval Ordnance Systems Command  
Department of the Navy  
Washington, D. C. 20360

Code ORD 9132  
Naval Ordnance Systems Command  
Department of the Navy  
Washington, D. C. 20360

CNM PM-1  
Strategic Systems Project Office  
Department of the Navy  
Washington, D. C. 20360

Technical Division (CNM PM 11-20)  
Deep Submergence Systems Project Office  
Department of the Navy  
Washington, D. C. 20360

Oceanographer of the Navy  
Washington, D. C. 20390

Commander  
Naval Oceanographic Office  
Washington, D. C. 20390

Dr. A. L. Slafkosky  
Scientific Advisor  
Commandant of the Marine Corps (CODE AX)  
Washington, D. C. 20380

Librarian Station 5-2  
Coast Guard Headquarters  
NASSIF Building  
400 7th Street, S.W.  
Washington, D. C. 20591

Office of Research and Development  
Maritime Administration  
441 G Street, N.W.  
Washington, D. C. 20235

Division of Ship Design  
Maritime Administration  
441 G Street, N.W.  
Washington, D. C. 20235

National Science Foundation  
Engineering Division  
1800 G Street, N.W.  
Washington, D. C. 20550

Dr. G. Kulin  
National Bureau of Standards  
Washington, D. C. 20234

Science & Technology Division  
Library of Congress  
Washington, D. C. 20540

Chief of Research & Development  
Office of Chief of Staff  
Department of the Army  
Washington, D. C. 20310

Professor A. Thiruvengadam  
Department of Mechanical Engineering  
The Catholic University of America  
Washington, D. C. 20017

Dr. A. S. Iberall, President  
General Technical Services, Inc.  
451 Penn Street  
Yeadon, Pennsylvania 19050

Commander  
Portsmouth Naval Shipyard  
Portsmouth, New Hampshire 03801